



**UNIVERSITY OF NAIROBI
FACULTY OF ENGINEERING
DEPARTMENT OF ELECTRICAL AND INFORMATION
ENGINEERING**

**OPTIMIZATION OF THE ELECTROLYTE AND ELECTRODE SOLID-
SOLID INTERFACE IN A SOLID-STATE LITHIUM ION BATTERY:
APPLICATION OF ELECTROSPRAY TECHNIQUE.**

By

KARUGA SUSAN WAIYEGO

S95/50279/2015

A thesis submitted in fulfillment for the degree of Doctor of Philosophy in Nuclear Science and Technology at the Department of Electrical and Information Engineering, University of Nairobi.

©2023

DECLARATION

This thesis is my original work and has not been presented for a degree in any other university.

Signature: 

Date: ...26/11/2023.....

Karuga Susan Waiyego
S95/50279/2015

Supervisors' approval

This thesis has been submitted with our approval as university supervisors:

Prof. Lydiah Njenga
Department of Chemistry,
University of Nairobi, Kenya

Signature  :

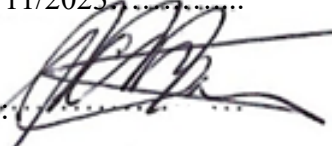
Date: 26/11/2023

Prof. E. M. Erik Kelder
Faculty of Applied Sciences,
Delft University of Technology, The Netherlands

Signature: 

Date: .26/11/2023.....

Prof. Jan C. M. Marijnissen
Visiting Professor,
University of Nairobi, Kenya

Signature: 

Date:26/11/2023.....

DEDICATION

I dedicate this work to my family. Thank you for the moral and spiritual support.

AKNOWLEDGEMENT

I am very grateful to God for the gift of life and opportunity to successfully complete this study. I am deeply indebted to my supervisors, Prof. Lydiah Njenga, Prof. Erik Kelder and Prof. Jan Marijnissen for their guidance, patience and mentorship. This endeavor would not have been possible without their support. I would like to express my deepest appreciation to the International Science Programme (ISP), Uppsala, Sweden, for the financial support offered through Prof. Michael Gatari. I would also like to thank Prof. Michael Gatari for all the advice and mentorship through out this project. I extend my sincere thanks to the Faculty of Applied Sciences in Delft University of Technology (TUDelft) for their collaboration in this research. I am grateful for the research exposure offered. I am also thankful to members of the Institute of Nuclear Science and Technilogy at the University of Nairobi for their support throughout this study. Finally, I would like to appreciate my family for their continuous encouragement and unfailing support.

ABSTRACT

Over time, the demand for thin film lithium ion batteries has grown due to technological developments that have led to the miniaturization of electronic devices which require smaller power sources. However, lithium ion batteries use flammable organic liquids as electrolytes posing a safety concern. The pursuit of solid-state electrolytes, characterized by enhanced safety and high ionic conductivities has gained significant attention. Nevertheless, ensuring the integrity between them and electrodes is crucial because unlike liquids, solids do not flow freely over surfaces limiting their integration hence poor contacts at their interfaces. For the design of thin films with good contact at their interface, this study employed the electrospray technique. A literature survey was conducted and key electrospray parameters were identified. A comprehensive design schedule for electrosprayed thin films with different surface morphologies was then developed. In addition, the cone-jet stability windows for commonly used solvents were experimentally determined by measuring voltage and flow rate values that sustained a stable cone. Thin films with porous and dense morphologies were then deposited on aluminium foil substrates and characterization of their surface morphologies was performed using scanning electron microscopy. To address the safety challenge in conventional electrolytes, $\text{Li}_6\text{PS}_5\text{Cl}$ solid-state electrolyte material was synthesized via solid-state method and its structural characterization was performed using x-ray diffraction. A bulk solid-state lithium ion cell was fabricated by pressing a three-layered pellet and characterized by galvanostatic cycling. As a result, the developed schedule provided a systematic way of designing thin films with different surface morphologies. The cone-jet stability windows for 2-propanol, ethylene glycol and NMP were defined using minimum and maximum flow rate values. From the morphological characterization of the deposited thin films, the observed surface morphologies were in agreement with the prediction of the design schedule. Using electrospray technique, thin films for solid-state lithium ion batteries with good contact at their interface were deposited without incorporating binders. The results of the galvanostatic cycling of the fabricated bulk solid-state lithium ion cells indicated low discharge capacities.

TABLE OF CONTENTS

DECLARATION	I
DEDICATION	II
ACKNOWLEDGEMENT	III
ABSTRACT.....	IV
LIST OF FIGURES	VIII
LIST OF TABLES	XI
ABBREVIATIONS AND ACRONYMS.....	XII
CHAPTER ONE	1
INTRODUCTION	1
1.1 BACKGROUND.....	1
1.2 PROBLEM STATEMENT	7
1.3 OBJECTIVES	9
1.4 JUSTIFICATION	9
1.5 SCOPE	11
CHAPTER TWO	12
LITERATURE REVIEW	12
2.1 BATTERIES	12
2.2 LITHIUM-ION BATTERY	15
2.2.1 Working principle of lithium ion batteries.....	16
2.3 ANODE MATERIALS FOR LITHIUM ION BATTERIES.....	17
2.4 CATHODE MATERIALS FOR LITHIUM ION BATTERIES.....	19
2.5 ELECTROLYTE MATERIALS FOR LITHIUM ION BATTERIES.....	21
2.5.1 Solid-state electrolyte materials for lithium ion batteries	23
2.6 THIN FILM DEPOSITION TECHNIQUES	26
2.6.1 Physical and chemical vapour deposition methods	27
2.6.2 Electrospray Technique	29
2.6.2.1 The cone-jet window.....	33

2.7 KEY ELECTROSPRAY PARAMETERS AND THEIR EFFECTS ON SURFACE MORPHOLOGY	35
2.7.1 Substrate Temperature	35
2.7.2 Type of Solvent.....	36
2.7.3 Concentration.....	36
2.7.4 Flow rate	37
2.7.5 Deposition time.....	38
2.8 APPLICATIONS OF ESD IN ENERGY PRODUCTION, STORAGE AND CONVERSION DEVICES	40
2.8.1 ESD for the fabrication of solar cells.....	40
2.8.2 ESD for the fabrication of supercapacitors.....	43
2.8.3 ESD for the fabrication of thin film lithium ion batteries.....	44
2.8.4 ESD for the fabrication of Light Emitting Diode (LEDs)	45
2.9 INSTRUMENTATION	47
2.9.1 Scanning Electron Microscopy (SEM).....	47
2.9.2 X-Ray Diffraction (XRD).....	50
CHAPTER THREE	54
METHODOLOGY	54
3.1 DEVELOPMENT OF THE DESIGN SCHEDULE	54
3.2 EQUIPMENT AND CHEMICALS	54
3.2.1 Equipment.....	54
3.2.2 Chemicals.....	54
3.3 DETERMINATION OF THE CONE-JET WINDOW.....	54
3.4 SYNTHESIS AND CHARACTERIZATION OF THE $\text{Li}_6\text{PS}_5\text{Cl}$ (ARGYRODITE) SOLID-STATE ELECTROLYTE MATERIAL	55
3.4.1 Synthesis of $\text{Li}_6\text{PS}_5\text{Cl}$ electrolyte material	55
3.4.2 Characterization of $\text{Li}_6\text{PS}_5\text{Cl}$ electrolyte material	55
3.5 ASSEMBLY AND CHARACTERIZATION OF A BULK SOLID-STATE LITHIUM ION CELL	56
3.5.1 Assembly of the bulk solid-state lithium ion cell	56
3.5.2 Characterization of the bulk solid-state lithium ion cell.....	57

3.6 DESIGN AND CHARACTERIZATION OF THIN FILMS WITH DIFFERENT SURFACE MORPHOLOGIES.....	57
3.6.1 Electrospray deposition of thin films.....	57
3.6.2 Characterization of thin film surface morphology.....	59
CHAPTER FOUR.....	61
RESULTS AND DISCUSSION	61
4.1. DEVELOPMENT OF THE DESIGN SCHEDULE	61
4.2. DETERMINATION OF THE CONE-JET WINDOW.....	65
4.3 XRD CHARACTERIZATION OF THE SYNTHESIZED ARGYRODITE (Li ₆ PS ₅ Cl) ELECTROLYTE MATERIAL.	71
4.4 ASSEMBLY OF THE BULK SOLID-STATE LITHIUM ION CELL	72
4.5 CHARACTERIZATION OF THE FABRICATED BULK SOLID-STATE LITHIUM ION CELL	72
4.6 DESIGN AND CHARACTERIZATION OF ELECTROSPRAYED THIN FILMS	78
CHAPTER FIVE	89
CONCLUSIONS AND RECOMMENDATIONS.....	89
5.1 CONCLUSIONS	89
5.2 RECOMMENDATIONS	90
REFERENCES.....	91
APPENDICES.....	151

LIST OF FIGURES

Figure 1.1. Comparison of energy densities for different rechargeable batteries based on weight and volume.....	4
Figure 1.2. Wearable OLED patch worn on the face for photo protection, acne treatment or skin rejuvenation and on the hand for wound healing or anti-inflammatory..	5
Figure 1.3. Schematic diagram of a wearable OLED patch with a flexible thin film battery..	6
Figure 1.4. Structure of a conventional lithium ion battery on the left and a solid-state lithium ion battery on the right.	8
Figure 1.5. Schematic illustration of dense (a) and porous (b) surface morphologies..	10
Figure 2.1. Li-ion battery working principle with a carbon anode and LiMn_2O_4 cathode..	17
Figure 2.2. Different solid-state electrolyte materials and their ionic conductivities at room temperature. The dotted line at the top indicates the typical lithium ion conductivity for liquid electrolytes like 1 M LiPF_6 in a mixed solvent of ethylene carbonate and dimethyl carbonate..	26
Figure 2.3. Schematic diagram of a) athermal and b) thermal PVD processes..	28
Figure 2.4. Schematic diagram thermal CVD setup..	29
Figure 2.5. Examples of electro spray modes. A. Dripping, B. Intermittent cone-jet, C. Cone-jet, varicose breakup, D. Cone-jet, whipping breakup and E. Multiple-jet.....	30
Figure 2.6. Schematic illustration of an electro spray setup.....	30
Figure 2.7. Schematic illustration of a CIGS solar cell..	41
Figure 2.8. Spray deposition process of perovskite films with and without an applied electric field..	42
Figure 2.9. Schematic illustration of an electric double layer capacitor.....	43
Figure 2.10. Schematic illustration of a thin film battery.....	45
Figure 2.11. Schematic illustration of a basic QD-LED.....	47
Figure 2.12. Schematic diagram of a scanning electron microscope.....	49
Figure 2.13. Main parts of an x-ray diffractometer..	51
Figure 2.14. Schematic representation used for Bragg's law. The diffracted x-rays show constructive interference when the distance between the two planes is an integer multiple of the wavelength.....	52

Figure 2.15. Illustration of a diffraction pattern..	53
Figure 3.1. Schematic representation of the electro spray setup used for deposition of thin films.	58
Figure 4.1. Voltage-flow rate curve used for the determination of the cone-jet window for 2-propanol.	69
Figure 4.2. Voltage-flow rate curve used for the determination of the cone-jet window for ethylene glycol.	70
Figure 4.3. Voltage-flow rate curve used for the determination of the cone-jet window for NMP.	70
Figure 4.4. The XRD pattern of $\text{Li}_6\text{PS}_5\text{Cl}$ solid-state electrolyte material that has been refined using GSAS-II software.	71
Figure 4.5. The first five charge-discharge curves of the fabricated bulk solid-state lithium ion cell cycled at a cut-off voltage of 3.7 V.	73
Figure 4.6. The first five charge-discharge curves of the bulk solid-state lithium ion cell cycled at a cut-off voltage of 4.3 V.	76
Figure 4.7. SEM image of a thin film generated by electro spraying 0.1 M LNMO precursor in 2-propanol at a flow rate of 1 mL h^{-1} and a substrate temperature of $200 \text{ }^\circ\text{C}$ for 3 h.	80
Figure 4.8. SEM image of thin film generated by electro spray of 0.3 M LNMO precursor in 2-propanol at a flow rate of 0.5 mL h^{-1} and a substrate temperature of $200 \text{ }^\circ\text{C}$ for 3 h.	81
Figure 4.9. SEM image of thin film generated by electro spray of 1 M LiCl precursor in DMSO (boiling point of $189 \text{ }^\circ\text{C}$) at a flow rate of 0.4 mL h^{-1} and a substrate temperature of $200 \text{ }^\circ\text{C}$ for 7 h.	82
Figure 4.10. SEM image of a thin film generated by electro spraying 1 M LNMO precursor in 2-propanol at a flow rate of 2 mL h^{-1} and a substrate temperature of $100 \text{ }^\circ\text{C}$ for 3 h.	83
Figure 4.11. SEM image of a thin film generated by electro spray using 0.04 M LNMO precursor in 2-propanol at a flow rate of 2 mL h^{-1} and a substrate temperature of $350 \text{ }^\circ\text{C}$ for 2 h.	84
Figure 4.12. SEM image of a thin film generated by electro spray using 0.04 M LNMO precursor in 2-propanol at a flow rate of 2 mL h^{-1} and a substrate temperature of $100 \text{ }^\circ\text{C}$ for 2 h.	84

Figure 4.13. SEM image of thin film generated by electrospray of 0.5 M LNMO precursor in 2-propanol and ethylene glycol at a flow rate of 2 mL h ⁻¹ and a substrate temperature of 200 °C for 1 h.	85
Figure 4.14. SEM image of thin film generated by electrospray of 0.05 M LiCl precursor in DMSO at a flow rate of 0.4 mL h ⁻¹ and a substrate temperature of 200 °C for 1 h.....	87
Figure 4.15. Cross section SEM image of two layers deposited sequentially using 0.5 M LNMO precursor in 2-propanol and ethylene glycol (1:1). Bottom dense layer was electrosprayed at a flow rate of 2 mL h ⁻¹ and a substrate temperature of 200 °C for 1 h. Top layer was electrosprayed at a flow rate of 0.5 mL h ⁻¹ and a substrate temperature of 200 °C for 3 h.	88

LIST OF TABLES

Table 2.1. A comparison of key characteristics for four different commonly used secondary batteries.....	15
Table 3.1. Electro spray parameters for different experiments.....	59
Table 4.1. A design schedule for electro sprayed thin films with different surface morphologies.....	61
Table 4.2. Properties of three different liquids whose cone-jet operation window was experimentally determined.....	66
Table 4.3. Calculated flow rate values for 2-propanol, NMP and ethylene glycol and their respective viscosity numbers.	67
Table 4.4. Experimentally determined flow rate and voltage values defining the cone-jet window for each precursor liquid used.	68
Table 4.5. A summary of charge and discharge capacities with the respective coulombic efficiencies for the first bulk solid-state cell.....	75
Table 4.6 A summary of charge and discharge capacities with the respective coulombic efficiencies for the second bulk solid-state cell.	77
Table 4.7 Properties of the precursor liquids and respective calculated droplet sizes.	79

ABBREVIATIONS AND ACRONYMS

ALD	Atomic layer deposition
a-Si	Amorphous silicon
BIPV	Building-integrated photovoltaics
BSE	Backscattered electrons
CdTe	Cadmium telluride
CdS	Cadmium sulfide
CIGS	Copper indium gallium selenide
CVD	Chemical vapour deposition
CO ₂	Carbon dioxide
DMSO	Dimethyl sulfoxide
EDL	Electric double layer
EESS	Electrical energy storage systems
EHDA	Electrohydrodynamic atomization
ESD	Electrostatic spray deposition
GHG	Greenhouse gases
IEA	International energy agency
LEDs	Light emitting diode
Li-ion	Lithium ion
LMNO	Lithium nickel manganese oxide
CH ₄	Methane
NO ₂	Nitrogen dioxide
NMC	Lithium nickel manganese cobalt oxide
NMP	N-Methyl-2-pyrrolidone
Ni-Cd	Nickel cadmium
Ni-H	Nickel metal hydride
OLEDs	Organic light emitting diodes
O ₃	Ozone
PBM	Photobiomodulation
PLD	Pulsed laser deposition
PVD	Physical vapour deposition
PV	Photovoltaic
Q _{min}	Minimum flow rate

Q_{\max}	Maximum flow rate
QDs	Quantum dots
SE	Secondary electrons
SEM	Scanning electron microscopy
UN-SDG	United Nations Sustainable Development Goals
VN	Viscosity number
$H_2O_{(g)}$	Water vapour
XRD	X-ray diffraction

CHAPTER ONE

INTRODUCTION

1.1 Background

Climate change is one of the most pervasive and threatening problems across the world today. This has been linked to the rising concentrations of greenhouse gases (GHG) like carbon dioxide (CO₂), methane (CH₄), nitrogen dioxide (NO₂), water vapour (H₂O_(g)) and ozone (O₃) in the atmosphere. Usually, an accumulation of these gases leads to a rise in temperature at the Earth's atmosphere and this process is known as the greenhouse effect. Usually, the greenhouse gases trap infrared radiation produced from the surface of the Earth following absorption of sunlight making the planet to heat up. Consequently, the changes in temperature have placed the ecosystems under stress and have also affected human well-being. Unfortunately, the mean global temperature has been increasing continuously with industrial revolution due to the increasing concentrations of greenhouse gases. Among these gases carbon dioxide is the most abundant since it accounts for about two-thirds of the total concentration of greenhouse gases and most of it has been reported to be produced from the burning of fossil fuels. Therefore, efforts to mitigate the increasing concentrations of CO₂ require urgent actions that can lead to rapid transition from fossil fuels to clean energy sources (Letcher, 2021; Rajak, 2021; Soeder, 2021; Clayton, 2020; Arroyo and Miguel, 2019; Houghton, 2005).

Irrespective of their finite nature and their contribution to global warming and climate change, more than 80 % of the global energy is generated from fossil fuels. Their domination in the global energy system is attributed to their high energy densities. This has led to their continued use with increasing population, technological and economic growth (Dale, 2022; Welsby et al., 2021; Kopp, 2020; Kotcher et al., 2019; GOK, 2018; Landrigan et al., 2018; Le Quéré et al., 2018). Some of the efforts that have been put in reducing GHG emissions include the integration of clean energy from renewable sources in electricity generation and also the replacement of internal combustion engines with battery powered electric vehicles (Ichikawa et al., 2020; Kodama, 2015; Poizot & Dolhem, 2011). As a result, renewable energy had its largest increase in 2019,

with an installed power capacity of more than 200 gigawatts. During this time, emissions remained stable but the world was still far from attaining its target of being carbon neutral and limiting global temperature rise to 1.5 °C, as indicated in the Paris Agreement (REN21, 2020; UN, 2019). Nevertheless, in 2021 the world experienced a rebound due to the extremely rapid economic recovery after Covid-19. In this year, carbon dioxide emission from energy combustion and industrial processes increased by 6 % from the recorded concentration in 2020 pushing emissions to the highest annual value of 36.3 gigatonnes (IEA, 2021). Such trends have made it difficult to achieve the sustainable development goals on affordable and clean energy and on climate action. Nonetheless, transitioning from fossil fuels to energy sources that are clean and renewable is an indispensable necessity (UN-SDG, 2022).

Therefore, to match the growing energy demands as well as support the rapid penetration of renewable energy, sources like solar, hydropower, wind, biomass and geothermal can reduce the over reliance on fossil fuels by providing energy that is clean. Moreover, economic and policy mechanisms needed to support the penetration of renewable energy systems have evolved over time. For instance, the automobile industry is experiencing a major reform with the shift to hybrid and electric vehicles (Sacchi et al., 2022; Saleh et al., 2022; Zhang et al., 2022; Iclodean et al., 2017). Nonetheless, the renewable energy sources are intermittent due to their dependency on time, location and weather. This compromises the reliability, resiliency and stability of the generated power. With an aim of solving this problem, the integration of electrical energy storage systems (EESS) into the power generation process has been considered as a viable and promising approach. This entails converting the generated electrical energy to a form, like chemical energy which can be stored in EESS, and later converting the stored energy back to electricity when needed (Looney, 2020; Wenge et al., 2020; Acar, 2018; Diouf & Pode, 2015; Pei et al., 2016; Poizot & Dolhem, 2011).

There are different types of electrical energy storage systems like mechanical, chemical, thermal and electrochemical systems and each of them presents its own limitations which influence its range of application. For renewable energy storage, electrochemical systems have gained a considerable attention over time due to their high efficiency, scalability and low maintenance. These systems have also shown flexibility in terms of

power and energy characteristics enabling them to meet different grid functions. Examples of such systems include batteries, super capacitors, fuel cells and photovoltaic devices (Al-Shaqsi et al., 2020; Hossain et al., 2020; Aneke & Wang, 2016; Cho et al., 2015; Badwal et al., 2014; Yoo et al., 2014). Among the electrochemical energy storage systems, rechargeable batteries are more popular and they have been used in providing both stationary and portable energy storage. They exhibit high efficiency, sizes independent of power, operation at room temperature, long charge and discharge cycle life (Kelder et al., 2018; Alotto et al., 2014). As indicated in Fig. 1.1, there is a wide range of rechargeable batteries in the market today such as lithium ion (Li-ion), lead acid, nickel metal hydride (Ni-H) and nickel cadmium (Ni-Cd).

Among the different battery systems, lead acid is the most used technology because of its maturity, affordability, reliability, fast response and low self-discharge rate. Nonetheless, a charge control method is required to protect the battery from over charging and over discharging leading to high maintenance costs (Banguero et al., 2018). Consequently, lithium ion batteries have gained preference over time because they provide high energy density, long cycle life, low self-discharge, abuse-tolerant properties and low maintenance. They also show an outstanding electrochemistry attributed to the small ionic radius, low molecular weight and low redox potential of lithium (Diouf & Poda, 2015; Hossain et al., 2020; Kotobuki & Koishi, 2013; Nitta et al., 2015; Raijmakers et al., 2019). Lithium ion batteries have also demonstrated great potential in the development of large scale energy storage systems and in the powering of electric vehicles. In addition, they have also found a wide application in portable electronic devices like digital cameras, laptop computers and cell phones (Liang et al., 2019a; Banguero et al., 2018; Ayoub & Karami, 2015; NED, 2013).

Lithium ion batteries can also provide reliable backup power for a nuclear power plant. To ensure the uninterrupted operation and safety in a nuclear power plant during the occurrence of a power failure, a reliable backup power system is needed. The main role of the backup power system is to supply power to critical electrical systems that ensure safety and reliability in the event of an emergency. Such systems include the emergency core cooling system, the containment and the shutdown system. In case of power

failure, a continuous supply of electricity is required in nuclear reactor to maintain cooling even after shut down. In the Fukushima nuclear accident that occurred in Japan following an earthquake, electrical systems were disrupted and there was no backup emergency power system. This led to inadequate cooling of the reactor and release of radioactive materials. In response to this, several countries reviewed their nuclear safety regulations by strengthening the requirement for an emergency power supply system. Conventionally, diesel generators have been applied as backup power systems but they face challenges related to maintenance, potential fuel supply disruptions and they leave behind a significant carbon footprint. Lithium ion battery is a promising technology due to its higher energy density, faster response times, reduced maintenance requirements and environmental friendliness (Abdussami and Gabbar, 2019; Chang and Sulley, 2018; S. Park et al., 2018).

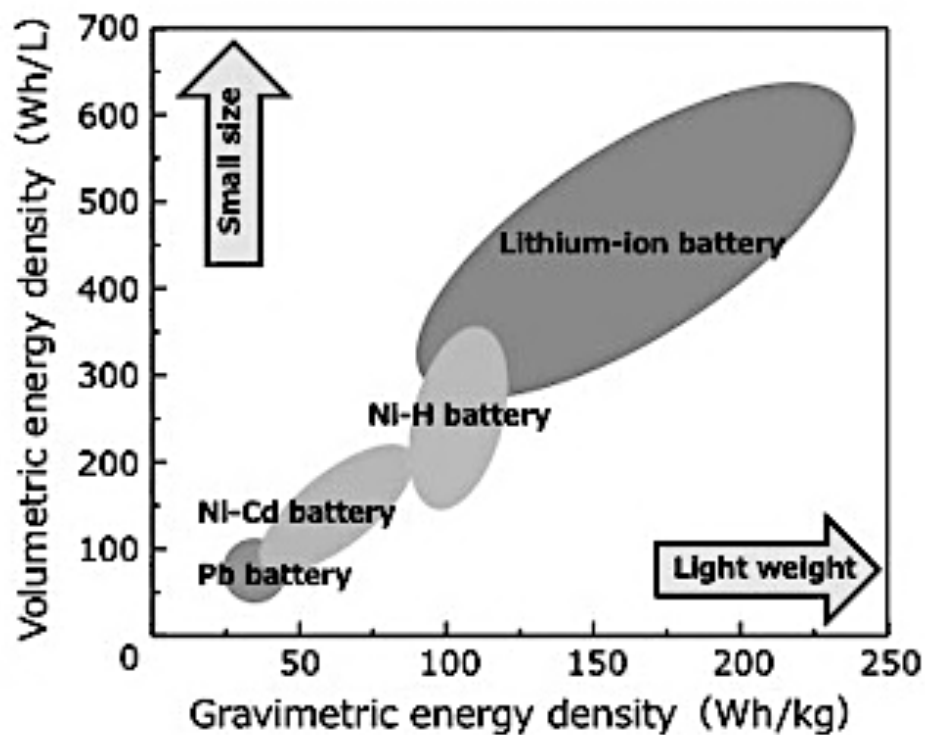


Figure 1.1. Comparison of energy densities for different rechargeable batteries based on weight and volume. Adapted from Notohara et al. (2020)

With the current technological developments, lithium ion batteries are also promising power sources for miniaturized electronic devices. Such devices include on-chip power sources, smart cards, microelectronic mechanical systems, implanted or wearable

medical elements like neuro-stimulators, drug delivery chips, cochlear implants, cardiac pace makers and smart lenses which could be used for artificial intelligence or health monitoring. For instance, Fig 1.2 shows a wearable photobiomodulation (PBM) OLED patch that induces therapeutic biological changes when molecules in body tissues or cells interact with light (Acha et al., 2020; Kanazawa et al., 2020; Liu et al., 2020; Liang et al., 2019a; Lee et al., 2018).

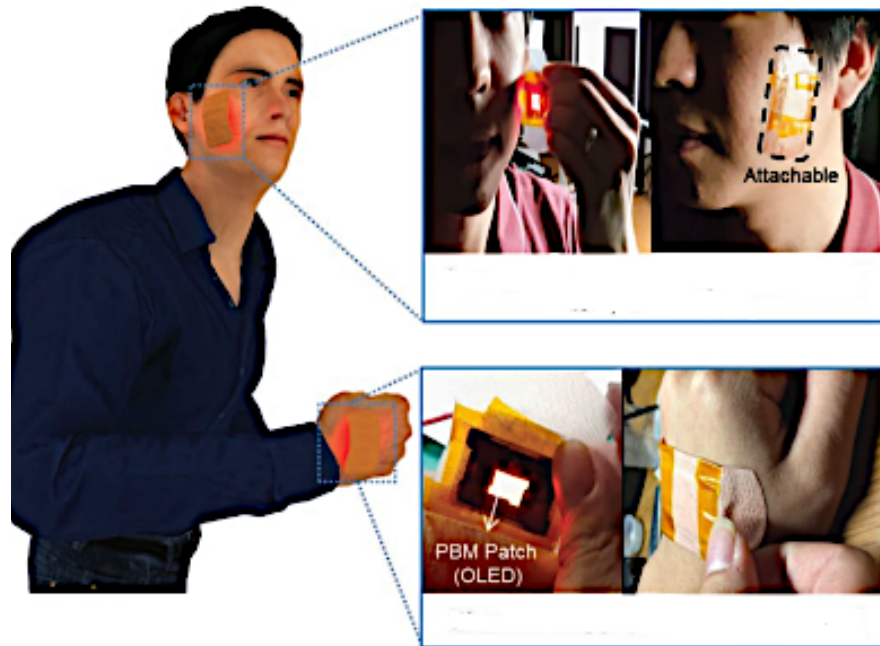


Figure 1.2. Wearable OLED patch worn on the face for photo protection, acne treatment or skin rejuvenation and on the hand for wound healing or anti-inflammatory. Adapted from Song et al. (2020).

As shown in Fig. 1.3, such miniaturized devices require an implanted battery with small dimensions that are similar to those of the device. This has led to the need for evolution in the conventional lithium ion batteries from their standard bulk sizes to thin film battery systems (Ge et al., 2020; Iclodean et al., 2017; Duluard et al., 2013). The fabrication of thin films can be achieved by different processes which involve material synthesis, material deposition onto a substrate, adhesion of the material onto the substrate and subsequent film growth. The selected fabrication process must however not compromise the electrochemical properties of the designed battery. In this study, electrospray deposition technique in the cone-jet mode was used to design and deposit thin films with different surface morphologies for thin film lithium ion batteries.

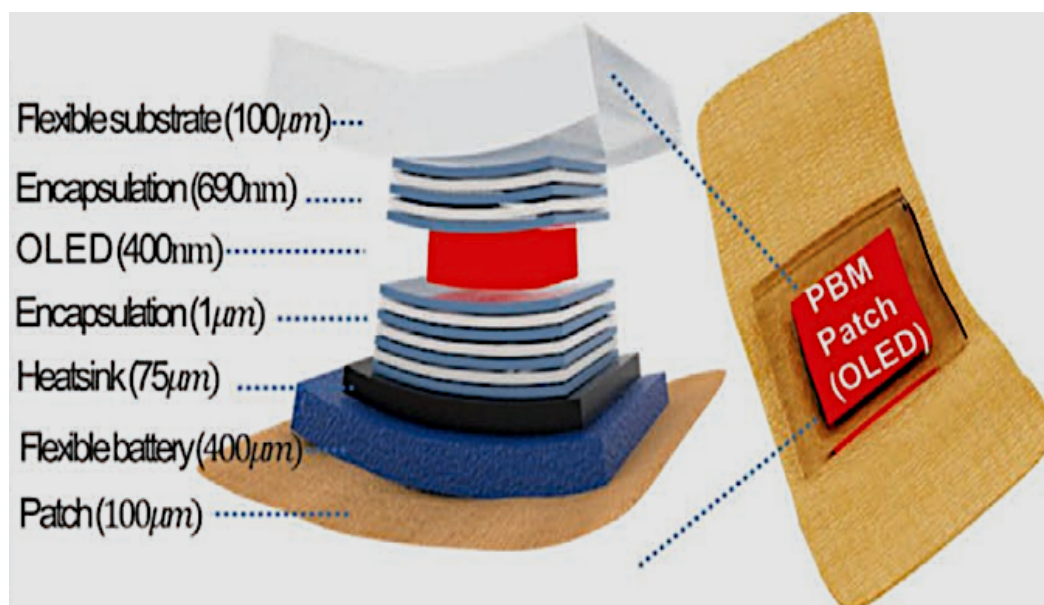


Figure 1.3. Schematic diagram of a wearable OLED patch with a flexible thin film battery. Adapted from Song et al. (2020).

Electrospray technique also referred to as electrohydrodynamic atomization (EHDA) or electrostatic spray deposition (ESD) is outstanding in the deposition of thin films due to its unique ability to generate droplets that are charged hence the achievement of higher deposition efficiency. In this process, an electric field is used to break up a liquid into airborne droplets. Usually, the applied electric field creates shear stress on the liquid's surface leading to elongation of a jet that disintegrates into tiny charged droplets. The droplets repel one another due to Coulomb repulsion among them, which causes self-dispersion on the substrate and uniform deposition on inhomogeneous surfaces (Lee et al., 2007; Yoon et al., 2003; Cao and Prakash, 2002; Nishizawa et al., 1998; Chen et al., 1995; van Zomeren et al., 1994). When performing an electrospray experiment, changing the flow rate and/or the applied electric field strength, leads to distinct electrospray modes. The electrospray modes differ in their droplet formation mechanism and droplet sizes. Among these modes, cone-jet is the most studied in production of thin layers due to its ability to generate particles that are spherical in shape, with a narrow size distribution and much smaller than the nozzle diameter (Agostinho et al., 2013; Jaworek et al., 2009)

In the cone-jet mode, scaling laws that define the electric current flowing through the liquid and the generated droplet size have been developed (Yurteri et al., 2010). These scaling laws show that by adjusting different parameters, droplet size and final particle size can be controlled easily (Scheideler & Chen, 2014). The ability to control generated droplet or particle sizes allows electrospray deposition technique in the cone-jet mode to find a wide application in different fields like nanotechnology and microelectronics (Jaworek & Sobczyk, 2008). Additionally, based on the liquid precursor's chemical and physical properties like conductivity, surface tension, density, concentration, viscosity and experimental parameters such as nature of the substrate, deposition time and deposition temperature, the surface morphology of the deposited film can be tailored to suit preference (Gañán-Calvo et al., 2018; Rosell-Llompart et al., 2018; Neagu et al., 2006). This is crucial because the final performance of a thin film is significantly influenced by its surface morphology (Kelder et al., 2018).

1.2 Problem statement

Lithium ion batteries use organic liquids as electrolytes which are flammable posing a safety concern (Fig. 1.4). Usually, they consist of lithium hexafluorophosphate (LiPF_6) dissolved in ethylene carbonate, dimethyl carbonate, propylene carbonate or their mixtures. The organic electrolytes make the batteries prone to fire accidents when operated under conditions that lead to mechanical, thermal or electrical abuse. Such abuse may be experienced in the occurrence of a short circuit, physical penetration or exposure to high temperatures. As a result, exothermic reactions get triggered within the battery resulting to a self-enhanced irreversible chain reaction. This is referred to as a thermal runaway and it leads to uncontrollable increase in temperature and pressure within the battery making it to explode into flames (Tran et al., 2022; Kong et al., 2018; Kalhoff et al., 2015). Several incidents of lithium ion battery and explosions have been reported. For instance, (Saxena et al., 2018) gives a comprehensive review of numerous e-cigarette fire and explosion incidents. In January 2013, all Boeing 787 Dreamliners were grounded indefinitely due to safety concerns over the failure of lithium ion batteries that provide auxiliary startup power and on-board backup power during flight (Williard et al., 2013). Also, a Tesla electric car was reported to catch fire in 2015 as a result of battery failure and for a similar reason Samsung had to recall Note 7 smartphones in 2016 (Xu et al., 2021a; Kong et al., 2018).

Attempts to replace the flammable organic liquid electrolytes with non-flammable solid-state electrolytes have not been successful. This is because unlike liquids, solids do not flow freely over surfaces therefore this limits integration of electrodes with the solid electrolyte hence poor contacts at their interfaces. Considering that charge transfer reactions take place at the contact interfaces, there is a need to adopt a technique that increases the contact areas between the battery's solid components. Otherwise, high resistances are experienced creating a hindrance to the development of high-power solid-state batteries (Joshi et al., 2021; Moitzheim et al., 2019; Kelder et al., 2018; Haruta et al., 2016; Wang et al., 2015a; Tatsumisago et al., 2013). Another drawback is that during charging and discharging cycles, lithium ion batteries experience capacity fading due to the resulting volume changes caused by contraction and expansion of the electrodes (Gantenbein et al., 2019; Koerver et al., 2017a; Tian et al., 2017; Luntz et al., 2015).

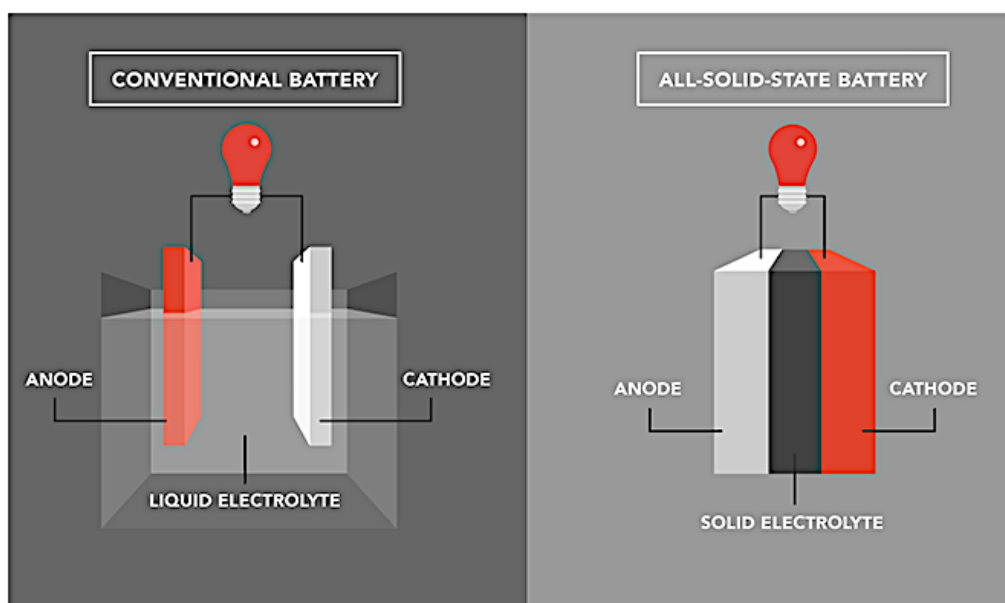


Figure 1.4. Structure of a conventional lithium ion battery on the left and a solid-state lithium ion battery on the right. Adapted from Lykiardopoulou (2021).

Therefore, for solid-state thin film lithium ion batteries to operate optimally there is need for a rational design process that promotes good interfacial contact between the electrodes and the solid-state electrolyte. The process must also allow for the design of thin films with different surface morphologies to accommodate the volume changes

during cycling. Though promising, the studies on electrospray technique do not give a systematic way of designing the different surface morphologies and the cone-jet operational window is also not clearly defined (Marijnissen et al., 2023).

1.3 Objectives

The main objective of this study was to design a dense electrolyte film and a porous electrode film with a good contact at their interface for thin film lithium ion batteries using electrospray technique.

Specific objectives

- i. To develop a design schedule for thin films with different surface morphologies.
- ii. To investigate the cone-jet operation window for commonly used electrospray solvents.
- iii. To design thin films with different surface morphologies.
- iv. To synthesize and characterize the selected solid-state electrolyte material.
- v. To assemble a bulk solid-state lithium ion cell.

1.4 Justification

With an aim of addressing climate change and its impacts, transitioning from fossil fuels to energy sources that are clean and renewable is an indispensable necessity as emphasized by the Sustainable Development Goal 13 on climate action. In addition, the adoption of renewable energy sources would ensure universal access to clean and affordable energy leading to the achievement of the Sustainable Development Goal 7 which focuses on ensuring access to affordable, reliable, sustainable and modern energy for all. To address the intermittency of these renewable energy sources, lithium ion batteries are promising energy storage systems because they show high energy densities, long lifespan and high power densities for different applications. For instance, they have found a wide application in portable electronic devices like cell phones, laptop computers and digital cameras. Over time, lithium ion batteries have also shown great potential in the development of large scale energy storage systems and in the powering of electric vehicles (Liang et al., 2019b; Banguero et al., 2018; Ayoub and Karami, 2015; NED, 2013). With the current technologically developments, lithium ion batteries are also promising power sources for miniaturized electronic devices (Duluard

et al., 2013; Ge et al., 2020; Iclodean et al., 2017). However, the next generation of lithium ion batteries should show diminished flammability by replacing the flammable organic liquid electrolytes with safer materials. Among the different materials under investigations, solid-state or inorganic electrolyte materials are a promising area of research for improving the safety of lithium ion batteries. This is because they are nonflammable and their ionic conductivities are high matching those of the commercialized organic liquid electrolytes (Baniya et al., 2023; Nikodimos et al., 2023; Chen et al., 2021a; Wu et al., 2021a; Schwietert et al., 2020; Liang et al., 2019c; Lv et al., 2019; Manthiram, 2017).

For the design of thin film solid-state lithium ion batteries several deposition techniques have been proposed. Most of these deposition techniques require high vacuum installations or high deposition temperatures leading to high production costs. However, electrospray technique is less expensive, easy to control and more efficient with almost all the materials being deposited on the substrate without wastage. In addition, electrospraying in the cone-jet mode produces spherical monodisperse droplets whose diameter is in the nano/micrometer range and model equations for droplet and particle size estimation are available. Further to this, different surface morphologies as illustrated in Fig. 1.5 can be achieved by altering experimental parameters and physicochemical properties of the precursor material (Bodnár et al., 2018; Hong et al., 2017; Jaworek et al., 2018a; Kelder et al., 2018; Yurteri et al., 2010).

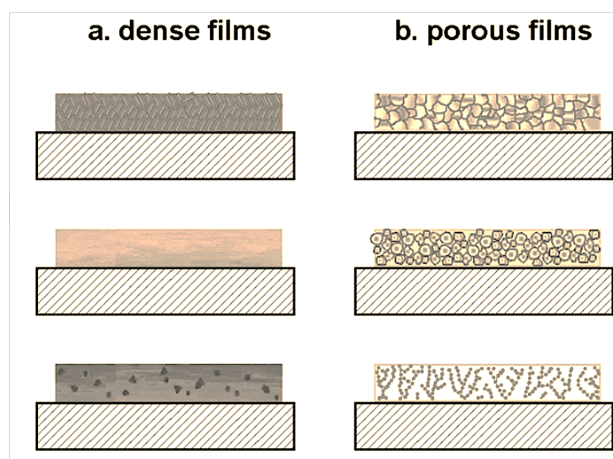


Figure 1.5. Schematic illustration of dense (a) and porous (b) surface morphologies. Adapted from Jaworek et al. (2016).

Usually, the preferred morphologies for lithium ion battery electrodes are porous or hollow surfaces. Such morphologies would solve the problem of capacity fading during cycling since they would provide enough room for contraction and expansion. Besides, these would offer more reaction sites and provide improved electron transport. On the contrary, the electrolyte layer is required to be dense so that it can be effective in inhibiting short circuits (Pei et al., 2016; Dickerson, 2012; Koike & Tatsumi, 2007; Koike and Tatsumi, 2005; Zhang et al., 2009; Yu et al., 2006a). In order to increase the area of contact between the solid-state electrolyte and the electrodes, electro spraying technique is promising. This is because of its unique ability to generate coatings from charged droplets hence higher deposition efficiency can be achieved even on inhomogeneous surfaces. While performing electro spray experiments, determination of the cone-jet operational window is important since it could also guide on how to modify the parameters of a precursor liquid (Marijnissen et al., 2023).

1.5 Scope

The selected solid-state electrolyte material for this study was the argyrodite ($\text{Li}_6\text{PS}_5\text{Cl}$). The material was synthesized via solid-state synthesis method and its structural characterization was performed using x-ray diffraction (XRD). Bulk lithium ion cells were fabricated to evaluate the performance of the synthesized electrolyte material. A design schedule for electro sprayed thin films was developed from literature. Also, cone-jet operation window for common electro spray liquids was defined experimentally and by deriving equations for the maximum and minimum flow rates. Thin films for lithium ion battery were then designed using the developed schedule. Surface characterization of the electro sprayed thin films was carried out using scanning electron microscopy (SEM). Characterization of the fabricated lithium ion cells was done by galvanostatic cycling.

CHAPTER TWO

LITERATURE REVIEW

2.1 Batteries

Batteries are dated back in the year 1800 when Alessandro Volta, an Italian physicist, invented the first source of continuous current. Over the decades, they have evolved from non-rechargeable (primary) to rechargeable (secondary) systems which convert chemical energy that is stored within them into electrical energy so as to produce electric current that can be used to perform work. Upon draining the internal capacity of a primary battery, it is discarded since its electrodes undergo irreversible chemical changes. Such reactions render the battery unchargeable hence disposable. Primary batteries are therefore commonly referred to as non-rechargeable batteries, disposable batteries or dry cells. Examples of such batteries include zinc carbon also known as Leclanché batteries, metal air depolarized batteries and alkaline zinc manganese dioxide. Such batteries are commonly used in flashlights, remote controls, clocks and portable radios. Primary batteries are also used in specialized applications like powering implantable cardiac pacemakers, hearing aids and computer memory back-ups (Owens et al., 2009; Viswanathan, 2017; Hosseiny and Wessling, 2011; Kordesch and Taucher-Mautner, 2009).

On the other hand, secondary batteries are more economical and ecofriendly since they can be reused after discharging. The batteries are uniquely identified according to their chemical compositions and each battery type shows unique characteristics like energy density, voltage, cycle life and self-discharge rate as indicated in Table 2.1. Among them, lead acid battery has the highest technical maturity and lowest cost. It also shows high stability and an overall efficiency of around 75 % to 85 %. However, its main drawbacks are short life cycle, bulky size, heavy weight, low specific energy and power, lead toxicity and high maintenance requirements. Using nickel oxide hydroxide and cadmium metal as electrodes, nickel cadmium batteries (Ni-Cd) have longer lifetimes and when subjected to high currents, they exhibit great capacity. However, they show adverse memory effects, which can lead to a significant deterioration in battery life. They are also more expensive and cadmium is highly toxic making them to be banned in several countries. Compared to lead acid batteries, Ni-Cd batteries have slightly

lower overall efficiencies of 60 % to 70 %. Another battery type is the nickel metal hydride (Ni-H) which uses nickel oxide hydroxide and a metal alloy as electrodes. It has a higher energy density than Ni-Cd batteries (1.5 to 2 times) and shows high power capability, it tolerates over charging and over discharging, it shows environmental compatibility and has a longer life span. However, this battery type is faced with the challenge of leakage and compared to lithium ion batteries, its energy density is relatively low. Consequently, lithium ion batteries stand out among secondary batteries because of their high energy efficiency in the range of 85 % to 95 %, high energy and power density, low rate of self-discharge, zero memory effect and relatively long cycle life. These properties allow them to provide high current usage and long-term operation as required by most electronic devices (Liang et al., 2019a; Ding et al., 2019; Acar, 2018; Kong et al., 2018; Yu et al., 2017; Sehwat et al., 2016; Cho et al., 2015; Deng, 2015).

To define the performance of a particular battery, capacity can be experimentally determined. It is the measure of the electrical charge stored in a battery expressed in ampere hours (Ah). Typically, it gives a clear indication of the maximum energy that can be drawn out of the battery due to electrochemical reactions taking place. It is determined by the cathode material's mass meaning that in order to obtain high capacity the mass of inactive compounds in the battery should be minimized. Nonetheless, a battery's capacity can change significantly from the nominal value since it is affected by the battery's age, operating temperature and the charging or discharging conditions. For instance, if a battery is quickly discharged using a current rate that is high, then the maximum energy that can be drawn out of that battery is reduced and a low battery capacity is recorded. Alternatively, if a battery is slowly discharged using a current rate that is low, more energy can be drawn out of the battery and a high battery capacity is recorded. Also, at high temperatures the battery capacity is higher than at low temperatures. However, intentionally elevating battery temperature so as to increase battery capacity is not recommended because it decreases a battery's lifetime (Aktaş & Kirçiçek, 2021; Bauomy et al., 2021; Honsberg & Bowden, 2019; Farahani, 2008; Kirchev, 2015).

Another important parameter is electromotive force which refers to the energy generated by the battery per coulomb of charge passing through it expressed in volts. It determines the energy density of the battery which is the available energy per given size. The higher the energy generated by the cell, the smaller the required size of the battery for a particular application. For instance, aqueous cells have an electromotive force of around 1.5 V which is the voltage at which dissociation of the water in the electrolyte occurs via electrolysis. Therefore, in a particular application more cells are connected to deliver required energy leading to large battery sizes compared to non-aqueous cells where a smaller number of cells are connected because they give higher electromotive force of 3 V or more leading to higher energy densities and smaller battery sizes (Aktaş & Kirçiçek, 2021; Farahani, 2008; Tamilselvi et al., 2021).

To evaluate the effectiveness of the transfer of electrons within a battery, coulombic efficiency also referred to as current efficiency or faradaic efficiency is used. Typically, it defines how efficiently a battery can convert energy from chemical to electrical form. Coulombic efficiency is obtained from the ratio of the discharge capacity (total charge drawn out of the battery) to the charge capacity (total charge put into the battery) over a full cycle. In a lithium ion battery, it is used as an indication of capacity loss per cycle. This helps in the prediction of the remaining battery cycle life. Coulombic efficiency can be affected by decomposition of the electrolyte, physical or chemical variations in electrode materials, ambient temperature and charge-discharge current rate (Nzereogu et al., 2022; Wang et al., 2021a; Wang et al., 2015; Xiao et al., 2020a; Yang et al., 2018).

Table 2.1. A comparison of key characteristics for four different commonly used secondary batteries. Adapted from (Liang et al., 2019b).

Characteristics	Li-ion	Ni-MH	Ni-Cd	Lead acid
In use since	1991	1990	1950	Late 1800s
Battery voltage (V)	3.7	1.2	1.2	2.0
Toxicity	Low	Low	High	High
Cycle life (to 80% of the initial capacity)	500-2000	1000	1500	300
Self-discharge per month (%)	< 10	30	20	5
Volumetric energy density (Wh L ⁻¹)	350 - 700	140 - 300	150 - 190	60 - 110
Gravimetric energy density (Wh kg ⁻¹)	170 - 250	60 - 120	40 - 60	30 - 50
Overcharge tolerance	Low	Low	Moderate	High
Operating temperature range	- 20 to 60	- 20 to 60	- 40 to 60	- 20 to 60
Fast charging time (h)	1 or less	1 - 4	1	8 - 16

2.2 Lithium-ion battery

Lithium-ion batteries show an exceptional combination of high energy and power density. Consequently, it is the technology of choice for electric vehicles and portable electronics. The lithium ion battery was invented by Akira Yoshino in the early 1980s with an aim of creating a small and light weight rechargeable battery for portable electronics (Yoshino, 2012). A decade later, in the early 1990s, the battery was commercialized by Sony to power a video camera. Currently, lithium ion batteries are applied widely in consumer electronics like digital cameras, laptops, mobile phones and other portable electronic devices. Other than the small devices, these batteries have also been used in electric tools, bicycles and automobile power supplies to meet the growing demand for energy and environmental conservation. To generate the needed voltage and capacity, several lithium ion cells are connected together in either parallel or series. Each cell consists of a positive electrode also known as the cathode, a negative electrode also known as the anode and an electrolyte in between the two electrodes which allows

ion transfer between them (Kelder et al., 2018; Notohara et al., 2020; Sehrawat et al., 2016; Tomaszewska et al., 2019). Conventionally lithium ion batteries use transition metal oxides (TMO) like lithium cobalt oxide (LiCoO₂), lithium manganese oxide (LiMn₂O₄) or lithium iron phosphate (LiFePO₄) as positive electrodes and graphite as negative electrode (Cheng et al., 2022; Feng et al., 2018; Zuo et al., 2017; Song et al., 2014; Nguyen et al., 2011). However, efforts to improve on the battery performance have led to the investigation of other materials as discussed in sections below.

2.2.1 Working principle of lithium ion batteries

During the operation of lithium ion batteries, reversible electrochemical reduction and oxidation reactions take place between the cathode and the anode. For a lithium ion battery with LiCoO₂ cathode and graphite anode, the operation voltage range is 3.7 to 4.2 V. To understand the battery chemistry, the LiCoO₂ cathode material is expressed as Li_xCoO₂ where 0.5 < x < 1.0 indicating the concentration range of lithium during operation. For instance, when the battery is fully discharged, x = 1 an electric current is therefore applied to charge the battery to x = 0.5. As shown in Fig. 2.1, the working principle of lithium ion batteries is based on charge and discharge processes whereby lithium ions are transferred between the cathode and the anode through the electrolyte. Discharge occurs when the battery is used as a source of power for electronic and electrical devices whereby the intensity of the discharging current depends on the power required by the device. During this process, the anode is oxidized and the cathode is reduced. Oxidation of a carbon anode causes the release of lithium ions from the carbon material into the electrolyte as shown in the half reaction below.



The released Li⁺ ions are then inserted/intercalated into the cathode under Co reduction from Co⁴⁺ to Co³⁺ as shown in the half reaction below.



The full reaction becomes;



Note that, the arrows indicate left to right for discharging and right to left for charging.

As observed from the above equations, the movement of ions from the anode to the cathode is accompanied by the release of electrons which flow in the external circuit

and chemical energy is converted to electrical energy. Ultimately, the discharge process lowers the battery voltage. During charging, an external voltage is applied to the circuit forcing electrons and lithium ions to flow from the positive electrode towards the negative electrode, in which case electrical energy is converted to chemical energy. In this process, oxidation takes place at the cathode and reduction at the anode. As mentioned earlier, the battery attains a voltage of 4.2 V when fully charged. Usually, low intensities of the charging current imply long charging times while high charging currents intensities imply short charging times. In summary, lithium ions are stored in the anode during the charging process and released during discharging (Theerthagiri et al., 2020; Raccichini et al., 2019; Trivedi et al., 2019; Da Silva et al., 2016).

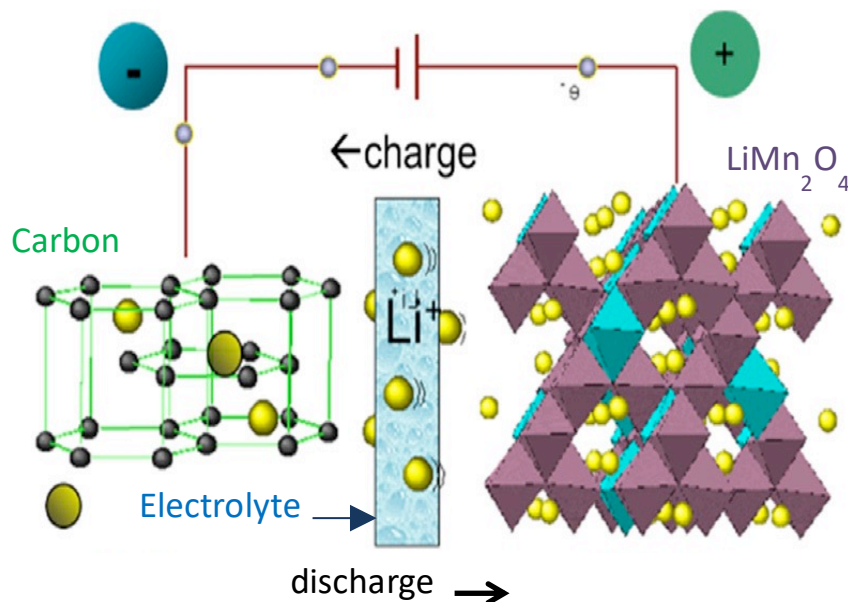


Figure 2.1. Li-ion battery working principle with a carbon anode and LiMn_2O_4 cathode. Adapted from Kelder et al. (2018).

2.3 Anode materials for lithium ion batteries

For the longest time, graphite has been used as the main negative electrode material in commercialized lithium ion batteries and it also serves as a universal reference when evaluating new materials. It is a popular commercial anode material because of its affordability, high conductivity, stable reversibility and long cycle life. However, graphite exhibits relatively low capacity which limits its feasibility in current market demands for high power lithium ion batteries (Zhao et al., 2022a; Andersen et al., 2021; Xiao et al., 2021; Zhang et al., 2021; Asenbauer et al., 2020; Moradi & Botte, 2016).

As a result, efforts to replace graphite with other materials that show high specific capacity have led to investigations of new materials. Among these materials is silicon which stands out because it has a high theoretical capacity (4200 mA h g^{-1}) compared to that of graphite ($\sim 370 \text{ mA h g}^{-1}$) as well as its attractive operating voltage of about 0.4 V. Silicon is considered economical and sustainable because of its abundance in nature and it is environment friendly. In addition, when paired with an appropriate cathode material, lithium ion batteries that produce high energy densities can be achieved. Nonetheless, the electrochemical performance of the silicon anode is compromised by its significant volume changes of up to 400 %, compared to 7 % for graphite. This occurs during charge and discharge cycles and it leads to poor cyclability and anode failure. Also, after the first lithiation process, at the interface with the electrolyte it reacts to form a mixed layer referred to as the solid electrolyte interface (SEI). This process is irreversible hence it depletes valuable lithium resources from both the electrolyte and the anode leading to performance degradation. Therefore, a lot of research efforts are underway with an aim of overcoming these key failures. For instance, composites of silicon and carbon have been developed and they show improved performance. This has been attributed to the excellent properties and unique structural designs of carbon materials (Majeed et al., 2023; Houache et al., 2022; Chen et al., 2021b; Li et al., 2021a; Shi et al., 2021; Li et al., 2020a; Zhou et al., 2020; Cen et al., 2019).

Another ideal anode material is lithium metal because of its high theoretical capacity of $3,860 \text{ mAh g}^{-1}$, compared to 370 mA h g^{-1} for graphite. Also compared to the graphite anode, lithium metal leads to 50 % enhancement in energy density and 35 % enhancement in specific energy. It was first adopted in 1976 but was soon replaced by graphite because of its severe capacity fading and potential fire hazards resulting from growth of dendrites. During cycling, the lithium metal anode forms hair-like dendrites which grow unevenly through the battery electrolyte leading to short circuits that can cause the battery to explode into fire pausing a safety concern. Currently, lithium metal is considered as a promising choice for the next generation of batteries therefore a lot of research is underway to address the pointed-out challenges (Houache et al., 2022; Luo et al., 2021; Wang et al., 2021b; Hatzell et al., 2020; Wang et al., 2020a; Zhang et al., 2020a; Zheng et al., 2020; Li et al., 2018a; Liu et al., 2018a). Also promising are

alloy anodes which comprise of alloys of metallic lithium with metals or intermetallic compounds like aluminum, tin, magnesium, indium, silver and antimony. They show high theoretical capacities which are two to ten times higher than that of the graphite anode. For instance, theoretical capacities for indium, tin, silicon and germanium alloys with lithium are 1012 mAh g⁻¹, 994 mAh g⁻¹, 3579 mAh g⁻¹ and 1600 mAh g⁻¹ respectively. Nonetheless, during charging and discharging cycles, they suffer large volume changes of up to 300 % leading to disintegration and loss of electrical contact between the alloy particles. Therefore, their commercial utilization has been hindered by the resulting low cycle life (Nzereogu et al., 2022; Cheng et al., 2021a; Han et al., 2021; Lu et al., 2021; Liang et al., 2020; Li et al., 2020b).

Lastly, with theoretical specific capacities ranging from 500 to 1000 mAh g⁻¹, transition metal oxide anodes (TMO, M = Mn, Fe, Ni, Co, Ti, Cu etc.) are also prospective anode materials. Compared with graphite anodes, they don't form dendrites hence provide better safety. Also, in comparison with alloy anodes, their production cost is lower. However, their commercial application is still immature, due to problems like poor conductivity, large volume expansion, voltage lag between charge and discharge, continuous electrolyte decomposition and low initial coulombic efficiency. However, it is important to note that for all these materials, numerous studies are underway to address the challenges encountered towards their commercialization (Chang et al., 2022; Fang et al., 2022; Yang et al., 2022a; Li et al., 2021; Reddy et al., 2020; Cao et al., 2017; Wang et al., 2017).

2.4 Cathode materials for lithium ion batteries

As mentioned earlier, transition metal oxides are the most common cathode materials for lithium ion batteries. Among them, lithium cobalt oxide (LiCoO₂) is the most predominant due to its relatively high theoretical specific capacity (274 mAh g⁻¹), low self-discharge, high operating voltage (~ 3.9 V), high electronic conductivity at room temperature (10⁻³ S cm⁻¹) and good cycling performance. It was first commercialized by Sony in early 1990s and is still used in consumer electronics. Nonetheless, its application is considered undesirable in some areas like powering electric vehicles (EV) due to its low energy density (~150 Wh kg⁻¹). For such applications, high energy densities can be achieved by using a cathode material with a combination of high

operating voltage (5 V) and large specific capacity ($> 200 \text{ mAh g}^{-1}$). Irrespective of the large specific capacity, cycling LiCoO_2 to voltages above 4.35 V leads to structural instabilities that reduce its usable specific capacity to about 150 mAh g^{-1} . Its other limitations include the high cost and toxicity of cobalt and poor thermal stability that leads to a runaway reaction when operated above $200 \text{ }^\circ\text{C}$. The thermal instability leads to an exothermic reaction between the battery's organic materials and the released oxygen causing the battery to burst into flames (Zhang et al., 2023a; Zhang et al., 2022; Manthiram & Goodenough, 2021; Cheng et al., 2021b; Li et al., 2021c; Kawashima et al., 2020; Wang et al., 2020b; Julien et al., 2019).

Consequently, the ever-growing demand for advanced lithium ion batteries has led to the investigation of other different types of transition metals like manganese, aluminium, iron and nickel. With an aim of attaining higher operating voltages, these transition metals have been used as substitutes for cobalt in LiCoO_2 and the resulting compounds have demonstrated promising performance. Examples of such compounds include lithium nickel oxide (LiNiO_2) which is lower in cost than LiCoO_2 due to the abundance of nickel and it exhibits a high energy density because of its high theoretical capacity (275 mAh g^{-1}). However, its chemical and thermal stability is inferior than that of LiCoO_2 and its structure is less ordered hindering lithiation and delithiation. In order to improve its stability and degree of ordering, partial substitution of nickel with cobalt has been considered resulting in $\text{LiNi}_{1-x}\text{Co}_x\text{O}_2$. In addition to cobalt, manganese has also been used to make $\text{LiNi}_{1-x-y}\text{Mn}_x\text{Co}_y\text{O}_2$ (NMC) which combines high capacity from nickel, low internal resistance from manganese and low costs due to less amount of cobalt. However, the presence of cobalt is important since it improves the material's electric conductivity. Its specific capacity is between 160 and 200 mAh g^{-1} depending on the ratio of nickel, manganese and cobalt. Nevertheless, efforts to improve its capacity by using higher amounts of nickel have not been successful since it has resulted to formation of materials with poor cycling performance and reduced thermal stability (Houache et al., 2022; Akhilash et al., 2021; Lipson et al., 2021; Pang et al., 2020; Stephan, 2020; Bianchini et al., 2019; de Biasi et al., 2019; Markevich et al., 2018; Yoon et al., 2018).

Another promising cathode material is LiMn_2O_4 (LMO) which is less costly and safer compared to LiCoO_2 . However, it has a lower capacity (148 mAh g^{-1}) and a short lifetime due to its structural instability. It also experiences severe capacity fading due to the dissolution of manganese ions into the electrolyte. To improve its performance, doping with other transition metals like iron, cobalt and nickel has been considered. For instance, nickel has been incorporated into the lithium manganese oxide structure to form $\text{LiMn}_{1.5}\text{Ni}_{0.5}\text{O}_4$ (LNMO). Though with a lower specific capacity (147 mAh g^{-1}) than LiCoO_2 , LNMO is cheaper, has got excellent thermal stability and higher operating voltage (4.7 V). However, it experiences severe capacity fading and it cannot achieve more than 200 cycles at 80 % capacity. It also suffers incompatibility with commercial electrolytes resulting in decomposition (Hou et al., 2023; Wang et al., 2023a; Houache et al., 2022; Siller et al., 2022; Zou et al., 2021; Amin et al., 2020; Madsen et al., 2019).

With a theoretical capacity of 170 mAh g^{-1} , LiFePO_4 (LFP) is another broadly studied cathode material due to its non-toxicity and low cost. In addition, it shows excellent thermal stability and good cycle stability owing to its strong bonds hence stable structure. Its main drawbacks limiting its commercialization include poor electronic conductivity in the range of 10^{-6} to $10^{-10} \text{ S cm}^{-1}$ and inadequate diffusion of lithium ions (Ahsan et al., 2021; Chen et al., 2022a; Ramasubramanian et al., 2022; Zhao et al., 2021). Finally, with an outstanding theoretical capacity of 294 mAh g^{-1} which is much higher than that of commonly studied cathode materials, vanadium pentoxide (V_2O_5) has gained a lot of interest. In addition, it is affordable, easy to prepare, abundant and exhibits high energy density. Nonetheless, the material is toxic and it is also unstable in aqueous electrolytes leading to dissolution of vanadium (Alsherari et al., 2023; McNulty et al., 2023; Parekh et al., 2023; Zhang et al., 2021b; Yan et al., 2020; Du et al., 2019; Yao et al., 2018).

2.5 Electrolyte materials for lithium ion batteries

The electrolyte serves as the medium for ion transfer between the cathode and the anode making it an essential battery component. It should show high ionic conductivity, zero electronic conductivity, electrochemical stability, thermal stability, wide electric potential range between which it is chemically stable, robustness and inertness to cell components (Arya & Sharma, 2020; Mishra et al., 2018; Li et al., 2016).

Conventionally, the electrolyte in a lithium ion battery is a solution consisting of a lithium salt like lithium hexafluorophosphate (LiPF_6) dissolved in an organic solvent. Usually, organic solvents like ethylene carbonate, dimethyl carbonate, propylene carbonate or their mixtures are used because of their higher ionic conductivities and practical operating temperature range. Unfortunately, lithium ion batteries are prone to fire accidents when operated under conditions leading to mechanical, thermal, or electrical abuse like in the occurrence of a short circuit, overcharging, over discharging, physical penetration, or exposure to high temperatures. In such conditions, exothermic reactions are triggered within the battery resulting to a self-enhanced chain reaction and uncontrollable temperature increase referred to as a thermal runaway which can cause the battery to explode into flames. In such cases the organic electrolytes pose a safety concern because of their high flammability (Kalhoff et al., 2015; Kong et al., 2018; Xu et al., 2021a). Several incidents of lithium ion batteries and explosions have been reported. For instance, (Saxena et al., 2018) gives a comprehensive review of numerous e-cigarette fire and explosion incidents. Also, all Boeing 787 Dreamliners were grounded indefinitely in January 2013 due to safety concerns over the failure of lithium ion batteries that provide auxiliary startup power and on-board backup power during flight (Williard et al., 2013). In addition, a Tesla electric car was reported to catch fire in 2015 as a result of battery failures and for a similar reason Samsung had to recall Note 7 smartphones in 2016 (Kong et al., 2018; Xu et al., 2021a). Other issues associated with the liquid electrolyte are possible leakages and bulky battery sizes (Arya & Sharma, 2020; Jiang et al., 2018a; Kalhoff et al., 2015).

Efforts to enhance the lithium ion battery's safety have triggered extensive research and developments like the addition of fire retardants to the organic based electrolytes (Dalavi et al., 2010; Jiang et al., 2018a; Dunn, 2013). Nevertheless, such additives increase the mass of the inactive materials in the battery compromising performance. Alternatively, ionic liquids have been considered as substitutes for organic liquids because of their nonflammability and broad electrochemical window but only a few have been found suitable. This is because their overall viscosities are one to two orders of magnitude higher than liquid organic electrolytes making their ionic conductivities three to four orders of magnitude lower (Kong et al., 2018; Park et al., 2010) . Solid electrolytes have also been investigated and among them are organic solid electrolytes,

which usually consist of a lithium salt and a high molecular weight polymer. Considering that ambient temperature conductivity is important, these materials only operate at temperatures above 60 °C hence not practical for many applications (Zheng et al., 2017a; Dalavi et al., 2010; Dias et al., 2000). Consequently, there have been efforts to lower these operating temperatures by adding plasticizers of lower molecular weight like ethylene carbonate, but this has been unsuccessful because they compromise the electrolyte's mechanical and chemical properties (Rangasamy et al., 2019). Another option that has been explored is the substitution of liquid organic electrolytes with solid inorganic electrolytes. In addition to their improved safety, the solid inorganic electrolytes offer a wider range of operating temperatures, higher energy densities due to their compatibility with high energy electrodes and high ionic conductivities which match those of the organic liquid electrolytes. However, their major drawback has been the poor solid electrode-electrolyte contacts (Xiao et al., 2019a; Richards et al., 2016; Wei et al., 2015; Ito et al., 2013; Kumar et al., 2010).

2.5.1 Solid-state electrolyte materials for lithium ion batteries

For the next generation of lithium ion batteries, an electrolyte material should show diminished flammability, high ionic conductivity, zero electronic conductivity, electrochemical stability that ensures safe coupling with high voltage cathodes to improve the battery's energy density, thermal stability, wide electrochemical window, affordability, robustness and inertness to cell components (Chen et al., 2022b; Karabelli et al., 2021; Arya & Sharma, 2020; Zhao et al., 2019a; Mishra et al., 2018). Solid-state electrolyte materials are a promising area of research for improving the performance and safety of lithium ion batteries. Compared to conventional organic liquid electrolytes, solid-state electrolytes have several advantages, like enhanced safety since they are less prone to leakage or combustion. Also, the resulting solid-state lithium ion batteries exhibit high energy densities due to their compatibility with high capacity electrodes. Their ionic conductivities are high matching those of the commercialized organic liquid electrolytes. In addition, they offer a wider range of operating temperatures (Baniya et al., 2023; Nikodimos et al., 2023; Xu et al., 2022; Chen et al., 2021a; Wu et al., 2021a; Schwietert et al., 2020; Liang et al., 2019c; Lv et al., 2019; Zheng et al., 2018). So far, different electrolyte materials have been identified for solid-state lithium ion batteries and they include nitrides, iodides, phosphates, oxides and

sulfides as shown in Fig. 2.2. Among these materials, sulfide-based lithium superionic conductors (thio-LISICON) have the highest lithium ion conductivity with values in the range of 10^{-2} S cm⁻¹ at room temperature. They consist of a wide range of compositions with the chemical structure Li₁₀MP₂S₁₂ where M = Si, Ge, or Sn. Studies have shown that chloride doping of this category of materials can greatly enhance their conductivity (Choi and Lee, 2019; Zhang et al., 2019). An example of the chloride-doped thio-LISICON material is Li_{9.54}Si_{1.74}P_{1.44}S_{11.7}Cl_{0.3} with an electronic conductivity of 2.5×10^{-2} S cm⁻¹ as reported by (Kato et al., 2016). These materials also portray soft mechanical properties which are considered favorable for enhancing good contact with the electrodes. Nevertheless, the precursor materials used for their synthesis are very costly hence limiting their applications (Tao et al., 2022; Kudu et al., 2018; Bachman et al., 2016; Ulissi et al., 2016). Following closely are the argyrodites, Li₆PS₅X (X is Cl, Br or I), whose lithium ion conductivities are in the range of 10^{-2} - 10^{-3} S cm⁻¹ at room temperature. Their advantage over LISICON-like materials is that their precursors are affordable hence their wide application. However, being sulfur based materials the stability of both categories deteriorates in air causing their conductivity to decrease significantly. This is usually accompanied with the release of hydrogen sulfide gas as a result of the interaction with water molecules in the air (Kim et al., 2023; Tsukasaki et al., 2022; Thakur and Majumder, 2021; Yu et al., 2021; Baktash et al., 2020; Yu et al., 2020; Zhang et al., 2020b; Zhang et al., 2020c; Kudu et al., 2018; Yubuchi et al., 2018).

Another category of solid-state electrolyte materials are oxides which include garnets, NASICONs and perovskites. These oxide materials are chemically stable in the atmosphere providing an alternative to sulfur-based counterparts. However, their main drawback is the low ionic conductivities (10^{-5} to 10^{-3} S cm⁻¹). For garnets, their general chemical formula is A₃B₂Si₃O₁₂ whereby A is a divalent cation like Mg²⁺, Ca²⁺, Fe²⁺, or Mn²⁺ and B is a trivalent cation like Fe³⁺, Cr³⁺ or Al³⁺. However, different doping strategies have been devised to synthesize lithium ion conducting garnets. For instance, (Murugan et al., 2007) discovered lithium lanthanum zirconium oxide (LLZO, Li₇La₃Zr₂O₁₂) and since then there has been an increasing interest in the development of garnet based solid-state lithium ion batteries. However, LLZO ionic conductivity (10^{-3} – 10^{-4} S cm⁻¹) is lower than that of the conventional liquid electrolyte (10^{-2} S cm⁻¹). Therefore, a lot of efforts are being made to optimize the garnet's ionic conductivity.

For instance, doping LLZO with elements like Ta⁵⁺, Nb⁵⁺, Te⁶⁺, W⁶⁺, Ti⁴⁺, Al³⁺ and Ga³⁺ has been reported (Dong et al., 2022; Liu et al., 2022; Qin et al., 2022; Gonzalez et al., 2021; Kim et al., 2020; Wang et al., 2020c; Zhao et al., 2019b; Duan et al., 2018; Liu et al., 2018b).

NASICON is an acronym for sodium super ion conductors. They are crystalline solids with a general formula A₁B₂(PO₄)₃ where A is a monovalent cation like Na or Li and B is either a single or a combination of tri, tetra and pentavalent ions like Ge, Si, Ti or Zr. Examples of these materials include LiTi₂(PO₄)₃, Li_{1+x}Al_xTi_{2-x}(PO₄)₃ (LATP), LiGe₂(PO₄)₃ (LGP) and Li_{1+x}Al_xGe_{2-x}(PO₄)₃ (LAGP). They have a rigid crystal framework which provides stability, but also have mobile ions that can move through the structure allowing for efficient ion transport (Tao et al., 2022; Yang et al., 2021; Hou et al., 2020; Nikodimos et al., 2020; DeWees & Wang, 2019; Xiao et al., 2019b; El-Shinawi et al., 2018; Meesala et al., 2018). Perovskite-type materials (ABO₃ where A = Ca, Sr, La; B = Al, Ti) have also attracted extensive attention. Numerous studies have reported different ionic conductivities in perovskite materials through the replacement of A and B sites with different ions. Examples of such materials are lithium lanthanum titanate electrolytes which can be expressed as Li_{3x}La_{(2/3)-x}TiO₃ (LLTO) with the value of x ranging from 0.04 to 0.16 (Chandra et al., 2022; Lu & Li, 2021; Yan et al., 2021; Salami et al., 2019; Hu et al., 2018; Li et al., 2018b).

With high lithium ion conductivity (10⁻³ S cm⁻¹) at ambient temperatures lithium nitrides show attractive properties for applications as solid-state electrolyte materials. However, their decomposition potential is too low (0.445 V) making them chemically unstable for practical applications (Chandran and Heitjans, 2016; Weppner, 2009; Gregory, 2008). For lithium hydrides and lithium halides, they are chemically stable and have been reported to show good compatibility with lithium electrodes. Their ionic conductivities are in the range of 10⁻³ to 10⁻⁴ S cm⁻¹ in high temperatures but at low temperatures, the ionic conductivities are compromised to about 10⁻⁸ S cm⁻¹ or lower rendering them unsuitable for practical applications (Wang et al., 2022; Gulino et al., 2021; Wang et al., 2021c; Gulino et al., 2020).

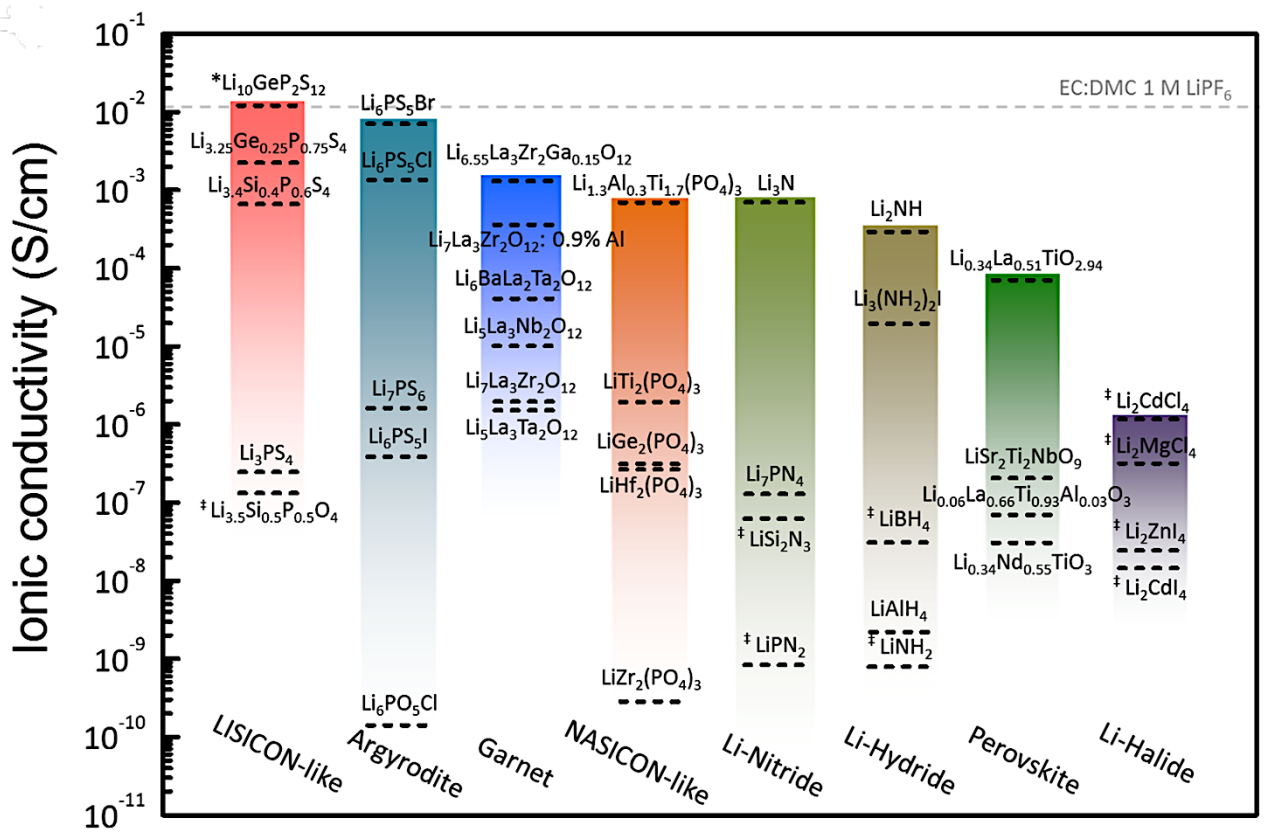


Figure 2.2. Different solid-state electrolyte materials and their ionic conductivities at room temperature. The dotted line at the top indicates the typical lithium ion conductivity for liquid electrolytes like 1 M LiPF₆ in a mixed solvent of ethylene carbonate and dimethyl carbonate. Adapted from Bachman et al. (2016).

2.6 Thin film deposition techniques

A thin film is a layer that is usually deposited on a selected substrate with a thickness typically in the order of nanometers to micrometers range. Thin films can be made from a wide variety of materials like polymers, metals and semiconductors. Compared to their bulk counterparts, thin films exhibit unique properties like increased reactivity, improved mechanical strength, enhanced optical and electrical properties. This is attributed to their small thicknesses and large surface areas. Commonly, they are used in a wide range of applications like in the manufacture of microelectronic devices, batteries, computer chips, solar cells and sensors. In addition, thin film coatings are used as protective coatings to improve durability and corrosion resistance of surfaces.

Among the different applications, thin film batteries are already a commercial reality with printed zinc manganese batteries being prevalent due to their safety, affordability

and ease to print. Nonetheless, these batteries are non-rechargeable and can only be used in single-use applications. The need for alternative rechargeable thin film batteries has led to research developments in printed nickel metal hydride and zinc air thin film batteries. Though lithium ion batteries would be a favourable choice because of their higher energy densities and longer cycle lives, the battery materials are not easy to print (Clement et al., 2022; Hilder et al., 2009; Huebner and Krebs, 2015). Therefore, to satisfy the demand for high energy density thin film batteries, different deposition techniques for lithium ion batteries have been studied as outlined below.

2.6.1 Physical and chemical vapour deposition methods

Conventionally, the deposition of thin film lithium ion batteries is performed by either physical vapour deposition methods (PVD) or chemical vapour deposition (CVD) methods. Examples of these methods include radio frequency sputtering, magnetron sputtering, pulsed laser deposition (PLD), spray pyrolysis, atomic layer deposition (ALD), thermal evaporation, sol-gel spin coating and electron beam evaporation. These processes involve synthesis of the deposition species, deposition of the synthesized species onto a substrate, adhesion of the species onto the substrate and subsequent film growth (Karimi et al., 2023; Wu et al., 2023; Fenech & Sharma, 2020; Julien and Mauger, 2019; Moitzheim et al., 2019).

For physical vapour deposition, it involves a physical discharge of atoms or molecules followed by their condensation and nucleation on a substrate in a controlled atmosphere consisting of low gas pressure in a vacuum. First the coating material in solid form is vaporized by a physical process that is either thermal or athermal (Fig. 2.3). The thermal PVD process typically consists of the following steps:

- I. Chamber preparation: The chamber is cleaned and pumped down to a low-pressure environment to eliminate any impurities or gases that could interfere with the deposition process.
- II. Material vaporization: The material to be deposited is heated in the chamber to achieve vaporization. It can be a compound, pure metal or alloy.
- III. Vapor deposition: As the target material is heated, it evaporates to form a vapour cloud within the chamber. This vapour consisting of atoms or molecules travels in straight lines colliding with other gas atoms or molecules present in the

chamber. The collision process leads to condensation and deposition of the vapour onto a substrate.

- IV. Substrate deposition: The substrate is carefully prepared and positioned within the chamber. The substrate material and geometry depend on the specific application and desired properties of the thin film. It can be a solid object like a wafer, a glass slide, or a metal component.
- V. Film growth: The vaporized material condenses on the substrate surface to form a thin film. The deposition parameters such as deposition rate, temperature and pressure are carefully controlled to achieve the desired film properties.

In athermal process, deposition occurs without significantly raising the temperature of the substrate or the vaporized material. This can be achieved using different processes like sputtering which involves the bombardment of a solid target material with high-energy ions. The ions dislodge atoms or molecules from the target surface, which then deposit onto the substrate to form a thin film. The energy transferred from the ions to the substrate during sputtering is generally low, resulting in minimal heating (Butt, 2022; Tarek et al., 2022; Prabakaran & Rajan, 2021; Abegunde et al., 2019; Baptista et al., 2018).

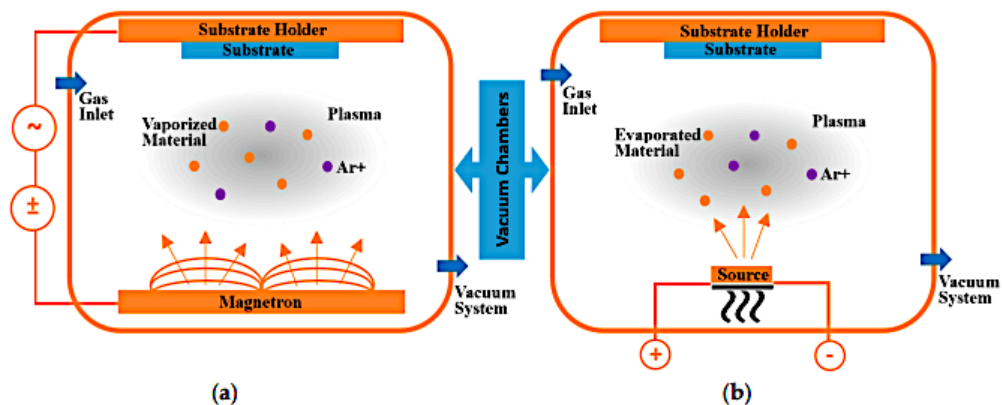


Figure 2.3. Schematic diagram of a) athermal and b) thermal PVD processes. Adapted from Baptista et al. (2018).

On the other hand, chemical vapour deposition is a technique where a solid or liquid material is converted into vapour after which the volatile precursor undergoes some chemical reaction on the substrate to produce the desired deposit. This normally

happens in a heated chamber under vacuum (Fig. 2.4). The chemical reactions can be initiated by heat resulting in thermal CVD, high frequency radiation like UV resulting in photo-assisted CVD or electric energy resulting in plasma-enhanced CVD. The chemical reactions are also controlled by different factors like the reactor configuration, reactor pressure, gas feedstock, gas partial pressures, gas ratios, deposition time and temperature. Chemical vapour deposition is widely used in industries especially in the deposition of refractory materials (nonmetallic materials that can withstand extremely high temperatures). For instance, it is applied on turbine blades to greatly increase their wear and thermal shock resistances Sun et al., 2021; Behera et al., 2020; Saeed et al., 2020; Morosanu, 2016). CVD processes have also been widely used in the deposition of thin films for lithium ion batteries (Chen et al., 2017; Loho et al., 2017; Tian et al., 2015; Wang and Yushin, 2015; Xie et al., 2015).

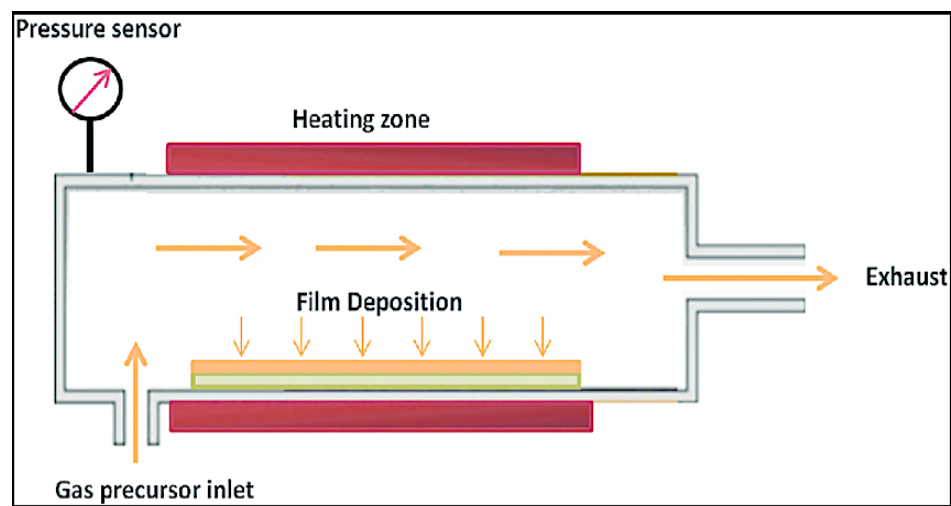


Figure 2.4. Schematic diagram thermal CVD setup. Adapted from Zhang et al. (2016).

2.6.2 Electro spray Technique

Electrospray is another deposition technique in which a liquid jet is broken up into droplets in the presence of electrical forces. There are different electro spray modes which can be achieved by changing the flow rate and/or the applied electric field strength. The main differences in these modes are in their droplet formation mechanism and droplet sizes. Usually, a precursor liquid is pumped through a nozzle at a low flow rate such that dripping is achieved with no applied electric field. By applying an electric field between the nozzle and the counter electrode other modes can be achieved as the electric field is increased instantaneously. Examples of different electro spray modes are

shown in Fig. 2.5 and they include dripping, intermittent cone-jet, spindle, cone-jet and multiple jet modes (Agostinho et al., 2018; Verdoold et al., 2014; Yurteri et al., 2010).

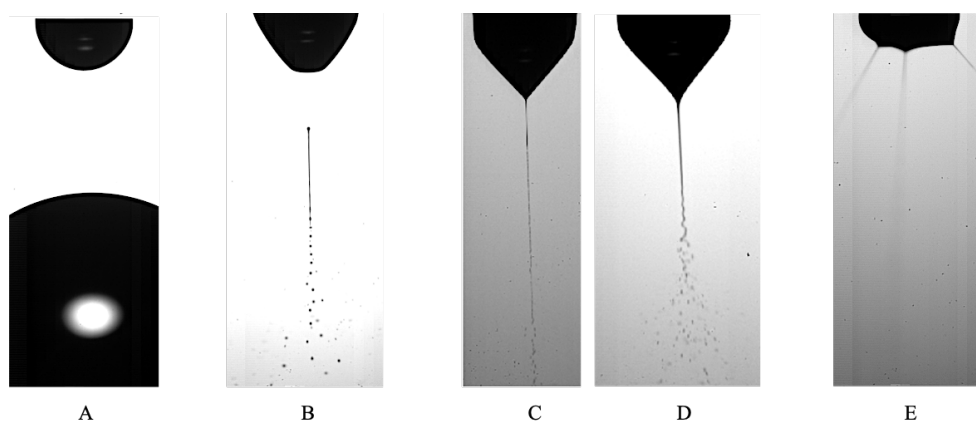


Figure 2.5. Examples of electro spray modes. A. Dripping, B. Intermittent cone-jet, C. Cone-jet, varicose breakup, D. Cone-jet, whipping breakup and E. Multiple-jet. Adapted from Verdoold et al. (2014) and Yurteri et al. (2010).

Normally, the cone-jet mode is of interest because of its stability and capability to generate spherical monodisperse droplets which are smaller than the nozzle diameter (Joshi et al., 2021). As mentioned, the precursor solution is pumped through a nozzle with an electrical voltage applied between the nozzle and a ground electrode which are not far apart (Fig. 2.6).

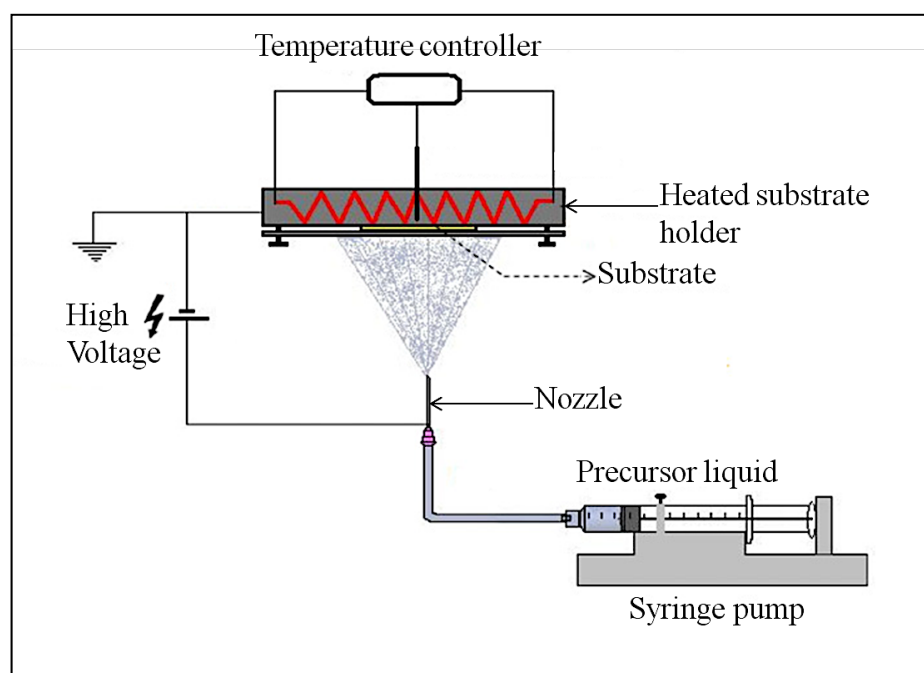


Figure 2.6. Schematic illustration of an electro spray setup. Adapted from Li et al.

(2011).

The resulting electric field creates a charge on the meniscus of the liquid in the nozzle. Owing to the electric field and the surface charge, the liquid meniscus experiences an electric stress. This electric stress can overcome surface tension and shape the meniscus into a cone, referred to as the Taylor cone, depending on the strength of the electric field and the liquid flow rate (Taylor, 1964). Charge carriers in the liquid consisting of ions are then accelerated towards the cone's apex and they collide with the surrounding liquid molecules causing them to also accelerate. Consequently, a thin liquid jet emerges from the cone's apex which breaks up into highly charged droplets.

Typically, in an electrospray experiment charged droplets are generated and directed towards a counter electrode, which can be a selected substrate. Upon evaporation of the solvent in the generated droplets, particles are formed. To estimate the sizes of these particles in cone-jet mode, different authors have derived scaling laws. As it will be seen, the electric current flowing through the liquid is a very important parameter in estimating droplet and particle sizes (Yurteri et al., 2010). In the determination of the jet's electric current, Gañán-Calvo et al. (1997) presented two distinct profiles, namely flat and non-flat profiles. According to them, liquids with high viscosity and high conductivity have a flat radial profile of the axial liquid velocity in the jet while liquids with low conductivity and low viscosity have a non-flat velocity profile in the jet. To differentiate between these two categories of liquids, the same authors developed a dimensionless number (Equation 2.4) later referred to as the viscosity number (VN) by Hartman (1998).

$$VN = \left(\frac{\gamma^3 \epsilon_0^2}{\mu^3 K^2 Q} \right)^{1/3} \quad (\text{Eqn. 2.4})$$

where, γ is surface tension of the precursor liquid (N m^{-1}), ϵ_0 is electric permittivity of a vacuum ($\text{C}^2 \text{ N}^{-1} \text{ m}^{-2}$), μ is absolute viscosity of the precursor liquid (Pa s), K is conductivity of the precursor liquid (S m^{-1}) and Q is flow rate of the precursor liquid ($\text{m}^3 \text{ s}^{-1}$). For precursor liquids with high viscosity and/or high conductivity the VN is relatively low. In practice, a flat radial velocity profile is assumed for viscosity numbers less than or equal to one, while a non-flat radial velocity profile is assumed for viscosity numbers greater than one. For a jet with a flat radial profile, Hartman et al. (1999) derived the equation for electric current as shown in Equation 2.5.

$$I^* = b(\gamma K Q)^{0.5} \quad (\text{Eqn. 2.5})$$

For liquids with a non-flat radial profile Hartman (1998) derived a formula to calculate the electric current which was later rewritten by Yurteri et al. (2010) in the form of Equation 2.6.

$$I = 0.41I^* + \frac{0.24I^{*2}}{E_{z,max}KQ} (Ar_{j0.41}^2 + B) \quad (\text{Eqn. 2.6})$$

where, I^* is jet current for a flat radial profile of axial liquid velocity, $b = 2.17$, γ is surface tension of the precursor liquid (N m^{-1}), K is conductivity of the precursor liquid (S m^{-1}), Q is flow rate of the precursor liquid ($\text{m}^3 \text{ s}^{-1}$), $E_{z,max}$, $r_{j0.41}$, A and B are all functions of known parameters. Later, Yurteri et al. (2010) combined Equations 2.5 and 2.6 in the form of a ratio as a function of viscosity number leading to Eqn 2.7.

$$I/I^* = (1 - 0.1 * VN^{0.45})^{-1} \quad (\text{Eqn. 2.7})$$

where, I is jet current for a non-flat radial profile of the axial velocity, I^* is jet current for a flat radial profile of the axial velocity and VN is the viscosity number.

Having calculated the jet's electric current, the mechanism by which droplets form during jet breakup is also important and must be considered when determining droplet sizes. This mechanism depends on the ratio of the electric normal stress to the surface tension stress on the liquid's surface. A low stress ratio (< 0.3) results in varicose breakup while a high stress ratio results in whipping breakup. In the former, main droplets of similar size are obtained, but in some cases, satellite or secondary droplets may also form, resulting in a bimodal size distribution. On the contrary, whipping breakup leads to a broad size distribution of the main droplets (Yurteri et al., 2010). For both mechanisms, Hartman et al. (2000) derived scaling laws for the main droplet size as shown below.

$$d_{d,varicose} = c_d \left(\frac{\rho \varepsilon_0 Q^4}{I^2} \right)^{1/6} \quad (\text{Eqn. 2.8})$$

Later, Yurteri et al. (2010) demonstrated that if the radial profile of the axial fluid velocity in the jet is flat, then the current scales according to Equation 2.5 and Equation 2.8 leads to Equation 2.9.

$$d_{d,varicose} = \frac{c_d}{b^{1/3}} \left(\frac{\rho \varepsilon_0 Q^3}{\gamma K} \right)^{1/6} \quad (\text{Eqn. 2.9})$$

where $d_{d,varicose}$ is droplet diameter in varicose breakup regime, c_d is approximately 2, ρ is precursor liquid density (kg m^{-3}), ε_0 is electric permittivity of a vacuum ($\text{C}^2 \text{ N}^{-1} \text{ m}^{-2}$), Q is flow rate of the precursor liquid ($\text{m}^3 \text{ s}^{-1}$), I is the jet's electric current, γ is

surface tension of the precursor liquid (N m^{-1}) and K is conductivity of the precursor liquid (S m^{-1}). By approximating the values of b and c_d to 2, which gives only a small deviation, Yurteri et al. (2010) obtained Equation 2.10.

$$d_{d, varicose} = \left(\frac{16\rho\varepsilon_0 Q^3}{\gamma K} \right)^{1/6} \quad (\text{Eqn. 2.10})$$

and in the whipping breakup regime, they obtained the droplet diameter from Equation 2.11.

$$d_{d, whipping} = \left(0.8 \frac{288\varepsilon_0 \gamma Q^2}{I^2} \right)^{1/3} \quad (\text{Eqn. 2.11})$$

where $d_{d, whipping}$ is droplet diameter in whipping breakup regime, γ is surface tension (N m^{-1}), Q is liquid flow rate ($\text{m}^3 \text{s}^{-1}$) and I is jet's electric current. To calculate the droplet size, both Equation 2.10 and Equation 2.11 are used and the smallest value obtained is assumed to be the correct value.

Having determined the size of the main droplets using Equation 2.10 or Equation 2.11, particle size can be estimated from the main droplet size as shown in Equation 2.12 (Yurteri et al., 2010).

$$d_p = \sqrt[3]{f \frac{\rho_{droplet}}{\rho_{particle}} d_{droplet}^3} \quad (\text{Eqn. 2.12})$$

where d_p is particle diameter, f is mass fraction of the dissolved material, $\rho_{droplet}$ is liquid density, $\rho_{particle}$ is final particle density and $d_{droplet}$ is the droplet diameter. However, this is only true for non-porous and non-hollow particles.

2.6.2.1 The cone-jet window

It is important to note that a stable cone-jet can only be achieved if electrospray is carried out in a limited voltage and flow rate window. The first quantitative description of this stability window was provided by Cloupeau and Prunet-Foch (1989). For selected liquid properties, this window is defined by a minimum flow rate (Q_{min}) and a maximum flow rate (Q_{max}). The former is the lowest flow rate at which a certain liquid can be electrosprayed in the cone-jet mode, while the latter is the flow rate beyond which the cone-jet becomes unsteady (Hartman, 1998). Due to the wide variety of complex issues around the maximum flow rate, there is no formula available to define it (Gañán-Calvo et al., 2018). However, several authors have reported on Q_{min} and different formulas have been proposed (Gañán-Calvo et al., 1997; Rosell-Llompart

and Fernández de la Mora, 1994; Gañan-Calvo, 1994). Nonetheless, the proposed formulas did not work for Chen and Pui (1997) and they reported significant deviations. In his work, Hartman (1998) suggested that the minimum flow rate is given by Equation 2.13.

$$Q_{min} \sim Q_0 = \frac{\varepsilon_o \gamma}{\rho K} \quad (\text{Eqn. 2.13})$$

where ε_o is electric permittivity of a vacuum, γ is surface tension of the liquid, ρ is liquid density and K is liquid conductivity. In a different study, Gañán-Calvo et al. (2013) developed two different scaling laws for Q_{min} after studying the forces influencing the stability of liquid ejection in the cone-jet mode. In cases where viscosity force was responsible for cone-jet instabilities, the minimum flow rate was calculated using Equation 2.14, while in cases where polarization force was responsible for cone-jet instabilities Equation 2.15 was used.

$$Q_{min,viscosity} = Q_0 \delta_\mu^{-1} \quad (\text{Eqn. 2.14})$$

$$Q_{min,polarization} = Q_0 \beta \quad (\text{Eqn. 2.15})$$

where $Q_0 = \frac{\varepsilon_o \gamma}{\rho K}$, as shown in Equation 2.13, δ_μ is electrohydrodynamic Reynolds number, $\beta = \varepsilon_i / \varepsilon_o$, ε_i is electrical permittivity and ε_o is electric permittivity of a vacuum ($\text{C}^2 \text{N}^{-1} \text{m}^{-2}$). Later, (Scheideler & Chen, 2014) adapted the Q_{min} equation as proposed by Rosell-Llompart & Fernández de la Mora, (1994) for liquids with low viscosity (Equation 2.16). In addition, they also derived an expression for high viscosity liquids (Equation 2.17).

$$Q_{min,low\ viscosity} \sim \frac{\varepsilon \gamma}{K \rho} \quad (\text{Eqn. 2.16})$$

$$Q_{min,high\ viscosity} \sim \frac{\gamma D^2}{\mu} \quad (\text{Eqn. 2.17})$$

In these equations Q_{min} is minimum flow rate ($\text{m}^3 \text{s}^{-1}$), ε is liquid permittivity, ε_o is electric permittivity of a vacuum ($\text{C}^2 \text{N}^{-1} \text{m}^{-2}$), γ is liquid surface tension (N m^{-1}), K is liquid electrical conductivity (S m^{-1}), ρ is liquid density (kg m^{-3}), D is outer nozzle diameter (m) and μ is liquid viscosity (Pa s). Note that Equation 2.16 by Scheideler & Chen (2014) is almost similar to Equation 2.13 by Hartman (1998). In another study, Gamero-Castaño & Magnani (2019) gave an extensive overview of Q_{min} and they concluded that minimum flow rate is a function of both the dielectric constant of the liquid (ε) and its Reynolds number (R_e).

$$R_e = \left(\frac{\rho \varepsilon_o \gamma^2}{\mu^3 K} \right)^{1/3} \quad (\text{Eqn. 2.18})$$

where ρ is liquid density (kg m^{-3}), ϵ_0 is electric permittivity of a vacuum ($\text{C}^2 \text{N}^{-1} \text{m}^{-2}$), γ is liquid surface tension (N m^{-1}), μ is liquid viscosity (Pa s) and K is liquid electrical conductivity (S m^{-1}).

On the contrary, these studies did not develop a formula that can be used to define the maximum flow rate (Q_{max}). This was attributed to the wide variety of complex issues around it (Castillo et al., 2018; Gañán-Calvo et al., 2018). Nonetheless, the effects of different parameters on Q_{max} have been studied. For instance, Tang and Gomez (1996) reported that the maximum liquid flow rate for the cone-jet decreases significantly with increasing diameter of the capillary. The dependency of Q_{max} on the nozzle diameter was also observed by Cloupeau and Prunet-Foch (1989). For a capillary of 0.5 mm a Q_{max} of about $0.3 \text{ mm}^3 \text{ s}^{-1}$ was observed while for a finer capillary Q_{max} was at least four times higher. According to Chen and Pui (1997), different factors can affect the operation window and they include the configuration of the set-up, physical properties of the liquid, wettability of the capillary and surrounding atmosphere. Also, Rosell-Llompart & Fernández de la Mora (1994) stated that unlike Q_{min} , Q_{max} is not independent of electrostatic parameters and cannot be determined at the meniscus, since it also depends also on the dynamics of the spray.

2.7 Key electrospray parameters and their effects on surface morphology

Based on the different properties of the precursor liquid and experimental parameters, different surface morphologies can be attained on the deposited film as highlighted in different studies

.

2.7.1 Substrate Temperature

Essentially, when depositing films by electrospraying, charged droplets are produced from a precursor liquid and they are directed at a substrate of choice. A solid layer is then formed after the solvent has evaporated, and this process can be accelerated by heating the substrate. Usually, the substrate temperature is set to be above or below the solvent boiling point. Consequently, different surface morphologies can be achieved depending on the choice of solvent and substrate temperature (Perednis et al., 2005). While keeping other parameters constant heating the substrate to a temperature above

the solvent boiling point, results in a dense layer. This is because the high temperature leads to evaporation of a big percentage of the solvent from the droplet surface. Consequently, the droplet size reduces but its overall electric charge remains constant and the Rayleigh limit is exceeded causing it to explode into many smaller droplets (Rahmanpour and Ebrahimi, 2017). The smaller droplets drift towards the substrate under electrostatic forces and they are expected to dry up into even smaller particles leading to a dense layer. Conversely, at relatively high flow rates the produced droplets are relatively big (Jo et al., 2014; Varga et al., 2010). According to Vercoulen (1995) such droplets are less likely to achieve Rayleigh break up and they dry up on the substrate to form relatively big particles that lead to a porous layer. At substrate temperatures ranging from 170 to 230 °C, Wang et al. (2009) observed a decrease in pore size with increasing substrate temperature. They prepared porous reticular Fe₂O₃ films using a 0.005 M precursor in a mixed solvent of 1, 2-propylene glycol and ethanol (boiling points of 188.2 °C and 78 °C respectively) at a flow rate of 2.4 mL h⁻¹.

2.7.2 Type of Solvent

While keeping other parameters constant, different surface morphologies can also be achieved with different solvents. For instance, Duong et al. (2013) studied six different alcohols and for the different solvents, they obtained different particle morphologies ranging from smooth spherical particles to collapsed shell morphology. They attributed the difference in particle morphologies to the fact that different solvents evaporate at different rates varying the droplet sizes. Larger droplets resulted in collapsed particles because of the increased mechanical instabilities. The effect of different solvents on film morphology was also reported by Lafont et al. (2012) who obtained a more porous film with 1-propanol than with ethanol (boiling points of 97 °C and 78 °C respectively) after electrospraying respective 0.1 M LiNi_{0.5}Mn_{1.5}O₄ precursors at a flow rate of 1 mL h⁻¹ and a substrate temperature of 350 °C.

2.7.3 Concentration

According to Gürbüz et al. (2016), an increase in concentration leads to an increase in the thickness of the film and this affects morphology. In their study, they electrosprayed SnO₂ precursor in ethanol (boiling point of 78 °C) at a substrate temperature of 250 °C for 1 h. Precursor concentrations were changed from 0.05 M to 0.2 M but flow rate was

kept constant at 7.2 mL h^{-1} . A crack free film was obtained from the 0.05 M precursor while a cracked film was obtained after increasing the concentration to 0.2 M . At high concentration, cracking was attributed to the non-uniform drying rate between the top and bottom layers of the thick film. Also, Bailly et al. (2012) reported a cracked film after electro spraying 0.1 M YSZ precursor in a mixed solvent of ethanol and butyl carbitol (boiling points of $78 \text{ }^\circ\text{C}$ and $231 \text{ }^\circ\text{C}$ respectively) at a substrate temperature of $400 \text{ }^\circ\text{C}$ and a flow rate of 0.5 mL h^{-1} for 1 h. In another study, Joshi et al. (2013) reported a dense film from a low concentration (0.05 M) $\text{SnCl}_4 \cdot 5\text{H}_2\text{O}$ precursor in propylene glycol (boiling point of $188.2 \text{ }^\circ\text{C}$) at a flow rate of 0.04 mL h^{-1} and a substrate temperature of $70 \text{ }^\circ\text{C}$ for 1 h.

2.7.4 Flow rate

It has also to be noted that among other parameters, flow rate controls the droplet size hence the final particle size. However, flow rate is not an absolute parameter since it is influenced by other factors as shown in Equation 2.13. Among these factors, conductivity is the most prominent and its variation can lead to a wide range of droplet sizes. Unfortunately, most of these parameters are not given by the authors of the literature cited here. Nonetheless, if the range of conductivity values is not too big it does not tremendously influence the droplet diameter. This is because in the equation for droplet size, the conductivity appears as a power of $1/6$ or $1/3$. On the contrary, if the range of conductivities is big the effect on droplet size is significant (Joshi et al., 2013). It is also important to know which flow rates can achieve the cone-jet mode. This is defined by a minimum and a maximum flow rate values and they form an operational window. At a constant conductivity, low flow rate produces relatively small droplets hence small particles while high flow rate produces relatively big droplets that dry up into big particles. From the works of Kavadiya et al. (2017), electro spraying $\text{CH}_3\text{NH}_3\text{PbI}_3$ perovskite precursor (14 mg mL^{-1}) in isopropyl alcohol (boiling point of $82.5 \text{ }^\circ\text{C}$) at flow rates of $0.03, 0.06, 0.09, 0.12$ and 0.15 mL h^{-1} at room temperature led to droplets of diameters $505.88, 635.9, 726.94, 799.33$ and 860.41 nm respectively and their reported evaporation times were $17.84, 28.22, 36.90, 44.64$ and $51.73 \text{ } \mu\text{s}$ respectively. The measured particle sizes were $75.36, 77.00, 109.23, 116.31$ and 113.43 nm respectively. Smaller particle sizes were achieved at lower flow rates and they led

to the production of smooth uniform films. However, as flow rate increased (above 0.06 mL h⁻¹) larger particles were obtained leading to increased film roughness.

According to (Hong et al., 2017), small droplets have a high rate of solvent evaporation leading to a particulate rough film while big droplets have a low rate of solvent evaporation leading to an uneven film with pinholes. Therefore, an intermediate droplet size is required in order to obtain a uniform dense film. They achieved this by electro spraying 30 % wt MAPbI₃ perovskite liquid precursor in dimethyl sulfoxide (boiling point of 189 °C) at a flow rate of 0.05 mL h⁻¹ and a substrate temperature of 65 °C for 2 min. Different morphological effects based on flow rate were also demonstrated by Ma and Qin (2005) during the electro spray of 0.02 M LiFePO₄ precursor solution in a mixed solvent of ethanol, glycol and butyl carbitol (boiling points of 78 °C, 197 °C and 231 °C respectively) at a substrate temperature of 120 °C. At a flow rate of 0.5 mL h⁻¹, the generated particles were big (> 400 nm) and they aggregated to form a porous morphology. On the contrary, at a flow rate of 0.05 mL h⁻¹ the generated particles were smaller (< 100 nm) and they formed a uniform dense film. Also, Yu et al. (2006b) reported a porous film with aggregated particles at a flow rate of 4 mL h⁻¹ using 0.02 M LiCoO₂ precursor in a mixed solvent of ethanol and glycol (boiling points of 78 °C and 197 °C respectively) at a substrate temperature of 350 °C deposited for 50 min.

2.7.5 Deposition time

Deposition time is also a very important parameter not only in determining the layer thickness but also the surface morphology. (Joshi et al., 2021) mentioned that by increasing the deposition time, morphology of the film can change from dense to porous. In a short deposition time, the film is thin and the droplets get into direct contact with the heated substrate. With increasing time, the film thickens and the substrate surface is completely covered causing consecutive landing droplets to experience varying contact angles that alter the surface morphology. The effects of deposition time on surface morphology were investigated by Gürbüz et al. (2016), who deposited 0.05 M SnO₂ film from an ethanol precursor (boiling point of 78 °C) at a substrate temperature of 250 °C and a flow rate of 7.2 mL h⁻¹ for various time intervals. At 20 min, they observed that the substrate was sparsely covered because of the small number

of liquid droplets. At 60 min, a lot of droplets had been deposited on the substrate covering the whole surface and it led to a homogenous porous film. After electro spraying a 0.1 M YSZ precursor in a mixed solvent of ethanol and butyl carbitol (boiling points of 78 °C and 231 °C respectively) at a substrate temperature of 400 °C and a flow rate of 0.5 mL h⁻¹, Neagu et al. (2006) reported a dense coating at 1 h and rough coatings at 4 and 12 h. They attributed the surface roughness to preferential landing of the droplets that occurred at longer deposition periods. For (Maršálek et al., 2015), they prepared manganese oxide layers from a 0.02 M precursor in a mixed solvent of ethanol and water (boiling points of 78 °C and 100 °C respectively) at a flow rate of 1 mL h⁻¹ and a substrate temperature of 200 °C. Deposition times between 10 and 30 min yielded relatively compact and thin layers while longer periods led to formation of agglomerates. In the study by Joshi et al. (2015), they obtained porous films using 0.1 M Bi₂WO₆ precursor in propylene glycol (boiling point of 188.2 °C) deposited at a substrate temperature of 120 °C and a flow rate of 0.04 mL h⁻¹ for 80 min. They reported increased film porosity with deposition time. In another study, Joshi et al. (2012) obtained a dense film using 0.3 M ZnO precursor solutions in propylene glycol (boiling point of 188.2 °C) at a flow rate of 0.075 mL h⁻¹ and a substrate temperature of 200 °C for 30 min. At short deposition times (10, 20, 40 and 60 min), Yoon et al. (2016) obtained uniform compact films from WO₃ precursor in mixed solvent of polyethylene and ethanol (boiling points of 200 °C and 78 °C respectively) at a substrate temperature of 80 °C and a flow rate of 0.08 mL h⁻¹. In other studies, long deposition time led to a porous reticular morphology. As indicated by Koike and Tatsumi (2007, 2005), droplets spread gradually on the substrate surface and the temperature at the surface of the droplet is higher than at its center. Therefore, the solvent at the droplet surface evaporates faster than at its center. This process leads to ring-shaped nucleation and precipitation that forms a reticular morphology on the substrate. An example is Ma et al. (2014) who electro sprayed 0.1 M MnO precursor in 1,2-dihydroxypropane (boiling point of 188.2 °C) at a substrate temperature of 240 °C and a flow rate of 1.5 mL h⁻¹ for 3 h. Another example is Yuan et al. (2017a) using 2 mM CoMn₂O₄ precursor in a mixture of ethanol and 1,2-propanediol (boiling points of 78 °C and 188.2 °C respectively) at a substrate temperature of 250 °C and a flow rate of 2 mL h⁻¹ for 4 h. Also, Yuan et al. (2017b) using 0.01 M Mn₂O₃ precursor in 1,2-propanediol (boiling point of 188.2 °C) at a substrate temperature of 200 °C and a flow

rate of 2 mL h⁻¹ for 3 h. The porosity of the film was observed to increase with deposition time as demonstrated by (Wang et al., 2011) who used a 0.03 M V₂O₅ precursor in a solvent mixture of water, ethanol and 1, 2 propylene glycol (boiling points of 100 °C, 78 °C and 188.2 °C) at a flow rate of 72 mL h⁻¹ and a substrate temperature of 260 °C for deposition times ranging from 4 – 12 h.

2.8 Applications of ESD in energy production, storage and conversion devices

Electrostatic spray deposition is a powerful technique in the deposition of materials taking into account that the particle sizes, their monodispersity and uniform distribution on a surface defines the quality of a thin film. For example, with an aim of depositing Co₃O₄ thin films on a glass substrate, the impact of an electric field during deposition process was confirmed by Abbas et al. (2017). From their findings, the film produced without an electric field showed defects on the surface like pin holes, cracks and crystal flakes while the film deposited in the presence of an electric field had a smoother, more uniform appearance with well-formed grains. Therefore, electrospray technique stands out compared to other methods for thin film deposition (Shui et al., 2004). This section highlights different areas where this novel technique has been applied to enhance the overall performance of materials for energy devices, such as lithium ion batteries, solar cells, capacitors and light emitting diodes.

2.8.1 ESD for the fabrication of solar cells

Solar cells, also known as photovoltaic (PV) cells, are devices that convert sunlight directly to electricity through a process called the photovoltaic effect. This occurs when photons from the sun strike the surface of a solar cell and they get absorbed by a semiconductor material. Consequently, electrons are released and they can be harnessed to generate an electric current. First generation solar cells are made from silicon and their efficiencies range from 12 % to 18 %. With an aim of achieving higher efficiencies and lowering costs, different materials have been investigated and they range from organics to inorganic semiconductors and from crystalline wafers to amorphous structures (Fegade and Jethave, 2021; Ciambelli et al., 2020; Nwaigwe et al., 2019). Consequently, second generation solar cells have been developed and they are considered to be more economical though with lower efficiencies (4 % to 11 %). Unlike

traditional silicon-based solar cells, which are made of thick, rigid wafers, the second-generation solar cells are made from thin films. As a result, they are flexible, lightweight and can be made into a variety of shapes and sizes. They are usually made using materials like perovskites, cadmium telluride (CdTe), amorphous silicon (a-Si) and copper indium gallium selenide (CIGS). Usually, they are fabricated by depositing thin layers of photovoltaic materials on selected substrates. Their applications include areas where weight and flexibility are important, like in portable devices or in building-integrated photovoltaics (BIPV) (Mughal et al., 2018; Bagher et al., 2015; Sharma et al., 2015; El Char et al., 2011).

As shown in Fig. 2.7, the second-generation solar cells consist of several layers made from different materials. These layers comprise of the energy absorber, the buffer/window layer, electrically conductive layer and the substrate. The buffer or window layer (e.g cadmium sulfide, CdS, in the case of CIGS solar cells) aids in electrical transitions between the energy absorber and the electrically conductive layer. For the substrate, glass or a flexible polymer material is used.

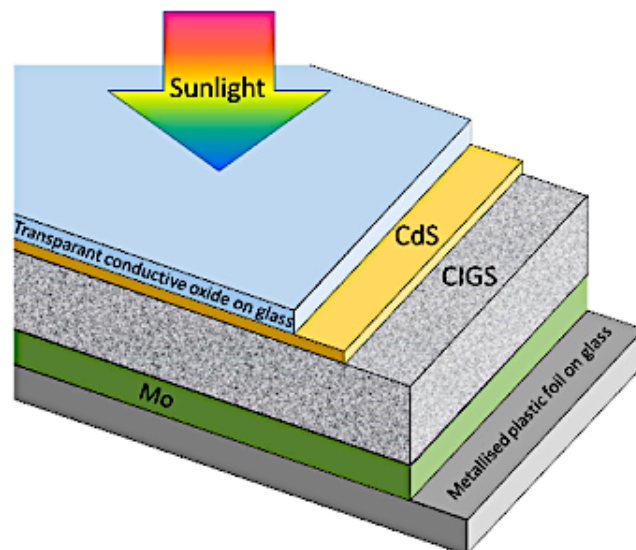


Figure 2.7. Schematic illustration of a CIGS solar cell. Adapted from Kelder et al. (2018).

Conventionally, the layers were deposited using physical or chemical vapour deposition techniques like spin coating, electrodeposition, screen printing, doctor blading, paste coating, precursor printing, and spray pyrolysis. Unfortunately, several drawbacks have

been reported on these methods like precursor material wastage, formation of non homogeneous surfaces, incomplete conversion of the precursor materials leading to formation of poor-quality films (Kelder et al., 2018). To achieve higher deposition efficiencies, electrospray deposition technique provides an effective method for fabrication of solar cells with desired surface morphologies and enhanced performances. Since the surface morphology of the active layers determines the performance of the solar cell in terms of light absorption and electronic transfer, homogeneous flat layers are required. In addition, smooth surface morphologies are desired to ensure efficient charge transport and optimal light absorption. However, certain types of textured surfaces can also be advantageous in enhancing the trapping of light and increasing the effective surface area of the device (Xu et al., 2020s; Zhao and Deng, 2020; Jiang, 2019; Jiang et al., 2018c; Fukuda et al., 2017).

For instance, during the fabrication of a perovskite solar cell, Chandrasekhar et al. (2016) observed a large variation between a film fabricated with an electric field and that fabricated without an electric field in terms of surface morphology and coverage (Fig. 2.8). For both films, the reported efficiencies were 11 % and 7.4 % respectively. The enhanced efficiency for the film deposited in the presence of an applied voltage was attributed to the formation of a more uniform and dense film with large perovskite crystals leading to efficient electron transfer.

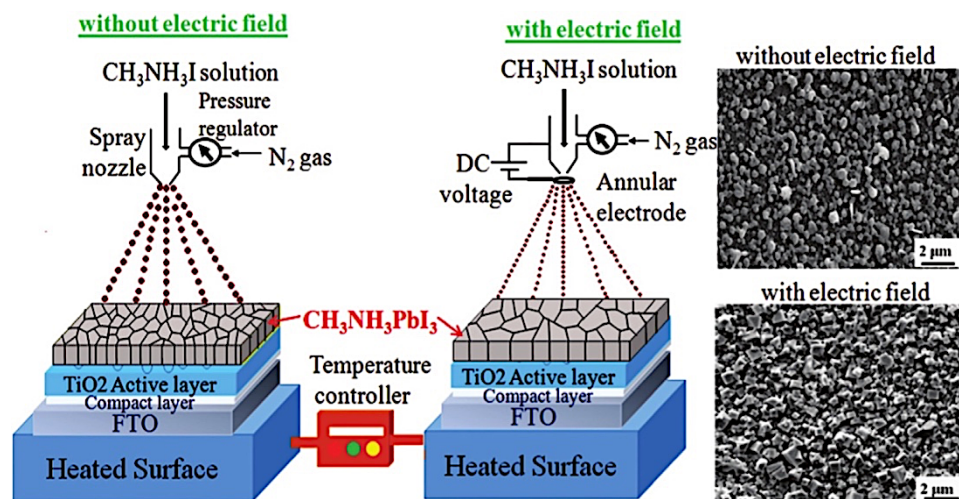


Figure 2.8. Spray deposition process of perovskite films with and without an applied electric field. Adapted from Chandrasekhar et al. (2016).

2.8.2 ESD for the fabrication of supercapacitors

Electric double layer capacitors which are also called ultracapacitors, electrochemical capacitors or supercapacitors are energy storage devices. Due to their high-power density, long life cycle and high-rate capacity, they have gained a lot of attention as potential power sources for the future smart energy era. Typically, their power and energy densities are in between those of dielectric capacitors and batteries. Though with lower energy density than batteries, supercapacitors can offer more rapid charge and discharge rates. Their energy storage phenomenon is based on the interactions between polarized electrodes and ions. This leads to accumulation of ions close to the electrode's surface forming an electric double layer (EDL). This layer is thin and it consists of ions that counterbalance the charge of the electrode (Fig. 2.9). Generally, ultracapacitors play an important role in the development of new technologies like energy storage applications in smart grids and also in portable devices (Simon and Gogotsi, 2020; Fic et al., 2018; Hu et al., 2015).

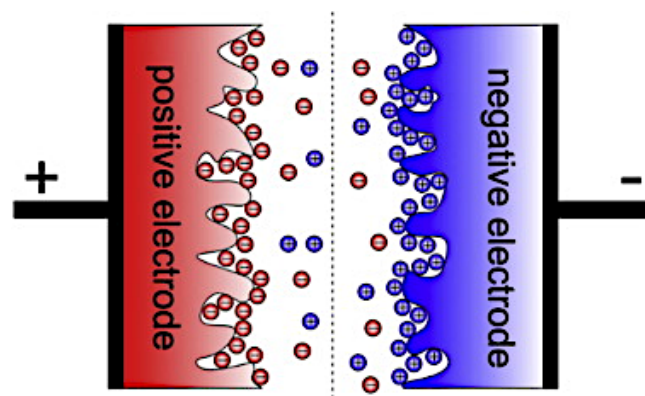


Figure 2.9. Schematic illustration of an electric double layer capacitor. Adapted from Fic et al. (2018).

With an aim of increasing their efficiency in different applications, investigations are underway on how to increase their energy density. Among the different strategies explored, improving the electrodes' performance seems promising. Usually, this performance enhancement is dependent on the surface area of the electrode material. Therefore, to increase the electrodes' surface area, porous structures are preferred and the smaller the pore size the larger the specific surface area (Choi and Yoon, 2015; Chen et al., 2013; Vu et al., 2013). Typically, the electrodes are made of carbon because

of its well-developed porosity, adequate pore size distribution and tunable surface chemistry. However, the carbon electrodes undergo degradation under high voltage.

Therefore, different electrode materials are under investigation and a combination of graphene and metal oxides has shown great potential. The composite electrodes have been reported to show excellent electrochemical stability, improved electrical conductivity and large specific surface area. Conventionally, the electrodes are fabricated by slurry casting method whereby the active materials are simply piled up on top of a metallic foil or foam. Unfortunately, this fabrication method gives rise to nonuniform layers with agglomerates leading to sluggish transport of electrons and ions which compromises the performance of the device (Habeeb and Al-Asadi, 2023; Li et al., 2023; Zhang et al., 2023b; Qi et al., 2022; Xu et al., 2020b). For the fabrication of uniform porous three-dimensional network electrodes, ESD can be adopted and enhanced performance has been reported in different studies (Chavhan et al., 2020; Chavhan and Ganguly, 2019; Cui et al., 2019; Maršálek et al., 2015).

2.8.3 ESD for the fabrication of thin film lithium ion batteries

Over time, the demand for thin film lithium ion batteries has grown due to technological developments that have led to the miniaturization of electronic devices. Such applications include implanted medical elements, on-chip power sources, smart cards and microelectronic mechanical systems. Also, in the medical field there is a growing potential in wearable electronics like cardiac pace makers or smart lenses which could be used for artificial intelligence or health monitoring (Kanazawa et al., 2020; Liu et al., 2020; Lee et al., 2018). To fabricate a thin film battery, the electrodes and the electrolyte materials should be deposited sequentially to form a multilayer structure as shown in Fig.2.10.

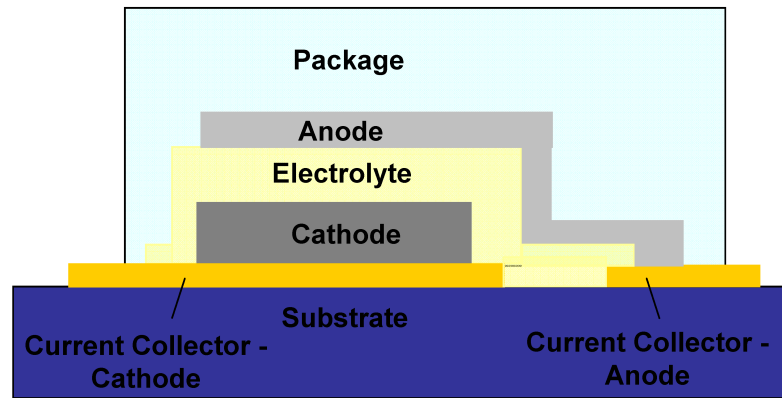


Figure 2.10. Schematic illustration of a thin film battery. Adapted from Garcia-Tamayo (2014).

The world's first thin film lithium ion battery was made in 1983 using vapour deposition technique. It consisted of titanium disulfide (TiS_2) cathode material, $\text{Li}_{3.6}\text{Si}_{0.6}\text{P}_{0.4}\text{O}_4$ solid electrolyte and lithium metal anode. The resulting cell was found feasible as a small source of power for electronic devices that require low current (Kanehori et al., 1983). Currently, different battery materials and deposition techniques are being investigated for the fabrication of thin film lithium ion batteries with enhanced performance (Egbuhuzor et al., 2023; Wu et al., 2023; Moitzheim et al., 2019; Matsuda et al., 2018). Considering that charge transfer takes place on the electrodes, surface morphology of the deposited thin films is of utmost importance. Different studies have investigated the effect of surface morphology on the performance of electrode films. They have reported that porous films show significantly higher performance than compact films and that such morphologies can be obtained using electrospray technique (Wang et al., 2020d; Bezza et al., 2019; Dhanabalan et al., 2017; Yuan et al., 2017a; Yuan et al., 2017c).

2.8.4 ESD for the fabrication of Light Emitting Diode (LEDs)

A light emitting diode is a semiconductor device which emits light when current flows through it. Compared to incandescent light sources, LEDs have several advantages like smaller size, longer lifetime, lower power consumption, improved efficiency, reliability and physical robustness. In addition, they are deemed friendly to the environment since they consist of less toxic materials. Nonetheless, LEDs have efficiencies of around 20 % since a significant amount of energy is converted into heat at the junctions

of the LED modules (Fakharuddin et al., 2022; Ren et al., 2021; Kneissl et al., 2019; Vannacci et al., 2019). Apart from reducing the emission efficiency the produced heat also shortens the lifetime of LEDs. Thermal control is thus a crucial tactic to address these drawbacks. One of the solutions provided is to create a junction between the LED and metal printed circuit board. This is achieved by forming an isolation layer with extremely low thermal conductivity. The isolation layer provides a large thermal resistance that makes the generated heat to be transferred rapidly to a heat sink improving the performance of the device (Su and Huang, 2020; Xu et al., 2020c; Ci et al., 2019; Jean et al., 2016; Shen et al., 2015).

Recently, studies have focused on fabrication of low-cost light emitting diodes that are flexible. Consequently, thin film organic light emitting diodes (OLEDs) have attracted enormous interest, because of their light weight and flexibility. The common deposition techniques for these thin films are vacuum deposition and casting. However, fabrication of the required multi-layered structure is complicated and the processes use harsh solvents which cause dissolution at the interfaces of different layers. Consequently, ESD has been explored as an interesting alternative with great potential in depositing multi layers with different morphologies (Bu et al., 2021; Song et al., 2020; Umbach et al., 2020).

2.8.5 ESD for the deposition of Quantum dots

Quantum dots (QDs) or semiconductor nanocrystals are a type of nanomaterials with quantum confinement effects. This means that they tightly confine electrons or electron-hole pairs (excitons) in all their three dimensions. Their sizes range from 2 to 10 nm and they exhibit optical and electronic properties (optoelectronic) depending on their size, shape and composition. For instance, when excited those of comparatively smaller size (lesser than 5 nm) emit shorter wavelengths in the energy range of green or blue light while larger ones emit longer wavelengths in the energy range of red or orange light. Usually, the electronic properties of quantum dots are intermediate to those of isolated molecules and bulk semiconductors. This class of nanomaterials is considered attractive due to unique properties like superior photostability and size-dependent optical properties. Therefore, they find applications in different fields like LEDs, laser diodes, solar cells, transistors, quantum computing and medical imaging

(Triana et al., 2023; Zia et al., 2022; Maxwell et al., 2020; Lian et al., 2019; Jha, 2018; Pawar et al., 2018; Kumar et al., 2018).

To effectively integrate quantum dots in the devices mentioned above, they must be precisely and accurately deposited in a pattern on predetermined locations. Conventional deposition techniques like spin coating have been used but they give rise to excessive wastage of materials and they also show little control on the patterns of the deposited film. Therefore, ESD can be used to deposit quantum dots whereby the size of particles and morphology can be systematically controlled (Li et al., 2022; Nguyen and Choi, 2020; Nguyen et al., 2018; Li et al., 2017).

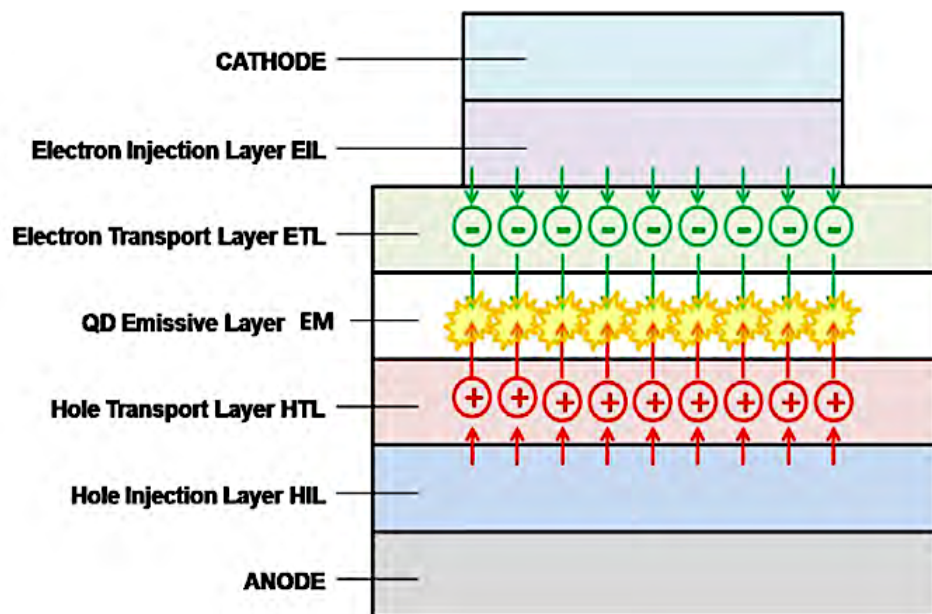


Figure 2.11. Schematic illustration of a basic QD-LED. Adapted from Ugarte et al., (2012).

2.9 Instrumentation

2.9.1 Scanning Electron Microscopy (SEM)

SEM is a non-destructive approach to surface analysis at nano scale and it is considered to be relatively inexpensive and rapid. It is therefore one of the most versatile techniques used for the characterization of surface morphologies in thin films. The technique requires the specimen under test to be electrically conductive, dry and clean. For non-conductive samples, a thin conductive coating like gold is applied to avoid the

build-up of static charges (de Haan et al., 2019; Rydz et al., 2019). As shown in Fig. 2.11, a suitable source, like a field emission gun or a tungsten filament, is used to generate a beam of electrons. The produced electrons are finely focused into a beam and accelerated through a high voltage. To control the path of the produced electrons a set of electromagnetic lenses is used because electrons cannot pass through normal glass lenses. These lenses are in the form of coils of wires upon which a magnetic field is created by applying current on them. The electromagnetic lenses comprise of a condenser lens and an objective lens. The former defines the size of the electron beam thus determining the resolution and the latter focuses the beam onto the sample surface. Scanning coils are also incorporated to deflect the electron beam along the x and y axis producing a raster scan over the sample surface (Vernon-Parry, 2000).

The electron beam then interacts with the sample in an elastic or inelastic manner. For elastic scattering, the incident electron beam gets deflected by the specimen's atomic nucleus or outer shell electrons of similar energy. During this process there is negligible energy loss and incident electrons are scattered through a wide angle. If the angle is more than 90° , such electrons are called backscattered electrons (BSE). On the other hand, during inelastic scattering the incident electron beam transfers a substantial amount of energy to the specimen atoms. The transferred energy depends on whether the electrons of the specimen have been excited singly or collectively and also on the binding energy of the electrons. In the event of ionization of the specimen atoms, secondary electrons (SE) are produced. They usually escape from the specimen with low energies that are less than 50 eV. Conventionally, a scanning electron microscope is operated under vacuum conditions to eliminate any interactions between the electrons and air or particles in air (Shah et al., 2019; Titus et al., 2019; Goldstein et al., 2018).

For the detection of BSE, solid state detectors are commonly used while scintillation detectors are used for SE. In the case of solid-state detection, a solid-state material like silicon or germanium crystal is used as the detecting medium. Upon interacting with the BSE, electron-hole pairs are produced within the crystal. These are the information carriers and their number depends on the energy of BSE. The migration of these charge carriers under an applied voltage generates an electric current. For the scintillation detector, it contains a material (scintillator) which interacts with the low energy SE to

produce light. The light is then collected in a photomultiplier tube for amplification. The resulting beam of electrons is then converted to an electric signal. The created electric signals then form images which are displayed on a computer screen (Faisal, 2021; Mohammed & Abdullah, 2018). Primarily, secondary electrons give topographical information about the sample by providing images with a high spatial resolution. This is because they escape from a very shallow, near-surface layer of the specimen. On the contrary, backscattered electrons are not as many as secondary electrons and they reemerge from the specimen with much higher energies. They also originate from deeper in the specimen producing images with slightly less resolution compared to secondary electrons. Mostly, they provide information about the composition of the specimen whereby elements with high atomic mass show brighter contrast (Vladár and Hodoroaba, 2020; Shah et al., 2019; Akhtar et al., 2018; Cardott and Curtis, 2018; Ul-Hamid, 2018).

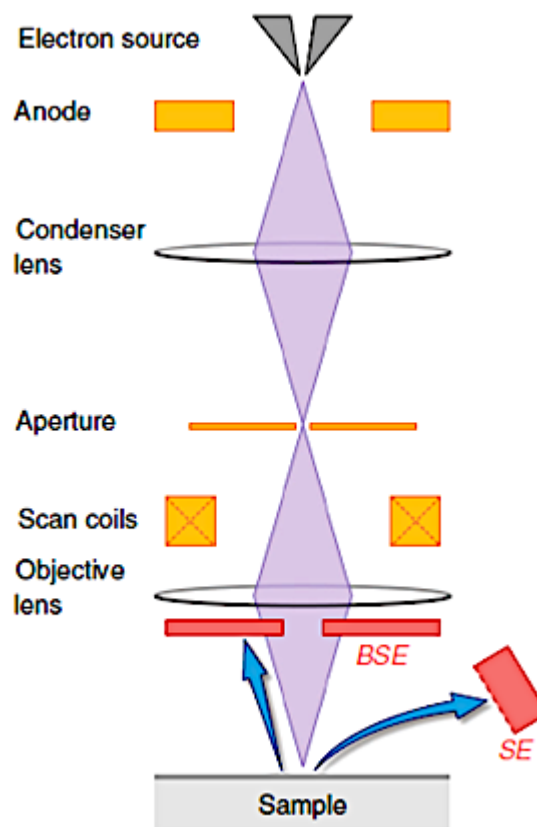


Figure 2.12. Schematic diagram of a scanning electron microscope. Adapted from Shah et al. (2019).

2.9.2 X-Ray Diffraction (XRD)

XRD is a rapid, non-destructive analytical technique that is used for characterization of crystalline materials. X-ray diffraction takes place in crystalline solids because their atomic spacing is in the range of 1 \AA (10^{-10} m) which is similar to the wavelengths of x-rays. As shown in Fig. 2.12, an x-ray diffractometer consists of a source of x-ray radiation (x-ray tube), a sample stage and an x-ray detector. In the x-ray tube, there is a cathode, usually made of tungsten filament, which is heated to generate electrons via thermionic emission. The produced electrons are then accelerated towards a metal anode using a voltage in the range of 10 kV to 60 kV that is applied across the hot filament (cathode). On the metal anode, the accelerated electrons remove an inner electron from the anode material via photoelectric effect and with an effort to fill the created vacancy, electronic transitions from outer shells to the inner shell take place. As a result of this transition, characteristic x-rays are emitted whose energy and wavelength are defined by the difference in the energy levels of the electrons involved in the transition and the anode material. Examples of possible anode materials include copper, cobalt, chromium and molybdenum. In the case of a copper anode which is commonly used in XRD, $\text{Cu K}_{\alpha 1}$, $\text{Cu K}_{\alpha 2}$ and Cu K_{β} are produced but a monochromator only allows the $\text{K}_{\alpha 1}$ to pass. Therefore, the energy of the emitted radiation is given by the energy difference between L_3 subshell (0.94 keV) and K subshell (8.98 keV) which amounts to 8.04 keV. This energy corresponds to a monochromatic beam with a wavelength of 0.1541 nm. Collimated beams of the produced radiation are then directed to a sample. For x-rays with wavelengths that are similar to the spacing between planes in a crystal structure ($1 \text{ \AA}/10^{-10} \text{ m}$), the crystal lattice of the sample functions like a three-dimensional diffraction grating (Ali et al., 2022; Khan et al., 2020; Epp, 2016; Bunaciu et al., 2015).

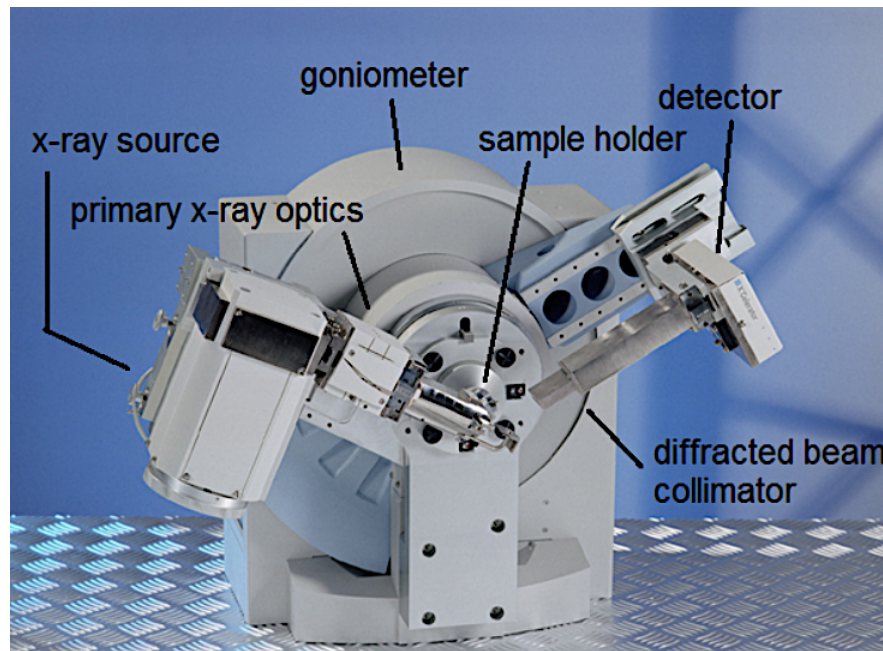


Figure 2.13. Main parts of an x-ray diffractometer. Adapted from Perkins (2022).

The geometry of an x-ray diffractometer is such that the sample rotates at an angle θ in the path of the collimated x-ray beam while the x-ray detector which is mounted on an arm to collect the diffracted x-rays rotates at an angle of 2θ . To enable this rotation, the sample holder and the detector are coupled to a goniometer (an instrument that allows rotation in precise angular positions). During analysis, the rotating sample interacts with x-rays which are produced in an x-ray tube and the intensity of the reflected x-rays is recorded by the rotating detector. Upon interacting with the sample, the x-rays can show either constructive interference or destructive interference. For constructive interference, the diffracted x-rays are in phase meaning that their wave peaks coincide. As a result, their wave energies add up increasing the x-ray amplitude. Conversely, for destructive interference the diffracted x-rays are out of phase meaning that they cancel out. In practical cases, the diffracted x-rays are partially in phase and partially out of phase. Among the two, constructive interference is of greatest importance and it is achieved when Bragg's law is obeyed (Equation 2.19). Considering that diffracted x-rays behave like they are reflected from planes within a crystalline material, Bragg's law considers two parallel planes of atoms which are separated by a distance d as shown in Fig. 2.13. When an x-ray beam is incident onto the crystalline sample with an angle of incidence θ , it gets reflected at the same angle θ . If the interplanar distance, d , is equal to a whole number, n , of wavelength, a constructive interference occurs.

Consequently, a diffraction pattern is observed on the computer monitor. As shown below, Bragg's law illustrates the relationship between the x-ray radiation wavelength, the crystalline sample's interplanar spacing and the diffraction angle.

$$n\lambda = 2d\sin\theta \quad (\text{Eqn. 2.19})$$

where n is an integer (1, 2, 3, 4, ...), λ is the beam wavelength, d is the spacing between the planes and θ is the angle of incidence. Using Bragg's law, the interplanar spacing (d) can be calculated. This allows for phase identification since each crystalline compound has got a set of unique d -spacings (Perkins, 2022; Ameh, 2019; Titus et al., 2019).

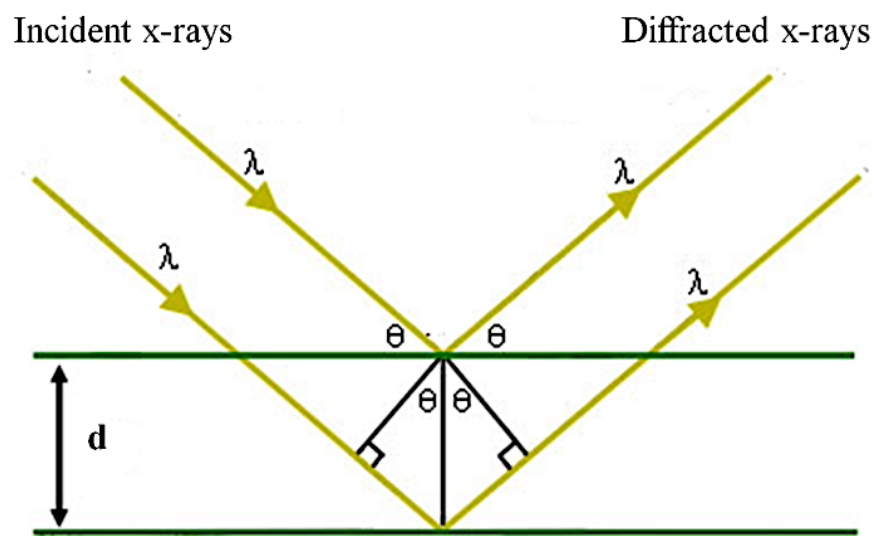


Figure 2.14. Schematic representation used for Bragg's law. The diffracted x-rays show constructive interference when the distance between the two planes is an integer multiple of the wavelength. Adapted from Darrell et al. (2016).

The main objective in an XRD analysis is usually to identify the crystal phases present in a sample using a search and match procedure. This is performed by comparing the obtained pattern from the material under test with an existing database found in the x-ray powder diffraction file that is compiled by the International Centre for Diffraction (Perkins, 2022). In addition, the obtained diffraction pattern can give information on phase composition, crystallite size, lattice, strain and crystallographic orientation as shown in Fig. 2.20. In case of multiple phases within a sample, areas under the peak can be calculated to get the quantity of each phase.

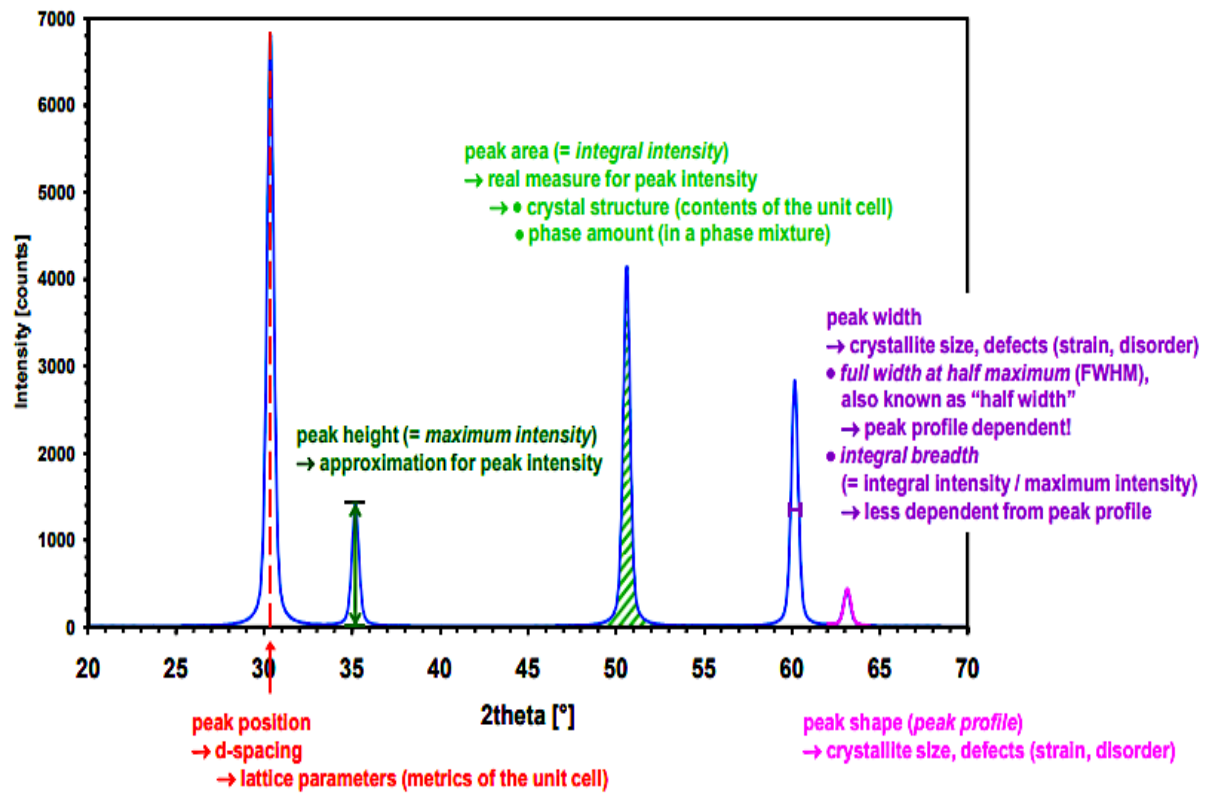


Figure 2.15. Illustration of a diffraction pattern. Adapted from Sharma et al. (2012).

CHAPTER THREE

METHODOLOGY

3.1 Development of the design schedule

A systematic schedule for the design of thin films with different surface morphologies using electrospray technique was developed from literature. It was based on the key parameters that affect electrospray and they include, precursor concentration, flow rate, substrate temperature and deposition time, as discussed in chapter 4.

3.2 Equipment and chemicals

The equipment and chemicals used for this study comprised of;

3.2.1 Equipment

The following equipments were used;

PANalytical X'Pert Pro X-ray diffractometer, JEOL JSM-6010LA Scanning electron microscope, Series 4000 Maccor battery tester, Glove box, Electrospray chamber, Fume hood, Analytical balance, Planetary ball mill, a pellet press, FUG HCN14-12500 high voltage power supply, KD Scientific 100 syringe pump, Optimum® general purpose stainless steel dispense tips (nozzles) and Watson-Marlow chemically-resistant hose.

3.2.2 Chemicals

Analytical reagent grade chemicals were used to synthesize the solid-state electrolyte material and to prepare precursors for thin films. All glassware was cleaned and rinsed with double distilled water.

3.3 Determination of the cone-jet window

To determine the stability window for cone-jet electrospray mode using different liquids, experiments were performed. The three different liquids used were 2-propanol, N-Methyl-2-pyrrolidone (NMP) and Ethylene Glycol. Their properties were determined and these included conductivity, density, surface tension, viscosity and

relative permittivity. The starting flow rate for each liquid was also calculated. The viscosity numbers (VN) were also calculated to verify whether the liquid profile was flat or non-flat. The pump was then set to the calculated flow rate and voltage was applied. For each liquid, electrospray experiments were carried by increasing the voltage slowly starting from zero until a stable cone-jet was observed. The voltage values between which the stable cone was observed were recorded as voltage one (V1) and voltage two (V2) and later used to plot the stability window.

3.4 Synthesis and characterization of the $\text{Li}_6\text{PS}_5\text{Cl}$ (argyrodite) solid-state electrolyte material

To synthesize the $\text{Li}_6\text{PS}_5\text{Cl}$ solid-state electrolyte material, the solid-state sintering method was used. Later the synthesized material was characterized using the x-ray diffraction (XRD) technique to confirm a pure crystalline structure with no impurities.

3.4.1 Synthesis of $\text{Li}_6\text{PS}_5\text{Cl}$ electrolyte material

Stoichiometric quantities of lithium sulfide (Li_2S , 99.98 %, Sigma Aldrich), phosphorus sulfide (P_2S_5 , 99 %, Sigma Aldrich) and lithium chloride (LiCl , 99.0 %, Sigma Aldrich) crystalline powders were used as the starting materials. The reagents were weighed in a glove box and put in a ball milling stainless jar with zirconia balls. Since the sulfur-based electrolyte material gets oxidized in oxygen, the glove box was filled with argon gas to provide an inert atmosphere, free from moisture and oxygen. The different powders were then mixed to homogeneity by mechanical milling process at a speed of 550 rotations per minute for 16 h. In a glove box filled with argon, the resulting homogenous powder was transferred and sealed into a quartz tube. The sealed tube containing the homogeneous mixture was annealed at a temperature of 550 °C in a furnace for 5 h. This process provided enough energy to break the bonds in the unit cells of the reactants. This induced diffusion of ions through their crystals allowing them to find new positions and form the new $\text{Li}_6\text{PS}_5\text{Cl}$ argyrodite compound.

3.4.2 Characterization of $\text{Li}_6\text{PS}_5\text{Cl}$ electrolyte material

Using x-ray diffraction, the prepared $\text{Li}_6\text{PS}_5\text{Cl}$ compound was analysed to determine the crystalline phase present. To prevent reaction of the sulfur-based sample with

oxygen and atmospheric moisture, the synthesized powder was put in an airtight XRD sample holder in a glove box filled with argon. The sample was then placed in the XRD instrument where a powder diffraction pattern was obtained. The radiation source used was the K- α line of copper at 1.5406 Å whereby the x-ray generator was operated at 45 kV and 40 mA. An XRD pattern was then collected and fitting was performed using GSAS-II software for identification of the crystal phase (Toby & Von Dreele, 2013).

3.5 Assembly and characterization of a bulk solid-state lithium ion cell

To analyse the electrochemical performance of the synthesized solid-state electrolyte material ($\text{Li}_6\text{PS}_5\text{Cl}$) prior to the design of a thin film cell, a standard laboratory scale lithium ion cell was fabricated and characterized as explained below.

3.5.1 Assembly of the bulk solid-state lithium ion cell

The bulk solid-state lithium ion cell was assembled by pressing the respective components (cathode, electrolyte and anode) into a three-layer pellet using a hydraulic press. The selected materials were; commercially acquired $\text{LiNi}_{1/3}\text{Mn}_{1/3}\text{Co}_{1/3}\text{O}_2$ (lithium nickel manganese cobalt oxide, NMC111) for the cathode, the synthesized solid-state electrolyte material ($\text{Li}_6\text{PS}_5\text{Cl}$) and commercially acquired indium foil for the anode. The assembly process comprised of several steps as highlighted below.

1. For the cathode, $\text{LiNi}_{1/3}\text{Mn}_{1/3}\text{Co}_{1/3}\text{O}_2$ cathode material, $\text{Li}_6\text{PS}_5\text{Cl}$ solid-state electrolyte and electron conductive carbon (TIMCAL, super P) were mixed to homogeneity in the ratio 45: 45: 10 by mechanical milling process at a speed of 110 rotations per minute for 1 h to form a composite cathode.
2. The electrolyte pellet was then pressed with a hydraulic press using 160 mg of $\text{Li}_6\text{PS}_5\text{Cl}$ material at a pressure of 6 MPa for 20 s.
3. This was followed by uniformly spreading 12 mg of the cathode mixture prepared in step (1) on top of the pressed electrolyte material and pressing the combination at 8 MPa for 20 s to form a two-layer pellet.
4. For the third layer of the pellet, a commercially acquired indium foil (anode material) was cut into a diameter of 7 mm and placed on top of the uncovered surface of the electrolyte layer. This was then pressed at 2 MPa for 20 s to form a three-layer pellet.
5. The process was repeated for a second cell.

3.5.2 Characterization of the bulk solid-state lithium ion cell

The assembled cells were charged and discharged (cycled) at room temperature using the Maccor battery tester. This was done by applying a constant current to the cell under test and recording its voltage response. From the data, plots of voltage versus capacity were obtained.

3.6 Design and characterization of thin films with different surface morphologies

The design of a thin film solid-state lithium ion cell was done by electrospraying. Using selected chemical reagents and following the developed design schedule in section 3.1, thin films with porous surface morphologies that can be used for electrodes and dense thin films that can be used for the electrolyte were designed. Characterization of their surface morphologies was then performed using scanning electron microscopy.

3.6.1 Electrospray deposition of thin films

The experiments were carried out using the electrospray set up shown in Fig. 3.1. It consists of a heated substrate holder, a nozzle, a high voltage power supply connected to the nozzle, a syringe pump where a precursor solution contained in a syringe is fed in a controlled flow rate via a chemically-resistant hose to the nozzle and a temperature controller connected to the substrate holder. The nozzle is held on a movable table which allows the adjustment of nozzle to substrate distance. The $\text{LiNi}_{0.5}\text{Mn}_{1.5}\text{O}_4$ (lithium nickel manganese oxide, LNMO) precursor solutions were prepared by dissolving stoichiometric amounts of reagent grade LiNO_3 (lithium nitrate), $\text{Mn}(\text{NO}_3)_2 \cdot 4\text{H}_2\text{O}$ (manganese nitrate tetrahydrate) and $\text{Ni}(\text{NO}_3)_2 \cdot 6\text{H}_2\text{O}$ (nickel nitrate hexahydrate) in 2-propanol or ethylene glycol. The LiCl (lithium chloride) precursor solutions were prepared by dissolving reagent grade lithium chloride in dimethyl sulfoxide ($(\text{CH}_3)_2\text{SO}$, DMSO). The properties of the prepared precursor solutions which included conductivity, density, surface tension and viscosity, were determined and they were used to calculate respective droplet sizes.

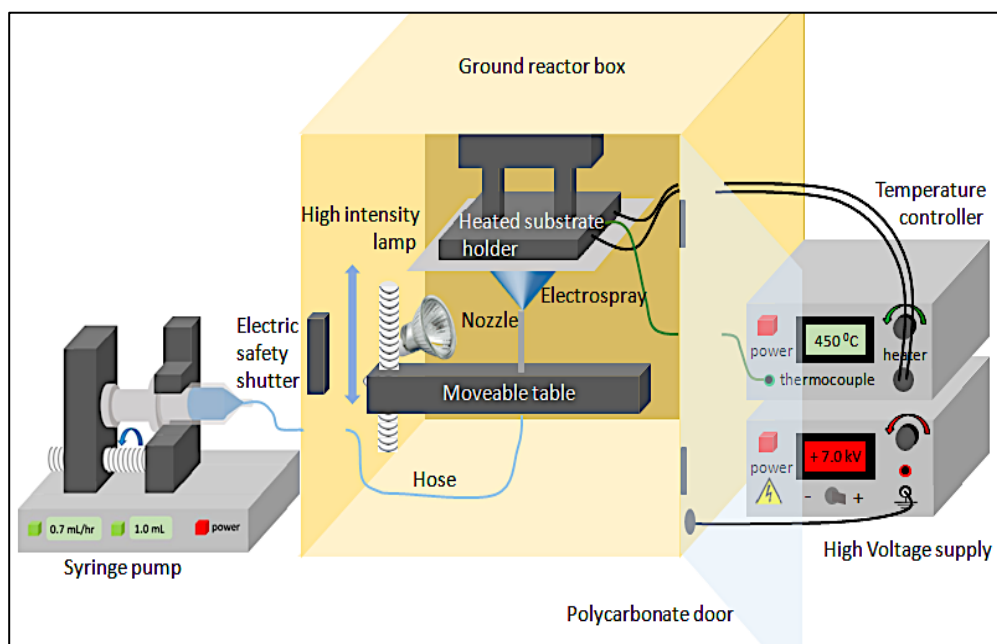


Figure 3.1. Schematic representation of the electro spray setup used for deposition of thin films.

The liquids were then pumped through a syringe to the nozzle at a selected flow rate, one at a time as identified with different experiments. For each experiment, the precursor was sprayed through a metallic nozzle of 1.54 mm internal diameter in the presence of an applied electric field. This field was created by applying a high voltage on the metallic nozzle which was adjusted for each experiment to yield a steady cone-jet. The steady state was ascertained when the liquid meniscus on the nozzle acquired the shape of a cone that did not relax back to a normal droplet shape. After spraying for a selected duration ranging from 1 to 7 h, a thin film was deposited on an aluminium foil substrate heated at a selected temperature ranging from 100 to 350 °C to evaporate the solvents (the boiling points were 82.5 °C for 2-propanol, 197.3 °C for ethylene glycol and 189 °C for DMSO). For the different experiments, the respective electro spray parameters are shown in Table 3.1.

Table 3.1. Electrospray parameters for different experiments.

No.	Precursor solution	nozzle to substrate distance (cm)	Flow rate (mL h ⁻¹)	Duration (h)	Substrate temperature (°C)
a	0.04 M LNMO in 2-propanol	3	2	2	100
b	0.04 M LNMO in 2-propanol	3	2	2	350
c	0.1 M LNMO in 2-propanol	3	1	2	200
d	0.3 M LNMO in 2-propanol	3	0.5	3	200
e	1 M LNMO precursor in 2-propanol	3	2	3	100
f	0.5 M LNMO in 2-propanol and ethylene glycol (1:1)	3	2	1	200
g	0.05 M LiCl in DMSO	3	0.4	1	200
h	1 M LiCl in DMSO	2	0.4	7	200

3.6.2 Characterization of thin film surface morphology

For each experiment, the electrosprayed thin film sample was trimmed using a sharp pair of scissors to a size that would fit well on the sample holder. The trimmed sample was then mounted on a sample holder using a double sided sticky conductive tape whose purpose was to hold the sample in place as well as increase conductivity and eliminate buildup of charge. The sample holder with the sample was then placed appropriately on the instrument's sample stage ready for analysis. During analysis, a beam of electrons is generated from the electron gun via thermionic emission by a

tungsten filament (tungsten is preferred due to its high melting point of 3422 °C). To accelerate the beam of produced electrons towards the mounted specimen, voltages in the range of 5 to 15 kV were applied on the electron gun. Considering that the spot size of the produced electron beam was too large to generate a sharp image, condenser and objective lenses were automatically applied to compress the electron beam spot size. The resulting focused electron beam was then directed on the sample for interaction to take place which was achieved by raster scanning over the sample surface. Consequently, secondary electrons and backscattered electrons were emitted from the sample and they were detected by respective detectors. The obtained signals were used for image formation which was observed on the computer monitor. The produced image magnification, intensity and brightness could be adjusted until a reasonable clear image was obtained.

CHAPTER FOUR

RESULTS AND DISCUSSION

4.1. Development of the design schedule

A design schedule was developed from literature. It provides a systematic way of obtaining specific surface morphologies by altering different electrospray parameters. As discussed later, earlier studies only point out on how different parameters affect morphology but they do not give a systematic way of designing the desired surface morphologies. Their outcomes are usually based on a trial-and-error method.

Table 4.1. A design schedule for electrosprayed thin films with different surface morphologies.

Experimental/precursor liquid parameters				Film morphology	References
High Concentration ($\geq 0.1M$)	High Flow rate	High substrate temperature	Long deposition time	Porous with agglomerates	(Perednis et al., 2005)
			Short deposition time*	Porous cracked film	(Bailly et al., 2012; Gürbüz et al., 2016)
		Low substrate temperature	Long deposition time	Porous reticular	(Ma et al., 2014)
			Short deposition time	Dense particulate	(Joshi et al., 2012; Perednis et al., 2005; Varga et al., 2010)

	Low Flow rate	High substrate temperature	Long deposition time	Porous with agglomerates	(Lafont et al., 2012; Neagu et al., 2006)
			Short deposition time	Dense particulate	(Bailly et al., 2012; Neagu et al., 2006)
		Low substrate temperature	Long deposition time	Porous with agglomerates	(Joshi et al., 2015)
			Short deposition time	Dense particulate	(Yoon et al., 2016)
Low Concentration (< 0.1M)	High Flow rate	High substrate temperature	Long deposition time	Porous reticular	(Wang et al., 2011; Yuan et al., 2017b)
			Short deposition time	Porous broccoli-like agglomerates	(Gürbüz et al., 2016; Varga et al., 2010; Yu et al., 2006b)
		Low substrate temperature	Long deposition time	Porous reticular	(Wang et al., 2009; Wang et al., 2011; Yuan et al., 2017a)
			Short deposition time	Porous particulate	(Hong et al., 2017; Jo et al.,

					2014; Kavadiya et al., 2017; Ma & Qin, 2005)
	Low Flow rate	High substrate temperature	Long deposition time	Porous with agglomerate	(Maršálek et al., 2015)
			Short deposition time	Dense particulate	(Maršálek et al., 2015)
		Low substrate temperature	Long deposition time	Porous reticular	(Koike and Tatsumi, 2007, 2005)
			Short deposition time	Dense particulate	(Hong et al., 2017; Joshi et al., 2013; Kavadiya et al., 2017; Ma & Qin, 2005)

As highlighted in the developed design schedule, key parameters in designing thin films with different surface morphologies using electrospray technique include precursor concentration, flow rate, substrate temperature and deposition time. The effects of these parameters on the surface morphology have been highlighted several studies. For instance, an increase in concentration leads to an increase in the thickness of the film and this affects morphology. In their study, Gürbüz et al. (2016) reported a dense film

from a 0.05 M precursor. A cracked film was observed after increasing the concentration to 0.2 M and this was attributed the film's non-uniform drying.

Among other parameters, it has to be noted that flow rate controls the droplet size hence the final particle size. However, flow rate is not an absolute parameter since it is influenced by other factors as shown in Equation 4.1 (Hartman, 1998).

$$Q_0 = \frac{\varepsilon_0 \gamma}{\rho K} \quad (\text{Eqn. 4.1})$$

where ε_0 is electric permittivity of a vacuum, γ is surface tension of the liquid, ρ is liquid density and K is liquid conductivity. Among these factors, conductivity is the most prominent and its variation can lead to a wide range of droplet sizes. Unfortunately, most of these parameters are not given by the authors of the literature cited here. Nonetheless, if the range of conductivity values is not too big it does not tremendously influence the droplet diameter. This is because in the equation for droplet size, the conductivity appears as a power of $1/6$ or $1/3$ as shown in Equations 4.2 and 4.3.

$$d_{d, \text{varicose}} = \left(\frac{16\rho\varepsilon_0 Q^3}{\gamma K} \right)^{1/6} \quad (\text{Eqn. 4.2})$$

$$d_{d, \text{whipping}} = \left(0.8 \frac{288\varepsilon_0 \gamma Q^2}{I^2} \right)^{1/3} \quad (\text{Eqn. 4.3})$$

where $d_{d, \text{varicose}}$ is droplet diameter in varicose breakup regime, ρ is precursor liquid density (kg m^{-3}), ε_0 is electric permittivity of a vacuum ($\text{C}^2 \text{N}^{-1} \text{m}^{-2}$), Q is flow rate of the precursor liquid ($\text{m}^3 \text{s}^{-1}$), γ is surface tension of the precursor liquid (N m^{-1}), K is conductivity of the precursor liquid (S m^{-1}), $d_{d, \text{whipping}}$ is droplet diameter in whipping breakup regime and I is jet's electric current (Yurteri et al., 2010). On the contrary, if the range of conductivities is big the effect on droplet size is significant (Joshi et al., 2013). It is also important to know which flow rates can achieve the cone-jet mode. This is defined by minimum and a maximum flow rate values and they form an operational window. When all other parameters are held constant, low flow rate produces relatively small droplets hence small particles while high flow rate produces relatively big droplets that dry up into big particles (Kavadiya et al., 2017; Hong et al., 2017).

Also, different surface morphologies can be achieved depending on the choice of solvent and substrate temperature (Perednis et al., 2005). Essentially, when making films by electrospraying, charged droplets are produced from a precursor liquid and

they are directed at a substrate of choice. A solid layer is then formed after the solvent has evaporated, and this process can be accelerated by heating the substrate. Usually, the substrate temperature is set to be above or below the solvent boiling point. While keeping other parameters constant heating the substrate to a temperature above the solvent boiling point, results in a dense layer. This is because the high temperature leads to evaporation of a big percentage of the solvent from the droplet surface. Consequently, the droplet size reduces but its overall electric charge remains constant and the Rayleigh limit is exceeded causing it to explode into many smaller droplets (Rahmanpour & Ebrahimi, 2017). The smaller droplets drift towards the substrate under electrostatic forces and they are expected to dry up into even smaller particles leading to a dense layer. Conversely, at relatively high flow rates the produced droplets are relatively big (Jo et al., 2014; Varga et al., 2010). According to Vercoulen (1995) such droplets are less likely to achieve Rayleigh break up and they dry up on the substrate to form relatively big particles that lead to a porous layer.

Deposition time is another very important parameter not only in determining the layer thickness but also the surface morphology. By increasing the deposition time, morphology of the film can change from dense to porous (Joshi et al., 2021). In a short deposition time, the film is thin and the droplets are sparsely distributed on the substrate. With increasing time, the film thickens and the substrate surface is completely covered causing consecutive landing droplets to experience varying contact angles that may alter the surface morphology.

4.2. Determination of the cone-jet window

The determined liquid properties for the three selected liquids are shown in Table 4.2.

Table 4.2. Properties of three different liquids whose cone-jet operation window was experimentally determined.

Physical parameters	Experiment 1	Experiment 2	Experiment 3
Solvent	2-Propanol	N-Methyl-2-pyrrolidone (NMP)	Ethylene Glycol
Boiling point (°C)	82.5	202	197.3
Conductivity (K) S m ⁻¹	0.0003	0.0011	0.0003
Density (ρ) kg m ⁻³	785	1027	1113
Surface tension (γ) N m ⁻¹	0.0217	0.0418	0.0473
viscosity (μ) Pa s	0.00238	0.00165	0.0161
Relative permittivity	19.26	33	37

As indicated in Table 4.3, results of the calculated minimum (Q_{\min}) and maximum (Q_{\max}) flow rate values were obtained using the formulas derived by Marijnissen et al. (2023) while viscosity number was calculated using the formula derived by Yurteri et al. (2020).

Table 4.3. Calculated flow rate values for 2-propanol, NMP and ethylene glycol and their respective viscosity numbers.

Equations	2- propanol	NMP	Ethylene Glycol
$Q_{\min(\text{flat profile})} = 6.1 Q_0, \text{ nl s}^{-1}$ (Eqn. 4.4)	5.0	2.0	7.6
$Q_0 = \frac{\varepsilon_0 Y}{\rho K}, \text{ nl s}^{-1}$ (Eqn. 4.5)	0.815	0.328	1.25
$VN = \left(\frac{\gamma^3 \varepsilon_0^2}{\mu^3 K^2 Q_{\min}}\right)^{1/3}$ (Eqn. 4.6)	0.5	0.8	0.1
$Q_{\max(\text{flat profile})} = 460.1 Q_0, \text{ nl s}^{-1}$ (Eqn. 4.7)	375	151	575
$VN = \left(\frac{\gamma^3 \varepsilon_0^2}{\mu^3 K^2 Q_{\max}}\right)^{1/3}$ (Eqn. 4.8)	0.1	0.2	0.03

The calculation of the flow rate values was critical in selecting an appropriate syringe size that would accommodate the required flow rate range for each liquid. The obtained viscosity numbers (VN) were less than unity (1) for all liquids confirming a flat profile (Yurteri et al., 2010).

From the experiments, it was observed that a steady cone could only be attained within a given range of the applied voltage. Starting with the lowest possible flow rate as determined by the pump, the voltage range within which a stable cone was observed using the naked eye was recorded. Just as it is reported in literature, a steady cone-jet could only be attained within a given range of the applied voltage for every selected flow rate (Gañán-Calvo et al., 2018; Hartman, 1998; Cloupeau & Prunet-Foch, 1989). Before attaining the lower voltage limit (V1), a pulsating cone was observed. Upon attaining V1, the cone became stable until a certain upper voltage limit (V2) was exceeded. Beyond V2, the cone became unstable and it split into multiple jets. The recorded values for voltage values V1 and V2 are shown in Table 4.4.

Table 4.4. Experimentally determined flow rate and voltage values defining the cone-jet window for each precursor liquid used.

Precursor liquid	Flow rate	Experiment 1		Experiment 2		Average	
		V ₁ (kV)	V ₂ (kV)	V ₁ (kV)	V ₂ (kV)	V ₁ (kV)	V ₂ (kV)
2-propanol	(nl s ⁻¹)						
	5.56	4.2	4.5	4.2	4.45	4.2	4.475
	13.89	4.25	4.8	4.25	4.75	4.25	4.775
	22.22	4.3	5.1	4.35	5.15	4.325	5.125
	27.78	4.35	5.15	4.4	5.3	4.375	5.225
	55.56	4.55	5.75	4.6	5.8	4.575	5.775
	138.89	5.2	6.1	5.1	6.2	5.15	6.15
	194.45	5.6	6.25	5.5	6.3	5.55	6.275
	277.78	6.1	6.45	6.0	6.45	6.05	6.45
	361.11	6.4	6.5	6.35	6.45	6.375	6.475
416.67	6.4	6.4	6.35	6.35	6.375	6.375	
NMP	27.78	8	8.9	8	8.8	8	8.85
	55.56	8.2	8.9	8.2	8.9	8.2	8.9
	83.33	8.4	8.95	8.4	8.95	8.4	8.95
	111.11	8.7	8.95	8.7	8.95	8.7	8.95
	138.89	9	9	9	9	9	9
Ethylene glycol	5.56	6.5	6.7	6.9	7.1	6.7	6.9
	8.33	6.5	6.8	6.9	7.4	6.7	7.1
	11.11	6.7	7	6.9	7.4	6.8	7.2
	13.89	6.8	7	6.9	7.4	6.9	7.2
	27.78	6.9	7.6	6.9	7.6	6.9	7.6
	55.56	6.8	7.7	6.8	7.7	6.8	7.7
	83.33	6.8	8.3	6.8	7.7	6.8	8
	111.11	6.8	8.3	6.8	7.7	6.8	8
	138.89	6.8	8.4	6.8	7.8	6.8	8.1
	277.78	7	8.4	7	7.8	7	8.1
	416.67	7.4	8.5	7.4	7.9	7.4	8.2
	555.56	8.4	8.5	8.4	8.5	8.4	8.5
583.34	8.4	8.4	8.4	8.4	8.4	8.4	

For each liquid, the experiment was performed in duplicate, and the average values used to plot a curve of voltage versus flow rate as shown below, which defined the cone-jet stability window. The lowest measured flow rate values on the left side of the curve gave experimental values for the minimum flow rates of 2-propanol and ethylene glycol while the highest measured flow rate values on the right side of the curves gave experimental maximum flow rates values for the three liquids. Unfortunately, for NMP the lowest flow rate value or a value close to it could not be measured with the available pump. On the plots, voltage 1 (V1) is presented as series 1 in blue while voltage 2 (V2) is presented as series 2 in red.

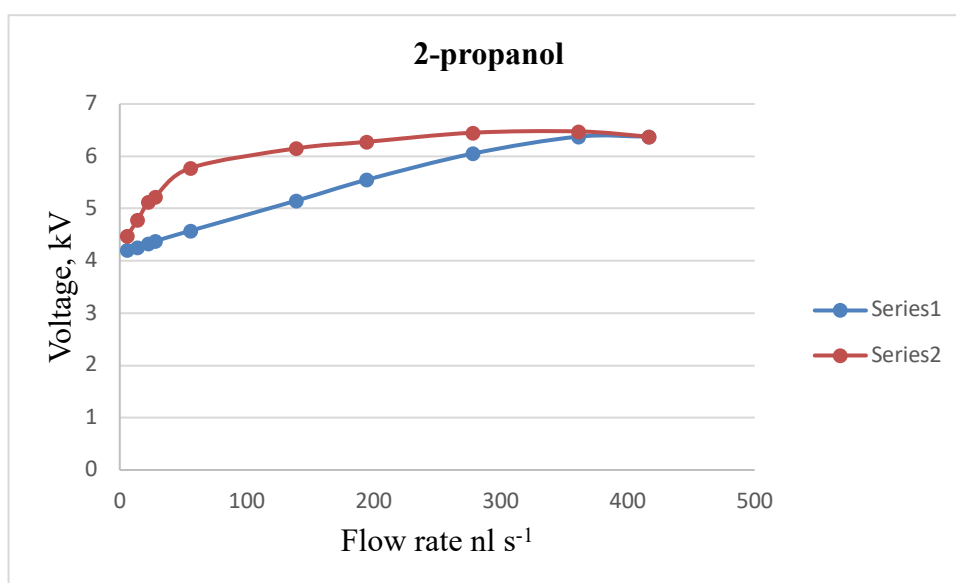


Figure 4.1. Voltage-flow rate curve used for the determination of the cone-jet window for 2-propanol.

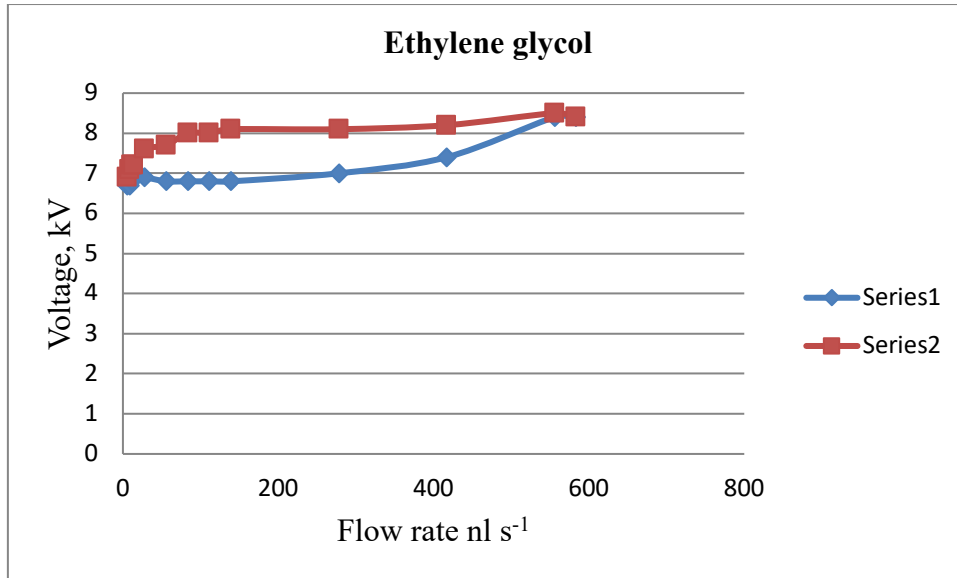


Figure 4.2. Voltage-flow rate curve used for the determination of the cone-jet window for ethylene glycol.

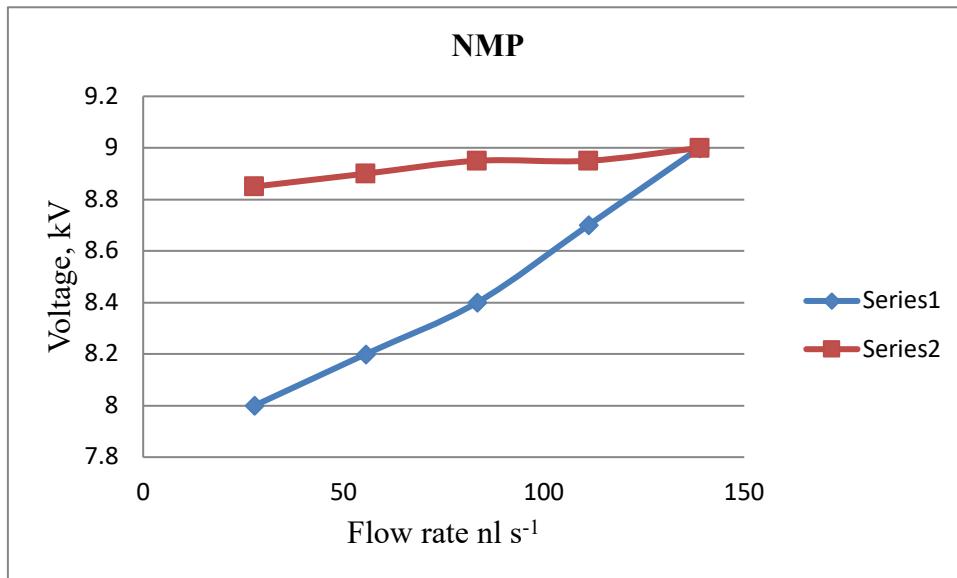


Figure 4.3. Voltage-flow rate curve used for the determination of the cone-jet window for NMP.

In summary, it was found that for 2-propanol $Q_{\min_calculated} = 5.0 \text{ nl s}^{-1}$, $Q_{\min_measured} = 5.6 \text{ nl s}^{-1}$, $Q_{\max_calculated} = 375 \text{ nl s}^{-1}$ and $Q_{\max_measured} = 416.7 \text{ nl s}^{-1}$. For NMP the results were; $Q_{\min_calculated} = 2.0 \text{ nl s}^{-1}$, $Q_{\min_measured}$ or a value close to it could not be experimentally obtained with the available pump, $Q_{\max_calculated} = 151 \text{ nl s}^{-1}$ and $Q_{\max_measured} = 138.9 \text{ nl s}^{-1}$. Finally for ethylene glycol it was found that $Q_{\min_calculated} =$

7.6 nl s^{-1} , $Q_{\text{min_measured}} = 5.6 \text{ nl s}^{-1}$, $Q_{\text{max_calculated}} = 575 \text{ nl s}^{-1}$ and $Q_{\text{max_measured}} = 583.3 \text{ nl s}^{-1}$.

4.3 XRD characterization of the synthesized argyrodite ($\text{Li}_6\text{PS}_5\text{Cl}$) electrolyte material.

Fig. 4.4 shows the XRD pattern of $\text{Li}_6\text{PS}_5\text{Cl}$ solid-state electrolyte material. The peaks on the diffraction pattern were obtained from the constructive interference of x-rays scattered by crystal planes within the $\text{Li}_6\text{PS}_5\text{Cl}$ crystalline material. The respective crystal planes are indicated on the pattern. In the pattern, the red line is the background. The dark blue peaks show the observed pattern after analysing $\text{Li}_6\text{PS}_5\text{Cl}$ crystalline material. The green peaks show the obtained pattern after fitting the standard parameters for $\text{Li}_6\text{PS}_5\text{Cl}$ material. The light blue plot at the bottom shows the difference between the measured and fitted patterns. The crystal structure of the material was identified to be a cubic crystalline structure in the space group F-43m with unit cell parameters of 9.85 \AA . These results were in good agreement with findings from other studies in literature and it indicated the successful synthesis of pure $\text{Li}_6\text{PS}_5\text{Cl}$ electrolyte material (Boulineau et al., 2012; Rajagopal et al., 2022; Randrema et al., 2021; C. Yu et al., 2018; C. Zhao et al., 2022).

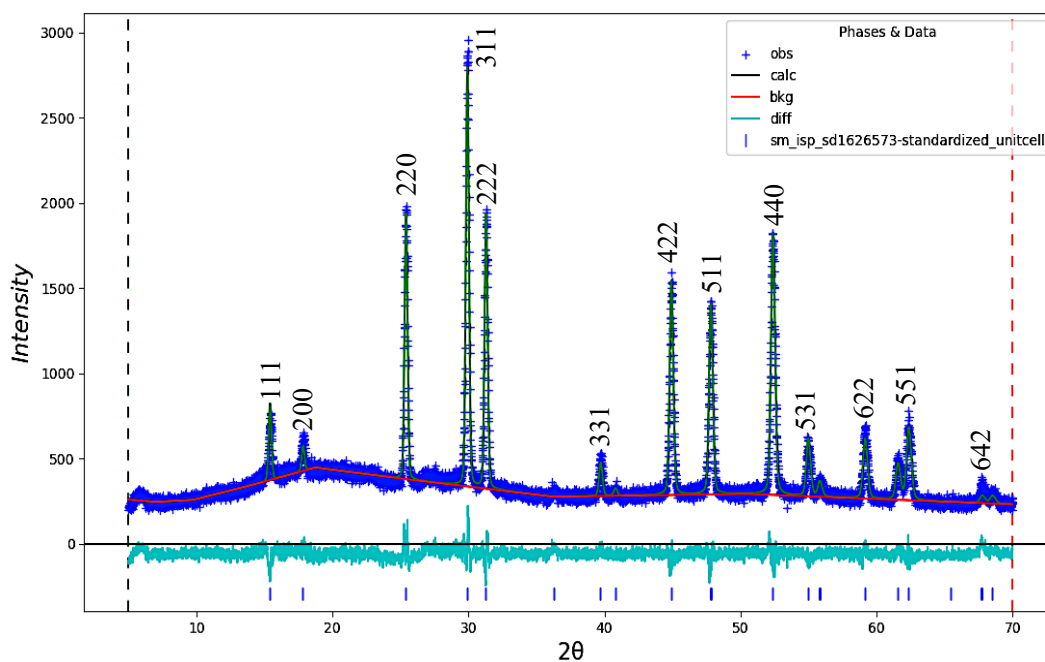


Figure 4.4. The XRD pattern of $\text{Li}_6\text{PS}_5\text{Cl}$ solid-state electrolyte material that has been refined using GSAS-II software.

4.4 Assembly of the bulk solid-state lithium ion cell

A composite cathode was used as described earlier in the methodology instead of using the selected cathode material in its pure form ($\text{LiNi}_{1/3}\text{Mn}_{1/3}\text{Co}_{1/3}\text{O}_2$). This was achieved by integrating the synthesized solid electrolyte ($\text{Li}_6\text{PS}_5\text{Cl}$) and carbon. The composite cathode would enhance intimacy between the electrolyte and the cathode layers reducing resistance at their interface. Also, it would improve transport kinetics within the battery by simultaneously providing electronic and ionic conduction paths between the cathode and the solid-state electrolyte material (Zeng et al., 2023; Giraldo et al., 2021; Sakuda, 2018; Noh et al., 2018).

4.5 Characterization of the fabricated bulk solid-state lithium ion cell

Discharge curves were obtained after cycling the cells. It was expected that initially a voltage would drop due to the battery's internal resistance and chemical reactions with flow of current. The voltage would then stabilize and remain relatively constant for a while forming a plateau. With continued discharge, the voltage would start to decline again which would be more rapid near the end of the discharge cycle. Fig. 4.5 shows five discharge curves of the bulk solid-state cell galvanostatically cycled at a charge/discharge rate of 0.05 C between 1 and 3.7 V potential range. The observed voltage plateau was 1.5 V. Schwietert et al., 2020 reported a voltage plateau of 1.2 V. The recorded initial discharge capacity was 32.6 mAh g^{-1} . From literature, the accessible capacity for NMC111 ($\text{LiNi}_{1/3}\text{Co}_{1/3}\text{Mn}_{1/3}\text{O}_2$) cathode material is between 150 and 160 mAh g^{-1} (Rosero-Navarro et al., 2019; Jung et al., 2017; Wu et al., 2017; Zheng, et al., 2017b Seidlmayer et al., 2016; Buchberger et al., 2015; Noh et al., 2013). The measured low discharge capacity could have been caused by poor solid-solid contacts between the electrodes and the electrolyte which limits lithium ion transfer (Giraldo et al., 2021; Noh et al., 2018). In a more recent study by (Tron et al., 2023) they reported that poor solid-solid contacts in solid-state lithium ion batteries were caused by large particle sizes of the cathode materials. Though they did not mention the actual values of the particle sizes, they compared two NMC ($\text{LiNi}_{0.8}\text{Mn}_{0.1}\text{Co}_{0.1}\text{O}_2$) cathode materials of different particle sizes and reported a higher discharge capacity (161 mAh g^{-1}) for the material with small particle size and a lower discharge capacity (93 mAh g^{-1}) for the material with big particle size for the first cycle. Therefore, small

particle sizes in the nano range would enhance intimacy between the cathode and the electrolyte leading to excellent battery performance (Bielefeld et al., 2019; Strauss et al., 2018; Phuc et al., 2017; Julien et al., 2016).

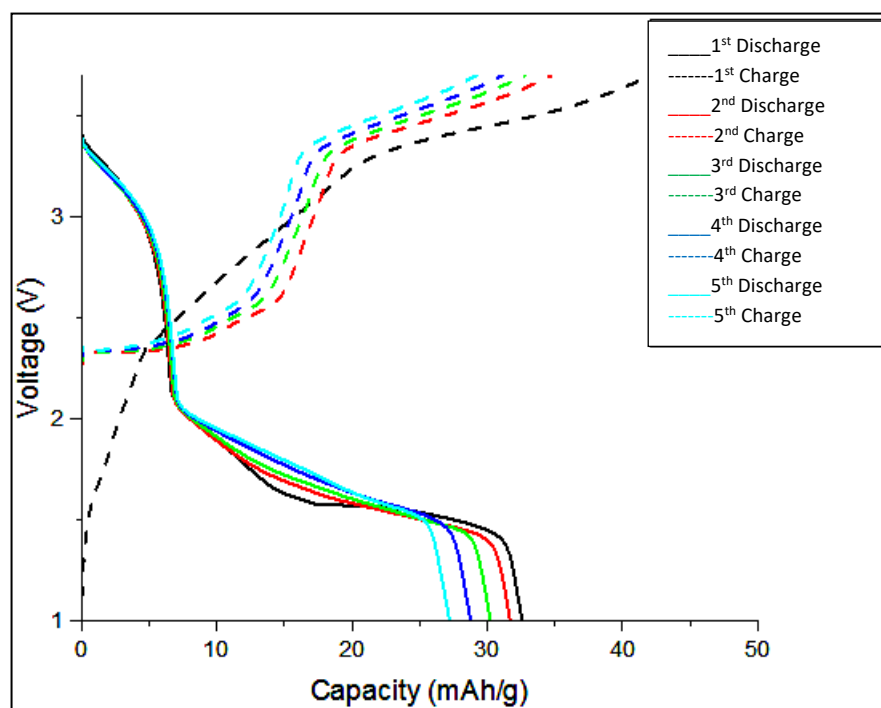


Figure 4.5. The first five charge-discharge curves of the fabricated bulk solid-state lithium ion cell cycled at a cut-off voltage of 3.7 V.

Another factor that might have contributed to the low discharge capacity is inhomogeneity in the cathode mixture. This can be solved by preparing a homogeneous cathode mixture using a solution-based method instead of mixing the solid precursors by mechanical milling. For instance, Matsuda et al. (2018) reported a lower initial discharge capacity of 27 mAh g^{-1} for the cathode mixture prepared by hand mixing the dry/solid precursors and a higher initial discharge capacity of 90 mAh g^{-1} was obtained for the cathode mixture prepared from a solution-based precursor. Also in their study, Rosero-Navarro et al. (2018) demonstrated that a solution-based method was more effective in promoting a good interface between the $\text{Li}_6\text{PS}_5\text{Cl}$ electrolyte and the NMC111 cathode material. They reported initial discharge capacities of 92 and 160 mAh g^{-1} for cathode mixtures prepared by mechanical milling of precursor powders and solution-based methods respectively. In a similar study, Calpa et al. (2019) using NCM111 cathode material and sulfide solid electrolyte ($\text{Li}_7\text{P}_3\text{S}_{11}$) prepared by liquid

phase and mechanical milling methods, reported initial discharge capacities of 154 mA h g⁻¹ and 46 mA h g⁻¹ respectively. According to Rosero-Navarro et al. (2018), the particle size of Li₆PS₅Cl particles synthesized from a solution-based method was more than ten times smaller compared with the particle size synthesized by mechanical milling method.

In addition, as much as the introduction of the solid-state electrolyte in the cathode material is critical as discussed in section 4.4, it can also compromise the energy density of the resulting battery. This is because the solid-state electrolyte material has got negligible contribution to the discharged capacity. Therefore, it should only be present in a very low amount in the cathode mixture, just enough to create the required ion conductivity. Consequently, a balance has to be established between lithium ion conduction and energy density. With 10 % of the solid-state electrolyte in the composite cathode, Rosero-Navarro et al. (2018) reported an initial discharge capacity of 120 mA h g⁻¹ from a cell with NMC111 cathode material, Li₆PS₅Cl electrolyte and indium foil anode. Also, chemical interactions between oxide cathode materials like LiNi_{1/3}Mn_{1/3}Co_{1/3}O₂ and sulfide solid-state electrolytes like Li₆PS₅Cl, which have been used in this study, could have led to the formation of a high internal resistance limiting the electrochemical performance of the fabricated battery (Deng et al., 2021; Wu et al., 2021b; Okuno et al., 2020; Xiao et al., 2019a; Koerver et al., 2017a).

From the discharge curves in Fig. 4.5, it is also evident that that discharge capacity decreased with cycling. The capacity loss demonstrated can be attributed to irreversible parasitic processes such as electrolyte decomposition. From previous studies, decomposition of the solid-state electrolyte leads to formation of insulating products at the interface which retard the mobility of lithium ions leading to a large interfacial charge transfer resistance during cycling (Auvergniot et al., 2017; Koerver, Walther, et al., 2017b). Surprisingly, the presence of carbon in the cathode mixture, like in this study, has also been reported to aggravate the electrochemical decomposition of solid-state electrolytes. Another challenge could be the volumetric change associated with the insertion and extraction of lithium ions in the electrodes especially in the indium anode. This strains the interface with the solid-state electrolyte and could lead to

mechanical failure of the cell (Tron et al., 2023; Ates et al., 2019; Yoon et al., 2018b; Zhang et al., 2017).

During the charging process, lithium ions are removed/deintercalated from the cathode material and inserted/intercalated into the anode material. On the contrary, when discharging, the process works in reverse whereby the anode releases lithium ions after losing electrons. The released lithium ions then pass through the electrolyte and they intercalate into the cathode. When the cathode material takes up more lithium during discharge than what had been delithiated during the previous charge then the coulombic efficiency is greater than 100 %. From Table 4.5, the charge capacity of the bulk cell is higher than the discharge capacity leading to a coulombic efficiency of 77.6 %. For a similar cell, coulombic efficiencies ranging from 75 to 90 % were reported (Dao et al., 2020). A low coulombic efficiency (less than 100 %) means that not all of the lithium ions were released from the positive electrode during charging returned to the positive electrode during discharging. This could be caused by irreversible reactions of the cathode material with the electrolyte material at the interface leading to formation of a solid electrolyte interface (SEI) layer. A loss of cathode material could also be due to irreversible structural changes. Alternatively, the capacity loss could be due to slow lithium intercalation kinetics (Zhou et al., 2019; Kasnatscheew et al., 2016).

Table 4.5. A summary of charge and discharge capacities with the respective coulombic efficiencies for the first bulk solid-state cell.

Cycle no.	Charge capacity (mAh g ⁻¹)	Discharge capacity (mAh g ⁻¹)	Coulombic efficiency (%)
1	42.0	32.6	77.6
2	34.7	31.7	91.4
3	32.8	30.2	92.1
4	31.1	28.8	92.6
5	29.2	27.2	93.2

With an aim of achieving higher discharge capacities, a second bulk cell was galvanostatically cycled at a higher cut-off voltage at the same charge/discharge rate of

0.05 C between 1 and 4.3 V potential range as shown in Fig. 4.6. The initial discharge capacity recorded was 64 mAh g⁻¹ which was twice the achieved capacity at a lower cut-off voltage of 3.7 V. The higher discharged capacity means that more lithium can be extracted/intercalated with a higher cutoff voltage. A similar observation was made by Zuo et al. (2021) who used NCM622 (LiNi_{0.6}Mn_{0.2}Co_{0.2}O₂) cathode material with a theoretical capacity of 277 mAh g⁻¹. They reported cut-off dependant capacities of 169 mAh g⁻¹ at 3.6 V, 182 mAh g⁻¹ at 3.7 V, 192 mAh g⁻¹ at 3.8 V and 200 mAh g⁻¹ at 3.9 V.

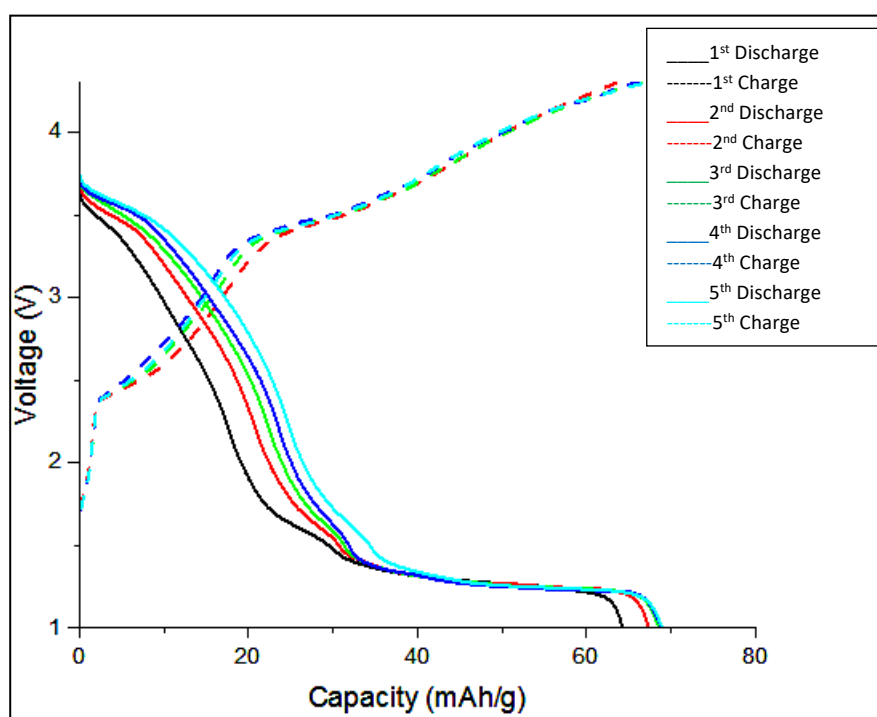


Figure 4.6. The first five charge-discharge curves of the bulk solid-state lithium ion cell cycled at a cut-off voltage of 4.3 V.

Unlike in the first cell, Table 4.6 shows that charge and discharge capacities increased with cycling in the second cell. The highest discharge capacity of 115 mA h g⁻¹ was recorded at the 16th cycle. However, after this cycle the capacity started fading up to 13.6 mA h g⁻¹ for the 50th cycle. The irregularities in the coulombic efficiencies and capacity fading were a clear indication of electrochemical instabilities. Therefore, the high cut-off voltage aggravated material degradation impeding performance of the cell.

Table 4.6 A summary of charge and discharge capacities with the respective coulombic efficiencies for the second bulk solid-state cell.

Cycle no.	Charge capacity (mAh g ⁻¹)	Discharge capacity (mAh g ⁻¹)	Coulombic efficiency (%)
1	72.9	64.3	88.2
2	70.1	67.4	96.1
3	71.6	68.6	95.8
4	72.0	68.7	95.7
5	72.8	69.0	94.7
6	71.0	68.0	95.8
7	71.4	67.5	94.5
8	70.4	66.8	94.9
9	68.1	64.0	94.0
10	71.8	68.2	95.0
11	66.4	62.8	94.6
12	84.8	82.2	97.0
13	89.6	84.4	94.1
14	95.3	90.4	94.8
15	110.1	102.9	93.4
16	123.6	115.3	93.3
17	118.0	106.3	90.1
18	94.7	88.2	93.2
19	89.7	83.3	92.9
20	91.6	86.5	94.4
21	89.1	84.6	95.0
22	83.8	80.1	95.5
23	115.6	77.3	66.9
24	81.0	75.5	93.2
25	78.3	76.2	97.4
26	81.7	75.9	92.9
27	75.7	70.9	93.7

28	73.1	70.6	96.7
29	73.8	69.1	93.6
30	67.2	64.5	96.0
31	66.3	61.0	92.1
32	61.4	59.9	97.6
33	64.0	58.6	91.5
34	58.8	56.2	95.7
35	56.2	51.0	90.8
36	53.5	51.3	96.0
37	50.3	47.2	93.7
38	47.5	46.2	97.2
39	48.1	40.3	83.8
40	41.1	40.8	99.4
41	41.3	39.2	95.0
42	40.3	35.2	87.4
43	33.8	30.4	89.8
44	30.2	29.9	99.1
45	34.1	34.7	101.8
46	33.2	26.6	80.0
47	26.6	23.0	86.6
48	22.1	19.4	87.5
49	20.5	23.3	113.8
50	27.0	13.6	50

4.6 Design and characterization of electrosprayed thin films

For the different electrospray deposition experiments, the determined values for liquid properties are shown in Table 4.7. Surface tension values were obtained from the dripping method described by Gianino (2006). Density values were acquired by determining the mass of the liquid and dividing it by its volume (IOP, 2007). Conductivity was obtained from a conductivity meter. Viscosity values were obtained from a simple viscometer (Daignault et al., 1990). From these parameters, expected droplet sizes were estimated as described by Yurteri et al., 2010.

Table 4.7 Properties of the precursor liquids and respective calculated droplet sizes.

No.	Precursor solution	Surface tension (N m ⁻¹)	Density (g cm ⁻³)	Conductivity (S m ⁻¹)	Viscosity (Pa s)	Flow rate (ml h ⁻¹)	Droplet size (μm)
1	0.04 M LNMO in 2-propanol	0.023	778	0.0268	0.002	2	2.08
2	0.1 M LNMO in 2-propanol	0.022	795	0.0595	0.002	1	1.26
3	0.3 M LNMO in 2-propanol	0.022	879	0.1501	0.002	0.5	0.74
4	1 M LNMO precursor in 2-propanol	0.020	1119.3	0.1775	0.003	2	1.11
5	0.5 M LNMO in 2-propanol and ethylene glycol (1:1)	0.028	946	0.1426	0.005	2	1.19
6	0.05 M LiCl in DMSO	0.044	1010	0.1252	0.002	0.4	0.73
7	1 M LiCl in DMSO	0.044	1136.2	0.6711	0.005	0.4	0.42

Just like in the case of Kavadiya et al. (2017), large flow rate values yielded bigger droplets. Different surface morphologies were then deposited and characterized using

SEM. As shown in Fig. 4.7, a thin film was deposited from a 0.1 M LNMO precursor solution in 2-propanol (boiling point of 82.5 °C) at a flow rate of 1 mL h⁻¹ for a duration of 3 h on an aluminium substrate that was heated at 200 °C. The obtained surface morphology was in agreement with the prediction of the design schedule (Table 4.1) since a porous morphology with agglomerates was achieved after electro spraying a high concentration precursor solution at a high flow rate on a substrate that is heated at a high temperature for long spray duration. In their study, Perednis et al. (2005) reported a similar morphology using a 0.1 M yttria-stabilized zirconia precursor solution in a solvent mixture of ethanol and 1-methoxy-2-propanol (boiling point range of 78 - 120 °C) sprayed at a flow rate of 5.6 mL h⁻¹ for a spray duration of 5 h on a substrate that was heated at a temperature of 260 °C.

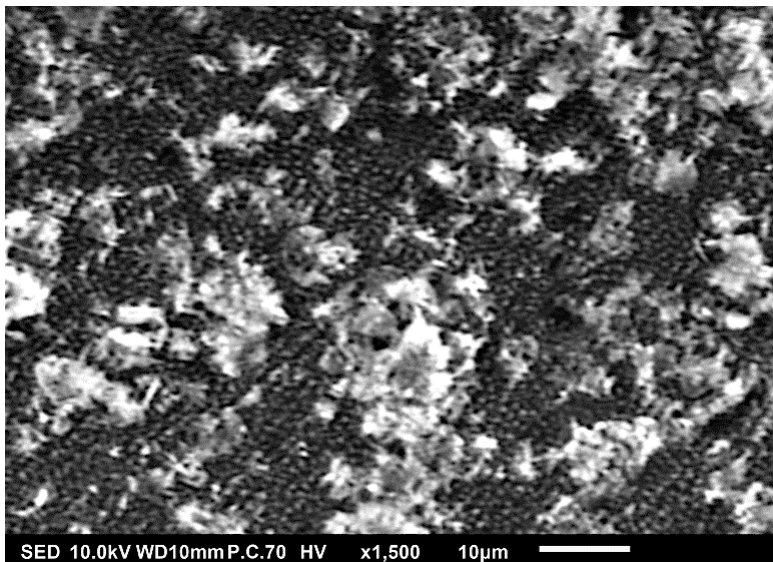


Figure 4.7. SEM image of a thin film generated by electro spraying 0.1 M LNMO precursor in 2-propanol at a flow rate of 1 mL h⁻¹ and a substrate temperature of 200 °C for 3 h.

Also Fig. 4.8 shows a porous thin film with agglomerates that was obtained when a 0.3 M LNMO precursor in 2-propanol (boiling point of 82.5 °C) was electro sprayed at a flow rate of 0.5 mL h⁻¹ for 3 h on an aluminium substrate heated at a temperature of 200 °C. The film's surface morphology was in agreement with the prediction of the design schedule when a high concentration precursor solution is electro sprayed at a low flow rate on a substrate heated at a high temperature for long spray duration. After electro spraying a 0.1 M YSZ precursor solution in a mixed solvent of ethanol and butyl

carbitol (boiling point range of 78 to 231 °C) at a flow rate of 0.5 mL h⁻¹ and a substrate temperature of 400 °C. Neagu et al. (2006) reported similar morphologies at 4 and 12 h. Also, Lafont et al., (2012) reported a similar morphology with 1-propanol (boiling points of 97 °C) after electro spraying 0.1 M LiNi_{0.5}Mn_{1.5}O₄ precursor solution at a flow rate of 1 mL h⁻¹ and a substrate temperature of 350 °C for 2 h.

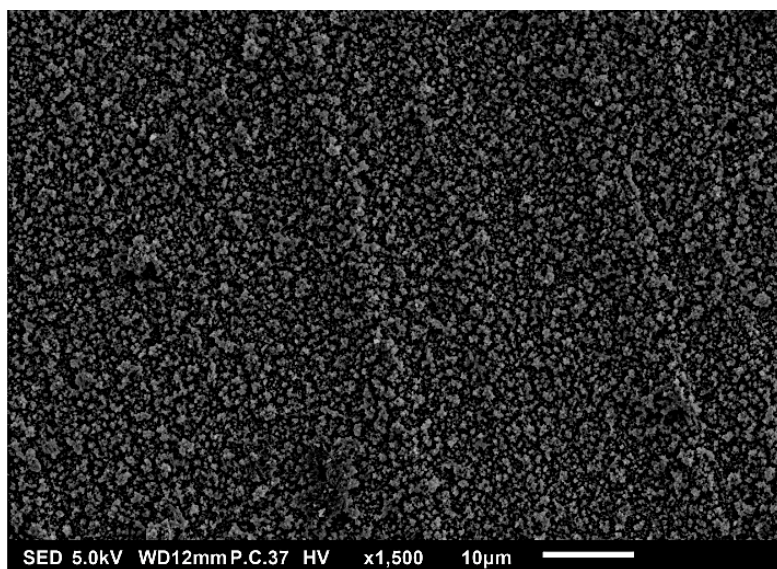


Figure 4.8. SEM image of thin film generated by electro spray of 0.3 M LNMO precursor in 2-propanol at a flow rate of 0.5 mL h⁻¹ and a substrate temperature of 200 °C for 3 h.

As shown in Fig. 4.9, another porous film with agglomerates was obtained when a 1 M LiCl precursor solution in DMSO (boiling point of 189 °C) was electro sprayed at a flow rate of 0.4 mL h⁻¹ for 7 h on a substrate that was heated at 200 °C. The surface morphology was in agreement with the prediction of the design schedule after electro spraying a high concentration precursor solution at a low flow rate on a substrate that is heated at a low temperature for a long duration. Using 0.1 M Bi₂WO₆ precursor in propylene glycol (boiling point of 188.2 °C), Joshi et al. (2015) deposited a thin film with a similar morphology at a flow rate of 0.04 mL h⁻¹ for 80 min on a heated substrate at a temperature of 120 °C. They also observed that film porosity increased with deposition time.

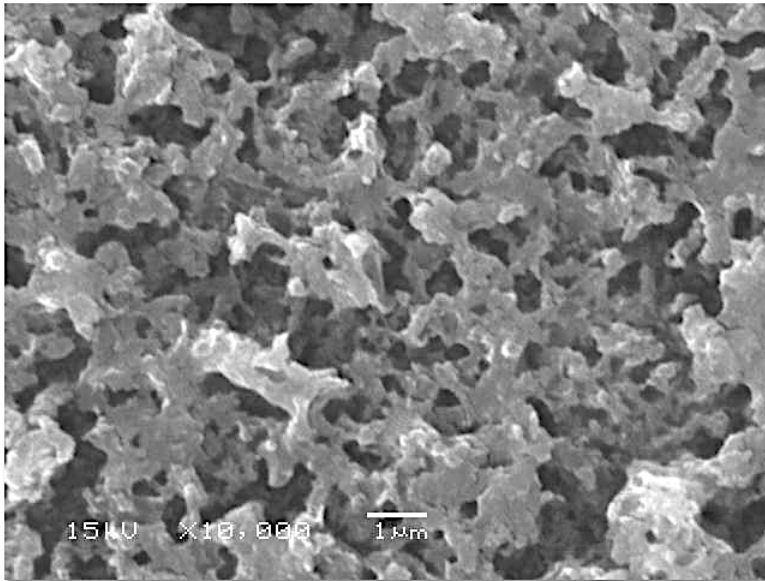


Figure 4.9. SEM image of thin film generated by electro spray of 1 M LiCl precursor in DMSO (boiling point of 189 °C) at a flow rate of 0.4 mL h⁻¹ and a substrate temperature of 200 °C for 7 h.

For the formation of the porous morphology with agglomerates, the generated droplets arrive on the substrate when completely dry forming a particulate layer. Subsequent droplets then experience resistance during charge transfer to the substrate. Consequently, preferential landing occurs in regions where the droplets manage to discharge. The droplets adhere on those positions and they dry up to form agglomerates.

In Fig. 4.10 a thin film with a porous reticular (mesh-like pattern) was obtained when a 1 M LNMO precursor solution in 2-propanol (boiling point of 82.5 °C) was sprayed at a flow rate of 2 mL h⁻¹ for 3 h on a substrate heated at 100 °C. The film's surface morphology was in agreement with the prediction of the design schedule after electro spraying a high concentration precursor solution at a high flow rate on a substrate that is heated at a low temperature for long spray duration. A similar morphology was reported by Ma et al. (2014) who electro sprayed 0.1 M MnO precursor in 1,2-dihydroxypropane (boiling point of 188.2 °C) at a substrate temperature of 240 °C and a flow rate of 1.5 mL h⁻¹ for 3 h.

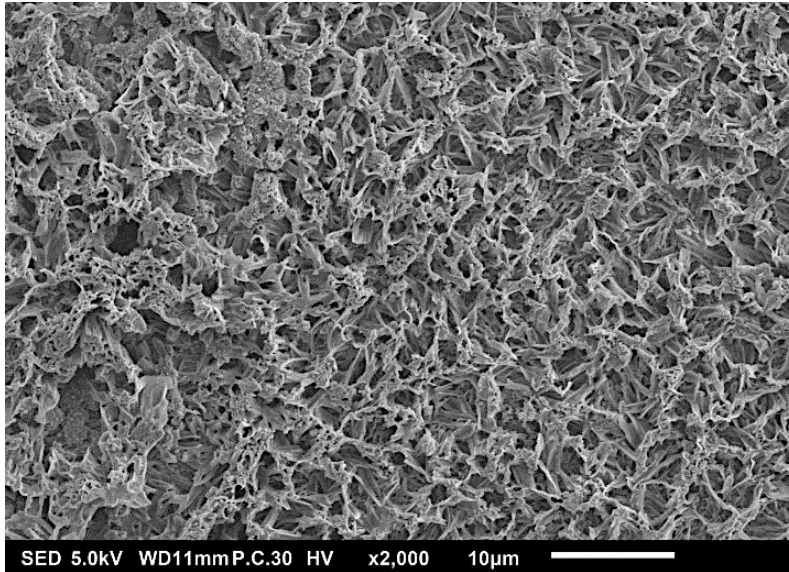


Figure 4.10. SEM image of a thin film generated by electro spraying 1 M LNMO precursor in 2-propanol at a flow rate of 2 mL h⁻¹ and a substrate temperature of 100 °C for 3 h.

Also Fig. 4.11 and Fig. 4.12 show thin films obtained when 0.04 M LNMO precursor solutions in 2-propanol (boiling point of 82.5 °C) was electro sprayed at a flow rate of 2 mL h⁻¹ for 2 h on an aluminium foil substrate heated to a temperature of 350 °C and 100 °C respectively. The films' surface morphologies were in agreement with the predictions of the design schedule after electro spraying a low concentration precursor solution at a high flow rate for long spray duration on a substrate that is heated at a high temperature (Fig. 4.11) or a low temperature (Fig. 4.12). Yuan et al. (2017b) reported a porous reticular film using 0.01 M CoMn₂O₄ precursor in 1,2-propanediol (boiling point of 188.2 °C) electro sprayed at a substrate temperature of 200 °C and a flow rate of 2 mL h⁻¹ for 3 h. Also, Wang et al. (2011) electro sprayed a 0.03 M V₂O₅ precursor in a solvent mixture of water, ethanol and 1,2 propylene glycol (boiling point range of 100 to 188.2 °C) at a flow rate of 72 mL h⁻¹ and a substrate temperature of 260 °C. For deposition times ranging from 4 to 12 h, the porosity of the film was observed to increase with deposition time.

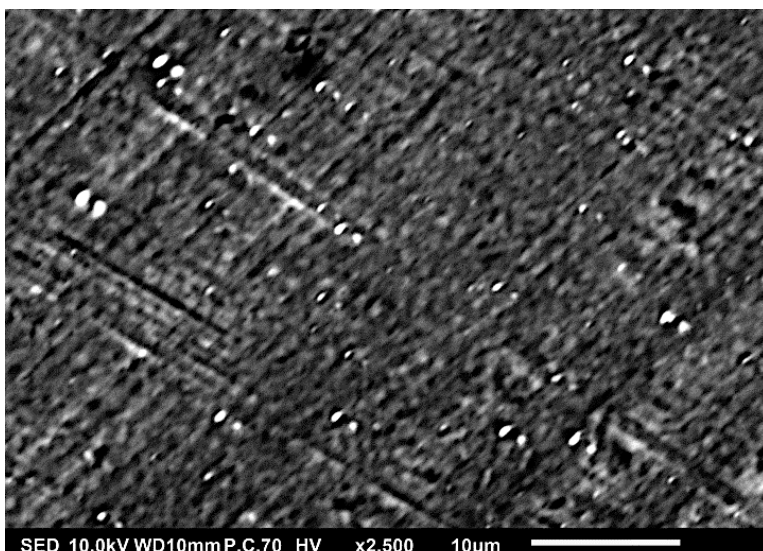


Figure 4.11. SEM image of a thin film generated by electrospray using 0.04 M LNMO precursor in 2-propanol at a flow rate of 2 mL h^{-1} and a substrate temperature of $350 \text{ }^{\circ}\text{C}$ for 2 h.

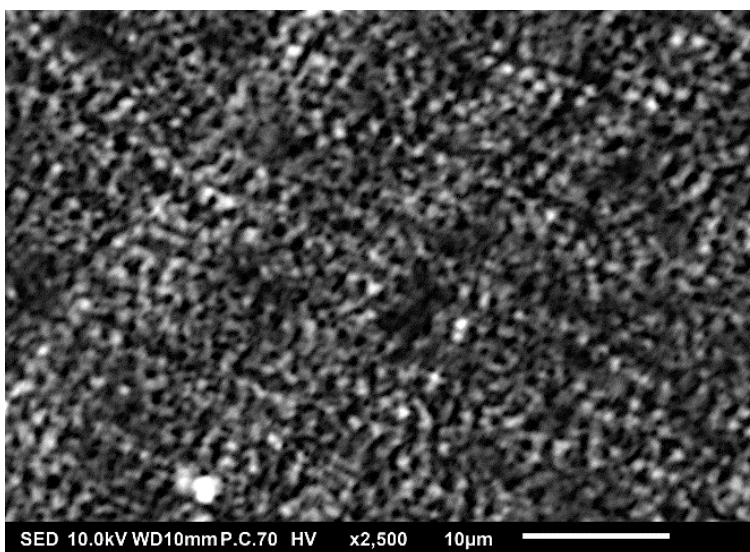


Figure 4.12. SEM image of a thin film generated by electrospray using 0.04 M LNMO precursor in 2-propanol at a flow rate of 2 mL h^{-1} and a substrate temperature of $100 \text{ }^{\circ}\text{C}$ for 2 h..

In the formation of the porous reticular morphology, the droplets spread gradually on the substrate surface. The temperature at the droplet edge is usually higher than at its centre. Therefore, the solvent at the droplet edge evaporates faster than at its centre. This process leads to ring-shaped nucleation and precipitation that forms a reticular morphology on the substrate. Comparing Figs. 4.11 and 4.12, it is clear that the film

becomes more compact with an increase in substrate temperature. This was also reported by Wang et al., (2009) who prepared porous reticular Fe_2O_3 films using a 0.005 M precursor in a mixed solvent of 1, 2-propylene glycol and ethanol (boiling points of 188.2 °C and 78 °C respectively) at a flow rate of 2.4 mL h⁻¹. At substrate temperatures ranging from 170 to 230 °C, they observed a decrease in pore size with increasing substrate temperature.

Dense surface morphologies were also observed. In Fig. 4.13, a thin dense particulate film was obtained when a 0.5 M LNMO precursor solution in a solvent mixture of 2-propanol and ethylene glycol (boiling point range of 82.5 – 197.3 °C) was electrospayed at a flow rate of 2 mL h⁻¹ for 1 h on an aluminium substrate at 200 °C. The film's surface morphology was in agreement with the prediction of the design schedule after electrospaying a high concentration precursor solution at a high flow rate on a substrate that is heated to a low temperature for a short duration. Joshi et al. (2012) obtained a similar morphology using 0.3 M ZnO precursor solutions in propylene glycol (boiling point of 188.2 °C) at a flow rate of 75 $\mu\text{L h}^{-1}$ and a substrate temperature of 200 °C for 30 min. In such cases, the generated droplets experienced a lower rate of solvent evaporation allowing them to spread on the substrate and establish close contact among themselves to form a dense layer.

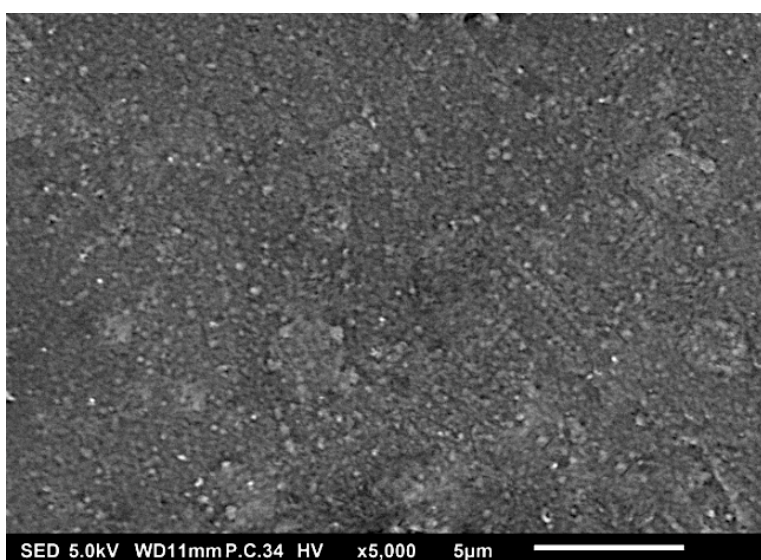


Figure 4.13. SEM image of thin film generated by electrospay of 0.5 M LNMO precursor in 2-propanol and ethylene glycol at a flow rate of 2 mL h⁻¹ and a substrate temperature of 200 °C for 1 h.

Also in Fig. 4.14 another dense thin film was obtained when a 0.05 M LiCl precursor solution in DMSO (boiling point of 189 °C) was electrosprayed at a flow rate of 0.4 mL h⁻¹ for 1 h on an aluminium foil substrate heated to a temperature of 200 °C. The film's surface morphology was in agreement with the prediction of the design schedule since it showed a dense particulate film obtained when a low concentration precursor solution is electrosprayed at a low flow rate on a substrate at a low temperature for a short time. Ma and Qin (2005) electrosprayed 0.02 M LiFePO₄ precursor solution in a mixed solvent of ethanol, glycol and butyl carbitol (boiling point range of 78 to 231 °C) at a substrate temperature of 120 °C. At a flow rate of 0.05 mL h⁻¹ the generated particles were smaller (< 100 nm) and they dried to form a uniform dense film. In another study, Joshi et al. (2013) reported a dense film from a 0.05 M SnCl₄.5H₂O precursor in propylene glycol (boiling point of 188.2 °C) at a flow rate of 0.04 mL h⁻¹ and a substrate temperature of 70 °C for 1 h. Similar observations were made by Kavadiya et al. (2017) who electrosprayed methylammonium lead iodide perovskite precursor (14 mg mL⁻¹) in isopropyl alcohol (boiling point of 82.5 °C) at different flow rates ranging from 0.03 to 0.15 mL h⁻¹ at room temperature. It was evident that the resulting droplet diameters increased with flow rate and they ranged from 505.88 to 860.41 nm respectively. The droplet evaporation times also increased with droplet sizes and they ranged from 17.84 to 51.73 μs respectively. Upon drying, the resulting particle sizes ranged from 75.36 to 113.43 nm respectively. It was reported that smaller particles were achieved at lower flow rates and they led to the production of smooth uniform films. It is therefore evident that small droplets dry up into even smaller particles leading to formation of a dense layer. This is further supported by the works of Hong et al. (2017) who electrosprayed 30 % wt methylammonium lead iodide perovskite liquid precursor in DMSO (boiling point of 189 °C) at a flow rate of 0.05 mL h⁻¹ and a substrate temperature of 65 °C for 2 min.

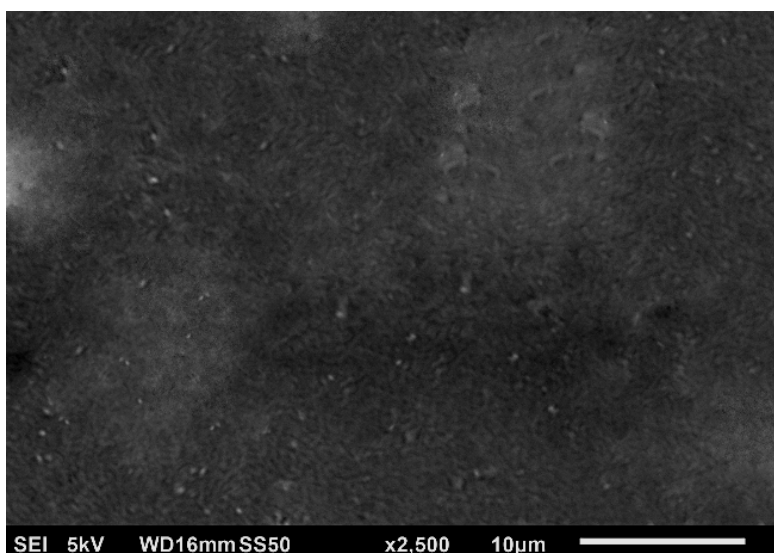


Figure 4.14. SEM image of thin film generated by electro spray of 0.05 M LiCl precursor in DMSO at a flow rate of 0.4 mL h^{-1} and a substrate temperature of $200 \text{ }^\circ\text{C}$ for 1 h.

Therefore, different porous and dense surface morphologies can be achieved using electro spray technique for different applications. In the context of electrode materials for solid-state lithium ion batteries, several studies have shown that a porous morphology is preferred for the electrodes when it comes to mitigating mechanical failure, electrical disconnection and capacity. These negative effects are usually caused by volume change of electrode materials during discharge and charge cycles. Though a comparison on the performance of the different porous morphologies has not yet been done, a lot of studies have emphasized on the effectiveness of a reticular porous morphology. In addition, this morphology has been highlighted for promoting lithium ion intercalation and increasing the overall surface area of contact at the interface with the electrolyte leading to superior electrochemical performance of the battery (Liu et al., 2019; Luo et al., 2017; Chen, et al., 2016b; Zhu et al., 2015a). On the contrary, a compact layer has been recommended for the electrolyte to enhance lithium ion conductivity and inhibit short circuiting. Usually, short circuiting occurs due to the formation of lithium dendrites on the anode over long time cycling. These dendrites are like protruding needles which cause the electrodes to come into direct contact inducing short circuit which leads to battery failure. Therefore, developing a very compact electrolyte layer is a critical approach in reducing space for lithium dendrite penetration (Jiang et al., 2018b; Liu et al., 2017; Tian et al., 2017; Zhang et al., 2014).

Fig. 4.15 shows a cross section SEM image of two layers deposited sequentially using 0.5 M LNMO precursor in 2-propanol and ethylene glycol (1:1). Bottom dense layer was electrospayed at a flow rate of 2 mL h⁻¹ and a substrate temperature of 200 °C for 1 h. Top porous layer was electrospayed at a flow rate of 0.5 mL h⁻¹ and a substrate temperature of 200 °C for 3 h. The layers were deposited to mimic a dense electrolyte layer and a porous electrode layer in contact with each other for a thin film lithium ion battery. The observed surface morphologies were in agreement with the predictions of the design schedule. A dense layer on the left side was achieved when a high concentration precursor solution was sprayed at a high flow rate on a substrate at a low temperature for a short time. On the right side, a porous layer was deposited using a high concentration precursor solution sprayed at a low flow rate and low temperature for a long time.

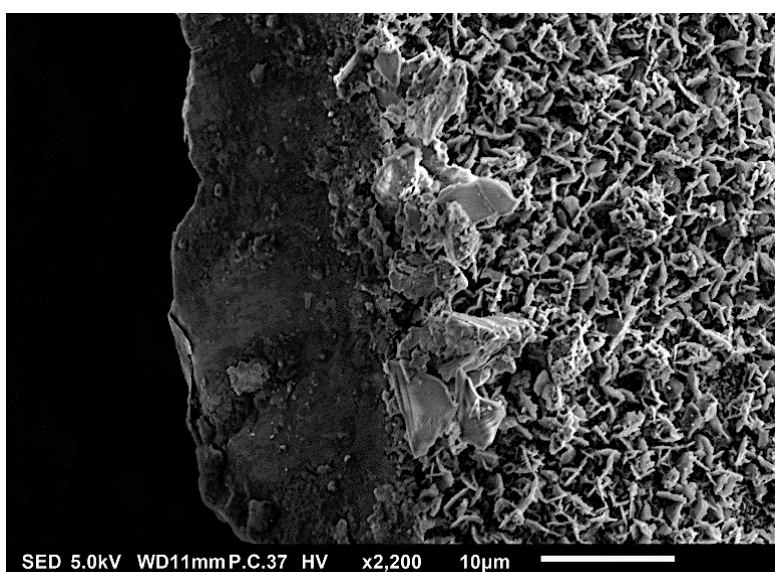


Figure 4.15. Cross section SEM image of two layers deposited sequentially using 0.5 M LNMO precursor in 2-propanol and ethylene glycol (1:1). Bottom dense layer was electrospayed at a flow rate of 2 mL h⁻¹ and a substrate temperature of 200 °C for 1 h. Top layer was electrospayed at a flow rate of 0.5 mL h⁻¹ and a substrate temperature of 200 °C for 3 h.

Ultimately, electrostatic spray deposition technique is promising in the layer-by-layer deposition of thin film lithium ion batteries without incorporating binders. This is critical in reducing the mass of inactive compounds in the battery.

CHAPTER FIVE

CONCLUSIONS AND RECOMMENDATIONS

5.1 Conclusions

Electrospray is a technique where an electrical force causes a liquid jet to fragment into droplets. It is outstanding because of the achieved high deposition efficiency and ability to produce thin films of different surface morphologies. The technique can be applied in the deposition of thin films for nano and micro electronics where performance of the deposited layers is determined by their morphologies.

In this study, a literature survey was conducted and key electrospray parameters were identified. A systematic design schedule for electrosprayed thin films with different surface morphologies was then developed. The schedule provided a systematic way of designing thin films with different surface morphologies and in contrast to the commonly used trial-and-error method, the schedule saved on time and reagents.

Considering that literature does not give general applicable formulas for minimum and maximum flow rates, the cone-jet windows for three commonly used solvents (2-propanol, ethylene glycol and NMP) were experimentally determined.

Following the design of thin films for li-ion batteries, electrospray experiments were performed and thin films with varying morphologies were deposited by controlling precursor concentration, precursor flow rate, substrate temperature and deposition time. Characterization of the surface morphologies was performed using scanning electron microscopy. The obtained results showed that surface morphologies of the deposited thin films agreed with the predictions of the developed design schedule. A good interfacial contact was also achieved between two layers deposited on each other without incorporating binders.

For the bulk solid-state li-ion cells, $\text{Li}_6\text{PS}_5\text{Cl}$ argyrodite electrolyte material was synthesized via solid-state sintering method and its cubic argyrodite crystalline structure confirmed using x-ray diffraction technique. Two bulk solid-state lithium ion cells were fabricated by pressing three-layer pellets comprising of the cathode mixture,

the electrolyte and the anode. Upon cycling, the bulk cells were found to be electrochemically unstable leading to low discharge capacities. This was attributed to inhomogeneity in the cathode mixture and poor interfacial contacts in the bulk cell.

5.2 Recommendations

1. The developed schedule should be adopted in the design of thin films for nano/micro electronics where performance of the deposited layers is determined by their surface morphologies.
2. Refinement of the cone-jet stability window should be done to provide accurate mathematical models.
3. Electro spray technique is recommended in the deposition of thin films with different surface morphologies and good interfacial contacts.
4. A solution-based method should be adopted for the preparation of the composite cathode to improve on homogeneity.
5. Weight ratios in the composite cathode should be optimized for enhanced electrochemical performance.

REFERENCES

- Abbas, T. A., Slewa, L. H., Khizir, H. A. and Kakil, S. A. (2017). Synthesis of cobalt oxide (Co_3O_4) thin films by electrostatic spray pyrolysis technique (ESP). *Journal of Materials Science: Materials in Electronics* 28, 1951 - 1957. DOI: 10.1007/s10854-016-5748-y.
- Abdussami, M. R. and Gabbar, H. A. (2019). Flywheel-based Micro Energy Grid for Reliable Emergency Back-up Power for Nuclear Power Plant. 2019 International Conference on Smart Energy Systems and Technologies (SEST), 1 – 6. <https://doi.org/10.1109/SEST.2019.8849063>.
- Abegunde, O. O., Akinlabi, E. T., Oladijo, O. P., Akinlabi, S. and Ude, A. U. (2019). Overview of thin film deposition techniques. *AIMS Materials Science* 6, 2, 174 - 199. DOI: 10.3934/matricsci.2019.2.174.
- Acar, C. (2018). A comprehensive evaluation of energy storage options for better sustainability. *Int J Energy Res.* 42, 3732 – 3746. DOI: 10.1002/er.4102.
- Acha, M. R., Soifer, E. and Hasin, T. (2020) Cardiac Implantable Electronic Miniaturized and Micro Devices. *Micromachines* 11, 10, 902. DOI: 10.3390/mi11100902.
- Agostinho, L. L. F., Bos, B., Kamau, A., Brouwer, S. P., Fuchs, E. C., and Marijnissen, J. C. M. (2018). Simple-jet mode electrosprays with water. Description, characterization and application in a single effect evaporation chamber. *Journal of Aerosol Science*, 125, 237 – 250. DOI: 10.1016/j.jaerosci.2018.04.010.
- Agostinho, L. L. F., Yurteri, C. U., Wartena, J., Brouwer, S. P., Fuchs, E. C. and Marijnissen, J. C. M. (2013). Insulated multinozzle system for electrohydrodynamic atomization in the simple-jet mode. *Appl. Phys. Lett.* 102, 194103. DOI: 10.1063/1.4806977.
- Ahsan, Z., Ding, B., Cai, Z., Wen, C., Yang, W., Ma, Y., Zhang, S., Song, G. and Javed, M. S. (2021). Recent progress in capacity enhancement of LiFePO_4 cathode for Li-ion

batteries. *Journal of Electrochemical Energy Conversion and Storage* 18, 1, 010801. DOI: 10.1115/1.4047222.

Akhilash, M., Salini, P. S., John, B. and Mercy, T. D. (2021). A journey through layered cathode materials for lithium ion cells – From lithium cobalt oxide to lithium-rich transition metal oxides. *Journal of Alloys and Compounds* 869, 159239. DOI: 10.1016/j.jallcom.2021.159239.

Akhtar, K., Khan, S. A., Khan, S. B. and Asiri, A. M. (2018). Scanning electron microscopy: Principle and applications in nanomaterials characterization. *Handbook of materials characterization* 113 - 145. DOI: 10.1007/978-3-319-92955-2_4.

Aktaş, A., and Kirçiçek, Y. (2021). Chapter 5 - Solar Hybrid Systems and Energy Storage Systems. In: Aktaş, A., Kirçiçek, Y. (eds), *Solar Hybrid Systems Development and Application*, pp 87 – 125. Academic Press, ISBN 9780323884990. DOI: 10.1016/B978-0-323-88499-0.00005-7.

Ali, A., Chiang, Y. W. and Santos, R. M. (2022). X-ray diffraction techniques for mineral characterization: A review for engineers of the fundamentals, applications, and research directions. *Minerals* 12, 2, 205. DOI: 10.3390/min12020205.

Alotto, P., Guarnieri, M. and Moro, F. (2014). Redox flow batteries for the storage of renewable energy: A review. *Renewable and Sustainable Energy Reviews* 29, 325 - 335. DOI: 10.1016/j.rser.2013.08.001.

Al-Shaqsi, A. Z. A., Sopian, K. and Al-Hinai, A. (2020). Review of energy storage services, applications, limitations, and benefits. *Energy Reports*, 6, 288 - 306. DOI: 10.1016/j.egy.2020.07.028.

Alsherari, S. A., Janene, F., Moulahi, A., Shili, H., Alnhas, I. and Mjejri, I. (2023). Vanadium oxide nanocomposite as electrode materials for lithium-ion batteries with high

specific discharge capacity and long cycling life. *Ionics* 29, 1, 61 - 70. DOI: 10.1007/s11581-022-04811-0.

Ameh, E. S. (2019). A review of basic crystallography and x-ray diffraction applications. *The international journal of advanced manufacturing technology* 105, 3289 - 3302. DOI: 10.1007/s00170-019-04508-1.

Amin, R., Muralidharan, N., Petla, R. K., Yahia, H. B., Al-Hail, S. A. J., Essehli, R., Daniel, C., Khaleel, M. A. and Belharouak, I. (2020). Research advances on cobalt-free cathodes for Li-ion batteries-The high voltage $\text{LiMn}_{1.5}\text{Ni}_{0.5}\text{O}_4$ as an example. *Journal of Power Sources* 467, 228318. DOI: 10.1016/j.jpowsour.2020.228318.

Andersen, H. L., Djuandhi, L., Mittal, U. and Sharma, N. (2021). Strategies for the analysis of graphite electrode function. *Advanced Energy Materials*, 11, 48, 2102693. DOI: 10.1002/aenm.202102693.

Aneke, M. and Wang, M. (2016). Energy storage technologies and real life applications - A state of the art review. *Applied Energy*, 179, 350 - 377. DOI: 10.1016/j.apenergy.2016.06.097.

Arroyo M. F. R. and Miguel L. J. (2019). The Trends of the Energy Intensity and CO_2 Emissions Related to Final Energy Consumption in Ecuador: Scenarios of National and Worldwide Strategies. *Sustainability* 12, 1, 20. DOI: 10.3390/su12010020.

Arya, A. and Sharma, A. L. (2020). A glimpse on all-solid-state Li-ion battery (ASSLIB) performance based on novel solid polymer electrolytes: a topical review. *J Mater Sci* 55, 6242 – 6304. DOI: 10.1007/s10853-020-04434-8.

Asenbauer, J., Eisenmann, T., Kuenzel, M., Kazzazi, A., Chen, Z. and Bresser, D. (2020). The success story of graphite as a lithium-ion anode material—fundamentals, remaining challenges, and recent developments including silicon (oxide) composites. *Sustainable Energy & Fuels* 4, 11, 5387 - 5416. DOI: 10.1039/D0SE00175A.

Ates, T., Keller, M., Kulisch, J., Adermann, T. and Passerini, S. (2019). Development of an all-solid-state lithium battery by slurry-coating procedures using a sulfidic electrolyte. *Energy Storage Materials*, 17, 204 - 210. DOI: 10.1016/j.ensm.2018.11.011.

Auvergniot, J., Cassel, A., Foix, D., Viallet, V., Sez nec, V. and Dedryvère, R. (2017). Redox activity of argyrodite $\text{Li}_6\text{PS}_5\text{Cl}$ electrolyte in all-solid-state Li-ion battery: An XPS study. *Solid State Ionics*, 300, 78 - 85. DOI: 10.1016/j.ssi.2016.11.029.

Ayoub, E. and Karami, N. (2015). Review on the charging techniques of a Li-Ion battery, Third International Conference on Technological Advances in Electrical, Electronics and Computer Engineering (TAECE), 50 - 55, DOI: 10.1109/TAECE.2015.7113599.

Bachman, J. C, Muy, S. Grimaud, A. Chang, H. H., Pour, N., Lux, S. F., Paschos, O., Maglia, F., Lupart, S., Lamp, P., Giordano, L. and Shao-Horn, Y. (2016). Inorganic Solid-State Electrolytes for Lithium Batteries: Mechanisms and Properties Governing Ion Conduction. *Chem Rev.* 116, 1, 140 - 62. DOI: 10.1021/acs.chemrev.5b00563.

Badwal, S. P. S., Giddey, S. S., Munnings, C., Bhatt, A. I. and Hollenkamp, A. F. (2014). Emerging electrochemical energy conversion and storage technologies. *Frontiers in Chemistry*, 2, 79. DOI: 10.3389/fchem.2014.00079.

Bagher, A. M., Vahid, M. M. A. and Mohsen, M. (2015). Types of solar cells and application. *American Journal of optics and Photonics* 3, 5, 94 - 113. DOI: 10.11648/j.ajop.20150305.17.

Bailly, N., Georges, S. and Djurado, E. (2012). Elaboration and electrical characterization of electrosprayed YSZ thin films for intermediate temperature-solid oxide fuel cells (IT-SOFC). *Solid State Ionics* 222 – 223, 17. DOI: 10.1016/j.ssi.2012.06.020.

Baktash, A., Reid, J. C., Yuan, Q., Roman, T. and Searles, D. J. (2020). Shaping the future of solid-state electrolytes through computational modeling. *Advanced Materials* 32, 18, 1908041. DOI: 0.1002/adma.201908041.

- Banguero, E., Correcher, A., Pérez-Navarro, A., Morant, F. and Aristizabal, A. (2018). A Review on Battery Charging and Discharging Control Strategies: Application to Renewable Energy Systems. *Energies*, 11, 1021. DOI: 10.3390/en11041021.
- Baniya, A., Pathak, R., Norris, B., Li, H., Rozyyev, V., Elam, J. W. and Qiao, Q. (2023). Next-generation battery technology based on solid-state electrolytes. In: *Green Sustainable Process for Chemical and Environmental Engineering and Science*, pp. 1 - 46. Elsevier. DOI: 10.1016/B978-0-323-90635-7.00006-3.
- Baptista, A., Silva, F., Porteiro, J., Míguez, J. and Pinto, G. (2018). Sputtering physical vapour deposition (PVD) coatings: A critical review on process improvement and market trend demands. *Coatings* 8, 11, 402. DOI: 10.3390/coatings8110402.
- Bauomy, M. F., Gamal, H. and Shaltout, A. A. (2021). Chapter 2 - Solar PV DC nanogrid dynamic modeling applying the polynomial computational method for MPPT. In: Azad, A. K. (eds), *Advances in Clean Energy Technologies*, pp 19 - 87. Academic Press. ISBN 9780128212219. DOI: 10.1016/B978-0-12-821221-9.00002-5.
- Behera, A., Mallick, P. and Mohapatra, S. S. (2020). Chapter 13 - Nanocoatings for anticorrosion: An introduction, In: Rajendran, S., Nguyen, T. A., Kakooei, S., Yeganeh, M., Li, Y. (eds), *Micro and Nano Technologies, Corrosion Protection at the Nanoscale*, pp. 227 – 243. Elsevier. DOI: 10.1016/B978-0-12-819359-4.00013-1.
- Bezza, I., Luais, E., Ghamouss, F., Zaghrioui, M., Tran-Van, F. and Sakai, J. (2019). LiCoO₂ with double porous structure obtained by electrospray deposition and its evaluation as an electrode for lithium-ion batteries. *Journal of Alloys and Compounds*, 805, 19 - 25. DOI: 10.1016/j.jallcom.2019.07.062.
- Bianchini, M., Roca-Ayats, M., Hartmann, P., Brezesinski, T. and Janek, J. (2019). There and back again - the journey of LiNiO₂ as a cathode active material. *Angewandte Chemie International Edition* 58, 31, 10434 - 10458. DOI: 10.1002/anie.201812472.

- Bielefeld, A., Weber, D. A. and Janek, J. (2019). Microstructural modeling of composite cathodes for all-solid-state batteries. *The Journal of Physical Chemistry C* 123, 3, 1626 - 1634. DOI: 10.1021/acs.jpcc.8b11043.
- Bodnár, E., Grifoll, J. and Rosell-Llompart, J. (2018). Polymer solution electrospraying: A tool for engineering particles and films with controlled morphology. *Journal of Aerosol Science* 125, 93 – 118. DOI: 10.1016/j.jaerosci.2018.04.012.
- Bu, I. Y. Y., Ke, H. W., Fu, Y. S. and Guo, T. F. (2021). Highly stable perovskite; Light CsPbBr₃/silica composite prepared via novel electrospray injection process. *Optik* 238, 166690. DOI: 10.1016/j.ijleo.2021.166690.
- Buchberger, I., Seidlmayer, S., Pokharel, A., Piana, M., Hattendorff, J., Kudejova, P., Gilles, R. and Gasteiger, H. A. (2015). Aging analysis of graphite/LiNi_{1/3}Mn_{1/3}Co_{1/3}O₂ cells using XRD, PGAA, and AC impedance. *Journal of The Electrochemical Society* 162, 14, A2737. DOI: 10.1149/2.0721514jes.
- Butt, M. A. (2022). Thin-film coating methods: a successful marriage of high-quality and cost-effectiveness-a brief exploration. *Coatings* 12, 8, 1115. DOI: 10.3390/coatings12081115.
- Calpa, M., Rosero-Navarro, N. C., Miura, A. and Tadanaga, K. (2019). Electrochemical performance of bulk-type all-solid-state batteries using small-sized Li₇P₃S₁₁ solid electrolyte prepared by liquid phase as the ionic conductor in the composite cathode. *Electrochimica acta* 296, 473 - 480. DOI: 10.1016/j.electacta.2018.11.035.
- Cao, K., Jin, T., Yang, L. and Jiao, L. (2017). Recent progress in conversion reaction metal oxide anodes for Li-ion batteries. *Materials Chemistry Frontiers* 1, 11, 2213 - 2242. DOI: 10.1039/C7QM00175D.

- Cao, F. and Prakash, J. (2002). A comparative electrochemical study of LiMn_2O_4 spinel thin-film and porous laminate. *Electrochimica Acta* 47, 1607 – 1613. DOI: 10.1016/S0013-4686(01)00884-2.
- Cardott, B. J. and Curtis, M. E. (2018). Identification and nanoporosity of macerals in coal by scanning electron microscopy. *International Journal of Coal Geology* 190, 205 - 217. DOI: 10.1016/j.coal.2017.07.003.
- Cen, Y., Fan, Y., Qin, Q., Sisson, R. D., Apelian, D. and Liang, J. (2019). Synthesis of Si anode with a microsized-branched structure from recovered Al scrap for use in Li-Ion batteries. *Journal of Power Sources*, 410 – 411, 31 – 37. DOI: 10.1016/j.jpowsour.2018.10.097.
- Chandra, S., Kim, Y., Vivona, D., Waluyo, I., Hunt, A., Schlueter, C., Lee, J. B., Horn, Y. S. and Yildiz, B. (2022). Thermally-driven reactivity of $\text{Li}_{0.35}\text{La}_{0.55}\text{TiO}_3$ solid electrolyte with LiCoO_2 cathode. *Journal of Materials Chemistry A* 10, 7, 3485 - 3494. DOI: 10.1039/D1TA08853J.
- Chandrasekhar, P. S., Kumar, N., Swami, S. K., Dutta, V. and Komarala, V. K. (2016). Fabrication of perovskite films using an electrostatic assisted spray technique: the effect of the electric field on morphology, crystallinity and solar cell performance. *Nanoscale*, 8(12), 6792–6800. DOI: 10.1039/C5NR08350H.
- Chandran, C. V. and Heitjans, P. (2016). Chapter One - Solid-State NMR Studies of Lithium Ion Dynamics Across Materials Classes. In: Webb, G. A. (eds), *Annual Reports on NMR Spectroscopy*, pp. 1 - 102. Academic Press, Volume 89. ISSN 0066-4103, ISBN 9780128047125. DOI: 10.1016/bs.arnmr.2016.03.001.
- Chang, H., Wu, Y. R., Han, X. and Yi, T. F. (2022). Recent developments in advanced anode materials for lithium-ion batteries. *Energy Materials* 1, 1, 100003. DOI: 10.20517/energymater.2021.02.

Chang, C. K. and Sulley, M. (2018). Lithium-ion stationary battery capacity sizing formula for the establishment of industrial design standard. *Journal of Electrical Engineering & Technology* 13, 6, 2561 – 2567.

Chavhan, M. P., Sethi, S. R. and Ganguly, S. (2020). Mixed metal oxides in synergy at nanoscale: Electrospray induced porosity of in situ grown film electrode for use in electrochemical capacitor. *Electrochimica Acta* 347, 136277. DOI: 10.1016/j.electacta.2020.136277.

Chavhan, M. P., and Ganguly, S. (2019). N-doped porous carbon film electrodes for electrochemical capacitor, made by electrospray of sol precursors. *Carbon* 154, 33 - 41. DOI: 10.1016/j.carbon.2019.07.091.

Chen, S. P., Lv, D., Chen, J., Zhang, Y. H. and Shi, F.N. (2022a). Review on Defects and Modification Methods of LiFePO₄ Cathode Material for Lithium-Ion Batteries. *Energy & Fuels* 36, 3, 1232 – 1251.

Chen, X., Guan, Z., Chu, F., Xue, Z., Wu, F. and Yu, Y. (2022b). Air-stable inorganic solid-state electrolytes for high energy density lithium batteries: Challenges, strategies, and prospects. *InfoMat* 4, 1, e12248. DOI: 10.1002/inf2.12248.

Chen, J., Wu, J., Wang, X. and Yang, Z. (2021a). Research progress and application prospect of solid-state electrolytes in commercial lithium-ion power batteries. *Energy Storage Materials* 35, 70 - 87. DOI: 10.1016/j.ensm.2020.11.017.

Chen, H., Wu, Z., Su, Z., Chen, S., Yan, C., Al-Mamun, M., Tang, Y. and Zhang, S. (2021b). A mechanically robust self-healing binder for silicon anode in lithium ion batteries. *Nano Energy*, 81, 105654. DOI: 10.1016/j.nanoen.2020.105654.

Chen, C., Eichel, R.-A., and Notten, P. H. L. (2017). Metal-organic chemical vapor deposition enabling all-solid-state Li-ion microbatteries: A short review. *Journal of Electroceramics*, 38, 2 – 4, 230 – 247. DOI: 10.1007/s10832-017-0090-1.

- Chen, C. Perdomo, P. J., Fernandez, M., Barbeito, A. and Wang, C. (2016b). Porous NiO/graphene composite thin films as high performance anodes for lithium-ion batteries. *Journal of Energy Storage* 8, 198 – 204.
- Chen, J., Li, C. and Shi, G. (2013). Graphene Materials for Electrochemical Capacitors. *The Journal of Physical Chemistry Letters* 4, 8, 1244 – 1253. DOI: 10.1021/jz400160k.
- Chen, D. R. and Pui D. Y. H. (1997), Experimental Investigation of Scaling Laws for Electrospraying: Dielectric Constant Effect, *Aerosol Science and Technology* 27, 3, 367 – 380. DOI: 10.1080/02786829708965479.
- Chen, C. H., Buysman, A. A. J., Kelder, E. M. and Schoonman, J. (1995). Fabrication of LiCoO₂ thin film cathodes for rechargeable lithium battery by electrostatic spray pyrolysis. *Solid State Ionics*, 80, 1 – 4. DOI: 10.1016/0167-2738(95)00140-2.
- Cheng, Y. W., Chen, C. H., Wang, S. A., Li, Y. C., Peng, B. L., Huang, J. H. and Liu, C. P. (2022). Propelling performance of silicon thin film lithium ion battery by appropriate dopants. *Nano Energy* 102, 107688. DOI: 10.1016/j.nanoen.2022.107688.
- Cheng, H., Shapter, J. G., Li, Y. and Gao, G. (2021a). Recent progress of advanced anode materials of lithium-ion batteries. *Journal of Energy Chemistry* 57, 451 – 468. DOI: 10.1016/j.jechem.2020.08.056.
- Cheng, T., Ma, Z., Qian, R., Wang, Y., Cheng, Q., Lyu, Y., Nie, A. and Guo, B. (2021b). Achieving stable cycling of LiCoO₂ at 4.6 V by multilayer surface modification. *Advanced Functional Materials* 31, 2, 2001974. DOI: 10.1002/adfm.202001974.
- Cho, J., Jeong, S. and Kim, Y. (2015). Commercial and research battery technologies for electrical energy storage applications. *Progress in Energy and Combustion Science* 48, 84 – 101. DOI: 10.1016/j.pecs.2015.01.002.

Choi, Y. S. and Lee, J. C. (2019). Electronic and mechanistic origins of the superionic conductivity of sulfide-based solid electrolytes. *Journal of Power Sources*, 415, 189 - 196. DOI: 10.1016/j.jpowsour.2019.01.071.

Choi, H. and Yoon, H. (2015). Nanostructured electrode materials for electrochemical capacitor applications. *Nanomaterials* 5, 2, 906 - 936. DOI: 10.3390/nano5020906.

Ci, H., Chang, H., Wang, R., Wei, T., Wang, Y., Chen, Z., Sun, Y., Dou, Z., Liu, Z., Li, J., Gao, P. and Liu, Z. (2019). Enhancement of heat dissipation in ultraviolet light-emitting diodes by a vertically oriented graphene nanowall buffer layer. *Advanced Materials* 31, 29, 1901624. DOI: 10.1002/adma.201901624.

Ciambelli, P., Guardia, G. L. and Vitale, L. (2020). Chapter 7 - Nanotechnology for green materials and processes. In: Basile, A., Centi, G., De Falco, M., Iaquaniello, G. (eds), *Studies in Surface Science and Catalysis*, pp. 97 – 116. Elsevier, Volume 179. ISSN 0167-2991, ISBN 9780444643377. DOI: 10.1016/B978-0-444-64337-7.00007-0.

Clayton, S. (2020). Climate anxiety: Psychological responses to climate change. *Journal of Anxiety Disorders* 74, 102263. DOI: 10.1016/j.janxdis.2020.102263.

Clement, B., Lyu, M., Sandeep Kulkarni, E., Lin, T., Hu, Y., Lockett, V., Greig, C., and Wang, L. (2022). Recent Advances in Printed Thin-Film Batteries. *Engineering*, 13, 238 – 261. DOI: 10.1016/j.eng.2022.04.002.

Cloupeau, M. and Prunet-Foch, B. (1989). Electrostatic Spraying of Liquids in Cone-Jet Mode. *Journal of Electrostatics* 22, 135 - 159. DOI: 10.1016/0304-3886(89)90081-8.

Cui, L., Cheng, C., Peng, F., Yang, Y., Li, Y., Jia, M. and Jin, X. (2019). A ternary MnO₂ - deposited RGO/lignin-based porous carbon composite electrode for flexible supercapacitor applications. *New Journal of Chemistry* 43, 35, 14084 - 14092. DOI: 10.1039/C9NJ02184A.

Daignault, L. G., Jackman, D. C. and Rillema, D. P. (1990). A simple and inexpensive student viscometer. *Journal of Chemical Education* 67, 1, 81.

Dalavi, S., Xu, M., Ravdel, B., Zhou, L. and Lucht, B. L. (2010). Nonflammable Electrolytes for Lithium-Ion Batteries Containing Dimethyl Methylphosphonate. *Journal of The Electrochemical Society*, 157, 10, A1113 - A1120. DOI: 10.1149/1.3473828.

Dale, S. (2022). BP Statistical Review of World Energy, 71st edition. Retrieved October 21, 2023, from <https://www.bp.com/content/dam/bp/business-sites/en/global/corporate/pdfs/energy-economics/statistical-review/bp-stats-review-2022-full-report.pdf>.

Dao, A. H., López-Aranguren, P., Zhang, J., Cuevas, F., & Latroche, M. (2020). Solid-state Li-ion batteries operating at room temperature using new borohydride argyrodite electrolytes. *Materials*, 13, 18, 4028. DOI: 10.3390/ma13184028.

Darrell, H. Eby, N., Goodge, J. and Mogk, D. (2016). X-ray reflection in accordance with Bragg's Law. Retrieved March 4, 2022, from https://serc.carleton.edu/research_education/geochemsheets/BraggsLaw.html.

de Biasi, L., Schiele, A., Roca-Ayats, M., Garcia, G., Brezesinski, T., Hartmann, P. and Janek, J. (2019). Phase transformation behavior and stability of LiNiO₂ cathode material for Li-ion batteries obtained from in situ gas analysis and operando X-ray diffraction. *ChemSusChem*, 12, 10, 2240 - 2250. DOI: 10.1002/cssc.201900032.

Deng, S., Sun, Q., Li, M., Adair, K., Yu, C., Li, J., Li, W., Fu, J., Li, X., Li, R., Hu, Y., Chen, N., Huang, H., Zhang, L., Zhao, S., Lu, S. and Sun, X. (2021). Insight into cathode surface to boost the performance of solid-state batteries. *Energy Storage Materials* 35, 661 - 668. DOI: 10.1016/j.ensm.2020.12.003.

Deng, D. (2015). Li-ion batteries: basics, progress, and challenges *Energy Science and Engineering* 3, 5, 385 – 418. DOI: 10.1002/ese3.95.

- DeWees, R. and Wang, H. (2019). Synthesis and properties of NaSICON-type LATP and LAGP solid electrolytes. *ChemSusChem*, 12, 16, 3713 - 3725. DOI: 10.1002/cssc.201900725.
- Dhanabalan, A., Yu, Y., Li, X., Bechtold, K., Maier, J. and Wang, C. (2017). Fabrication of tin-carbon composite anode material by electrospinning and electrostatic spray deposition for lithium rechargeable battery. *Conference Proceedings of SPIE 7679*, 76792I - 1.
- Dias, F. B., Plomp, L. and Veldhuis, J. B. (2000). Trends in polymer electrolytes for secondary lithium batteries. *Journal of Power Sources* 88, 169. DOI: 10.1016/S0378-7753(99)00529-7.
- Dickerson, J. H. and Boccaccini, A. R. (2012). *Electrophoretic Deposition of Nanomaterials*. Springer, New York. ISBN: 978-1-4419-9690-9. DOI: 10.1007/978-1-4419-9730-2.
- Ding, Y., Cano, Z. P., Yu, A., Lu, J. and Chen, Z. (2019). Automotive Li-Ion Batteries: Current Status and Future Perspectives. *Electrochemical Energy Reviews* 2, 1 – 28. DOI: 10.1007/s41918-018-0022-z.
- Diouf, B. and Pode, R. (2015). Potential of lithium-ion batteries in renewable energy. *Renewable Energy*, 76, 375 - 380. DOI: 10.1016/j.renene.2014.11.058.
- Dong, B., Haworth, A. R., Yeandel, S. R., Stockham, M. P., James, M. S., Xiu, J., Wang, D., Goddard, P., Johnston, K. E. and Slater, P. R. (2022). Halogenation of $\text{Li}_7\text{La}_3\text{Zr}_2\text{O}_{12}$ solid electrolytes: a combined solid-state NMR, computational and electrochemical study. *Journal of Materials Chemistry A*, 10, 20, 11172 - 11185. DOI: 10.1039/D1TA07309E.
- Du, L., Lin, H., Ma, Z., Wang, Q., Li, D., Shen, Y., Zhang, W., Rui, K., Zhu, J. and Huang, W. (2019). Using and recycling V_2O_5 as high performance anode materials for sustainable

lithium ion battery. *Journal of Power Sources*, 424, 158 - 164. DOI: 10.1016/j.jpowsour.2019.03.103.

Duan, H., Zheng, H., Zhou, Y., Xu, B. and Liu, H. (2018). Stability of garnet-type Li ion conductors: An overview. *Solid State Ionics*, 318, 45-53. DOI: 10.1016/j.ssi.2017.09.018.

Duluard, S., Paillassa, A., Puech, L., Vinatier, P., Turq, V., Rozier, P., Lenormand, P., Taberna, P., Simon, P. and Ansart, F. (2013). Lithium conducting solid electrolyte $\text{Li}_{1.3}\text{Al}_{0.3}\text{Ti}_{1.7}(\text{PO}_4)_3$ obtained via solution chemistry. *Journal of the European Ceramic Society* 33, 1145 – 1153. DOI: 10.1016/j.jeurceramsoc.2012.08.005.

Dunn, R. P. (2013). Flame Retardant Incorporation into Lithium-Ion Batteries. PhD dissertation, University of Rhode Island. <https://doi.org/10.23860/diss-dunn-ronald-2013>.

Duong, A. D., Sharma, S., Peine, K. J., Gupta, G., Satoskar, A. R., Bachelder, E. M., Wyslouzil, B. E. and Ainslie, K. M. (2013). Electrospray Encapsulation of Toll-Like Receptor Agonist Resiquimod in Polymer Microparticles for the Treatment of Visceral Leishmaniasis. *Molecular Pharmaceutics* 10, 3, 1045 - 1055. DOI: 10.1021/mp3005098.

Egbuhuzor, M., Nwafor, S., Umunnakwe, C. and Egoigwe, S. (2023). Thin-Film Batteries: Fundamental and Applications. In *Thin Films - Deposition Methods and Applications*. IntechOpen. DOI: 10.5772/intechopen.109734.

El Chaar, L., Lamont, L. A. and El Zein, N. (2011). Review of photovoltaic technologies. *Renewable and sustainable energy reviews* 15, 5, 2165 - 2175. DOI: 10.1016/j.rser.2011.01.004.

El-Shinawi, H., Regoutz, A., Payne, D. J., Cussen, E. J. and Corr, S. A. (2018). NASICON $\text{LiM}_2(\text{PO}_4)_3$ electrolyte (M = Zr) and electrode (M = Ti) materials for all solid-state Li-ion batteries with high total conductivity and low interfacial resistance. *Journal of Materials Chemistry A* 6, 13, 5296 - 5303. DOI: 10.1039/C7TA08715B.

- Epp, J. (2016). X-ray diffraction (XRD) techniques for materials characterization. In *Materials characterization using nondestructive evaluation (NDE) methods*, pp. 81 - 124. Woodhead Publishing. DOI: 10.1016/B978-0-08-100040-3.00004-3.
- Faisal, M. (2021). Morphology by electron microscopy. In: Sabu T., Nandakumar K., Ann Rose Abraham, A. R. (eds), *Fundamentals and Properties of Multifunctional Nanomaterials*, pp 423 – 461. Elsevier. ISBN 978-0-12-822352-9. DOI: 10.1016/C2019-0-00953-3.
- Fakharuddin, A., Gangishetty, M. K., Abdi-Jalebi, M., Chin, S. H., bin Mohd Yusoff, A. R., Congreve, D. N., Tress, W., Deschler, F., Vasilopoulou, M. and Bolink, H. J. (2022). Perovskite light-emitting diodes. *Nature Electronics*, 5, 4, 203 - 216. DOI: 10.1038/s41928-022-00745-7.
- Fang, S., Bresser, D. and Passerini, S. (2022). Chapter 4- Transition Metal Oxide Anodes for Electrochemical Energy Storage in Lithium- and Sodium-Ion Batteries. In: Nanda, J., Augustyn, V. (eds), pp. 55 - 99. DOI: 10.1002/9783527817252.ch4. Wiley Online Library.
- Farahani, S. (2008). Chapter 6 - Battery Life Analysis. In: Farahani, S. (eds), *ZigBee Wireless Networks and Transceivers*, pp. 207 - 224. Newnes. ISBN 9780750683937. DOI: 10.1016/B978-0-7506-8393-7.00006-6.
- Fenech, M. and Sharma, N. (2020). Pulsed Laser Deposition-based Thin Film Microbatteries. *Chemistry – An Asian Journal*, 15, 12, 1829 - 1847. DOI: 10.1002/asia.202000384.
- Fegade, U. A. and Jethave, G. N. (2021). Chapter 15 - Photocatalytic reduction of CO₂ in hydrocarbon: A greener approach for energy production. In: Ghaedi, M. (eds), *Interface Science and Technology*, pp. 871 - 915. Elsevier, Volume 32. ISSN 1573-4285, ISBN 9780128188064, DOI: 10.1016/B978-0-12-818806-4.00006-1.

Feng, K., Li, M., Liu, W., Kashkooli, A. G., Xiao, X., Cai, M. and Chen, Z. (2018). Silicon-based anodes for lithium-ion batteries: from fundamentals to practical applications. *Small* 14, 8, 1702737. DOI: 10.1002/sml.201702737.

Fic, K., Platek, A., Piwek, J. and Frackowiak, E. (2018). Sustainable materials for electrochemical capacitors. *Materials today* 21, 4, 437 - 454. DOI: 10.1016/j.mattod.2018.03.005.

Fukuda, T., Toda, A., Takahira, K., Kuzuhara, D. and Yoshimoto, N. (2017). Improved performance of organic photovoltaic cells with PTB7-Th: PC71 BM by optimized solvent evaporation time in electrospray deposition. *Organic Electronics* 48, 96 - 105. DOI: 10.1016/j.orgel.2017.05.049.

Gamero-Castaño M. and Magnani, M. (2019). The minimum flow rate of electrosprays in the cone-jet mode. *Journal of Fluid Mechanics* 876, 553 – 572. DOI: 10.1017/jfm.2019.569.

Ganan-Calvo, A. M. López-Herrera, J. M. Herrada, M. A. Ramos, A. and Montanero, J. M. (2018). Review on the physics electrospray: from electrokinetics to the operating conditions of single and coaxial Taylor cone-jets, and AC electrospray. *Journal of Aerosol Science* 125, 32 - 56. DOI: 10.1016/j.jaerosci.2018.05.002.

Gañán-Calvo A. M., Rebollo-Muñoz N. and Montanero J. M. (2013), The minimum or natural rate of flow and droplet size ejected by Taylor cone-jets: Physical symmetries and scaling laws. *New Journal of Physics* 3, 15, 1367 - 2630. DOI: 10.1088/1367-2630/15/3/033035.

Ganan-Calvo, A. M. Davila, J. and Barrero, A. (1997). Current and Droplet Size in the Electrospraying of Liquids. Scaling Laws. *Journal of Aerosol Science* 28, 2, 249 - 275. DOI: 10.1016/S0021-8502(96)00433-8.

Gañan-Calvo, A. M. (1994). The size and charge of droplets in the electrospraying of polar liquids in cone-jet mode, and the minimum droplet size. *Journal of Aerosol Science* 25, 1, 309 – 310. DOI: 10.1016/0021-8502(94)90384-0.

Gantenbein, S., Schönleber, M., Weiss, M. and Ivers-Tiffée, E. (2019). Capacity Fade in Lithium-Ion Batteries and Cyclic Aging over Various State-of-Charge Ranges. *Sustainability* 11, 6697. DOI: 10.3390/su11236697.

Garcia-Tamayo, E. (2014). Advanced Thin Layer Deposition of Materials for Li-ion Batteries via Electrospray. PhD Thesis, TUDelft.

Ge, S., Leng, Y., Liu, T., Longchamps, R. S., Yang, X., Gao, Y., Wang, D., Wang, D. and Wang, C. (2020). A new approach to both high safety and high performance of lithium-ion batteries. *Science Advances* 6, eaay7633. DOI: 10.1126/sciadv.aay7633.

Gianino, C. (2006). Measurement of surface tension by the dripping from a needle. *Physics Education*, 41, 5, 440. DOI: 10.1088/0031-9120/41/5/010.

Giraldo, S., Nakagawa, K., Vásquez, F. A., Fujii, Y., Wang, Y., Miura, A., Calderón, J. A., Rosero-Navarro, N. C., and Tadanaga, K. (2021). Preparation of composite electrodes for all-solid-state batteries based on sulfide electrolytes: an electrochemical point of view. *Batteries*, 7, 4, 77. DOI: 10.3390/batteries7040077.

Goldstein, J. I., Newbury, D. E., Michael, J. R., Ritchie, N. W., Scott, J. H. J., and Joy, D. C. (2018). Scanning electron microscope (SEM) instrumentation. *Scanning Electron Microscopy and X-Ray Microanalysis*, 65 - 91. Springer, New York, NY. ISBN 978-1-4939-6676-9. DOI: 10.1007/978-1-4939-6676-9_5.

Gonzalez, P. P. M., Song, S., Cao, S., Rannalter, L. Z., Pan, Z., Xiang, X., Shen, Q. and Chen, F. (2021). Garnet-type solid electrolyte: Advances of ionic transport performance and its application in all-solid-state batteries. *Journal of Advanced Ceramics* 1 - 40. DOI: 10.1007/s40145-021-0489-7.

GOK, Government of Kenya (2018). National Climate Change Action Plan: 2018 - 2022. Nairobi: Ministry of Environment and Forestry. Retrieved September 30, 2022, from <https://www.lse.ac.uk/GranthamInstitute/wp-content/uploads/2018/10/8737.pdf>.

Gregory, D. H. (2008). Lithium nitrides as sustainable energy materials. *The Chemical Record*, 8, 4, 229 - 239. DOI: 10.1002/tcr.20151.

Gulino, V., Brighi, M., Murgia, F., Ngene, P., De Jongh, P., Černý, R. and Baricco, M. (2021). Room-temperature solid-state lithium-ion battery using a LiBH₄ - MgO composite electrolyte. *ACS Applied Energy Materials* 4, 2, 1228 - 1236. DOI: 10.1021/acsaem.0c02525.

Gulino, V., Barberis, L., Ngene, P., Baricco, M. and De Jongh, P. E. (2020). Enhancing Li-ion conductivity in LiBH₄-based solid electrolytes by adding various nanosized oxides. *ACS Applied Energy Materials* 3, 5, 4941 - 4948. DOI: 10.1021/acsaem.9b02268.

Gürbüz, M., Günkaya, G. and Doğan, A. (2016). Electro spray deposition of SnO₂ films from precursor solution. *Surface Engineering* 32, 10, 725 - 732. DOI: 10.1080/02670844.2015.1108048.

de Haan, K., Ballard, Z. S., Rivenson, Y., Wu, Y. and Ozcan, A. (2019). Resolution enhancement in scanning electron microscopy using deep learning. *Scientific Reports* 9, 12050. DOI: 10.1038/s41598-019-48444-2.

Habeeb, A. I. and Al-Asadi, A. S. (2023). Fabrication of hybrid graphene nanosheets/Vanadium (V) oxide nanoparticles composite electrodes for supercapacitor application. *Solid State Communications* 360, 115024. DOI: 10.1016/j.ssc.2022.115024.

Han, S. Y., Lee, C., Lewis, J. A., Yeh, D., Liu, Y., Lee, H. W. and McDowell, M. T. (2021). Stress evolution during cycling of alloy-anode solid-state batteries. *Joule* 5, 9, 2450 - 2465. DOI: 10.1016/j.joule.2021.07.002.

Hartman, R. P. A., Brunner, D. J., Camelot, D. M. A., Marijnissen, J. C. M. and Scarlett, B. (2000). Jet Break-Up in Electrohydrodynamic Atomization in the Cone-Jet Mode. *J. Aerosol Sci.*, 31, 1 65 - 95. DOI: 10.1016/S0021-8502(99)00034-8.

Hartman, R. P. A., Brunner, D. J., Camelot, D. M. A. Marijnissen, J. C. M. and Scarlett, B. (1999). Electrohydrodynamic Atomization in the Cone-Jet Mode Physical Modeling of the Liquid Cone and Jet. *J. Aerosol Sci.*, 30, 7, 823 - 849. DOI: 10.1016/S0021-8502(99)00033-6.

Hartman, R. P. A. (1998). Electrohydrodynamic Atomization in the Cone-Jet Mode. From Physical Modelling to Powder Production. PhD Thesis Delft University of Technology, Delft, The Netherlands, 1998. ISBN 90-9012086-6. <http://resolver.tudelft.nl/uuid:1e45ec16-5860-4977-8585-edaaeaa99f6b>.

Haruta, M., Shiraki, S., Ohsawa, T., Suzuki, T., Kumatani, A., Takagi, Y., Shimizu, R. and Hitosugi, T. (2016). Preparation and in-situ characterization of well-defined solid electrolyte/electrode interfaces in thin-film lithium batteries, *Solid State Ionics*, 285, 118 – 121. DOI: 10.1016/j.ssi.2015.06.007.

Hatzell, K. B., Chen, X. C., Cobb, C., Dasgupta, N. P., Dixit, M. B., Marbella, L. E., McDowell, M. T., Mukherjee, P., Verma, A., Viswanathan, V., Westover, A. and Zeier, W. G. (2020). Challenges in lithium metal anodes for solid state batteries. *ACS Energy Letters* 5, 3, 922 - 934. DOI: 10.1021/acseenergylett.9b02668.

Hilder, M., Winther-Jensen, B., and Clark, N. B. (2009). Paper-based, printed zinc–air battery. *Journal of Power Sources*, 194, 2, 1135 – 1141.

Hong, S. C., Lee, G., Ha, K., Yoon, J., Ahn, N., Cho, W., Park, M. and Choi, M. (2017). Precise morphology control and continuous fabrication of perovskite solar cells using droplet-controllable electrospray coating system, *ACS Applied Materials & Interfaces* 9, 7879 – 7884. DOI: 10.1021/acsami.6b15095.

Honsberg, C. B. and Bowden, S. G. (2019). Photovoltaics Education Website Retrieved June 29, 2023, from <https://www.pveducation.org/pvcdrom/battery-characteristics/battery-capacity>.

Hossain, E., Faruque, H. M. R., Sunny, S. H., Mohammad, N. and Nawar, N. (2020). A Comprehensive Review on Energy Storage Systems: Types, Comparison, Current Scenario, Applications, Barriers, and Potential Solutions, Policies, and Future Prospects. *Energies*, 13, 3651. DOI: 10.3390/en13143651.

Hosseiny, S. S. and Wessling, M. (2011). Chapter 13 - Ion exchange membranes for vanadium redox flow batteries. In: Basile, A., Nunes, S. P. (eds), *Advanced Membrane Science and Technology for Sustainable Energy and Environmental Applications*, pp. 413 – 434. Woodhead Publishing Series in Energy. ISBN 9781845699697. DOI: 10.1533/9780857093790.4.413.

Hou, X., Liu, X., Wang, H., Zhang, X., Zhou, J. and Wang, M. (2023). Specific Countermeasures to Intrinsic Capacity Decline Issues and Future Direction of LiMn_2O_4 Cathode. *Energy Storage Materials* 57, 577 - 606. DOI: 10.1016/j.ensm.2023.02.015.

Hou, M., Liang, F., Chen, K., Dai, Y. and Xue, D. (2020). Challenges and perspectives of NASICON-type solid electrolytes for all-solid-state lithium batteries. *Nanotechnology* 31, 13, 132003. DOI 10.1088/1361-6528/ab5be7.

Houache, M. S. E., Yim, C. H., Karkar, Z. and Abu-Lebdeh, Y. (2022). On the Current and Future Outlook of Battery Chemistries for Electric Vehicles - Mini Review. *Batteries*, 8, 70. DOI: 10.3390/batteries8070070.

Houghton, J. (2005). Global warming. *Reports on Progress in Physics* 68, 1343. DOI 10.1088/0034-4885/68/6/R02.

Hu, Z., Sheng, J., Chen, J., Sheng, G., Li, Y., Fu, X. Z., Wang, L., Sun, R. and Wong, C. P. (2018). Enhanced Li ion conductivity in Ge-doped $\text{Li}_{0.33}\text{La}_{0.56}\text{TiO}_3$ perovskite solid

electrolytes for all-solid-state Li-ion batteries. *New Journal of Chemistry* 42, 11, 9074 - 9079. DOI: 10.1039/C8NJ01113C.

Hu, C. C., Xu, H., Liu, X., Zou, F., Qie, L., Huang, Y. and Hu, X. (2015). VO₂/TiO₂ nanosponges as binder-free electrodes for high performance supercapacitors. *Scientific Reports* 5, 16012. DOI: 10.1038/srep16012.

Huebner, G. and Krebs, M. (2015). Printed, flexible thin-film-batteries and other power storage devices. In *Handbook of Flexible Organic Electronics* (pp. 429–447). Elsevier. DOI: 10.1016/B978-1-78242-035-4.00018-X.

Ichikawa, T. and Mizushima, H. (2020). Automobile Related Products for Environmental Conservation and Energy Saving. Hitachi Chemical Technical Report No.69. Retrieved September 30, 2022, from https://www.mc.showadenko.com/english/report/062/62_sou.pdf.

Iclodean, C., Varga, B., Burnete, N., Cimerdean, D. and Jurchiș, B. (2017). Comparison of Different Battery Types for Electric Vehicles. *IOP Conf. Series: Materials Science and Engineering* 252, 012058. DOI: 10.1088/1757-899X/252/1/012058.

IEA, International Energy Agency (2021). *Global Energy Review: CO₂ Emissions in 2021: Global emissions rebound sharply to highest ever level*. Retrieved September 30, 2022, from <https://iea.blob.core.windows.net/assets/c3086240-732b-4f6a-89d7-db01be018f5e/GlobalEnergyReviewCO2Emissionsin2021.pdf>.

IOP, Institute of Physics (2007). *Properties of Matter: Measuring the density of liquids*. Retrieved October 20, 2015, from <https://spark.iop.org/measuring-density-liquids>.

Ito, Y., Sakuda, A., Ohtomo, T., Hayashi, A. and Tatsumisago, M. (2013). Preparation of Li₂S-GeS₂ solid electrolyte thin films using pulsed laser deposition. *Solid State Ionics*, 236, 1 - 4. DOI: 10.1016/j.ssi.2013.01.014.

- Jaworek, A. Sobczyk, A. T. and Krupa, A. (2018). Electrospray application to powder production and surface coating. *Journal of Aerosol Science*, 125, 57 - 92. DOI: 10.1016/j.jaerosci.2018.04.006.
- Jaworek, A., Sobczyk, A. T., Krupa, A., Marchewicz, A., Krella, K. and Czech, T. (2016). Thin Films by EHDA - A Review. *International Journal of Plasma Environmental Science & Technology*, 10(1), 29–34.
- Jaworek, A., Sobczyk, A. T., Krupa, A., Lackowski, M. and Czech, T. (2009). Electrostatic deposition of nano thin films on metal substrate. *Bulletin of the Polish Academy of Sciences: Technical Sciences* 57, 1, 63 – 70. DOI: 10.2478/V10175-010-0106-3.
- Jaworek, A. and Sobczyk, A. T. (2008). Electro spraying route to nanotechnology: An overview. *Journal of Electrostatics* 66, 197 – 219. DOI: 10.1016/j.elstat.2007.10.001.
- Jean, M. D., Jiang, J. B., Xu, M. S. and Chien, J. Y. (2016). Using AlN-coated heat sink to improve the heat dissipation of LED packages. *MATEC Web of Conferences* 71, 04005. DOI: 10.1051/mateconf/20167104005.
- Jha, M. (2018). Chapter 22 - Current Trends in Industrial Scale Synthesis of Quantum Dots and Its Application in Electronics. In: Hussain, C. M. (eds), *Micro and Nano Technologies, Handbook of Nanomaterials for Industrial Applications*, pp. 381 – 385. Elsevier. ISBN 9780128133514. DOI: 10.1016/B978-0-12-813351-4.00023-7.
- Jiang, Y. (2019). Scalable Fabrication of High Efficiency Hybrid Perovskite Solar Cells by Electrospray (Doctoral dissertation, Virginia Polytechnic Institute and State University). <http://hdl.handle.net/10919/101052>.
- Jiang, L., Wang, Q., Li, K., Ping, P., Jiang, L. and Sun, J. (2018a). A self-cooling and flame-retardant electrolyte for safer lithium ion batteries. *Sustainable Energy Fuels* 2, 1323 - 1331. DOI: 10.1039/C8SE00111A.

Jiang, J., Zheng, G., Zhu, P., Liu, J., Liu, Y., Wang, X., Li, W. and Guo, S. (2018b) Controlling of Electro Spray Deposition for Micropatterns. *Micromachines* 9, 72. DOI: 10.3390/mi9020072.

Jiang, Y., Wu, C., Li, L., Wang, K., Tao, Z., Gao, F., Cheng, W., Cheng, J., Zhao, X. Y., Priya, S. and Deng, W. (2018c). All electro spray printed perovskite solar cells. *Nano Energy*, 53, 440-448. DOI: 10.1016/j.nanoen.2018.08.062.

Jo, Y. J., Kim, Y. H., Jo, Y. H., Seong, J. G., Chang, S. Y., Van Tyne, C. J. and Lee, W. H. (2014). Microporous Ti Implant Compact Coated with Hydroxyapatite Produced by Electro-Discharge-Sintering and Electrostatic Spray Deposition. *Journal of Nanoscience and Nanotechnology* 14, 8439 - 8444. DOI: 10.1166/jnn.2014.9933.

Joshi, B., Samuel, E., Kim, Y., Yarin, A. L., Swihart, M. T. and Yoon, S. S. (2021). Electrostatically Sprayed Nanostructured Electrodes for Energy Conversion and Storage Devices. *Advanced Functional Materials*, 31, 14, 2008181. DOI: 10.1002/adfm.202008181.

Joshi, B., Yoon, H., Kim, H., Kim, M., Mali, M. G., Al-Deyab, S. S. and Yoon, S. S. (2015). Heterojunction photoanodes for solar water splitting using chemical-bath-deposited In_2O_3 micro-cubes and electro-sprayed Bi_2WO_6 textured nanopillars. *RSC Advances* 5, 104, 85323 - 85328. DOI: 10.1039/C5RA16833C.

Joshi, B. N., Yoon, H. and Yoon, S. S. (2013). Structural, optical and electrical properties of tin oxide thin films by electrostatic spray deposition. *Journal of Electrostatics*, 71, 1, 48 – 52. DOI: 10.1016/j.elstat.2012.11.024.

Joshi, B. N., Yoon, H., Kim, H. Y., Oh, J. H., Seong, T. Y., James, S. C. and Yoon, S. S. (2012). Effect of Zinc Acetate Concentration on Structural, Optical and Electrical Properties of ZnO Thin Films Deposited by Electrostatic Spray on an ITO Substrate. *Journal of The Electrochemical Society*, 159, 8, H716 – H721. DOI: 10.1149/2.077208jes.

Julien, C. M., Mauger, A. and Hussain, O. M. (2019). Sputtered LiCoO₂ cathode materials for all-solid-state thin-film lithium microbatteries. *Materials* 12, 17, 2687. DOI: 10.3390/ma12172687.

Julien, C., Mauger, A., Zaghbi, K. and Groult, H. (2016). Optimization of layered cathode materials for lithium-ion batteries. *Materials* 9, 7, 595. DOI: 10.3390/ma9070595.

Jung, R., Metzger, M., Maglia, F., Stinner, C. and Gasteiger, H. A. (2017). Oxygen release and its effect on the cycling stability of LiNi_xMn_yCo_zO₂ (NMC) cathode materials for Li-ion batteries. *Journal of The Electrochemical Society* 164, 7, A1361. DOI: 10.1149/2.0021707jes.

Kalhoff, J., Eshetu, G. G., Bresser, D. and Passerini, S. (2015). Safer Electrolytes for Lithium-Ion Batteries: State of the Art and Perspectives. *ChemSusChem* 8, 13, 2154 - 2175. DOI: 10.1002/cssc.201500284.

Kanazawa, S., Baba, T., Yoneda, K., Mizuhata, M. and Kanno, I. (2020). Deposition and performance of all solid-state thin-film lithium-ion batteries composed of amorphous Si/LiPON/VO-LiPO multilayers. *Thin Solid Films* 697, 137840. DOI: 10.1016/j.tsf.2020.137840.

Kanehori, K., Matsumoto, K., Miyauchi, K. and Kudo, T. (1983). Thin film solid electrolyte and its application to secondary lithium cell *Solid State Ion.* 9 – 10, 1445 – 8. DOI: 10.1016/0167-2738(83)90192-3.

Karabelli, D., Birke, K. P. and Weeber, M. A. (2021). Performance and Cost Overview of Selected Solid-State Electrolytes: Race between Polymer Electrolytes and Inorganic Sulfide Electrolytes. *Batteries* 7, 18. DOI: 10.3390/batteries7010018.

Karimi, Z., Sadeghi, A. and Ghaffarinejad, A. (2023). The comparison of different deposition methods to prepare thin film of silicon-based anodes and their performances in Li-ion batteries. *Journal of Energy Storage*, 72, 108282. DOI:10.1016/j.est.2023.108282.

Kasnatscheew, J., Evertz, M., Streipert, B., Wagner, R., Klöpsch, R., Vortmann, B., Hahn, H., Nowak, S., Amereller, M., Gentshev, A. C., Lamp P. and Winter, M. (2016). The truth about the 1st cycle Coulombic efficiency of $\text{LiNi}_{1/3}\text{Co}_{1/3}\text{Mn}_{1/3}\text{O}_2$ (NCM) cathodes. *Physical chemistry chemical physics* 18, 5, 3956 - 3965. DOI: 10.1039/C5CP07718D.

Kato, Y., Hori, S., Saito, T., Suzuki, K., Hirayama, M., Mitsui, A., Yonemura, M., Iba, H. and Kanno, R. (2016). High-power all-solid-state batteries using sulfide superionic conductors. *Nature Energy* 1, 4, 16030. DOI: 10.1038/nenergy.2016.30.

Kavadiya, S., Niedzwiedzki, D. M., Huang, S. and Biswas, P. (2017). Electro-spray-Assisted Fabrication of Moisture-Resistant and Highly Stable Perovskite Solar Cells at Ambient Conditions. *Advanced Energy Materials* 1700210. DOI: 10.1002/aenm.201700210.

Kawashima, K., Ohnishi, T. and Takada, K. (2020). High-rate capability of LiCoO_2 cathodes. *ACS Applied Energy Materials* 3, 12, 11803 - 11810. DOI: 10.1021/acsaem.0c01973.

Kelder, E. M. Marijnissen, J. C. M. and Karuga, S. W. (2018). EDHA for energy production, storage and conversion devices. *Journal of Aerosol Science* 125, 119 - 147. DOI: 10.1016/j.jaerosci.2018.04.011.

Khan, H., Yerramilli, A. S., D'Oliveira, A., Alford, T. L., Boffito, D. C. and Patience, G. S. (2020). Experimental methods in chemical engineering: X-ray diffraction spectroscopy - XRD. *The Canadian journal of chemical engineering* 98, 6, 1255 - 1266. DOI: doi.org/10.1002/cjce.23747.

Kim, H. M., Subramanian, Y. and Ryu, K. S. (2023). Improved electrochemical and air stability performance of SeS_2 doped argyrodite lithium superionic conductors for all-solid-state lithium batteries. *Electrochimica Acta*, 141869. DOI: 10.1016/j.electacta.2023.141869.

Kim, J. Y., Jung, S., Kang, S. H., Lee, M. J., Jin, D., Shin, D. O., Lee, Y. G., and Lee, Y. M. (2022). All-solid-state hybrid electrode configuration for high-performance all-solid-state batteries: Comparative study with composite electrode and diffusion-dependent electrode. *Journal of Power Sources* 518, 230736. DOI: 10.1016/j.jpowsour.2021.230736.

Kim, A., Woo, S., Kang, M., Park, H. and Kang, B. (2020). Research progresses of garnet-type solid electrolytes for developing all-solid-state Li batteries. *Frontiers in chemistry*, 8, 468. DOI: 10.3389/fchem.2020.00468.

Kirchev, A. (2015). Chapter 20 - Battery Management and Battery Diagnostics. In: Moseley, P. T., Garche, J. (eds), *Electrochemical Energy Storage for Renewable Sources and Grid Balancing*, pp 411 – 435. Elsevier. ISBN 9780444626165. DOI: 10.1016/B978-0-444-62616-5.00020-6.

Kneissl, M., Seong, T. Y., Han, J. and Amano, H. (2019). The emergence and prospects of deep-ultraviolet light-emitting diode technologies. *Nature photonics* 13, 4, 233 - 244. DOI: 10.1038/s41566-019-0359-9.

Kodama, H. (2015). *Electrical Energy Storage Devices & Systems*. Hitachi Chemical Technical Report No.57. Retrieved September 30, 2022, from https://www.mc.showadenko.com/english/report/057/57_sou.pdf.

Koerver, R., Aygün, I., Leichtweiß, T., Dietrich, C., Zhang, W., Binder, J. O., Hartmann, P., Zeier, W. G. and Janek, J. (2017a). Capacity Fade in Solid-State Batteries: Interphase Formation and Chemomechanical Processes in Nickel-Rich Layered Oxide Cathodes and Lithium Thiophosphate Solid Electrolytes. *Chem. Mater.* 29, 5574 – 5582. DOI: 10.1021/acs.chemmater.7b00931.

Koerver, R., Walther, F., Aygün, I., Sann, J., Dietrich, C., Zeier, W. G. and Janek, J. (2017b). Redox-active cathode interphases in solid-state batteries. *Journal of Materials Chemistry A*, 5, 43, 22750 - 22760. DOI: 10.1039/C7TA07641J.

- Koike, S. and Tatsumi, K. (2007). Preparation and performances of highly porous layered LiCoO₂ films for lithium batteries. *Journal of Power Sources* 174, 976 – 980. DOI: 10.1016/j.jpowsour.2007.06.219.
- Koike, S. and Tatsumi, K. (2005). Preparation and morphology of three-dimensional structured LiMn₂O₄ films. *Journal of Power Sources* 146, 241 – 244. DOI: 10.1016/j.jpowsour.2005.03.038.
- Kong, L., Li, C., Jiang, J. and Pecht, M. G. (2018). Li-Ion Battery Fire Hazards and Safety Strategies. *Energies* 11, 9, 2191. DOI: 10.3390/en11092191.
- Kopp, O. C. (2020). Fossil fuel. *Encyclopedia Britannica*. Retrieved September 30, 2022 from <https://www.britannica.com/science/fossil-fuel>.
- Kordesch, K. and Taucher-Mautner, W. (2009). HISTORY - Primary Batteries. In: Garche, J. (eds), *Encyclopedia of Electrochemical Power Sources*, pp. 555 - 564. Elsevier. ISBN 9780444527455. DOI: 10.1016/B978-044452745-5.00003-4.
- Kotcher, J., Maibach, E. and Choi, W. (2019). Fossil fuels are harming our brains: Identifying key messages about the health effects of air pollution from fossil fuels. *BMC Public Health* 19, 1079. DOI: 10.1186/s12889-019-7373-1.
- Kotobuki, M. and Koishi, M. (2013). Preparation of Li_{1.5}Al_{0.5}Ti_{1.5}(PO₄)₃ solid electrolyte via a sol–gel route using various Al sources. *Ceramics International*, 39, 4645 – 4649. DOI: 10.1016/j.ceramint.2012.10.206.
- Kudu, O. U., Famprakis, T., Fleutot, B., Braida, M. D., Le Mercier, T., Islam, M. S. and Masquelier, C. (2018). A review of structural properties and synthesis methods of solid electrolyte materials in the Li₂S – P₂S₅ binary system. *Journal of Power Sources* 407, 31 - 43. DOI: 10.1016/j.jpowsour.2018.10.037.
- Kumar, D. S., Kumar, B. J., Mahesh, H. M. (2018). Chapter 3 - Quantum Nanostructures (QDs): An Overview. In: Bhagyaraj, S. M., Oluwafemi, O. S., Kalarikkal, N., Thomas, S.

(eds), *Micro and Nano Technologies, Synthesis of Inorganic Nanomaterials*, pp. 59 – 88. Woodhead Publishing. ISBN 9780081019757. DOI: 10.1016/B978-0-08-101975-7.00003-8.

Kumar, B., Kumar, J., Leese, R., Fellner, J. P. Rodrigues, S. J. and Abraham, K. M. (2010). A Solid-State, Rechargeable, Long Cycle Life Lithium-Air Battery. *Journal of The Electrochemical Society*, 157, 1, A50 - A54. DOI: 10.1149/1.3256129.

Lafont, U., Anastasopol, A., Garcia-Tamayo, E. and Kelder, E. (2012). Electrostatic spray pyrolysis of $\text{LiNi}_{0.5}\text{Mn}_{1.5}\text{O}_4$ films for 3D Li-ion microbatteries. *Thin Solid Films* 520, 3464 – 3471. DOI: 10.1016/j.tsf.2011.12.041.

Landrigan, P. J., Fuller, R., Acosta, N. J. R., Adeyi, O., Arnold, R., Basu, N., et al. (2018). The lancet commission on pollution and health. *The Lancet* 391, 10119, 462 – 512. DOI: 10.1016/S0140-6736(17)32345-0.

Lee, H., Kim, S., Kim, K. B., and Choi, J. W. (2018). Scalable fabrication of flexible thin-film batteries for smart lens applications. *Nano Energy* 53, 225 - 231. DOI: 10.1016/j.nanoen.2018.08.054.

Lee, T., Cho, K., Oh, J. and Shin, D. (2007). Fabrication of LiCoO_2 cathode powder for thin film battery by aerosol flame deposition. *Journal of Power Sources* 174, 394 - 399. DOI: 10.1016/j.jpowsour.2007.06.136.

Letcher, T. M. (2021). 1 - Global warming - a complex situation. In: Letcher, T. M. (eds), *Climate Change (Third Edition)*, pp 3 – 17. Elsevier. ISBN 9780128215753. DOI: 10.1016/B978-0-12-821575-3.00001-3.

Le Quéré, C., Andrew, R. M., Friedlingstein, P., Sitch, S., Hauck, J., Pongratz, J. et al. (2018). Global Carbon Budget 2018. *Earth Syst. Sci. Data*, 10, 2141 – 2194. DOI: 10.5194/essd-10-2141-2018.

Li, L., Yu, L., Guo, C., Xiong, X., Fan, F., Yang, W., She, F., He, C., and Kong, L. (2023). Green Fabrication of Agglomeration-Reductive and Electrochemical-Active Reduced Graphene Oxide/Polymerized Proanthocyanidins Electrode for High-Performance Supercapacitor. *ACS Applied Engineering Materials*. DOI: 10.1021/acsaenm.2c00090.

Li, Z., Pan, Z. and Zhong, X. (2022). Recent Development of Quantum Dot Deposition in Quantum Dot-Sensitized Solar Cells. *Transactions of Tianjin University*, 28, 374 - 384. DOI: 10.1007/s12209-022-00322-1.

Li, P., Kim, H., Myung, S. T. and Sun, Y. K. (2021a). Diverting exploration of silicon anode into practical way: a review focused on silicon-graphite composite for lithium ion batteries. *Energy Storage Materials* 35, 550 - 576. DOI: 10.1016/j.ensm.2020.11.028.

Li, Q., Li, H., Xia, Q., Hu, Z., Zhu, Y., Yan, S., Ge, C., Zhang, Q., Wang, X., Shang, X., Fan, S., Long, Y., Gu, L., Miao, G. X., Yu, G. and Moodera, J. S. (2021b). Extra storage capacity in transition metal oxide lithium-ion batteries revealed by in situ magnetometry. *Nature materials* 20, 1, 76 - 83. DOI: 10.1038/s41563-020-0756-y.

Li, J., Lin, C., Weng, M., Qiu, Y., Chen, P., Yang, K., Huang, W., Hong, Y., Li, J., Zhang, M., Dong, C., Zhao, W., Xu, Z., Wang, X., Xu, K., Sun, J. and Pan, F. (2021c). Structural origin of the high-voltage instability of lithium cobalt oxide. *Nature Nanotechnology* 16, 5, 599 - 605. DOI: 10.1038/s41565-021-00855-x.

Li, Z., Zhang, Y., Liu, T., Gao, X., Li, S., Ling, M., Liang, C. Zheng, J. and Lin, Z. (2020a). Silicon anode with high initial coulombic efficiency by modulated trifunctional binder for high-areal-capacity lithium-ion batteries. *Advanced Energy Materials* 10, 20, 1903110. DOI: 10.1002/aenm.201903110.

Li, H., Yamaguchi, T., Matsumoto, S., Hoshikawa, H., Kumagai, T., Okamoto, N. L. and Ichitsubo, T. (2020b). Circumventing huge volume strain in alloy anodes of lithium batteries. *Nature Communications* 11, 1584. DOI: 10.1038/s41467-020-15452-0.

- Li, B., Wang, Y. and Yang, S. (2018a). A material perspective of rechargeable metallic lithium anodes. *Advanced Energy Materials*, 8, 13, 1702296. DOI: 10.1002/aenm.201702296.
- Li, Y., Xu, H., Chien, P. H., Wu, N., Xin, S., Xue, L., Park, K., Hu, Y. Y. and Goodenough, J. B. (2018b). A perovskite electrolyte that is stable in moist air for lithium-ion batteries. *Angewandte Chemie International Edition* 57, 28, 8587 - 8591. DOI: 10.1002/anie.201804114.
- Li, C., Novak, S., Denisov, S. A., McClenaghan, N. D., Patel, N., Agarwal, A., Kathleen Richardson, K. and Deng, W. (2017). Electro spray deposition of quantum dot-doped $\text{Ge}_{23}\text{Sb}_7\text{S}_{70}$ chalcogenide glass films. *Thin Solid Films* 626, 194 - 199. DOI: 10.1016/j.tsf.2017.02.030.
- Li, Q., Chen, J., Fan, L., Kong, X. and Lu, Y. (2016). Progress in electrolytes for rechargeable Li-based batteries and beyond. *Green Energy & Environment* 1, 1, 18 - 42, DOI: 10.1016/j.gee.2016.04.006.
- Li, X., Dhanabalan, A. and Wang, C. (2011). Enhanced electrochemical performance of porous NiO-Ni nanocomposite anode for lithium ion batteries. *Journal of Power Sources* 196, 9625 - 9630. DOI: 10.1016/j.jpowsour.2011.06.097.
- Lian, Y., Zhang, W., Ding, L., Zhang, X., Zhang, Y., Wang, X. (2019). Chapter 8 - Nanomaterials for Intracellular pH Sensing and Imaging. In: Wang, X., Chen, X. (eds), *Micro and Nano Technologies, Novel Nanomaterials for Biomedical, Environmental and Energy Applications*, pp. 241 – 273. Elsevier. ISBN 9780128144978. DOI: 10.1016/B978-0-12-814497-8.00008-4.
- Liang, S., Cheng, Y. J., Zhu, J., Xia, Y. and Müller-Buschbaum, P. (2020). A chronicle review of nonsilicon (Sn, Sb, Ge) - based lithium/sodium-ion battery alloying anodes. *Small Methods* 4, 8, 2000218. DOI: 10.1002/smtd.202000218.

Liang, X., Tan, F., Wei, F. and Du, J. (2019a). Research progress of all solid-state thin film lithium battery. *IOP Conf. Series: Earth and Environmental Science* 218, 012138. DOI: 10.1088/1755-1315/218/1/012138.

Liang, Y., Zhao, C., Yuan, H., Chen, Y., Zhang, W., Huang, J., Yu, D., Liu, Y., Titirici, M., Chueh, Y., Yu, H. and Zhang, Q. (2019b). A review of rechargeable batteries for portable electronic devices. *InfoMat.* 1, 6 – 32. DOI: 10.1002/inf2.12000.

Liang, J., Luo, J., Sun, Q., Yang, X., Li, R. and Sun, X. (2019c). Recent progress on solid-state hybrid electrolytes for solid-state lithium batteries. *Energy Storage Materials* 21, 308 - 334. DOI: 10.1016/j.ensm.2019.06.021.

Lipson, A. L., Ross, B. J., Durham, J. L., Liu, D., LeResche, M., Fister, T. T., Liu, L., and Kim, K. (2021). Stabilizing NMC 811 Li-Ion Battery Cathode through a Rapid Coprecipitation Process. *ACS Applied Energy Materials* 4, 2, 1972 - 1977. DOI: 10.1021/acsaem.0c03112.

Liu, X., Xiao, Z., Peng, H., Jiang, D., Xie, H., Sun, Y., Zhong, S., Qian, Z., and Wang, R. (2022). Rational Design of LLZO/Polymer Solid Electrolytes for Solid-State Batteries. *Chemistry - An Asian Journal*, e202200929. DOI: 10.1002/asia.202200929.

Liu, H., Zhang, G., Zheng, X., Chen, F. and Duan, H. (2020). Emerging miniaturized energy storage devices for microsystem applications: from design to integration. *International Journal of Extreme Manufacturing* 2, 042001. DOI: 10.1088/2631-7990/abba12.

Liu, Z., Yuan, X., Zhang, S., Wang, J., Huang, Q., Yu, N., Zhu, Y., Fu, L., Wang, F., Chen, Y. and Wu, Y. (2019). Three-dimensional ordered porous electrode materials for electrochemical energy storage. *NPG Asia Materials*, 11, 12. DOI: 10.1038/s41427-019-0112-3.

- Liu, B., Zhang, J. G. and Xu, W. (2018a). Advancing lithium metal batteries. *Joule* 2, 5, 833 - 845. DOI: 10.1016/j.joule.2018.03.008.
- Liu, Q., Su, X., Lei, D., Qin, Y., Wen, J., Guo, F., Wu, Y. A., Rong, Y., Kou, R., Xiao, X., Aguesse, F., Bareño, J., Ren, Y., Lu, W. and Li, Y. (2018b). Approaching the capacity limit of lithium cobalt oxide in lithium ion batteries via lanthanum and aluminium doping. *Nature Energy* 3, 11, 936 - 943. DOI: 10.1038/s41560-018-0180-6.
- Liu, Y., Lin, D., Yuen, P. Y., Liu, K., Xie, J., Dauskardt, R. H. and Cui, Y. (2017). An artificial solid electrolyte interphase with high Li-ion conductivity, mechanical strength, and flexibility for stable lithium metal anodes. *Advanced Materials* 29, 10, 1605531. DOI: 10.1002/adma.201605531.
- Loho, C., Djenadic, R., Bruns, M., Clemens, O., & Hahn, H. (2017). Garnet-Type $\text{Li}_7\text{La}_3\text{Zr}_2\text{O}_{12}$ Solid Electrolyte Thin Films Grown by CO_2 - Laser Assisted CVD for All-Solid-State Batteries. *Journal of The Electrochemical Society*, 164, 1, A6131 – A6139. DOI: 10.1149/2.0201701jes.
- Looney, B. (2020). BP Statistical Review of World Energy, 69th edition. Retrieved September 12, 2023, from, <https://www.bp.com/content/dam/bp/business-sites/en/global/corporate/pdfs/energy-economics/statistical-review/bp-stats-review-2020-full-report.pdf>
- Lu, Y., Zhao, C. Z., Zhang, R., Yuan, H., Hou, L. P., Fu, Z. H., Chen, X., Huang, J. Q. and Zhang, Q. (2021). The carrier transition from Li atoms to Li vacancies in solid-state lithium alloy anodes. *Science advances*, 7, 38. DOI: 10.1126/sciadv.abi552.
- Lu, J. and Li, Y. (2021). Perovskite-type Li-ion solid electrolytes: a review. *Journal of Materials Science: Materials in Electronics* 32, 9736 - 9754. DOI: 10.1007/s10854-021-05699-8.

Luntz, A. C., Voss, J. and Reuter, K. (2015). Interfacial Challenges in Solid-State Li Ion Batteries. *The Journal of Physical Chemistry Letters*, 6, 4599 – 4604. DOI: 10.1021/acs.jpcllett.5b02352.

Luo, Z., Qiu, X., Liu, C., Li, S., Wang, C., Zou, G., Hou, H and Ji, X. (2021). Interfacial challenges towards stable Li metal anode. *Nano Energy* 79, 105507. DOI: 10.1016/j.nanoen.2020.105507.

Luo, Y., Chen, C., Chen, L., Zhang, M. and Wang, T. (2017). 3D reticular pomegranate-like $\text{CoMn}_2\text{O}_4/\text{C}$ for ultrahigh rate lithium-ion storage with re-oxidation of manganese. *Electrochimica Acta* 241, 244 – 251. DOI: 10.1016/j.electacta.2017.04.149.

Lv, F., Wang, Z., Shi, L., Zhu, J., Edström, K., Mindemark, J. and Yuan, S. (2019). Challenges and development of composite solid-state electrolytes for high-performance lithium ion batteries. *Journal of Power Sources* 441, 227175. DOI: 10.1016/j.jpowsour.2019.227175.

Lykiardopoulou, I. (2021). Why solid-state EV batteries are better than their lithium-ion counterpart. Retrieved September 12, 2023, from, <https://thenextweb.com/news/why-solid-state-ev-batteries-are-better-than-lithium-ion-counterpart>.

Ma, X. H., Wan, Q. Y., Huang, X., Ding, C. X., Jin, Y., Guan, Y. B. and Chen, C. H. (2014). Synthesis of three-dimensionally porous MnO thin films for lithium-ion batteries by improved Electrostatic Spray Deposition technique. *Electrochimica Acta* 121, 15 - 20. DOI: 10.1016/j.electacta.2013.12.004.

Ma, J., and Qin. Q. (2005). Electrochemical performance of nanocrystalline LiMPO_4 thin-films prepared by electrostatic spray deposition. *Journal of Power Sources* 148, 66 - 71. DOI: 10.1016/j.jpowsour.2005.01.041.

Madsen, K. E., Wade, K. A., Haasch, R. T., Buchholz, D. B., Bassett, K. L., Nicolau, B. G. and Gewirth, A. A. (2019). Origin of enhanced cyclability in covalently modified

LiMn_{1.5}Ni_{0.5}O₄ cathodes. *ACS Applied Materials & Interfaces* 11, 43, 39890 - 39901. DOI: 10.1021/acsami.9b12912.

Majeed, M. K., Iqbal, R., Hussain, A., Majeed, M. U., Ashfaq, M. Z., Ahmad, M., Rauf, S. and Saleem, A. (2023). Silicon-based anode materials for lithium batteries: recent progress, new trends, and future perspectives, *Critical Reviews in Solid State and Materials Sciences*, published online: 06 Feb 2023. DOI: 10.1080/10408436.2023.2169658.

Manthiram, A. and Goodenough, J. B. (2021). Layered lithium cobalt oxide cathodes. *Nature Energy* 6, 3, 323 - 323. DOI: 10.1038/s41560-020-00764-8.

Marijnissen, J. C. M., Yurteri, C. U., Karuga, S. W. and Hartman, R. P. A. (2023). On the minimum and maximum flow rate of electrospaying: A practical approach, based on fundamentals, for design purposes. *Journal of Electrostatics* 124, 103809. DOI: 10.1016/j.elstat.2023.103809.

Markevich, E., Salitra, G., Talyosef, Y., Kim, U. H., Ryu, H. H., Sun, Y. K. and Aurbach, D. (2018). High-performance LiNiO₂ cathodes with practical loading cycled with Li metal anodes in fluoroethylene carbonate-based electrolyte solution. *ACS Applied Energy Materials* 1, 6, 2600 - 2607. DOI: 10.1021/acsaem.8b00304.

Maršálek, J., Chmelař, J., Povedič, J. and Kosek, J. (2015). Morphological and electrochemical study of Mn_xO_y nanoparticle layers prepared by electrospaying. *Chemical Engineering Science* 123, 292 - 299. DOI: 10.1016/j.ces.2014.10.044.

Matsuda, R., Hirahara, E., Phuc, N. H. H., Muto, H., Tsukasaki, H., Mori, S. and Matsuda, A. (2018). Preparation of LiNi_{1/3}Mn_{1/3}Co_{1/3}O₂/Li₃PS₄ cathode composite particles using a new liquid-phase process and application to all-solid-state lithium batteries. *Journal of the Ceramic Society of Japan* 126, 10, 826 - 831. DOI: 10.2109/jcersj2.18080.

Maxwell, T., Campos, M. G. N., Smith, S., Doomra, M., Thwin, Z. and Santra, S. (2020). Chapter 15 - Quantum Dots. In: Chung, E. J., Leon, L., Rinaldi, C. (eds), *Micro and Nano*

Technologies, Nanoparticles for Biomedical Applications, pp. 243 - 265. Elsevier. ISBN 9780128166628. DOI: 10.1016/B978-0-12-816662-8.00015-1.

McNulty, R. C., Penston, K., Amin, S. S., Stal, S., Lee, J. Y., Samperi, M., García, L. P., Cameron, J. M., Johnson, L. R., Amabilino, D. B. and Newton, G. N. (2023). Self-Assembled Surfactant - Polyoxovanadate Soft Materials as Tuneable Vanadium Oxide Cathode Precursors for Lithium - Ion Batteries. *Angewandte Chemie*, e202216066. DOI: 10.1002/ange.202216066.

Meesala, Y., Chen, C. Y., Jena, A., Liao, Y. K., Hu, S. F., Chang, H. and Liu, R. S. (2018). All-solid-state Li-ion battery using $\text{Li}_{1.5}\text{Al}_{0.5}\text{Ge}_{1.5}(\text{PO}_4)_3$ as electrolyte without polymer interfacial adhesion. *The Journal of Physical Chemistry C* 122, 26, 14383 - 14389. DOI: 10.1021/acs.jpcc.8b03971.

Mishra, A., Mehta, A., Basu, S., Malode, S. J., Shetti, N. P., Shukla, S. S., Nadagouda, M. N. and Aminabhavi, T. M. (2018). Electrode materials for lithium-ion batteries. *Materials Science for Energy Technologies* 1, 2, 182 – 187. DOI: 10.1016/j.mset.2018.08.001.

Mohammed, A. and Abdullah, A. (2018). Scanning Electron Microscopy (SEM): A Review. *Proceedings of 2018 International Conference on Hydraulics and Pneumatics - HERVEX November 7 - 9, Băile Govora, Romania*. ISSN 1454 – 8003.

Moitzheim, S., Put, B. and Vereecken, P. M. (2019). Advances in 3D Thin-Film Li-Ion Batteries. *Advanced Materials Interfaces*, 6, 15, 1900805. DOI: 10.1002/admi.201900805.

Moradi, B. and Botte, G. G. (2016). Recycling of graphite anodes for the next generation of lithium ion batteries. *J. Appl Electrochem* 46, 123 – 148. DOI: 10.1007/s10800-015-0914-0.

Morosanu, C. E. (2016). *Thin films by chemical vapour deposition (Vol. 7)*. Elsevier. ISBN: 9781483291734.

- Mughal, S., Sood, Y. R. and Jarial, R. K. (2018). A review on solar photovoltaic technology and future trends. *International Journal of Scientific Research in Computer Science, Engineering and Information Technology* 4, 1, 227 - 235.
- Murugan, R., Thangadurai, V. and Weppner, W. (2007). Fast Lithium Ion Conduction in Garnet-Type $\text{Li}_7\text{La}_3\text{Zr}_2\text{O}_{12}$. *Angew Chem. Int. Ed. Engl.* 46, 41, 7778 - 7781. DOI: 10.1002/anie.200701144.
- Neagu, R., Djurado, E., Ortega, L. and Pagnie, T. (2006). ZrO_2 -based thin films synthesized by electrostatic spray deposition: Effect of post-deposition thermal treatments. *Solid State Ionics* 177, 1443 - 1449. DOI: 10.1016/j.ssi.2006.06.024.
- NED (2013). *The Electric Energy. Lithium and Lithium-ion battery technology*. Retrieved September 12, 2017, from <http://theelectricenergy.com/lithium-and-lithium-ion-battery/>.
- Nguyen, T. C. and Choi, W. S. (2020). Electrospray mechanism for quantum dot thin-film formation using an electrohydrodynamic jet and light-emitting device application. *Sci Rep* 10 11075. DOI: 10.1038/s41598-020-67867-w.
- Nguyen, T. C., Can, T. T. T. and Choi, W. S. (2018). Electrohydrodynamic jet-sprayed quantum dots for solution-processed light-emitting-diodes. *Optical Materials Express* 8, 12, 3738 - 3747. DOI: 10.1364/OME.8.003738.
- Nguyen, H. T., Yao, F., Zamfir, M. R., Biswas, C., So, K. P., Lee, Y. H., Kim, S. M., Cha, S. N., Kim, J. M. and Pribat, D. (2011). Highly Interconnected Si Nanowires for Improved Stability Li-Ion Battery Anodes. *Advanced Energy Materials* 1. 6, 1154 - 1161. DOI: 10.1002/aenm.201100259.
- Nikodimos, Y., Su, W. N. and Hwang, B. J. (2023). Halide Solid-State Electrolytes: Stability and Application for High Voltage All-Solid-State Li Batteries. *Advanced Energy Materials* 13, 3, 2202854. DOI: 10.1002/aenm.202202854.

- Nikodimos, Y., Tsai, M. C., Abrha, L. H., Weldeyohannis, H. H., Chiu, S. F., Bezabh, H. K., Shitaw, K. N., Fenta, F. W., Wu, S. H., Su, W. N., Yang, C. C. and Hwang, B. J. (2020). Al–Sc dual-doped $\text{LiGe}_2(\text{PO}_4)_{3-a}$ NASICON-type solid electrolyte with improved ionic conductivity. *Journal of Materials Chemistry A* 8, 22, 11302 - 11313. DOI: 10.1039/D0TA00517G.
- Nishizawa, M., Uchiyama, T., Dokko, K., Yamada, K., Matsue, T. and Uchida, I. (1998). Electrochemical Studies of Spinel LiMn_2O_4 Films Prepared by Electrostatic Spray Deposition. *Bulletin of the Chemical Society of Japan* 71, 2011 – 2015. DOI: 10.1246/bcsj.71.2011.
- Nitta, N., Wu, F., Lee, J. T. and Yushin, G. (2015). Li-ion battery materials: Present and future. *Materials Today* 18, 5, 252 – 264. DOI: 10.1016/j.mattod.2014.10.040.
- Noh, S., Nichols, W. T., Cho, M. and Shin, D. (2018). Importance of mixing protocol for enhanced performance of composite cathodes in all-solid-state batteries using sulfide solid electrolyte. *Journal of Electroceramics* 40, 293 – 299. DOI: 10.1007/s10832-018-0129-y.
- Noh, H. J., Youn, S., Yoon, C. S., and Sun, Y. K. (2013). Comparison of the structural and electrochemical properties of layered $\text{Li}[\text{Ni}_x\text{Co}_y\text{Mn}_z]\text{O}_2$ ($x = 1/3, 0.5, 0.6, 0.7, 0.8$ and 0.85) cathode material for lithium-ion batteries. *Journal of power sources* 233, 121 - 130. DOI: 10.1016/j.jpowsour.2013.01.063.
- Notohara, H., Urita, K. and Moriguchi, I. (2020). Tin Oxide Materials Synthesis, Properties, and Applications. In: M. O. Orlandi (eds), Chapter 14 - Tin oxide electrodes in Li and Na-ion batteries, pp 411 – 439. ISBN 978-0-12-815924-8. Elsevier. DOI: 10.1016/C2017-0-04048-X.
- Nwaigwe, K. N., Mutabilwa, P. and Dintwa, E. (2019). An overview of solar power (PV systems) integration into electricity grids. *Materials Science for Energy Technologies* 2, 3, 629 - 633. <https://doi.org/10.1016/j.mset.2019.07.002>.

- Nzereogu, P. U., Omah, A. D., Ezema, F. I., Iwuoha, E. I. and Nwanya, A. C. (2022). Anode materials for lithium-ion batteries: A review. *Applied Surface Science Advances* 9, 100233. DOI: 10.1016/j.apsadv.2022.100233.
- Okuno, Y., Haruyama, J. and Tateyama, Y. (2020). Comparative study on sulfide and oxide electrolyte interfaces with cathodes in all-solid-state battery via first-principles calculations. *ACS Applied Energy Materials*, 3, 11, 11061 - 11072. DOI: 10.1021/acsaem.0c02033.
- Owens, B. B., Reale, P. and Scrosati, B. (2009). PRIMARY BATTERIES - Overview. In: Garche, J. (eds), *Encyclopedia of Electrochemical Power Sources*, pp. 22 - 27. Elsevier. ISBN 9780444527455. DOI: 10.1016/B978-044452745-5.00096-4.
- Pang, B., Huang, J., Ge, J., Luo, Y., Zhou, M., Luo, Y. and Okada, S. (2020). Improved electrochemical properties of LiCoO_2 via Ni, Mn Co-doping from $\text{LiNi}_{0.8}\text{Co}_{0.1}\text{Mn}_{0.1}\text{O}_2$ for rechargeable lithium-ion batteries. *Electrochemistry* 88, 4, 295 - 299. DOI: 10.5796/electrochemistry.19-00074.
- Parekh, M. H., Palanisamy, M. and Pol, V. G. (2023). Reserve lithium-ion batteries: Deciphering in situ lithiation of lithium-ion free vanadium pentoxide cathode with graphitic anode. *Carbon* 203, 561 - 570. DOI: 10.1016/j.carbon.2022.11.085.
- Park, S., Kim, Y.-M., Lee, P.-Y. and Kim, J. (2018). A study on application of the Lithium-ion battery for coping with extended station blackout. *53rd International Universities Power Engineering Conference (UPEC)*, 1 – 5. DOI: 10.1109/UPEC.2018.8541963.
- Park, M., Zhang, X., Chung, M., Less, G. B. and Sastry, A. M. (2010). A review of conduction phenomena in Li-ion batteries. *Journal of Power Sources* 195, 7904 – 7929. DOI: 10.1016/j.jpowsour.2010.06.060.
- Pawar, R. S., Upadhaya, P. G., Patravale, V. B. (2018). Chapter 34 - Quantum Dots: Novel Realm in Biomedical and Pharmaceutical Industry. In: Hussain, C. M. (eds), *Micro and*

Nano Technologies, Handbook of Nanomaterials for Industrial Applications, pp. 621 - 637. Elsevier. ISBN 9780128133514. DOI:10.1016/B978-0-12-813351-4.00035-3.

Pei, Z., Li, Z. and Zheng, X. (2016). Porous Materials for Lithium-Ion Batteries. *Journal of Nanoscience and Nanotechnology*, 16, 9028 – 9049. DOI: 10.1166/jnn.2016.12907.

Perednis, D., Wilhelm, O., Pratsinis, S. E. and Gauckler, L. J. (2005). Morphology and deposition of thin yttria-stabilized zirconia films using spray pyrolysis. *Thin Solid Films* 474, 84 - 95. DOI: 10.1016/j.tsf.2004.08.014.

Perkins, D. (2022). Diffraction and Mineral Analysis. "Mineralogy". Open Educational Resources. Digital Publisher University of North Dakota. Retrieved April 6, 2023, from [https://geo.libretexts.org/Bookshelves/Geology/Mineralogy_\(Perkins_et_al.\)/12%3A_X-ray_Diffraction_and_Mineral_Analysis](https://geo.libretexts.org/Bookshelves/Geology/Mineralogy_(Perkins_et_al.)/12%3A_X-ray_Diffraction_and_Mineral_Analysis).

Phuc, N. H. H., Morikawa, K., Mitsuhiro, T., Muto, H. and Matsuda, A. (2017). Synthesis of plate-like Li₃PS₄ solid electrolyte via liquid-phase shaking for all-solid-state lithium batteries. *Ionics* 23, 2061 – 2067. DOI: 10.1007/s11581-017-2035-8.

Poizot, P. and Dolhem, F. (2011). Clean energy new deal for a sustainable world: from non-CO₂ generating energy sources to greener electrochemical storage devices. *Energy Environ. Sci.*, 4, 2003 - 2009. DOI: 10.1039/C0EE00731E.

Prabakaran, S. and Rajan, M. (2021). Chapter One - Biosynthesis of nanoparticles and their roles in numerous areas. In: Verma, S. K. and Das, A. K. (eds) *Comprehensive Analytical Chemistry*, pp. 1 - 47. Elsevier 94. ISBN 9780323898812. DOI: 10.1016/bs.coac.2021.02.001.

Qi, B., Ren, K., Lin, Y., Zhang, S., Wei, T. and Fan, Z. (2022). Design of layered-stacking graphene assemblies as advanced electrodes for supercapacitors. *Particuology* 60, 1 - 13. DOI: 10.1016/j.partic.2021.03.001.

Qin, Z., Xie, Y., Meng, X., Qian, D., Mao, D., Ma, X., Shan, C., Chen, J., Wan, L. and Huang, Y. (2022). Recycling garnet-type electrolyte toward superior cycling performance for solid-state lithium batteries. *Energy Storage Materials*, 49, 360-369. DOI: 10.1016/j.ensm.2022.04.024.

Raccichini, R., Amores, M. and Hinds, G. (2019). Critical review of the use of reference electrodes in Li-ion batteries: a diagnostic perspective. *Batteries*, 5, 1, 12. DOI: 10.3390/batteries5010012.

Rahmanpour, M. and Ebrahimi, R. (2017). Numerical Simulation of Highly Charged Droplets Dynamics with Primary Break-up in Electrospray at Sub Rayleigh Limit. *Journal of Applied Fluid Mechanics* 10, 2, 541 - 550. DOI: 10.18869/ACADPUB.JAFM.73.239.26186.

Raijmakers, L. H. J., Danilov, D. L., Eichel, R. A. and Notten, P. H. L. (2019). A review on various temperature-indication methods for Li-ion batteries. *Applied Energy* 240, 918 - 945. DOI: 10.1016/j.apenergy.2019.02.078.

Rajak, J. (2021). A Preliminary Review on Impact of Climate change and our Environment with Reference to Global Warming. *International Journal of Environmental Sciences* 10, 1, 11 - 14. ISSN: 2277-1948 (CIF: 3.654).

Rangasamy, V. S., Thayumanasundaram, S. and Locquet, J. P. (2019). Solid polymer electrolytes with poly(vinyl alcohol) and piperidinium based ionic liquid for Li-ion batteries. *Solid State Ionics* 333, 76 – 82. DOI: 10.1016/j.ssi.2019.01.024.

Ramasubramanian, B., Sundarrajan, S., Chellappan, V., Reddy, M. V., Ramakrishna, S. and Zaghbi, K. (2022). Recent Development in Carbon-LiFePO₄ Cathodes for Lithium-Ion Batteries: A Mini Review. *Batteries* 8, 10, 133. DOI: 10.3390/batteries8100133.

Reddy, R. C. K., Lin, J., Chen, Y., Zeng, C., Lin, X., Cai, Y. and Su, C. Y. (2020). Progress of nanostructured metal oxides derived from metal–organic frameworks as anode materials

for lithium-ion batteries. *Coordination Chemistry Reviews* 420, 213434. DOI: 10.1016/j.ccr.2020.213434.

Ren, A., Wang, H., Zhang, W., Wu, J., Wang, Z., Penty, R. V. and White, I. H. (2021). Emerging light-emitting diodes for next-generation data communications. *Nature Electronics* 4, 8, 559 - 572. DOI: 10.1038/s41928-021-00624-7.

REN21, Renewables 2020 Global Status Report. (2020). Retrieved September 30, 2022, from https://www.globalwomennet.org/wpcontent/uploads/2020/06/GSR2020_Full_Report_with_Endnotes.pdf.

Richards, W. D., Miara, L. J., Wang, Y., Kim, J. C. and Ceder, G. (2016). Interface Stability in Solid-State Batteries. *Chemistry of Materials* 28, 1, 266 - 273. DOI: 10.1021/acs.chemmater.5b04082.

Rosell-Llompart, J., Grifoll, J. and Loscertales, I. G. (2018). Electrosprays in the cone-jet mode: From Taylor cone formation to spray development. *Journal of Aerosol Science* 125, 2 – 31. DOI: 10.1016/j.jaerosci.2018.04.008.

Rosell-Llompart, J. and Fernández de la Mora, J. (1994). Generation of monodisperse droplets 0.3 to 4 μm in diameter from electrified cone-jets of highly conducting and viscous liquids. *Journal of Aerosol Science* 25, 6, 1093 - 1119, DOI: 10.1016/0021-8502(94)90204-6.

Rosero-Navarro, N.C., Miura, A. and Tadanaga, K. (2019). Preparation of lithium ion conductive $\text{Li}_6\text{PS}_5\text{Cl}$ solid electrolyte from solution for the fabrication of composite cathode of all-solid-state lithium battery. *J Sol-Gel Sci Technology* 89, 303 – 309. DOI: 10.1007/s10971-018-4775-y.

Rosero-Navarro, N. C., Miura, A. and Tadanaga, K. (2018). Composite cathode prepared by argyrodite precursor solution assisted by dispersant agents for bulk-type all-solid-state batteries. *Journal of power sources* 396, 33 - 40. DOI: 10.1016/j.jpowsour.2018.06.011.

Rydz, J., Šišková, A. and Eckstein, A. A. (2019). Scanning Electron Microscopy and Atomic Force Microscopy: Topographic and Dynamical Surface Studies of Blends, Composites, and Hybrid Functional Materials for Sustainable Future. *Advances in Materials Science and Engineering*, 6871785. DOI: 10.1155/2019/6871785.

Sacchi, R., Bauer, C., Cox, B. and Mutel, C. (2022). When, where and how can the electrification of passenger cars reduce greenhouse gas emissions? *Renewable and Sustainable Energy Reviews* 162, 112475. DOI: 10.1016/j.rser.2022.112475.

Saeed, M., Alshammari, Y., Majeed, S. A. and Al-Nasrallah, E. (2020). Chemical vapour deposition of graphene - Synthesis, characterisation, and applications: A review. *Molecules*, 25, 17, 3856. DOI: 10.3390/molecules25173856.

Sakuda, A. (2018). Favorable composite electrodes for all-solid-state batteries. *Journal of the Ceramic Society of Japan* 126, 9, 675 - 683. DOI: 10.2109/jcersj2.18114.

Salami, T. J., Imanieh, S. H., Lawrence, J. G. and Martin, I. R. (2019). Amorphous glass-perovskite composite as solid electrolyte for lithium-ion battery. *Materials Letters* 254, 294 - 296. DOI: 10.1016/j.matlet.2019.07.084.

Saleh, M., Milovanoff, A., Posen, I. D., MacLean, H. L. and Hatzopoulou, M. (2022). Energy and greenhouse gas implications of shared automated electric vehicles. *Transportation Research Part D: Transport and Environment* 105, 103233. DOI: 10.1016/j.trd.2022.103233.

Saxena, S., Kong, L. and Pecht, M. G. (2018). Exploding E-Cigarettes: A Battery Safety Issue. *IEEE Access* 6, 21442 – 21466. DOI: 10.1109/ACCESS.2018.2821142.

Scheideler, W. J. and Chen, C. (2014). The minimum flow rate scaling of Taylor cone-jets issued from a nozzle. *Applied Physics Letters* 104, 024103. DOI: 10.1063/1.4862263.

Schwietert, T. K., Arszewska, V. A., Wang, C., Yu, C., Vasileiadis, A., de Klerk, N. J. J., Hageman, J., Hupfer, T., Kerkamm, I., Xu, Y., van der Maas, E., Kelder, E. M., Ganapathy, S. and Wagemaker, M. (2020). Clarifying the relationship between redox activity and electrochemical stability in solid electrolytes. *Nat. Mater.* 19, 428 – 435. DOI: 10.1038/s41563-019-0576-0.

Sehrawat, P., Julien, C. and Islam, S. S. (2016). Carbon nanotubes in Li-ion batteries: A review. *Materials Science and Engineering: B*, 213, 12 – 40. DOI: 10.1016/j.mseb.2016.06.013.

Seidlmayer, S., Buchberger, I., Reiner, M., Gigl, T., Gilles, R., Gasteiger, H. A. and Hugenschmidt, C. (2016). First-cycle defect evolution of $\text{Li}_{1-x}\text{Ni}_{1/3}\text{Mn}_{1/3}\text{Co}_{1/3}\text{O}_2$ lithium ion battery electrodes investigated by positron annihilation spectroscopy. *Journal of Power Sources* 336, 224 - 230. DOI: 10.1016/j.jpowsour.2016.10.050.

Shah, F. A., Ruscsák, K. and Palmquist, A. (2019). 50 years of scanning electron microscopy of bone - a comprehensive overview of the important discoveries made and insights gained into bone material properties in health, disease, and taphonomy. *Bone Res* 7, 15. DOI: 10.1038/s41413-019-0053-z.

Shi, Q., Zhou, J., Ullah, S., Yang, X., Tokarska, K., Trzebicka, B., Ta, H. Q., Rummeli, M. H. (2021). A review of recent developments in Si/C composite materials for Li-ion batteries. *Energy Storage Materials* 34, 735 – 754. DOI: 10.1016/j.ensm.2020.10.026.

Shui, J. L., Jiang, G. S., Xie, S. and Chen, C. H. (2004). Thin films of lithium manganese oxide spinel as cathode materials for secondary lithium batteries. *Electrochimica Acta* 49, 2209 – 2213. DOI: 10.1016/j.electacta.2004.01.002.

Sharma, S., Jain, K. K. and Sharma, A. (2015). Solar cells: in research and applications - a review. *Materials Sciences and Applications* 6, 12, 1145. DOI: 10.4236/msa.2015.612113.

Sharma, R., Bisen, D. P. Shukla, U. and Sharma, B. G. (2012). X-ray diffraction: a powerful method of characterizing nanomaterials. *Recent Research in Science and Technology* 4, 8, 77 - 79. Retrieved October 8, 2022, from <https://updatepublishing.com/journal/index.php/rrst/article/view/933>.

Shen, W. Q., Zhu, Y. W. and Wang, G. L. (2015). Luminescent properties of $\text{Sr}_4\text{Si}_3\text{O}_8\text{Cl}_4:\text{Eu}^{2+}, \text{Bi}^{3+}$ phosphors for near UV InGaN-based light-emitting-diodes. *Applied Science* 5, 1494 – 1502. DOI: 10.3390/app5041494.

Siller, V., Gonzalez-Rosillo, J. C., Eroles, M. N., Baiutti, F., Liedke, M. O., Butterling, M., Attallah, A. G., Hirschmann, E., Wagner, A., Morata, A. and Tarancón, A. (2022). Nanoscaled LiMn_2O_4 for Extended Cycling Stability in the 3 V Plateau. *ACS Applied Materials & Interfaces* 14, 29, 33438 - 33446. DOI: 10.1021/acsami.2c10798.

Da Silva, S. P., Silva, P. R. C. and Scarminio, A. U. J. (2016). Analysis of A Commercial Portable Lithium-Ion Battery Under Low Current Charge-Discharge Cycles. *Quim. Nova* 39, 8, 901 – 905. DOI: 10.5935/0100-4042.20160109.

Simon, P. and Gogotsi, Y. (2020). Perspectives for electrochemical capacitors and related devices. *Nat. Mater.* 19, 1151 – 1163. DOI: 10.1038/s41563-020-0747-z.

Soeder, D. J. (2021). Fossil Fuels and Climate Change. In: *Fracking and the Environment*. Springer international publishing. DOI: 10.1007/978-3-030-59121-2_9.

Song, J., Lee, H., Jeong, E. G., Choi, K. C. and Yoo, S. (2020). Organic light-emitting diodes: pushing toward the limits and beyond. *Advanced Materials* 32, 35, 1907539. DOI:10.1002/adma.201907539.

Song, J., Zhou, M., Yi, R., Xu, T., Gordin, M. L., Tang, D., Yu, Z., Regula, M. and Wang, D. (2014). Interpenetrated Gel Polymer Binder for High-Performance Silicon Anodes in

Lithium-ion Batteries. *Advanced Functional Materials* 24, 37, 5904 – 5910. DOI: 10.1002/adfm.201401269.

Stephan, A. K. (2020). A pathway to understand NMC cathodes. *Joule* 4, 8, 1632 - 1633. DOI: 10.1016/j.joule.2020.08.004.

Strauss, F., Bartsch, T., de Biasi, L., Kim, A. Y., Janek, J., Hartmann, P. and Brezesinski, T. (2018). Impact of cathode material particle size on the capacity of bulk-type all-solid-state batteries. *ACS Energy Letters* 3, 4, 992 - 996. DOI: 10.1021/acseenergylett.8b00275.

Su, J. C. and Huang, S. B. (2020). Package structure of polarized white chip-on-board light-emitting diode with high thermal conductivity. *Optics & Laser Technology* 126, 106065. DOI: 10.1016/j.optlastec.2020.106065.

Sun, L., Yuan, G., Gao, L., Yang, J., Chhowalla, M., Gharahcheshmeh, M. H., Gleason, K. K., Choi, Y. S., Hong, B. H. and Liu, Z. (2021). Chemical vapour deposition. *Nat Rev Methods Primers* 1, 5. DOI: 10.1038/s43586-020-00005-y.

Tamilselvi, S., Gunasundari, S., Karuppiah, N., Razak, R. K. A., Madhusudan, S., Nagarajan, V. M., Sathish, T., Shamim, M. Z. M., Saleel, C. A. and Afzal, A. (2021). A Review on Battery Modelling Techniques. *Sustainability* 13, 18, 10042. DOI: 10.3390/su131810042.

Tang, K. and Gomez, A. (1996). Monodisperse electrosprays of low electric conductivity liquids in the cone-jet mode, *Journal of Colloid and Interface Science* 184, 2, 500 - 511, DOI: 10.1006/jcis.1996.0645.

Tao, B., Ren, C., Li, H., Liu, B., Jia, X., Dong, X., Zhang, S., and Chang, H. (2022). Thio-/LISICON and LGPS-Type Solid Electrolytes for All-Solid-State Lithium-Ion Batteries. *Advanced Functional Materials* 32, 34, 2203551. DOI: 10.1002/adfm.202203551.

Tarek, A. H., Lai, C. W., Razak, B. A. and Wong, Y. H. (2022). Physical Vapour Deposition of Zr-Based Nano Films on Various Substrates: A Review. *Current Nanoscience* 18, 3, 347 - 366. DOI: 10.2174/1573413717666210809105952.

Tatsumisago, M., Nagao, M. and Hayashi, A. (2013). Recent development of sulfide solid electrolytes and interfacial modification for all-solid-state rechargeable lithium batteries. *Journal of Asian Ceramic Societies*, 1, 17 – 25. DOI: 10.1016/j.jascer.2013.03.005.

Taylor, G. I. (1964). Disintegration of Water Drops in An Electric Field. *Proc. R. Soc. A* 280, 383 - 397. DOI: 10.1098/rspa.1964.0151.

Thakur, A. K. and Majumder, M. (2021). Li₆PS₅X (X= Cl, Br, or I): A Family of Li-Rich Inorganic Solid Electrolytes for All-Solid-State Battery. In *Electrode Materials for Energy Storage and Conversion*, pp. 109 - 139. CRC Press.

Theerthagiri, J., Lee, S. J., Shanmugam, P. and Choi, M. Y. (2020). Nanostructured, Functional, and Flexible Materials for Energy Conversion and Storage Systems. In Pandikumar, A. and Rameshkumar, P. (eds), Chapter 1 - Basic principles in energy conversion and storage, pp 1 – 14. Elsevier, ISBN 9780128195529. DOI: 10.1016/B978-0-12-819552-9.00001-4.

Tian, Y., Shi, T., Richards, W. D., Li, J., Kim, J. C., Bo, S. and Ceder, G. (2017). Compatibility issues between electrodes and electrolytes in solid-state batteries. *Energy & Environmental Science. Energy Environ. Sci.* 10, 1150 - 1166. DOI: 10.1039/c7ee00534b.

Tian, R., Liu, H., Jiang, Y., Chen, J., Tan, X., Liu, G., Zhang, L., Gu, X., Guo, Y., Wang, H., Sun, L., and Chu, W. (2015). Drastically Enhanced High-Rate Performance of Carbon-Coated LiFePO₄ Nanorods Using a Green Chemical Vapor Deposition (CVD) Method for Lithium Ion Battery: A Selective Carbon Coating Process. *ACS Applied Materials & Interfaces*, 7, 21, 11377 – 11386. DOI: 10.1021/acsami.5b01891.

Titus, D., Samuel, E. J. J. and Roopan, S. M. (2019). Chapter 12 - Nanoparticle characterization techniques. In: Shukla, A. K. and Iravani, S. (Eds), Green Synthesis, Characterization and Applications of Nanoparticles. Elsevier, pp 303 – 319. DOI: 10.1016/B978-0-08-102579-6.00012-5.

Tomaszewska, A., Chu, Z., Feng, X., O'Kane, S., Liu, X., Chen, J., Ji, C., Endler, E., Li, R., Liu, L., Li, Y., Zheng, S., Vetterlein, S., Gao, M., Du, J., Parkes, M., Ouyang, M., Marinescu, M., Offer, G. and Wu, B. (2019). Lithium-ion battery fast charging: A review, *eTransportation* 1, 100011. DOI: 10.1016/j.etrans.2019.100011.

Tran, M. K., Mevawalla, A., Aziz, A., Panchal, S., Xie, Y. and Fowler, M. (2022). A review of lithium-ion battery thermal runaway modeling and diagnosis approaches. *Processes* 10, 6, 1192. DOI: 10.3390/pr10061192.

Triana, M. A., Camargo, R. J., Wu, S. T., Lanzafame, R.J. and Dong, Y. (2023). Quantum dot materials, devices, and their applications in photomedicine. In: Henini, M., Rodrigues, M. O. (eds), *Quantum Materials, Devices, and Applications*, pp. 155 - 200. Elsevier. ISBN 9780128205662. DOI: 10.1016/B978-0-12-820566-2.00005-3.

Trivedi, S., Lobo, K., and Ramakrishna Matte, H. S. S. (2019). Fundamentals and Sensing Applications of 2D Materials. In: Hywel, M., Rout, C. S. and Late, D. J. (eds), *Chapter 3 - Synthesis, Properties, and Applications of Graphene*, pp 25 - 90. Woodhead Publishing. ISBN 9780081025772. DOI: 10.1016/B978-0-08-102577-2.00003-8.

Tron, A., Hamid, R., Zhang, N., and Beutl, A. (2023). Rational Optimization of Cathode Composites for Sulfide-Based All-Solid-State Batteries. *Nanomaterials* 13, 2, 327. DOI: 10.3390/nano13020327.

Tsukasaki, H., Sano, H., Igarashi, K., Wakui, A., Yaguchi, T. and Mori, S. (2022). Deterioration process of argyrodite solid electrolytes during exposure to humidity-

controlled air. *Journal of Power Sources* 524, 231085. DOI: 10.1016/j.jpowsour.2022.231085.

Ugarte, I., Castell, I., Palomares, E. and Pacios, R. (2012). Quantum Dots as a Light Indicator for Emitting Diodes and Biological Coding. In *Quantum Dots - A Variety of New Applications*. InTech. DOI: 10.5772/34865.

Ul-Hamid, A. (2018). *A beginners' guide to scanning electron microscopy*, Vol. 1, pp. 402. Cham, Switzerland: Springer International Publishing. ISBN: 978-3-030-07498-2. <https://doi.org/10.1007/978-3-319-98482-7>.

Ulissi, U., Agostini, M., Ito, S., Aihara, Y. and Hassoun, J. (2016). All solid-state battery using layered oxide cathode, lithium-carbon composite anode and thio-LISICON electrolyte. *Solid State Ionics* 296, 13 - 17. DOI: 10.1016/j.ssi.2016.08.014.

Umbach, T. E., Röllgen, S., Schneider, S., Klesper, H., Umbach, A. M. and Meerholz, K. (2020). Low-Refractive Index Layers in Organic Light-Emitting Diodes via Electrospray Deposition for Enhanced Outcoupling Efficiencies. *Advanced Engineering Materials* 22, 5, 1900897. DOI: 10.1002/adem.201900897.

UN, United Nations Climate Change. (2019). Strengthening synergies between the Paris agreement on climate change and the 2030 agenda for sustainable development. Retrieved February 12, 2021, from https://sustainabledevelopment.un.org/content/documents/25256WEB_version.pdf.

UN-SDG, United Nations Sustainable Development Goals. (2022). *The SDGs in Action*. Retrieved October 4th, 2022, from <https://www.undp.org/sustainable-development-goals>.

van Zomeren, A. A., Kelder, E. M. Marijnissen, J. C. M. and Schoonman, J. (1994). The Production of Thin Films of LiMn_2O_4 by Electrospraying. *Journal of Aerosol Science* 25, 6, 1229 - 1235. DOI: 10.1016/0021-8502(94)90211-9.

- Vannacci, E., Granchi, S., Calzolari, M. and Biagi, E. (2019). Applications of light emitting diodes as sensors of their own emitted light. *Opto-Electronics Review* 27, 4, 355 - 362. DOI: 10.1016/j.opelre.2019.11.008.
- Varga, A., Brunelli, N. A., Louie, M. W., Giapis, K. P. and Haile, S. M. (2010). Composite nanostructured solid-acid fuel-cell electrodes via electrospray deposition. *Journal of Materials Chemistry* 20, 30, 6309. DOI :10.1039/C0JM00216J.
- Vercoulen, P. H. W. (1995). *Electrostatic Processing of Particles: A tool in particle technology*. PhD Thesis, Delft University of Technology.
- Verdoold, S. Agostinho, L. L. F. Yurteri, C. U. and Marijnissen, J. C. M. (2014). A generic electrospray classification. *Journal of Aerosol Science* 67, 87 - 103. DOI: 10.1016/j.jaerosci.2013.09.008.
- Vernon-Parry, K. D. (2000). Scanning electron microscopy: an introduction. *III-Vs Review* 13, 4, 40 - 44. DOI: 10.1016/S0961-1290(00)80006-X.
- Viswanathan, B. (2017). Chapter 12 – Batteries. In: Viswanathan, B. (eds), *Energy Sources* pp. 263 - 313. Elsevier. ISBN 9780444563538. DOI: 10.1016/B978-0-444-56353-8.00012-5.
- Vladár, A. E. and Hodoroba, V. D. (2020). Characterization of nanoparticles by scanning electron microscopy. In *Characterization of nanoparticles*, pp. 7 - 27. Elsevier. DOI: 10.1016/B978-0-12-814182-3.00002-X.
- Vu, A., Li, X., Phillips, J., Han, A., Smyrl, W. H., Bühlmann, P. and Stein, A. (2013). Three dimensionally ordered mesoporous (3DOM) carbon materials as electrodes for electrochemical double-layer capacitors with ionic liquid electrolytes. *Chemistry of Materials* 25, 21, 4137 - 4148. DOI: 10.1021/cm400915p.

- Wang, J., Xu, Y., Wang, J. and Ding, X. (2023a). New strategy for enhancing the electrochemical performance of LiMn_2O_4 cathode material. *Journal of Alloys and Compounds* 932, 167642. DOI: 10.1016/j.jallcom.2022.167642.
- Wang, C., Liang, J., Kim, J. T. and Sun, X. (2022). Prospects of halide-based all-solid-state batteries: From material design to practical application. *Science Advances* 8, 36. DOI: 10.1126/sciadv.adc9516.
- Wang, S., Fan, Y., Stroe, D. I., Fernandez, C., Yu, C., Cao, W., Chen, Z. (2021a). Chapter 1 - Lithium-ion battery characteristics and applications. In: Wang, S., Fan, Y., Stroe, D. I., Fernandez, C., Yu, C., Cao, W., Chen, Z. (eds), *Battery System Modeling*, pp 1 - 46. Elsevier. ISBN 9780323904728. DOI: 10.1016/B978-0-323-90472-8.00003-2.
- Wang, Q., Liu, B., Shen, Y., Wu, J., Zhao, Z., Zhong, C. and Hu, W. (2021b). Confronting the Challenges in Lithium Anodes for Lithium Metal Batteries. *Advanced Science* 8, 17, 202101111. DOI: 10.1002/advs.202101111.
- Wang, K., Ye, Q., Zhang, J., Huang, H., Gan, Y., He, X. and Zhang, W. (2021c). Halide Electrolyte Li_3InCl_6 -Based All-Solid-State Lithium Batteries with Slurry-Coated $\text{LiNi}_{0.8}\text{Co}_{0.1}\text{Mn}_{0.1}\text{O}_2$ Composite Cathode: Effect of Binders. *Frontiers in Materials* 8, 727617. DOI: 10.3389/fmats.2021.727617.
- Wang, R., Cui, W., Chu, F. and Wu, F. (2020a). Lithium metal anodes: Present and future. *Journal of Energy Chemistry* 48, 145 - 159. DOI: 10.1016/j.jechem.2019.12.024.
- Wang, K., Wan, J., Xiang, Y., Zhu, J., Leng, Q., Wang, M., Xu, L. and Yang, Y. (2020b). Recent advances and historical developments of high voltage lithium cobalt oxide materials for rechargeable Li-ion batteries. *Journal of Power Sources*, 460, 228062. DOI: 10.1016/j.jpowsour.2020.228062.
- Wang, C., Fu, K., Kammampata, S. P., McOwen, D. W., Samson, A. J., Zhang, L., Hitz, G. T., Nolas, A. M., Wachsman, E. D., Mo, Y., Thangadurai, V. and Hu, L. (2020c).

Garnet-type solid-state electrolytes: materials, interfaces, and batteries. *Chemical reviews* 120, 10, 4257 - 4300. DOI: 10.1021/acs.chemrev.9b00427.

Wang, J., Li, C., Chen, D., Sun, C. and Yang, Z. (2020d). Interlayered MoS₂/rGO thin film for efficient lithium storage produced by electrospray deposition and far-infrared reduction. *Applied Surface Science*, 499, 143940. DOI: 10.1016/j.apsusc.2019.143940.

Wang, R., Feng, L., Yang, W., Zhang, Y., Zhang, Y., Bai, W., Liu, B., Zhang, W., Chuan, Y., Zheng, Z. and Guan, H. (2017). Effect of different binders on the electrochemical performance of metal oxide anode for lithium-ion batteries. *Nanoscale research letters*, 12, 1 - 11. DOI: 10.1186/s11671-017-2348-6.

Wang, X. and Yushin, G. (2015). Chemical vapor deposition and atomic layer deposition for advanced lithium ion batteries and supercapacitors. *Energy & Environmental Science*, 8, 7, 1889 – 1904. DOI: 10.1039/C5EE01254F.

Wang, Y., Liu, B., Li, Q., Cartmell, S., Ferrara, S., Deng, Z. D. and Xiao, J. (2015a). Lithium and lithium ion batteries for applications in microelectronic devices: A review. *Journal of Power Sources* 286, 330 - 345. DOI: 10.1016/j.jpowsour.2015.03.164.

Wang, W., Wei, X., Choi, D., Lu, X., Yang, G. and Sun, C. (2015). Chapter 1 - Electrochemical cells for medium- and large-scale energy storage: fundamentals. In: Menictas, C., Skyllas-Kazacos, M., Lim, T. M. (eds), *Energy. Advances in Batteries for Medium and Large-Scale Energy Storage*, pp. 3 - 28. Woodhead Publishing. ISBN 9781782420132. DOI: 10.1016/B978-1-78242-013-2.00001-7.

Wang, S., Li, S., Sun, Y., Feng, X. and Chen, C. (2011). Three-dimensional porous V₂O₅ cathode with ultra high rate capability. *Energy & Environmental Science* 4, 8, 2854 - 2857. DOI: 10.1039/c1ee01172c.

Wang, L., Xu, H. W., Chen, P. C., Zhang, D. W., Ding, C. X. and Chen, C. H. (2009). Electrostatic spray deposition of porous Fe₂O₃ thin films as anode material with improved

electrochemical performance for lithium-ion batteries. *Journal of Power Sources* 193, 846 - 50. DOI: 10.1016/j.jpowsour.2009.03.063.

Wei, J., Kim, H., Lee, D. C., Hu, R., Wu, F., Zhao, H., Alamgir, F. M. and Yushin, G. (2015). Influence of annealing on ionic transfer and storage stability of $\text{Li}_2\text{S-P}_2\text{S}_5$ solid electrolyte. *Journal of Power Sources* 294, 494 - 500. DOI: 10.1016/j.jpowsour.2015.06.074.

Welsby, D., Price, J., Pye, S. and Ekins, P. (2021). Unextractable fossil fuels in a 1.5 °C world. *Nature* 597, 230 – 234. DOI: 10.1038/s41586-021-03821-8.

Wenge, C., Pietracho, R., Balischewski, S., Arendarski, B., Lombardi, P., Komarnicki, P. and Kasprzyk, L. (2020). Multi Usage Applications of Li-Ion Battery Storage in a Large Photovoltaic Plant: A Practical Experience. *Energies*, 13, 4590. DOI: 10.3390/en13184590.

Weppner, W. (2009). Secondary Batteries – Lithium Rechargeable Systems. All Solid-State Battery. (2009). In: Jürgen, G. (eds), pp. 162 – 168. *Encyclopedia of Electrochemical Power Sources*, Elsevier. ISBN 9780444527455. DOI: 10.1016/B978-044452745-5.00210-0.

Williard, N., He, W., Hendricks, C. and Pecht, M. (2013). Lessons Learned from the 787 Dreamliner Issue on Lithium-Ion Battery Reliability. *Energies* 6, 4682 – 4695. DOI: 10.3390/en6094682.

Wu, B., Chen, C., Danilov, D. L., Eichel, R.-A. and Notten, P. H. L. (2023). All-Solid-State Thin Film Li-Ion Batteries: New Challenges, New Materials, and New Designs. *Batteries* 9, 3, 186. DOI: 10.3390/batteries9030186.

Wu, Y., Wang, S., Li, H., Chen, L., and Wu, F. (2021a). Progress in thermal stability of all-solid-state-Li-ion-batteries. *InfoMat* 3, 8, 827 - 853. DOI: 10.1002/inf2.12224.

Wu, J., Shen, L., Zhang, Z., Liu, G., Wang, Z., Zhou, D., Wan, H., Xu, X. and Yao, X. (2021b). All-Solid-State Lithium Batteries with Sulfide Electrolytes and Oxide Cathodes. *Electrochem. Energ. Rev.* 4, 101 - 135 DOI: 10.1007/s41918-020-00081-4.

Wu, F., Yan, Y., Wang, R., Cai, H., Tong, W. and Tang, H. (2017). Synthesis of $\text{LiNi}_{1/3}\text{Mn}_{1/3}\text{Co}_{1/3}\text{O}_2$ @ graphene for lithium-ion batteries via self-assembled polyelectrolyte layers. *Ceramics International* 43, 10, 7668 - 7673. DOI: 10.1016/j.ceramint.2017.03.066.

Xiao, H., Ji, G., Ye, L., Li, Y., Zhang, J., Ming, L., Zhang, B. and Ou, X. (2021). Efficient regeneration and reutilization of degraded graphite as advanced anode for lithium-ion batteries. *Journal of Alloys and Compounds* 888, 161593. DOI: 10.1016/j.jallcom.2021.161593.

Xiao, J., Li, Q., Bi, Y., Cai, M., Dunn, B., Glossmann, T., Liu, J., Osaka, T., Sugiura, R., Wu, B., Yang, J., Zhang J. G. and Whittingham, M. S. (2020a). Understanding and applying coulombic efficiency in lithium metal batteries. *Nature Energy* 5, 8, 561 - 568. DOI: 10.1038/s41560-020-0648-z.

Xiao, Y., Wang, Y., Bo, S.-H., Kim, J. C., Miara, L. J. and Ceder, G. (2019a). Understanding interface stability in solid-state batteries. *Nature Reviews Materials*, 5(2), 105–126. <https://doi.org/10.1038/s41578-019-0157-5>.

Xiao, W., Wang, J., Fan, L., Zhang, J. and Li, X. (2019b). Recent advances in $\text{Li}_{1+x}\text{Al}_x\text{Ti}_{2-x}(\text{PO}_4)_3$ solid-state electrolyte for safe lithium batteries. *Energy Storage Materials* 19, 379 - 400. DOI: 10.1016/j.ensm.2018.10.012.

Xie, J., Oudenhoven, J. F. M., Harks, P.-P. R. M. L., Li, D. and Notten, P. H. L. (2015). Chemical Vapor Deposition of Lithium Phosphate Thin-Films for 3D All-Solid-State Li-Ion Batteries. *Journal of The Electrochemical Society*, 162(3), A249–A254. DOI: 10.1149/2.0091503jes.

Xu, L., Li, J., Shuai, H., Luo, Z., Wang, B., Fang, S., Zou, G., Hou, H., Peng, H and Ji, X. (2022). Recent advances of composite electrolytes for solid-state Li batteries. *Journal of Energy Chemistry* 67, 524 - 548. DOI: 10.1016/j.jechem.2021.10.038.

Xu, B., Lee, J., Kwon, D., Kong, L. and Pecht, M. (2021a). Mitigation strategies for Li-ion battery thermal runaway: A review. *Renewable and Sustainable Energy Reviews* 150, 111437. DOI: 10.1016/j.rser.2021.111437.

Xu, S., Cheng, N., Yin, H., Cao, D. and Mi, B. (2020a). Electrospray preparation of CuInS₂ films as efficient counter electrode for dye-sensitized solar cells. *Chemical Engineering Journal*, 397, 125463. DOI: 10.1016/j.cej.2020.125463.

Xu, J., Wu, L., Liu, Y., Zhang, J., Liu, J., Shu, S., Kang, X., Song, Q., Liu, D., Huang, F. and Hu, Y. (2020b). NiO - rGO composite for supercapacitor electrode. *Surfaces and Interfaces* 18, 100420. DOI: 10.1016/j.surfin.2019.100420.

Xu, H., Wang, X., Li, Y., Cai, L., Tan, Y., Zhang, G., Wang, Y., Li, R., Liang, D., Song, T. and Sun, B. (2020c). Prominent heat dissipation in perovskite light-emitting diodes with reduced efficiency droop for silicon-based display. *The Journal of Physical Chemistry Letters* 11, 9, 3689 - 3698. DOI: 10.1021/acs.jpcclett.0c00792.

Yan, S., Yim, C. H., Pankov, V., Bauer, M., Baranova, E., Weck, A., Merati, A. and Abu-Lebdeh, Y. (2021). Perovskite solid-state electrolytes for lithium metal batteries. *Batteries* 7, 4, 75. DOI: 10.3390/batteries7040075.

Yan, B., Li, X., Fu, X., Zhang, L., Bai, Z. and Yang, X. (2020). An elaborate insight of lithiation behavior of V₂O₅ anode. *Nano Energy* 78, 105233. DOI: 10.1016/j.nanoen.2020.105233.

Yang, X., Wang, H., Song, Y., Liu, K., Huang, T., Wang, X., Zhang, C. and Li, J. (2022a). Low-temperature synthesis of a porous high-entropy transition-metal oxide as an anode for

high-performance lithium-ion batteries. *ACS Applied Materials & Interfaces*, 14, 23, 26873 - 26881. DOI: 10.1021/acsami.2c07576.

Yang, K., Chen, L., Ma, J., He, Y. B. and Kang, F. (2021). Progress and perspective of $\text{Li}_{1+x}\text{Al}_x\text{Ti}_{2-x}(\text{PO}_4)_3$ ceramic electrolyte in lithium batteries. *InfoMat* 3, 11, 1195 - 1217. DOI: 10.1002/inf2.12222.

Yang, F., Wang, D., Zhao, Y., Tsui, K. L. and Bae, S. J. (2018). A study of the relationship between coulombic efficiency and capacity degradation of commercial lithium-ion batteries. *Energy*, 145, 486 - 495. DOI: 10.1016/j.energy.2017.12.144.

Yao, J., Li, Y., Massé, R. C., Uchaker, E. and Cao, G. (2018). Revitalized interest in vanadium pentoxide as cathode material for lithium-ion batteries and beyond. *Energy Storage Materials*, 11, 205-259. DOI: 10.1016/j.ensm.2017.10.014.

Yoo, H. D., Markevich, E., Salitra, G., Sharon, D. and Aurbach, D. (2014). On the challenge of developing advanced technologies for electrochemical energy storage and conversion. *Materials Today* 17, 3. DOI: 10.1016/j.mattod.2014.02.014.

Yoon, C. S., Kim, U. H., Park, G. T., Kim, S. J., Kim, K. H., Kim, J. and Sun, Y. K. (2018a). Self-passivation of a LiNiO_2 cathode for a lithium-ion battery through Zr doping. *ACS Energy Letters* 3, 7, 1634 - 1639. DOI: 10.1021/acsenergylett.8b00805.

Yoon, K., Kim, J. J., Seong, W. M., Lee, M. H. and Kang, K. (2018b). Investigation on the interface between $\text{Li}_{10}\text{GeP}_2\text{S}_{12}$ electrolyte and carbon conductive agents in all-solid-state lithium battery. *Sci Rep* 8, 8066. DOI: 10.1038/s41598-018-26101-4.

Yoon, H., Mali, M. G., Kim, M., Al-Deyab, S. S. and Yoon, S. S. (2016). Electrostatic spray deposition of transparent tungsten oxide thin-film photoanodes for solar water splitting. *Catalysis Today* 260, 89 - 94. DOI: 10.1016/j.cattod.2015.03.037.

Yoon, W., Chung, K., Oh, K. and Kim, K. (2003). Changes in electronic structure of the electrochemically Li-ion deintercalated LiMn_2O_4 system investigated by soft X-ray

absorption spectroscopy. *Journal of Power Sources* 119 – 121, 706 – 709. DOI: 10.1016/S0378-7753(03)00221-0.

Yoshino, A. (2012). The Birth of the Lithium-Ion Battery. *Angewandte Chemie International Edition* 51, 24, 5798 – 5800. DOI: 10.1002/anie.201105006.

Yu, C., Zhao, F., Luo, J., Zhang, L. and Sun, X. (2021). Recent development of lithium argyrodite solid-state electrolytes for solid-state batteries: synthesis, structure, stability and dynamics. *Nano Energy* 83, 105858. DOI: 10.1016/j.nanoen.2021.105858.

Yu, C., Li, Y., Willans, M., Zhao, Y., Adair, K. R., Zhao, F., Li, W., Deng, S., Liang, J., Banis, M. N., Li, R., Huang, H., Zhang, L., Yang, R., Lu, S., Huang, Y. and Sun, X. (2020). Superionic conductivity in lithium argyrodite solid-state electrolyte by controlled Cl-doping. *Nano Energy* 69, 104396. DOI: 10.1016/j.nanoen.2019.104396.

Yu, Q., Xiong, R., Lin, C., Shen, W. and Deng, J. (2017). "Lithium-Ion Battery Parameters and State-of-Charge Joint Estimation Based on H-Infinity and Unscented Kalman Filters," *IEEE Transactions on Vehicular Technology* 66, 10, 8693 – 8701. DOI: 10.1109/TVT.2017.2709326.

Yu, Y., Shi, Y. and Chen, C. (2006a). Effect of Lithia and Substrate on the Electrochemical Performance of a Lithia/Cobalt Oxide Composite Thin-Film Anode. *Chem. AsianJ.* 1 826 - 831. DOI: 10.1002/asia.200600157.

Yu, Y., Shui, J. L. Jin, Y. and Chen, C. H. (2006b). Electrochemical performance of nano-SiO₂ modified LiCoO₂ thin films fabricated by electrostatic spray deposition (ESD). *Electrochimica Acta* 51: 3292 - 3296. DOI: 10.1016/j.electacta.2005.09.021.

Yuan, J., Chen, C., Hao, Y., Zhang, X., Agrawal, R., Wang, C., Li, X., Hao, Y., Liu, B., Li, Q. and Xie, Y. (2017a). Three-dimensionally porous CoMn₂O₄ thin films grown on Ni foams for high-performance lithium-ion battery anodes. *Journal of Materials Science* 52, 5751 - 5758. DOI: 10.1007/s10853-017-0810-6.

Yuan, T., Y. Jiang, Q. Wang, B. Pan, and M. Yan. (2017b). Pseudocapacitance-Enhanced High-Rate Lithium Storage in “Honeycomb”-like Mn_2O_3 Anodes. *ChemElectroChem* 4, 3, 565 - 569. DOI: 10.1002/celec.201600588.

Yuan, J., Zhang, X., Chen, C., Hao, Y., Agrawal, R., Wang, C., Li, W., Yu, H., Yua, Y., Zhu, X., Xiong, Z. and Xie, Y. (2017c). Facile fabrication of three-dimensional porous ZnO thin films on Ni foams for lithium ion battery anodes. *Materials Letters*, 190, 37-39. DOI: 10.1016/j.matlet.2016.12.126.

Yubuchi, S., Uematsu, M., Deguchi, M., Hayashi, A. and Tatsumisago, M. (2018). Lithium-ion-conducting argyrodite-type $\text{Li}_6\text{PS}_5\text{X}$ ($\text{X} = \text{Cl}, \text{Br}, \text{I}$) solid electrolytes prepared by a liquid-phase technique using ethanol as a solvent. *ACS Applied Energy Materials* 1, 8, 3622 - 3629. DOI: 10.1021/acsaem.8b00280.

Yurteri, C. U. Hartman, R. P. A. and Marijnissen, J. C. M. (2010). Producing Pharmaceutical Particles via Electrospraying with an emphasis on Nano and Nano structured Particles - A Review. *KONA Powder and Particle Journal* 28, 91 – 115. DOI: 10.14356/kona.2010010.

Zeng, Z., Cheng, J., Li, Y., Zhang, H., Li, D., Liu, H., Ji, F., Sun, Q. and Ci, L. (2023). Composite cathode for all-solid-state lithium batteries: progress and perspective. *Materials Today Physics*, 101009. DOI: 10.1016/j.mtphys.2023.101009.

Zhang, W., Zhang, X., Cheng, F., Wang, M., Wan, J., Li, Y., Xu, J., Liu, Y., Sun, S., Xu, Y., Fang, C., Li, Q., Han, J. and Huang, Y. (2023a). Enabling stable 4.6 V LiCoO_2 cathode through oxygen charge regulation strategy. *Journal of Energy Chemistry*, 76, 557 - 565. DOI: 10.1016/j.jechem.2022.09.034.

Zhang, Y., Ding, P., Wu, W., Kimura, H., Shen, Y., Wu, D., Xie, X., Hou, C., Sun, X., Yang, X. Y. and Du, W. (2023b). Facile synthesis of reduced graphene oxide @ Co_3O_4 composites derived from assisted liquid-phase plasma electrolysis for high-performance

hybrid supercapacitors. *Applied Surface Science* 609, 155188. DOI: 10.1016/j.apsusc.2022.155188.

Zhang, S. D., Qi, M. Y., Guo, S. J., Sun, Y. G., Tan, X. X., Ma, P. Z., Li, J. Y., Yuan, R. Z., Cao, A. M. and Wan, L. J. (2022). Advancing to 4.6 V Review and Prospect in Developing High – Energy - Density LiCoO₂ Cathode for Lithium-Ion Batteries. *Small Methods* 6, 5, 2200148. DOI: 10.1002/smt.202200148.

Zhang, H., Yang, Y., Ren, D., Wang, L. and He, X. (2021a). Graphite as anode materials: Fundamental mechanism, recent progress and advances. *Energy Storage Materials* 36, 147 – 170. DOI: 10.1016/j.ensm.2020.12.027.

Zhang, X., Sun, X., Li, X., Hu, X., Cai, S. and Zheng, C. (2021b). Recent progress in rate and cycling performance modifications of vanadium oxides cathode for lithium-ion batteries. *Journal of Energy Chemistry* 59, 343 - 363. DOI: 10.1016/j.jechem.2020.11.022.

Zhang, X., Yang, Y. and Zhou, Z. (2020a). Towards practical lithium-metal anodes. *Chemical Society Reviews* 49, 10, 3040 - 3071. DOI: 10.1039/C9CS00838A.

Zhang, J., Li, L., Zheng, C., Xia, Y., Gan, Y., Huang, H., Liang, C., He, X., Tao, X. and Zhang, W. (2020b). Silicon-doped argyrodite solid electrolyte Li₆PS₅I with improved ionic conductivity and interfacial compatibility for high-performance all-solid-state lithium batteries. *ACS Applied Materials & Interfaces* 12, 37, 41538 - 41545. DOI: 10.1021/acsami.0c11683.

Zhang, J., Zheng, C., Li, L., Xia, Y., Huang, H., Gan, Y., Liang, C., He, X., Tao, X. and Zhang, W. (2020c). Unraveling the intra and intercycle interfacial evolution of Li₆PS₅Cl-based all-solid-state lithium batteries. *Advanced energy materials*, 10, 4, 1903311. DOI: 10.1002/aenm.201903311.

- Zhang, B., Yang, L., Wang, L. W. and Pan, F. (2019). Cooperative transport enabling fast Li-ion diffusion in Thio-LISICON $\text{Li}_{10}\text{SiP}_2\text{S}_{12}$ solid electrolyte. *Nano Energy* 62, 844 - 852. DOI: 10.1016/j.nanoen.2019.05.085.
- Zhang, W., Leichtweiß, T., Culver, S. P., Koerver, R., Das, D., Weber, D. A., Zeier, W. G. and Janek, J. (2017). The detrimental effects of carbon additives in $\text{Li}_{10}\text{GeP}_2\text{S}_{12}$ -based solid-state batteries. *ACS applied materials & interfaces* 9, 41, 35888 - 35896. DOI: 10.1021/acsami.7b11530.
- Zhang, Q., Sando, D., and Nagarajan, V. (2016). Chemical route derived bismuth ferrite thin films and nanomaterials. *Journal of Materials Chemistry C*, 4, 19, 4092 – 4124. DOI: 10.1039/C6TC00243A.
- Zhang, Y., Chen, F., Tu, R., Shen, Q. and Zhang, L. (2014). Field assisted sintering of dense Al-substituted cubic phase $\text{Li}_7\text{La}_3\text{Zr}_2\text{O}_{12}$ solid electrolytes. *Journal of Power Sources* 268, 960 - 964. DOI: 10.1016/j.jpowsour.2014.03.148.
- Zhang, P., Guo, Z. P., Kang, S. G., Choi, Y. J., Kim, C. J., Kim, K. W. and Liu, H. K. (2009). Three dimensional $\text{Li}_2\text{O-NiO-CoO}$ composite thin-film anode with network structure for lithium ion batteries. *Journal of Power Sources* 189, 566 – 570. DOI: 10.1016/j.jpowsour.2008.10.107.
- Zhao, L., Ding, B., Qin, X. Y., Wang, Z., Lv, W., He, Y. B., Yang, Q. H. and Kang, F. (2022a). Revisiting the Roles of Natural Graphite in Ongoing Lithium-Ion Batteries. *Advanced Materials* 34, 18, 2106704. DOI: 10.1002/adma.202106704.
- Zhao, Q. F., Zhang, S. Q., Hu, M. Y., Wang, C. and Jiang, G. H. (2021). Recent Advances in LiFePO_4 Cathode Materials for Lithium-Ion Batteries. *First-Principles Research. Int. J. Electrochem. Sci.* 16, 211226, 2. DOI: 10.20964/2021.12.11.
- Zhao, X. and Deng, W. (2020). Printing photovoltaics by electrospray. *Opto-Electronic Advances* 3, 6, 190038 - 1. DOI: 10.29026/oea.2020.190038.

Zhao, W., Yi, J., He, P. and Zhou, H. (2019a). Solid-state electrolytes for lithium-ion batteries: fundamentals, challenges and perspectives. *Electrochemical Energy Reviews* 2, 574 - 605. DOI: 10.1007/s41918-019-00048-0.

Zhao, Y., Yan, J., Cai, W., Lai, Y., Song, J., Yu, J. and Ding, B. (2019b). Elastic and well-aligned ceramic LLZO nanofiber based electrolytes for solid-state lithium batteries. *Energy Storage Materials* 23, 306 - 313. DOI: 10.1016/j.ensm.2019.04.043.

Zheng, Z., Ye, H. and Guo, Z. (2020). Recent Progress in Designing Stable Composite Lithium Anodes with Improved Wettability. *Advanced Science* 7, 22, 2002212. DOI: 10.1002/advs.202002212.

Zheng, F., Kotobuki, M., Song, S., Lai, M. O. and Lu, L. (2018). Review on solid electrolytes for all-solid-state lithium-ion batteries. *Journal of Power Sources* 389, 198 - 213. DOI: 10.1016/j.jpowsour.2018.04.022.

Zheng, J., Dang, H., Feng, X., Chien, P. H. and Hu, Y. Y. (2017a). Li-ion transport in a representative ceramic–polymer–plasticizer composite electrolyte: $\text{Li}_7\text{La}_3\text{Zr}_2\text{O}_{12}$ – polyethylene oxide–tetraethylene glycol dimethyl ether. *Journal of Materials Chemistry A*, 5, 18457. DOI: 10.1039/c7ta05832b.

Zheng, J., Yan, P., Zhang, J., Engelhard, M. H., Zhu, Z., Polzin, B. J., Trask, S., Xiao, J., Wang, C. and Zhang, J. G. (2017b). Suppressed oxygen extraction and degradation of $\text{LiNi}_x\text{Mn}_y\text{Co}_z\text{O}_2$ cathodes at high charge cut-off voltages. *Nano Research* 10, 4221 – 4231. DOI:10.1007/s12274-017-1761-6.

Zhou, Y., Yang, Y., Hou, G., Yi, D., Zhou, B., Chen, S., Lam, T. D., Yuan, F., Golberg, D. and Wang, X. (2020). Stress-relieving defects enable ultra-stable silicon anode for Li-ion storage. *Nano Energy* 70, 104568. DOI: 10.1016/j.nanoen.2020.104568.

- Zhou, H., Xin, F., Pei, B. and Whittingham, M. S. (2019). What Limits the Capacity of Layered Oxide Cathodes in Lithium Batteries? *ACS Energy Letters* 4, 8, 1902 – 1906. DOI: 10.1021/acseenergylett.9b01236.
- Zhu, C., Kopold, P., Li, W., van Aken, P. A. Maier, J. and Yu, Y. (2015a). Engineering nanostructured electrode materials for high performance sodium ion batteries: a case study of a 3D porous interconnected WS₂/C nanocomposite. *Journal of Materials Chemistry A* 3, 20487. DOI: 10.1039/C5TA05758B.
- Zia, R., Iftikhar, M., Rafiq, A., Hakim, S., Nawaz, M. S., Imran, A., Bajwa, S. Z. (2022). Nanosensors for microbial detection in soil. In: Denizli, A., Nguyen, T. A., Rajendran, S., Yasin, G., Nadda, A. K. (eds), *Micro and Nano Technologies, Nanosensors for Smart Agriculture*, pp. 367 – 400. Elsevier. ISBN 9780128245545. DOI:10.1016/B978-0-12-824554-5.00003-3.
- Zou, F., Nallan, H. C., Dolocan, A., Xie, Q., Li, J., Coffey, B. M., Ekerdt, J. G. and Manthiram, A. (2021). Long-life LiNi_{0.5}Mn_{1.5}O₄/graphite lithium-ion cells with an artificial graphite-electrolyte interface. *Energy Storage Materials* 43, 499 – 508. DOI: 10.1016/j.ensm.2021.09.033.
- Zuo, T. T., Rueß, R., Pan, R., Pan, R., Walther, F., Rohnke, M., Hori, S., Kanno, R., Schröder, D. and Janek, J. (2021). A mechanistic investigation of the Li₁₀GeP₂S₁₂|LiNi_{1-x-y}CoxMnyO₂ interface stability in all-solid-state lithium batteries. *Nat Commun* 12, 6669. DOI: 10.1038/s41467-021-26895-4.
- Zuo, X., Zhu, J., Müller-Buschbaum, P. and Cheng. Y. J. (2017). Silicon based lithium-ion battery anodes: a chronicle perspective review. *Nano Energy* 31, 113 – 143. DOI: 10.1016/j.nanoen.2016.11.013.



EDHA for energy production, storage and conversion devices

E.M. Kelder^{a,*}, J.C.M. Marijnissen^b, S. Waiyego Karuga^b

^a Delft University of Technology, Faculty of Applied Sciences, Department of Radiation Science and Technology, Mekelweg 15, 2629 BJ Delft, The Netherlands

^b University of Nairobi, Nuclear Science and Technology, University Way, Nairobi, Kenya



ARTICLE INFO

Keywords:

EHDA
Electrospraying
ESD
Li-ion batteries, Solar cells
(O)LEDs

ABSTRACT

Electrohydrodynamic atomization (EHDA) or electrospraying stands out in thin film deposition because of its unique ability to form charged droplets, initiating higher deposition efficiencies in electrostatic spray deposition. Considering that the quality of a thin film depends on the particle sizes, their monodispersity and uniform distribution on the surface, electrospray is a powerful tool in materials synthesis. Therefore, this review looks at different areas where this novel technique has been used to improve on the overall performance of materials for energy devices, such as solar cells, photoelectrochemical cells, rechargeable batteries and beyond, capacitors, and (O)LEDs, including quantum dots.

1. Introduction

Electrohydrodynamic atomization (EHDA) or electrospraying stands out in thin film deposition because of its unique ability to form charged droplets hence higher deposition efficiency, i.e. electrostatic spray deposition (ESD), which term will be used further throughout this chapter. It involves disintegration of a liquid into airborne droplets by applying an electric field which causes shear stress on the liquid surface leading to elongation of a jet that breaks up into small charged droplets. Due to the mutual Coulomb repulsion among the droplets, there is self-dispersion on the substrate hence no agglomeration resulting in uniform deposition on inhomogeneous surfaces (Lee, Cho, Oh, & Shin, 2007; Yoon, Chung, Oh, & Kim, 2003; Cao & Prakash, 2002; Nishizawa et al., 1998; Chen, Buysman, Kelder, & Schoonman, 1995; van Zomeren et al., 1994). For instance, with an aim of synthesizing Co_3O_4 thin films on a glass substrate, Abbas, Slewa, Khizir, and Kakil (2017) confirmed the effect of an electric field during deposition. From their results, the film deposited with no electric field showed flaws like crystal flakes, pin holes and many cracks on the surface while the film grown under an electric field appeared smoother and more homogeneous with well-formed grains. With these observations,

Abbreviations: AlN, Aluminium Nitride; AN, Acetonitrile; CB, Chlorobenzene; CIGS, Cu-In-Ga-Se; CIGSse, Cu(InGa)(Sse)₂; CIS, Copper Indium Sulfides/Selenides; CNT, Carbon Nanotube; CN-PPV, poly[2,5-di(hexyloxy)cyanoterephthalylidene]; CV, Cyclic Voltammetry; CZTS, Copper-Zinc-Tin-Sulfide; CZTSe, Copper-Zinc-Tin-Selenide; CZTSSe, Copper-Zinc-Tin-Sulfide/selenide; DCB, Dichlorobenzene; DCE, 1,2-dichloroethane; EC, Electrochemical Capacitor; EHDA, ElectroHydroDynamic Atomization (EHDA); EL, ElectroLuminescence; EML, Emissive Layer; ESAVD, ElectroSpray Assisted Vapour Deposition; ESD, Electrostatic Spray Deposition; FF, Fill Factor; FTO, Fluorinated Tin Oxide; GNP, Graphene Nano-Platelet; GO, Graphene Oxide; IR, InfraRed; Ir(mppy)₃, tris(2-(4-tolyl)phenylpyridine)iridium; ITO, Indium Tin Oxide; LED, Light Emitting Diode; LIB, Lithium Ion Battery; Li-S, Lithium Sulfur; MEH-PPV, poly[2-methoxy-5-(2ethylhexyloxy)-1,4-phenylenevinylene]; MPBL, Multifunctional Polysulfide Blocking Layer; MWNT, Multi-Walled Carbon Tube; NPC-S, Hybrid Sulfur and Nitrogen-Doped Porous Carbon Sheet (NPCS); NVP, Sodium Vanadium Phosphate ($\text{Na}_3\text{V}_2(\text{PO}_4)_3$); OLED, Organic Light Emitting Diode; OPV, Organics PhotoVoltaics; OTFT, Organic Thin Film Transistors; PAN, Polyacrylnitrile; PBD, 2-(4-biphenyl)-5-(4-tert-butylphenyl)-1,3,4-oxadiazole; PCE, Power Conversion Efficiency; PCNF, Porous Carbon-NanoFiber; PEC, PhotoElectrochemical Cell; PECVD, Plasma-Enhanced Chemical Vapour Deposition; PEDOT:PSS, poly(3,4-ethylenedioxythiophene); polystyrene sulfonate; PLED, Polymer Light-Emitting Diode; PSC, Perovskite Based Solar Cells; PVK, Poly(N-vinyl carbazole); rGO, reduced Graphene Oxide; RHE, Reversible Hydrogen Electrode; SEM, Scanning Electrochemical Microscopy; TCO, Transparent Conductive Oxide; TPD, N,N'diphenyl-N,N'-bis(3-methylphenyl)-[1,1-biphenyl]-4,4'-diamine; QD, Quantum Dot; XRD, X-Ray Diffraction

* Corresponding author.

<https://doi.org/10.1016/j.jaerosci.2018.04.011>

Received 31 October 2017; Received in revised form 30 April 2018; Accepted 30 April 2018

Available online 03 May 2018

0021-8502/ © 2018 Elsevier Ltd. All rights reserved.

electrospray seems therefore advantageous to other thin film deposition techniques (Shui et al., 2004).

During an electrospray experiment, altering the applied electric field strength and/or the flow rate (the liquid kinetic energy) results in different electrospray modes. These modes differ in their droplet sizes and droplet formation mechanism. Among them, the cone-jet mode is the most studied one in thin layer production because of its ability to produce spherical particles, much smaller than the nozzle diameter, with a narrow size distribution (Agostinho, 2013; Jaworek, Sobczyk, Krupa, Lackowski, & Czech, 2009). For the cone jet mode, scaling laws, for the electric current through the liquid and the droplet size, have been developed (Yurteri et al., 2010). The scaling laws depict that droplet sizes and final particle sizes can be easily controlled by adjusting different parameters, if we are indeed in the cone-jet domain with respect to flow rate and applied potential (Scheideler & Chen, 2014). With the advances in technology, this allows electrospray in the cone jet mode to find a wide application in different areas like microelectronics and nanotechnology (Jaworek & Sobczyk, 2008). Also depending on the physical and chemical properties of the liquid precursor such as density, surface tension, conductivity, concentration and viscosity, and experimental parameters like deposition temperature, deposition time, nature of the substrate, the surface morphology can be tailored (designed) to suit the preference (Neagu, Djurado, Ortega, & Pagnier, 2006). These parameters are discussed in great detail in another section of this special issue (Ganan-Calvo, Lopez-Herrera, Herrada, Ramos, & Montanero, 2018; Rosell-Llompert, Grifoll, & Loscertales, 2018). Obviously, the morphology of the deposited layer plays a crucial role in the final performance, e.g. for solar cells usually homogeneous flat layers are required while for ionic and electronic transfer from and out one layer to the other, rough layers are concerned in for instance battery electrodes.

Considering that the quality of a thin film depends on the particle sizes, their monodispersity and uniform distribution on the surface, electrospray is a powerful tool in material synthesis. The deposition parameters are extensively discussed in another part of this special issue (Bodnár, Grifoll, & Rosell-Llompert, 2018; Jaworek, Sobczyk, & Krupa, 2018)

Therefore, this review looks at different areas where the novel technique has been used to improve on the overall performance of materials for energy devices, which started with the paper of van Zomeren, Kelder, Marijnissen, and Schoonman (1994) for Li-ion batteries, and since then, more than 150 papers appeared on this subject. This amount is almost equal to the number of papers that arose on other energy device subjects discussed here, such as solar cells, photoelectrochemical cells, (O)LEDS including quantum dots, capacitors, and fuel cells. This last topic however, is described in another section of this special issue. (Castillo, Martin, Rodriguez-Perez, Higuera, & Garcia-Ybarra, 2018)

2. ESD for energy production (solar cells and photo-electrochemical cells)

2.1. Solar cells

In solar cells, surfaces are often deciding the performance of the device in terms of light absorption and electronic behaviour. Hence, thin film fabrication methods are of utmost importance for achieving optimal operation of the solar cell. For the Si-based and GaAs solar cells these depositions are typically based on vacuum methods and or oxygen- and moisture-free environments (sputtering, (PE)CVD, and (co-)evaporation). In contrast, potential future type solar cells like Copper Indium Sulfides/Selenides (CIS), perovskites (Fig. 1) and organic-type solar cells may use non-vacuum methods such as spin-coating, electro-deposition, screen-printing, doctor-blading, paste-coating, precursor-printing, and spray pyrolysis. (Abernathy, Bates, Anani, Haba, & Smestad, 1984; Eberspacher, Fredric, Pauls, & Serra, 2001; Mooney & Radding, 1982; Panthani et al., 2008; Roncallo, Painter, Cousins, Lane, & Rogers, 2008; Shay, Wagner, & Kasper, 1975; Yoon et al., 2012).

Each of these methods has its pros and cons in terms of processing, chemistry, and final performance. For instance, spray pyrolysis was used by Mitzi, Kosbar, Murray, Copel, and Afzali (2004); Mitzi, Copel, and Murray (2006); Mitzi et al., (2008, 2009) and Milliron, Mitzi, Copel, and Murray (2006) who deposited a Cu-In-Ga-Se (CIGS) layer, giving a solar cell power conversion efficiency of 10.3%. One of their precursors was hydrazine, and due to its reactivity and toxicity, it limits its widespread use. Ahn et al. (2010) coated a substrate with a $\text{Cu}(\text{NO})_2$ and InCl_3 solution by using a doctor-blade method, but the efficiency was as low as 2%. In the following sections, an overview is given to address the issues in more detail by using ESD for fabrication of potential future solar cells based on

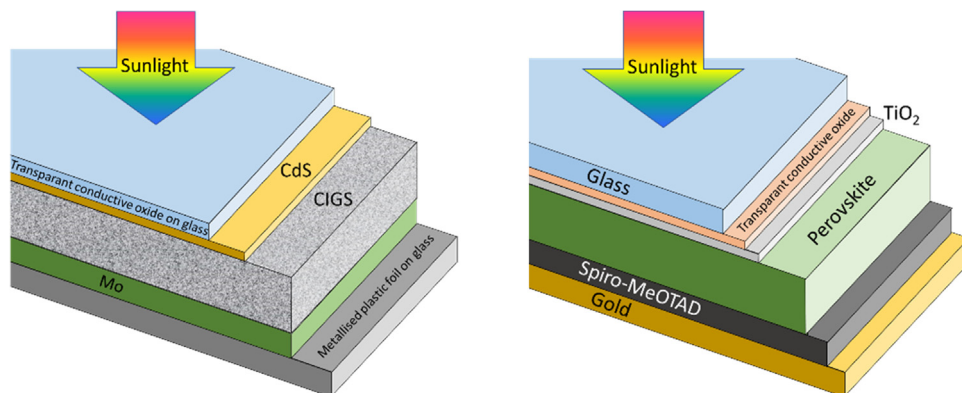


Fig. 1. CIS solar cell (left) and Perovskite solar cell (right).

Table 1Previous studies on CuInSe₂ solar cells produced by spraying solution-based precursors (Yoon et al., 2012).

Solvent	Substrate	Deposition temperature	Conversion efficiency	Reference
Ethanol/deionized water	Pyrex	180–200 °C (< 300 °C)	N.A.	Boungnot, Duchemin, and Savelli (1986)
Ethanol	Stainless steel	300–360 °C	N.A.	Shirakata, Murakami, Kariya, and Isomura (1996)
Water, ethanol	Pyrex, quartz	350–550 °C	2%	Tomar and Garcia (1982)
1,2-propanediol	Glass	300 °C	3.15%	Raja-Ram et al. (1986)

CIS's, perovskites and organic materials. This paragraph also includes photo-electrochemical cells.

2.1.1. CIS-type solar cells

Table 1 (Yoon et al., 2012) summarises previous spraying studies for CIS based solar cells. These CIS-based solar cells are attractive because of:

- favourable optical and electrical properties: band gap tuneable from 1 to 2.4 eV by selection of the Ga to S ratio.
- high photon absorption coefficients.
- high power-conversion efficiencies compared to other systems.

Nevertheless, implementation of CIS-based solar cells is still hampered by high manufacturing costs as a result of the processing method via the earlier mentioned conventional vacuum deposition methods. Hence, non-vacuum-based deposition techniques would significantly reduce costs and may thus accelerate market penetration.

Production of ESD CIS solar cells was shown with an initial low conversion efficiency (Yoon et al., 2012). Optimized precursor flow rates, which varied with the thermo-electrical properties of the dissolving solvents, were discussed. The effect of substrate temperature on the thin precursor films was also examined and are shown in Fig. 2. These precursor films then were selenized, performed in a vacuum evaporator equipped with a Knudsen-type effusion cell, at typically 530 °C for 30 min, under a Se flux regulated by the effusion cell temperature.

The deposition operating conditions that yielded the most uniform layer was used to produce cells for the necessary post-selenization process. The cells were then further covered with CdS and ZnO layers on top of the CuInSe layer. Light-illuminated current-density voltage (*J-V*) curves demonstrate a power conversion efficiency of $\eta = 1.75\% \pm 0.09$ with an open-circuit voltage of $V_{OC} = 0.23$ V, a short-circuit current density of $J_{SC} = 21.72$ mA/cm², and a fill factor $FF = 0.34$ (Fig. 3) Room for improving the cell conversion efficiency by reducing or removing the carbon layer originating from our highly viscous solvents, was to be expected, as shown below.

The morphologies of the carbon- and oxygen-free Cu(InGa)(SSe)₂ (CIGSSe) absorber thin films prepared by ESD are shown in the

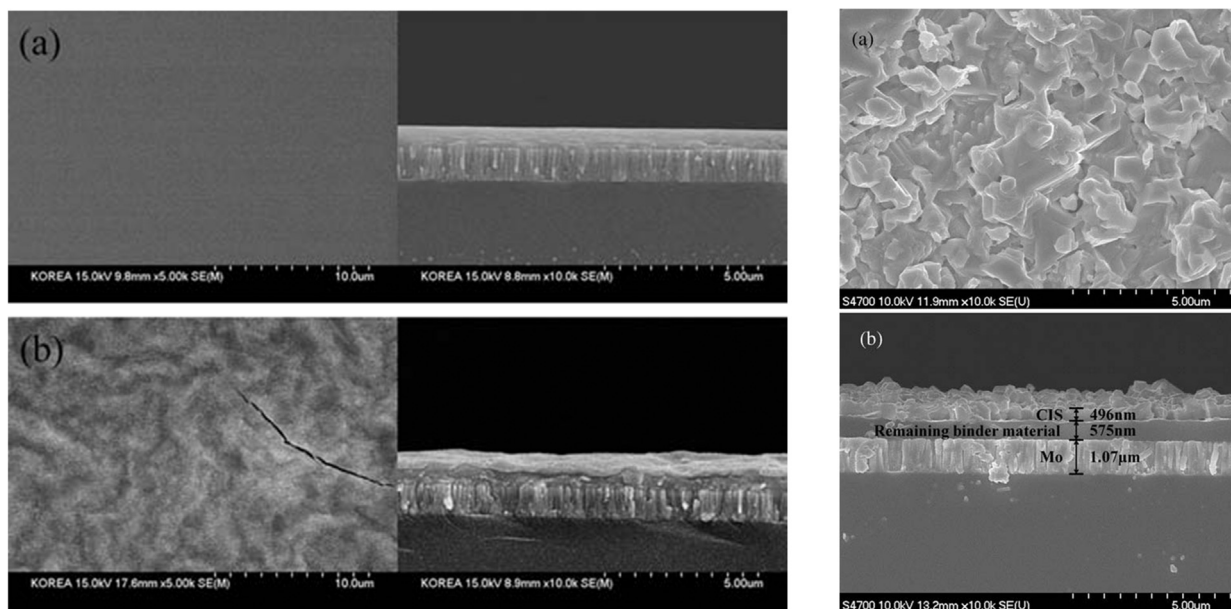


Fig. 2. Left panel: Morphologies of Cu-In films from propylene glycol solvent deposited at 100 °C (a), and 200 °C (b). Left and right images are top and side views, respectively. Right panel: (a) Top and (b) side views of a CIS thin film with selenium doping. Reprinted with permission from Yoon et al., 2012.

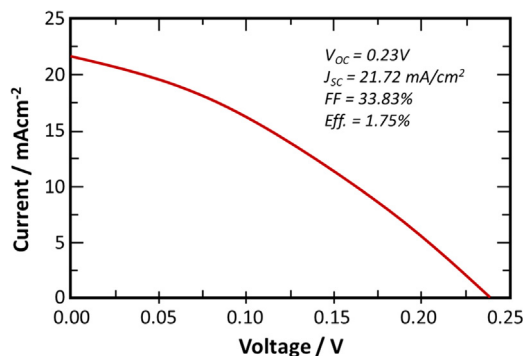


Fig. 3. I–V characteristics of the CIS solar cell on a molybdenum-coated substrate (Redrawn from Yoon et al., 2012).

left panel of Fig. 4 (Yoon et al., 2014). Similarly a polycrystalline chalcopyrite CIGS₂ absorber with a large-faceted flat-grained morphology was prepared after sulfurization and selenization and is presented in the right panel of Fig. 4.

A solar cell with a 4.63% conversion efficiency was produced with $V_{OC} = 410$ mV, $J_{SC} = 21$ mA/cm², and $FF = 0.5337$ for an active area of 0.46 cm² (Fig. 5).

Also, electrospun nanofibers were used to construct a 3D CuInS₂ solar cell with enhanced surface area on a ESD CuInS₂ layer (see Fig. 6) (Yoon et al., 2015). The electrospun CuInS film was annealed to crystallize the film, which was then sulfurized in a H₂S/N₂ environment to remove oxides. Both XRD and Raman characterization confirmed the formation of CuInS₂. SEM images (Fig. 6) revealed a 3D web-like, fibrous structure of the film. AFM data showed that the surface area had nearly doubled after incorporating the 3D nanostructure. The solar cell has a standard Mo/CIS/CdS/i-ZnO/n-ZnO/Al structure.

Finally, the fabricated CIS nanofiber cell had a $V_{OC} = 0.21$ V, $J_{SC} = 9.07$ mA/cm², $FF = 35.64\%$ (Fig. 7), and a conversion efficiency of 0.66% with an active area of 0.44 cm². The low efficiency was attributed to a limitation in the TCO sputtering process, which did not yield a complete penetration of the transparent conductive oxide (TCO) materials into the open pores between CIS/CdS fibers, which may eventually be improved by using metal nanowires together with indium tin oxide (ITO) nanoparticles.

A low cost, scalable electrostatic spray assisted vapour deposition (ESAVD) method using DMSO as solvents was employed to deposit Copper-Zinc-Tin-Sulfide (CZTS) absorbers (Altamura, Wang, & Choy, 2015). In order to further improve the efficiency, an ultrathin ZnO intermediate layer was deposited between CZTS₂ and Mo to minimize absorber decomposition at the back contact surface. The thin ZnO layer no longer existed after treatment with selenium (SEM images in Fig. 8) because Zn was incorporated into the CZTS₂ absorber and O was replaced by Se (Sample I).

The reaction between ZnO and Se vapour reduced the thickness of high resistance Mo(S,Se) layer formed during selenization. For another sample (Sample II) with a thin ZnO intermediate layer, the Zn/Sn ratio after selenization was lower than the reference sample. It was concluded that preventing decomposition of CZTSe in the vicinity of the Mo back contact allows a reduction of the loss of Sn during the annealing, which suggests the existence of a relationship between the loss of Sn and the formation of secondary phases at the back region of the absorbers. Comparison between Raman spectrum of Sample I and Sample II proved that a thin ZnO layer successfully reduced the decomposition of CZTS₂ at the back contact surface. The improvement of the CZTS₂/Mo interface due to the intermediate layer was also reflected in the quality of the derived photovoltaic devices leading to an improved efficiency for ESAVD-deposited kesterite of 4.03% with ESD.

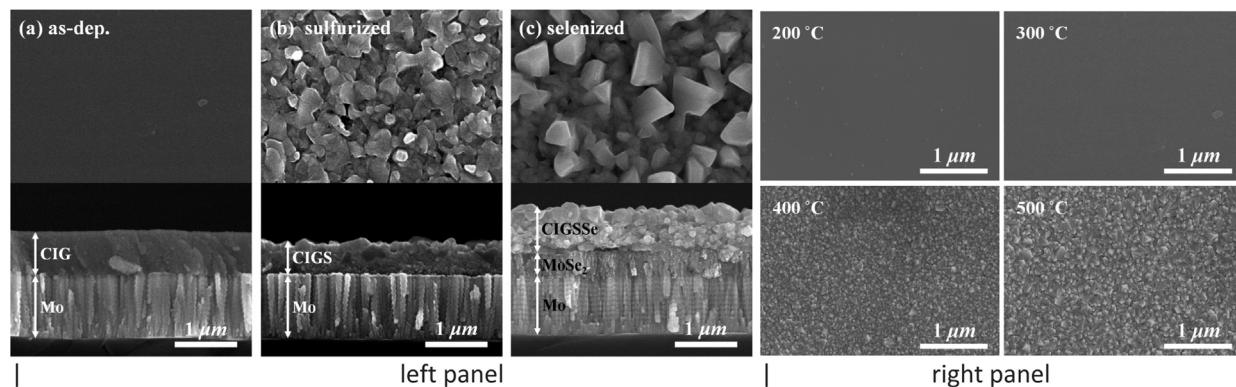


Fig. 4. Left panel: Top-view (top row) and cross-sectional (bottom row) SEM images of the (a) as-deposited CuInGa film, (b) sulfurized Cu(InGa)S₂ film, and (c) selenized Cu(InGa)(SSe)₂ film; Right panel: Top-view SEM images showing the effect of the airannealing temperature on the surface morphology and grain size of the as-deposited film (before sulfurization). Reprinted with permission from Yoon et al., 2014).

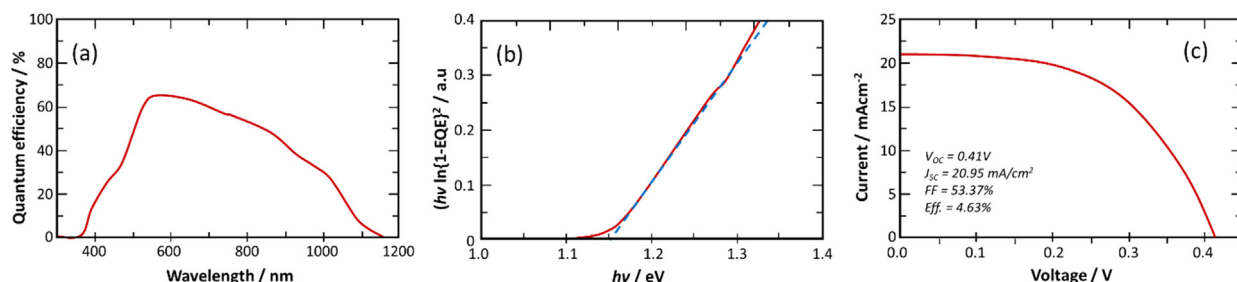


Fig. 5. (a) External quantum efficiency, (b) estimation of the band gap, and (c) I-V characteristics of the CIGSs solar cell on a molybdenum-coated substrate. (Redrawn from Yoon et al., 2014).

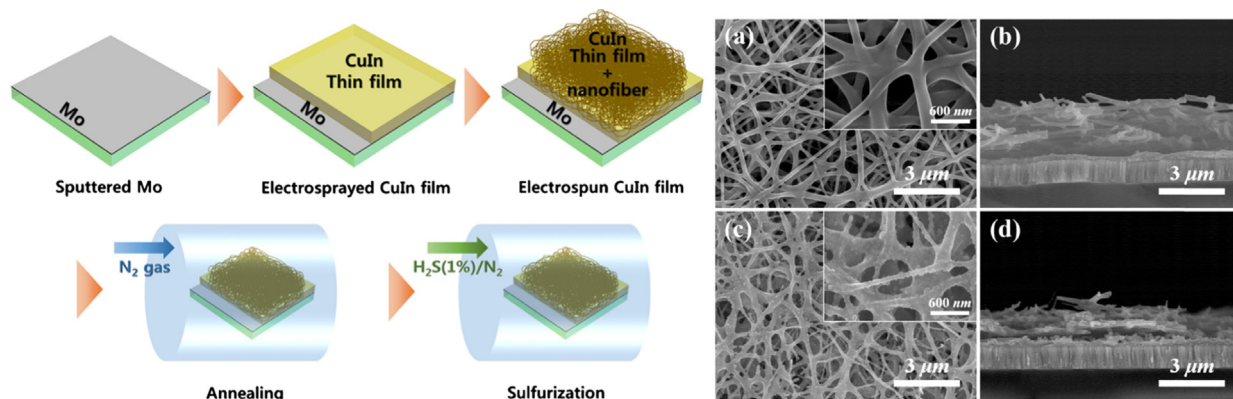


Fig. 6. Fabrication of 3D nanostructured CIS (left), and SEM image of annealed (a and b) and sulfurized (c and d) 3D nanostructured CIS absorber layer. Reprinted with permission from Yoon et al., 2015.

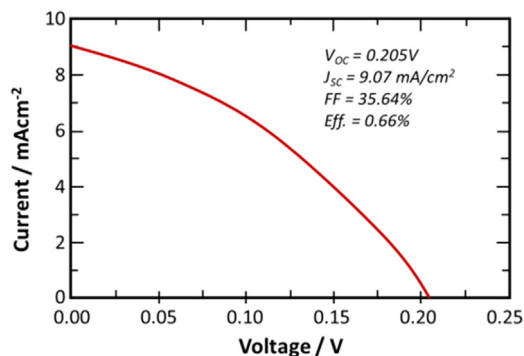


Fig. 7. I-V characteristics of the CIS solar cell on a Mo-coated substrate. (Redrawn from Yoon et al., 2015).

2.1.2. Perovskite-based solar cells (PSCs)

Within the last years, perovskites have made enormous progress as solar cell materials, with a power conversion efficiency reaching up to 17%, (Jeon et al., 2015, 2014; Lee, Seol, Cho, & Park, 2014; Jeon et al., 2014a; Nie et al., 2015), or higher when based on a planar architecture containing mixed halide perovskite ($\text{CH}_3\text{NH}_3\text{PbI}_{3-x}\text{Cl}_x$) materials (Zhou et al., 2014), and beyond that (http://www.nrel.gov/ncpv/images/efficiency_chart.jpg). Hence, PSCs are becoming highly interesting next generation solar cell devices for converting solar energy. Unfortunately, PSCs show severe problems with respect to incorporated defects leading to a hysteresis in the I-V characteristics (Nie et al., 2015). Thus, improving the perovskite film surface coverage is an important field, where the process plays a crucial role. Several techniques were reported to obtain large crystals with uniform perovskite films, via solution methods, (Burschka et al., 2013; Docampo et al., 2014; Jeon et al., 2014b) thermal evaporation, (Liu, Johnston, & Snaith, 2013) and spray coating (Barrows et al., 2014; Ramesh et al., 2015), including either a one-step solution or a two-step sequential deposition technique to obtain uniform, and dense perovskite films (Jeon et al., 2014a; Nie et al., 2015). A modified two-step sequential deposition method (solution-vapour) was used by initially spin coating followed by vapour deposition (Hu et al., 2014; Xiao et al., 2014). Unfortunately, these methods reveal serious disadvantages:

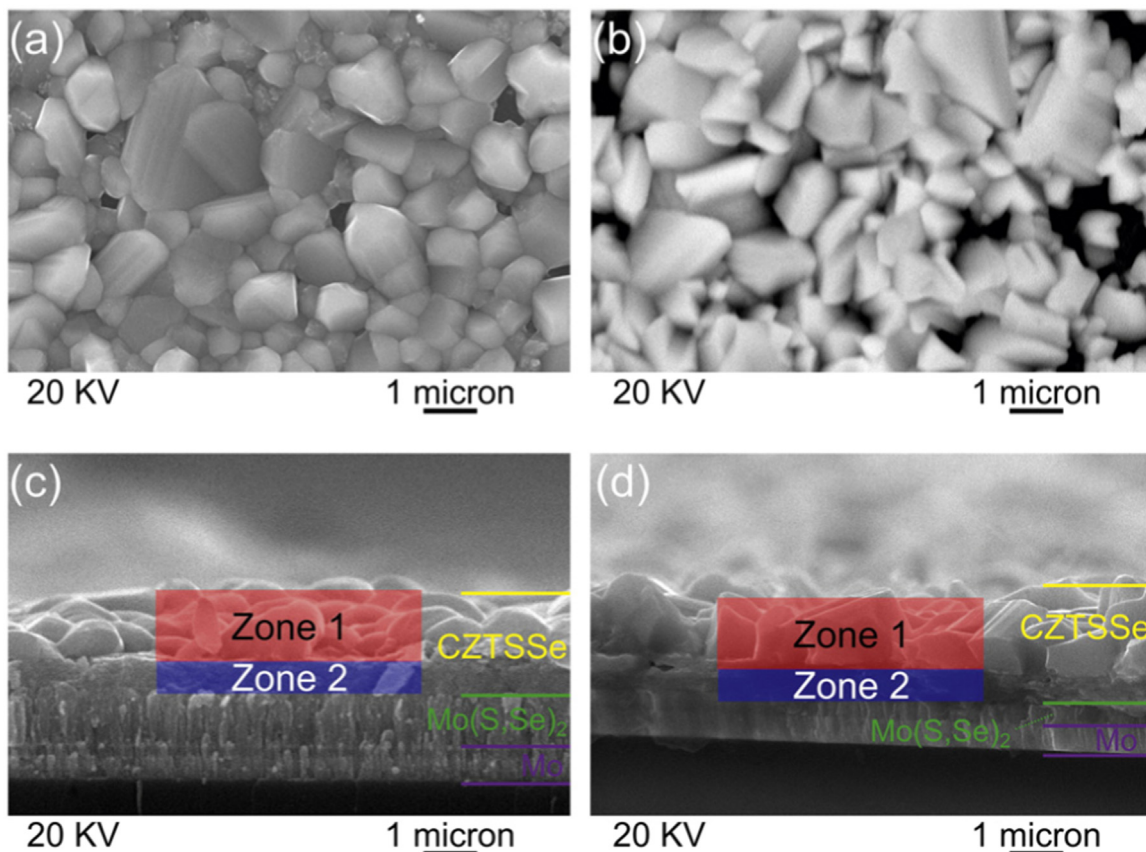


Fig. 8. Top-view and cross-section SEM images of CZTSSe after selenium treatment for Sample I (a, c) and Sample II (b, d). Reprinted with permission from Altamura et al., 2015.

- waste of precursor materials.
- formation of island like perovskite structures creating reduced surface coverage with pinholes.
- incomplete conversion of the precursor leads to formation of poor quality perovskite films.

In order to make perovskites more attractive for market implementation, control of the deposition is important. Usually, spray methods lead to small grain size and thus pin hole formation, but also to incorporation of impurities (Krishna, Dutta, & Paulson, 2003). Hence, in order to achieve enhanced electronic properties, the morphology and crystallinity of the perovskite films need to be improved. It is however stressed that the method used was performed with voltages that does not allow actual electro spraying, but uses merely a high voltage as assistance to the standard spraying (Fig. 9) (Chandrasekhar, Kumar, Swami, Dutta, & Komarala, 2016). Nevertheless, deposition may be expected with full electro spraying as well.

2.1.3. Organic solar cells

In Organic Photovoltaic (OPV) devices typically photogenerated excitons are dissociated by the photovoltaic energy gap, and then the charges are separated by the built-in potential created the electrodes. In order to do so, the electrode layers need to be well-adjusted so as to make sharp interfaces at the p-n junction. The processing allows similar critical issues as required for the deposition of (O)LEDs, and thus will be discussed there. Most recently, ESD has been used to fabricate OPV layers of P₃HT:PCBM active layers with bulk heterojunction (Fukuda et al., 2011, 2012; Kim et al., 2010a, 2010b; Kim, Kim, Lee, & Lee, 2012a; Kim et al., 2012b; Park et al., 2011) and multi-layer structures (Ali et al., 2012), but also as to deposit poly(3,4-ethylenedioxythiophene): polystyrene sulfonate (PEDOT:PSS) as hole transport layer (Kim et al., 2012a, 2012b) or as an electrode (Kim et al., 2012a, 2012b). An active layer of P3HT:PC61BM led to a PCE of ~3.00% using acetic acid as additive in ESD, which is comparable to that of the OPV device fabricated by spin coating (Zhao et al., 2014). A molecular ordered uniform P3HT:PCBM thin film with the high crystallinity deposited by ESD showed a PCE of 2.0% (Fukuda et al., 2016). Ordered PTB₇-Th:PC71 BM polymers with specific sizes were fabricated via ESD to form thin films. By optimizing solvent evaporation and thickness of the layers, a power conversion efficiency (PCE) of 8.6% was obtained. Very recently ESD was applied to fabricate a multilayered (three-component) device structure (Fukuda, Toda, Takahira, Kuzuhara, & Yoshimoto, 2017).

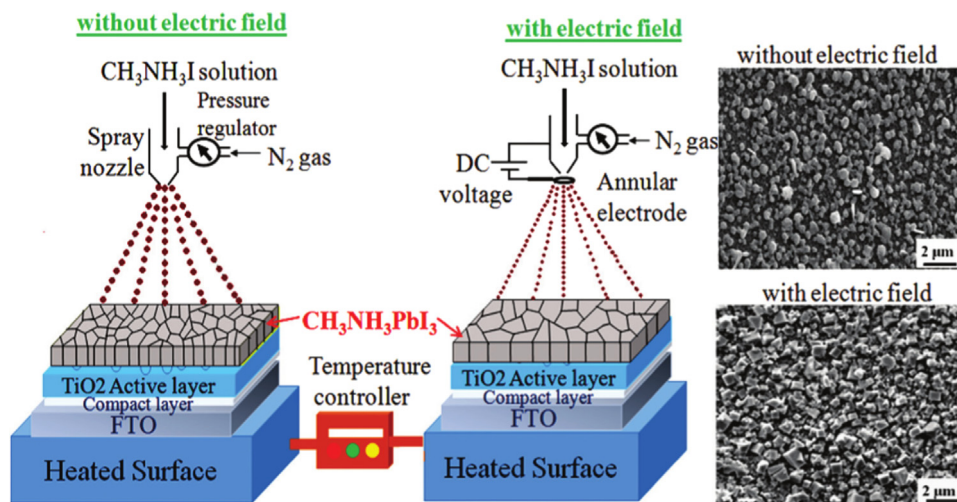


Fig. 9. Scheme of the spray deposition process of perovskite films with (2 kV) and without electric field, together with the corresponding film surface morphologies. Reprinted with permission from Chandrasekhar et al., 2016.

2.2. Photoelectrochemical cells

Photoelectrochemical cells (PECs) are solar cells that provide electricity to typically produce hydrogen via electrolysis of water, i.e. water splitting (Fig. 10).

The active electrode is often a modified TiO₂ layer. Dye-sensitized solar cells prepared by ESD immersed in aqueous solution (Fujimoto, Kado, Takashima, Kaneto, & Hayase, 2006), with a I₃⁻ electrolyte, showed higher J_{sc} than those prepared by conventional coating methods, which was assigned to the presence of a better ionic path in the TiO₂, due to the specifically formed morphology. The results are shown in Fig. 11.

ESD was also used to deposit CdSe QDs onto nanostructured TiO₂ films to form a photovoltaic cell electrode (Li, Jiao, Xie, & Li, 2015). Compared to conventional processes like dip coating with linker-containing molecules or chemical bath deposition, ESD has shown uniform deposition of QDs as mentioned earlier, and here it is used to cover a nanostructured TiO₂ surface without linker-molecules. ESD allows preserving the physical and the optical properties of the QDs. To optimise the final energy conversion efficiency for the photolysis of water, various different concentrations and deposition times were employed. The as-deposited films were annealed later on, to ensure binding between the QDs and the TiO₂ surface. Despite that a small number of deposited QDs limit the number of absorbed photons, multiple layers of QDs cause more defects and trap sites enhancing electron-hole recombination ascribed to inhibition of the transportation of photo-generated electrons into TiO₂.

Beside the standard TiO₂ material, Nanostructured spinel zinc ferrite (ZnFe₂O₄) thin films were prepared on transparent conductive substrates via ESD at 400 °C, followed by annealing (Wang et al., 2017). The ZnFe₂O₄-film thickness played an important role in the PEC performance, where porous thin films with an enlarged interfacial area between ZnFe₂O₄ and the electrolyte were obtained, which led to an increased discharge potential, due to an increased number of active sites giving an enhanced photocurrent of 53 μA/cm² at 1.23 V versus RHE.

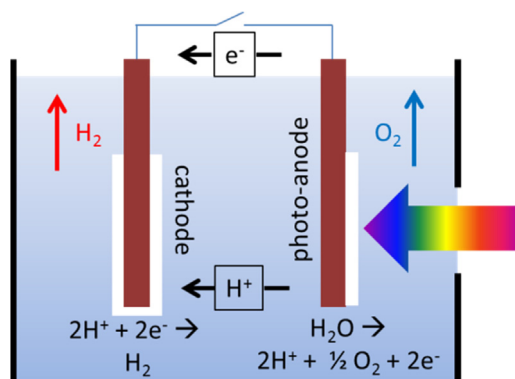


Fig. 10. Photo-electrochemical cell.

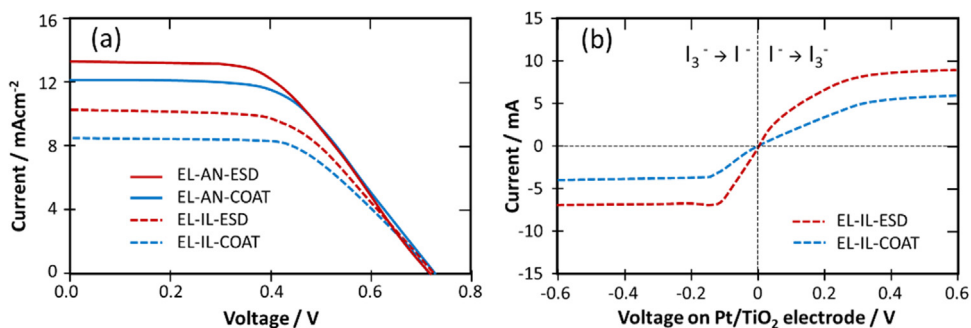


Fig. 11. (a) I-V curves for dye-sensitized solar cells fabricated with conventional coating (COAT) and ESD. EL-AN and EL-IL stands for acetonitrile (AN) and ionic liquid (IL) electrolyte (EL), respectively. All film thicknesses were 9 μm . (b) Limiting current measurement for cells with a TiO_2 layer prepared by conventional coating and ESD. Redrawn from Fujimoto et al. (2006).

3. ESD for energy storage (batteries and capacitors)

3.1. Lithium ion batteries (LIBs)

Today, Li-ion batteries are the major rechargeable electricity carriers for consumer electronics and also electric vehicles, and might be in the near and/or long future. In Fig. 12 a scheme of the working principles of a Li-ion battery is presented.

Both electrode materials, positive and negative, can be and were synthesized using ESD. For the positive electrode layered structures (LiMO_2 , with M any combination of transition metal ions), spinels (LiM_2O_4 , with M any combination of transition metal ions), and olivines (LiMPO_4 , with M typically a combination of iron and cobalt ions) were identified. For the negative electrode all sorts of transition metal oxides are being tested as well as many metals and alloys. Both have been made via ESD, either via composites with spraying the actual powder, or via a chemical deposition reaction during spraying. The performances of the materials are typically measured on flat coatings, so as to reduce the influence of the interface between the electrode and electrolyte, as well as to accurately measure the surface area of the interface. Here an overview is given of several materials with respect to surface morphology and composition for positive electrodes. With respect to negative electrode materials synthesized by the ESD, an thorough review was written by Li and Wang (2013). The attention there was focused on three different anode categories: (1) insertion anodes, such as graphite, $\text{Li}_4\text{Ti}_5\text{O}_{12}$ and TiO_2 , etc.; (2) alloying–de-alloying anodes, such as Sn and SnO_2 , etc.; and (3) conversion reaction anodes, such as NiO, Fe_2O_3 , Co_3O_4 , CoO, and Cu_2O . Hence, this part will not be further discussed here.

ESD was employed to fabricate various morphologies of cathode materials for Li-ion batteries as reported by Chen et al. (1996a, b). Since then, many other cathode materials having several different morphologies (Sun et al., 2013) have been formed and described in the literature. It is stressed that in order to characterize various materials properties, flat surfaces are often used. These properties comprise structural information (XRD, IR-RAMAN, etc) and electrochemical information (e.g. diffusion coefficients, ionic and electronic conductivities) (Nishizawa et al., 1998; Dokko et al., 2004; Mohamedi et al., 2002a, b, c; Chung et al., 2004; Shu et al., 2003; Chung et al., 2005).

Since charge transfer of either electrons or ions is an important issues for electrodes in devices, the morphology of it, is of utmost importance, because it will reflect the exchange area of these charge carriers. Here a short overview of the electrode performance will be given on the basis of flat, rough (porous), and reticular structures, also with respect to their composition. Since there are so many different process parameters to vary in order to obtain a certain layer, it is too difficult to make a well-justified comparison, also in the light of the length of the paper. Nevertheless, several results are given so as to show the actual importance of the various

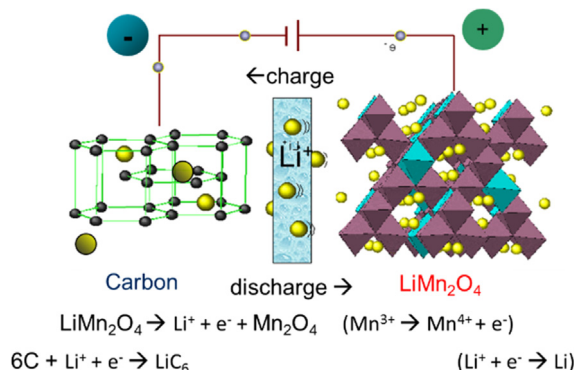


Fig. 12. Li-ion battery principles with a LiMn_2O_4 cathode and carbon anode as an example.

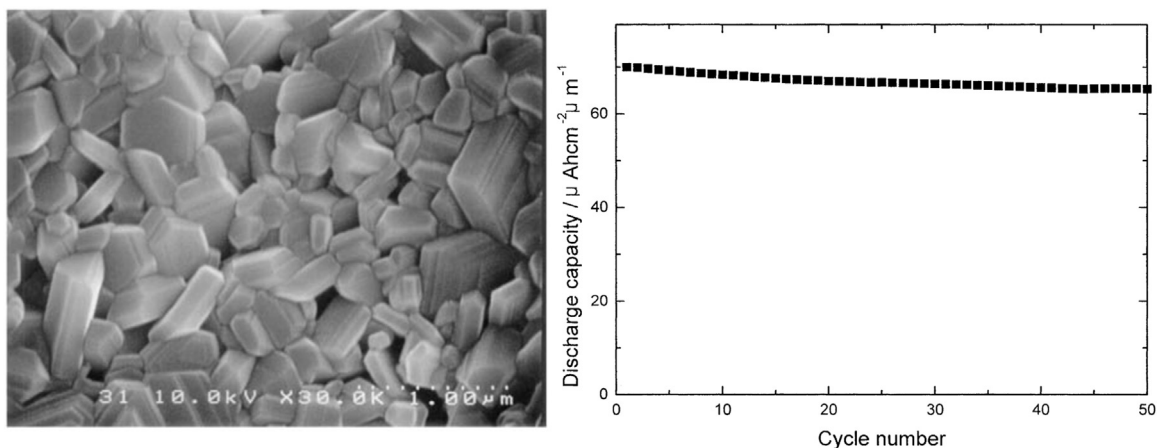


Fig. 13. (a) SEM of LiCoO₂ film annealed at 600 C and (b) Cycle performance. Reprinted with permission from Yoon et al., 2001.

morphologies on cathode performance.

For the layered structures LiMO₂, LiCoO₂ has been taken as a positive electrode material example (Koike & Tatsumi, 2007; Yoon et al., 2001). It is clear from Fig. 13 and Fig. 14 that the capacity of the most porous structure is significantly higher than the non-porous structure. The power performance of those layers are also found to be higher than the non-reticular ones. This is a phenomenon that has been observed for most of the reticular structures compared to the flat or other rough and porous structures.

In order to further improve the performance of the films, the materials were coated (Hu et al., 2008) or modified with an indifferent additive such as nano-particles of silica (Fig. 15) (Yu, Shui, Jin, & Chen, 2006). With the latter, an improved performance is clearly observed.

Obviously, the layered structures can be further improved by stabilising the structures by replacing certain amounts of cobalt by other transition metal ions or aluminium. For example, Li(Ni,Co,Ti)O₂ compounds was prepared by ESD with a combinatorial method (Fig. 16) (Fujimoto, Ikezawa, & Ito, 2011; Fujimoto, Onoda, & Ito, 2007a, 2007b).

The charge–discharge characteristics of the Li(Ni,Co,Ti)O₂ powder were recorded in a voltage range from 4.2 to 2.8 V at 1 C and those were found to retain their capacity better than pure LiCoO₂ at the same C-rate (Fig. 17). (Fujimoto et al., 2011)

Despite the great performance of the reticular structures for a 3D solid state battery a dense flat coating on a high aspect ratio surface is important for fast electronic charge transfer, which may be problematic for the reticular structures as the contact area with the current collector is minimal. The advantage of ESD in that respect is that it is possible to coat surfaces with aspect ratios of 10, as shown in Fig. 18 with LiNi_{0.5}Mn_{1.5}O₄ electrode material. (Lafont, Anastasopol, Garcia-Tamayo, & Kelder, 2012). It is stressed that in Fig. 18d, the cross-section was taken along the red line of Fig. 18c.

The LiFePO₄ olivine cathode materials are of interest today, but not much has been reported on ESD for these materials, most likely because the production of the material itself usually occurs under certain strict atmospheres, which makes it difficult to deposit these layers in one step. Nevertheless, its counterpart, LiCoPO₄ (Yu et al., 2006) was fabricated where the impurities Li₃PO₄ and Li₃PO₄ work as protective coating and electronic enhancer, respectively (Fig. 19) (Shui, Yu, Yang, & Chen, 2006).

Another advantage of ESD is to form composite layers. Several papers reported on improving the electrode performance by depositing composite electrodes either anodes or cathodes (García-Tamayo et al., 2011; Cho, Hwang, Kim, Bae, & Yoon, 2016; Wu et al., 2015a; Wu et al., 2015b; Dhanabalan, Li, Agrawal, Chen, & Wang, 2013; Damien, Anjusree, Sreekumaran Nair, & Shajumon, 2016). These improvements are then explained by an increase in the electronic and ionic migration processes induced by the

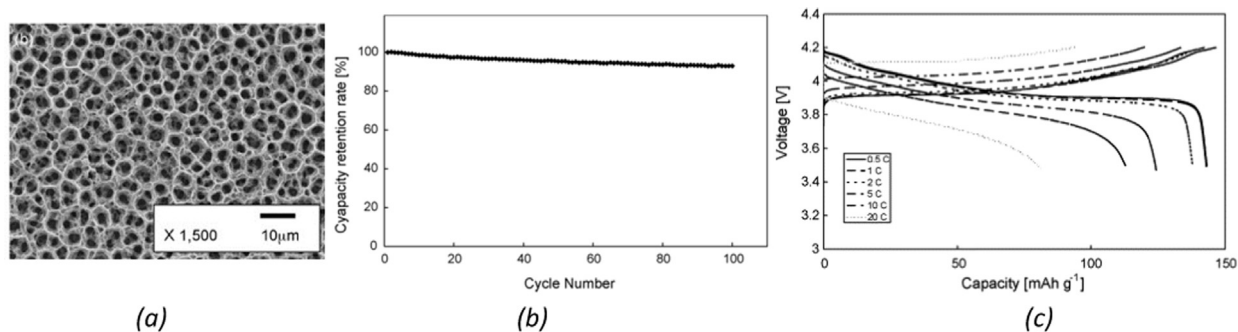


Fig. 14. (a) SEM images of surface morphologies of LiCoO₂ films prepared by ESD after heat treated at 650 °C for 2 h, (b) cycle performance and (c) rate performance. Reprinted with permission from Koike & Tatsumi (2007).

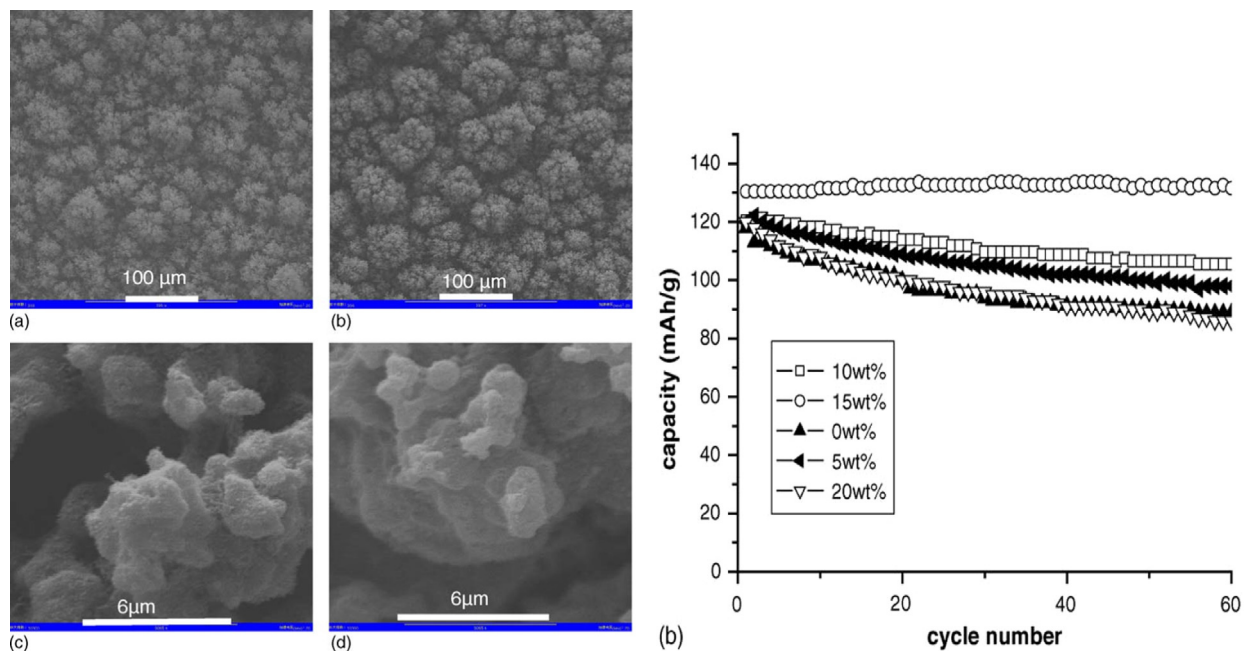


Fig. 15. Left panel: scanning electron microscopy pictures of a LiCoO₂ thin film (a and c) and a LiCoO₂-15 wt% SiO₂ thin film (b and d). (69). Right panel: capacity and cycle performance as a function of silica content. Reprinted with permission from Yu et al. (2006).

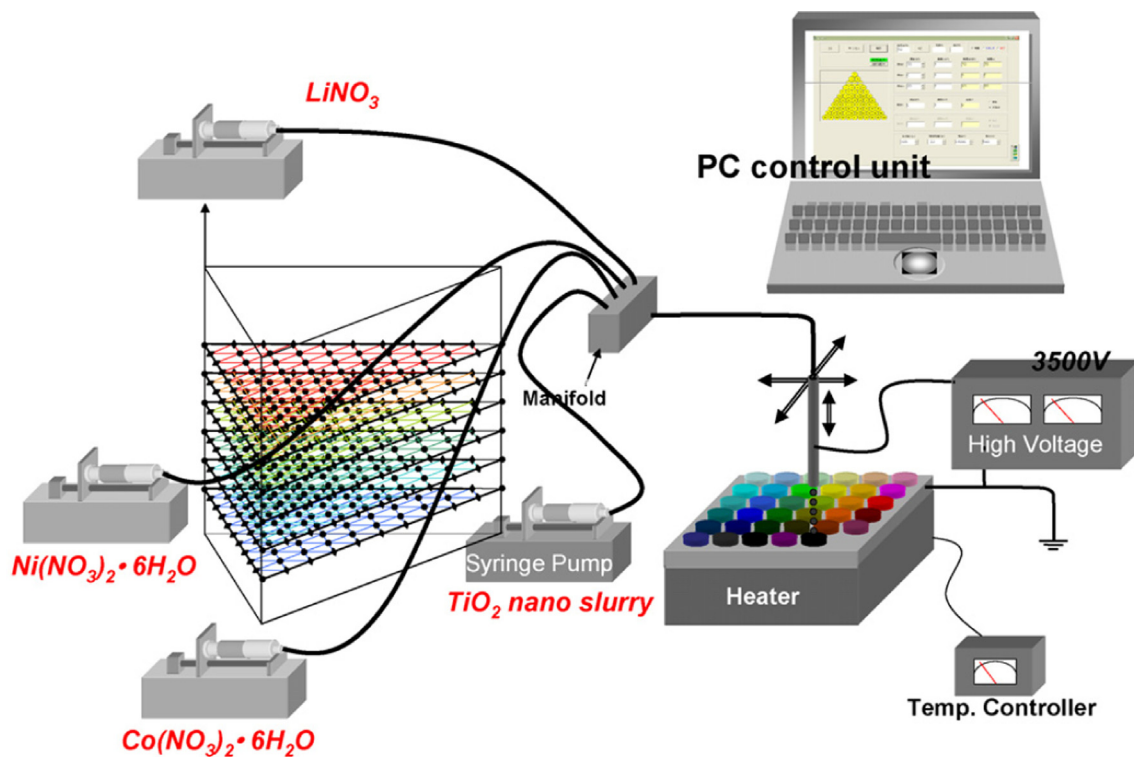


Fig. 16. Scheme of the so-called M-ist Combi system based on an electrostatic atomization method. Reprinted with permission from Fujimoto et al. (2007a, 2007b).

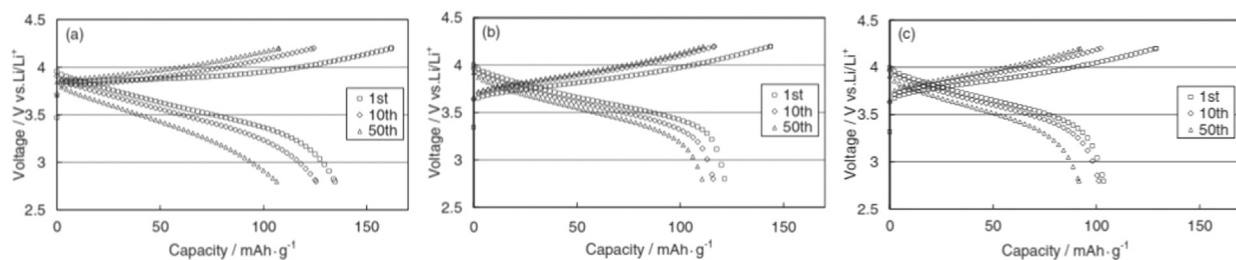


Fig. 17. Charge–discharge curves of $\text{LiNi}_{0.4}\text{Co}_{0.6-x}\text{Ti}_x\text{O}_2$ electrodes: (a) $x = 0$, (b) $x = 0.1$ and (c) $x = 0.2$. Reprinted with permission from Fujimoto et al. (2011).

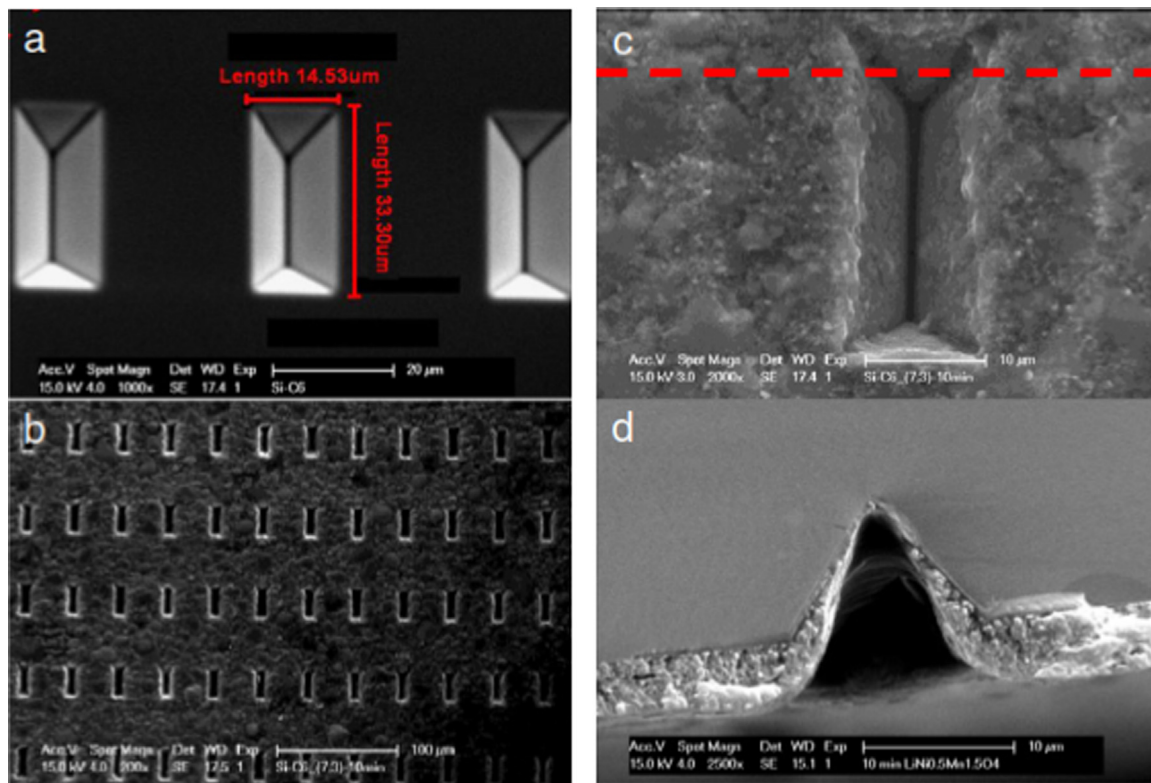


Fig. 18. SEM images of Si wafer showing 3D architecture (a) before and (b, c) after film deposition. (d) Cross section along the red dotted line of (c) showing the film thickness. Reprinted with permission from Lafont et al. (2012).

interfaces created between the electrode material and the additive (Fig. 20).

3.2. Beyond Li-ion batteries

3.2.1. Na-ion batteries

The high energy density of batteries and the high power density of supercapacitors are combined in a self-supported interpenetrating 3D tricontinuous $\text{Na}_3\text{V}_2(\text{PO}_4)_3$ -rGO-CNT cathode made via ESD, where the cathode is directly deposited on the current collectors without any conductive additives or binders (Zhu, Kopold, van Aken, Maier, & Yu, 2016). The $\text{Na}_3\text{V}_2(\text{PO}_4)_3$ -rGO-CNT material used as an anode as well as a cathode shows outstanding rate capability and long cycling stability (Fig. 21). At a current density of 100 C, the sodium cathode can still deliver a specific capacity of 82 mAh/g ($\sim 70\%$ theoretical capacity), which is almost as high as observed for supercapacitors but with a much higher energy density. It also shows an outstanding cycling stability, as at a current density of 10 C, the capacity still maintains 96% of its initial capacity, even after 2000 cycles.

A freestanding alluaudite $\text{Na}_{2+2x}\text{Fe}_{2-x}(\text{SO}_4)_3$ @porous carbon-nanofiber (PCNF) hybrid film is fabricated by combining electrospinning and ESD (Yu et al., 2016). The obtained highly porous graphitic-like carbon-nanofibers intimately envelopes the sulfate nanoparticles, resulting in a hybrid sulfate@PCNF network. This conductive network shows a very flexible and stable architecture, where the freestanding film demonstrates fast electron/ion transport and superior cycling stability, capable of high rate ultralong-

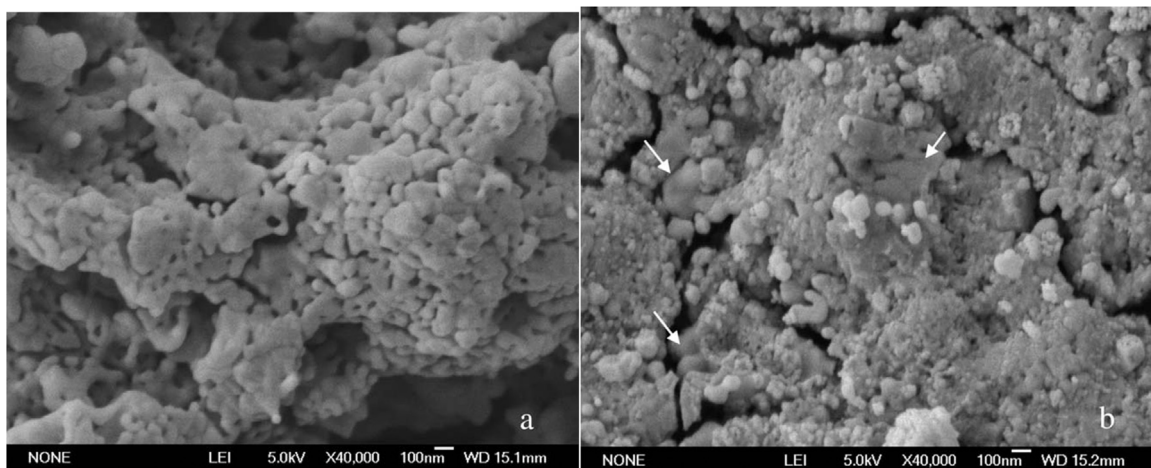


Fig. 19. SEM images of ESD synthesized $\text{Li}_{1.0}\text{CoPO}_4$ (a) and $\text{Li}_{1.8}\text{CoPO}_4$ (b) films. The arrows in (b) indicate the uncovered areas. Reprinted with permission from Shui et al. (2006).

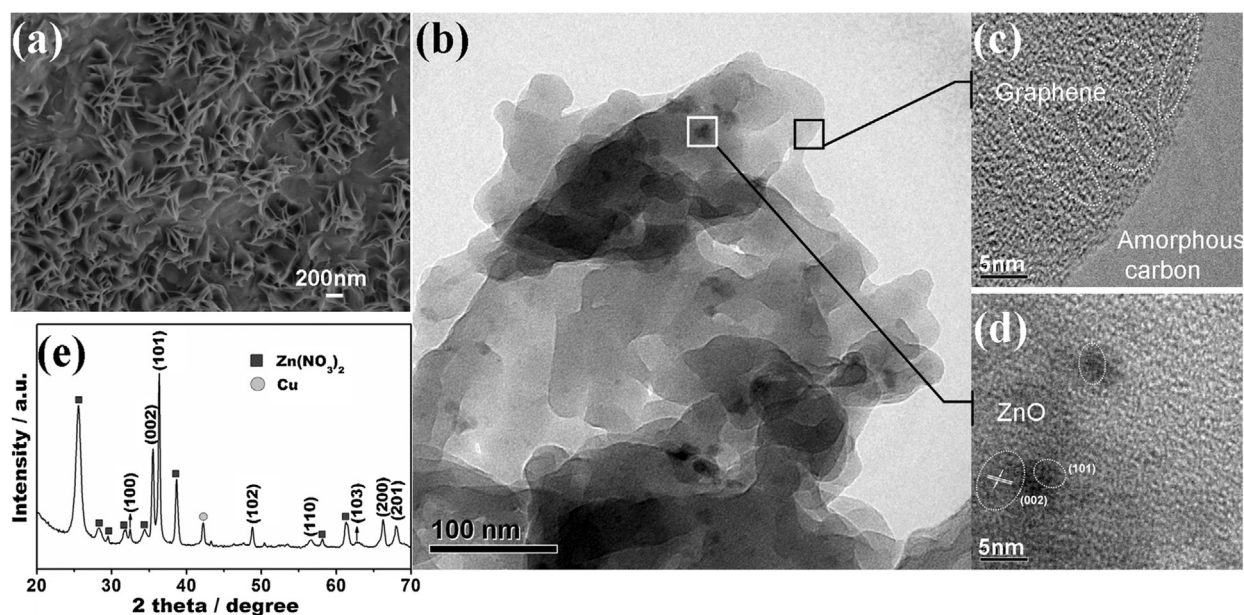


Fig. 20. SEM (a) and TEM, (b) images of nanostructure ZnO/rGO composite films; HRTEM of rGO, (c) from light area and ZnO, (d) from dark area; and XRD pattern, (e) of ZnO/rGO deposited on copper substrates by ESD. Reprinted with permission from Wu et al. (2015b).

term cycling. It retains more than 95% of its initial capacity even after 500 cycles at rates up to 40 C (Fig. 22).

3.2.2. Li-sulfur batteries

Ultrathin multifunctional coatings (~ 100 nm) on cathodes for a Li-S batteries which will effectively block polysulfide shuttling has been fabricated by ESD (Niu et al., 2016). This layer warrants fast ion diffusion without adding too much to the volume or weight, and prevents sufficient blocking of polysulfides to arrive at the counter electrode so as to avoids shorts (Fig. 23).

Black Pearl 2000 was uniformly dispersed in mixtures of water and ethanol (1:1 (V/V)) via sonication, to which PEDOT:PSS was added (Niu et al., 2016). This suspension was thus sprayed at 10 mL/h with a nozzle (20 gauge size) at 21 kV with a substrate to nozzle distance of 5 cm for 5 min to form a uniform MPBL coating (Fig. 24). The multifunctional polysulfide blocking layer (MPBL) exhibits a good cycling performance with only 0.042% capacity decay per cycle at 1 C for 1000 cycles and an excellent rate performance with a high capacity of 615 mAh/g at 3 C.

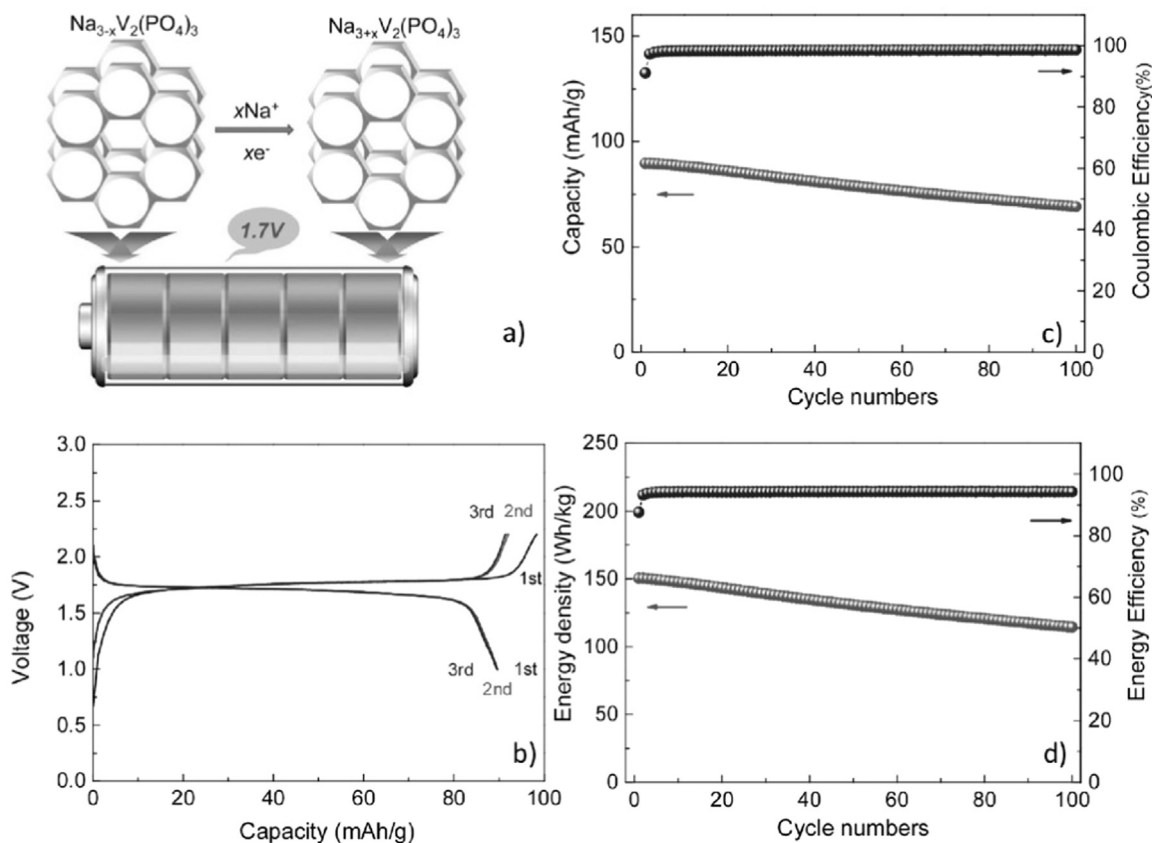


Fig. 21. a) Scheme of a symmetric full sodium battery using interpenetrating 3D tricontinuous NVP:rGO-CNT as both positive and negative electrodes. b) Galvanostatic charging–discharging profiles for the first three cycles at 10 C. c) Cycling performance and Coulombic efficiency for 100 cycles at 10 C. d) Discharge energy density and energy efficiency at 10 C versus cycle numbers. Reprinted with permission from [Zhu et al. \(2016\)](#).

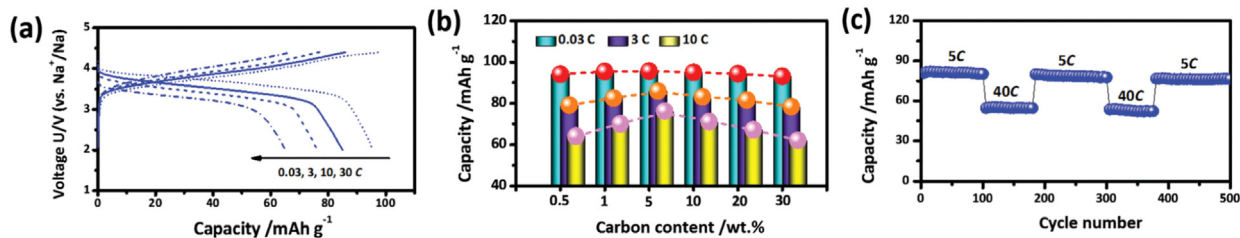


Fig. 22. (a) Galvanostatic charge/discharge curves of the hybrid nanofibers at various rates: 0.03 C, 3 C, 10 C and 30 C. (b) Comparison of discharge capacities at different current densities for the hybrid nanofibers with various carbon contents. (c) High-rate and long-term cycling properties of the hybrid nanofiber. Reprinted with permission from [Yu et al. \(2016\)](#).

3.3. Capacitors

Electrochemical capacitors (ECs), also known as supercapacitors or ultracapacitors, gained enormous interest as potential power source for the future smart energy era, due to their high power density, long life cycle, and high rate capacity ([Largeot et al., 2008](#); [Pognon, Brousse, Demarconnay, & Belanger, 2011](#)). In order to achieve that a higher energy density without influencing other electrochemical properties is required. Among the electrode materials, metal oxides provide higher energy densities than conventional carbon materials and showed improved electrochemical stability over polymer materials. This carbon based material for micro-capacitors, however, showed interesting performance made via ESD. On the other hand, the low electrical conductivity of oxides has significantly influenced their performance ([Lee et al., 2005a](#); [Lee, Cuomo, Cho, & Keusseyan, 2005b](#); [Wang, Casalongue, Liang, & Dai, 2010](#); [Wu, Li, & Lin, 2011](#)). A combination of both, such as graphene metal oxide composites has shown great potential for application in ECs due to their improved electrical conductivity, large specific surface area and excellent electrochemical stability ([Mao et al., 2012](#); [Qu et al., 2012](#); [Zangmeister, 2010](#); [Zhang et al., 2010](#)). The challenge is thus to form these graphene-based materials as restacking during the preparation process is an issue: the strong π - π interactions in graphene oxide (GO) usually results in irreversible

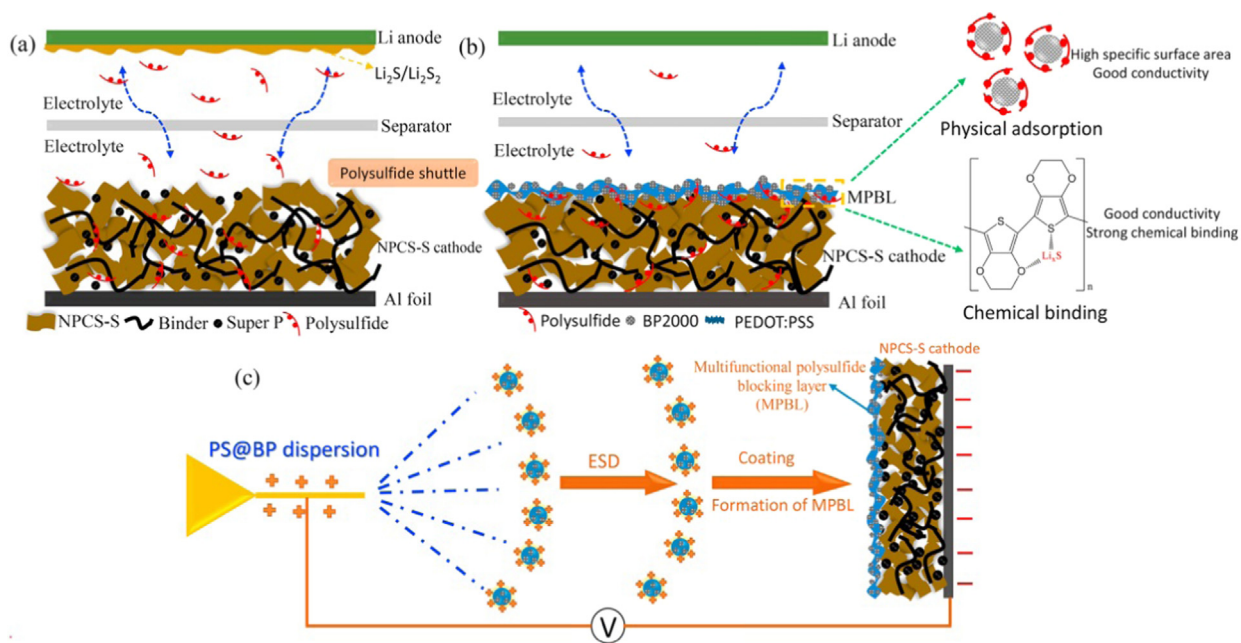


Fig. 23. Scheme of the electrode configurations for (a) a conventional uncoated cathode and (b) a MPBL-coated cathode for Li-S battery. (c) Scheme of the procedure for fabricating a MPBL-coated electrode. Reprinted with permission from Niu et al. (2016).

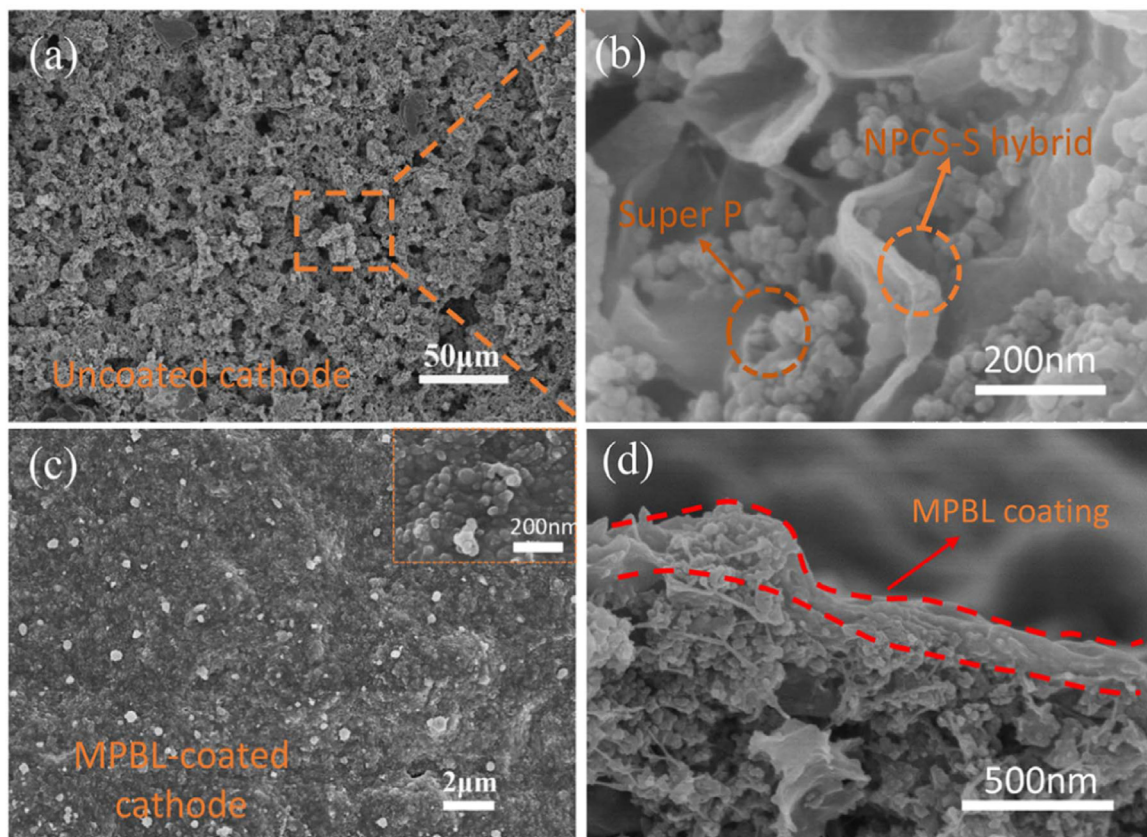


Fig. 24. (a, b) SEM images of uncoated hybrid nitrogen-doped porous carbon sheet (NPCS-S) cathode. (c, d) Surface and cross-section SEM images of the MPBL-coated NPCS-S cathode. Reprinted with permission from Niu et al. (2016).

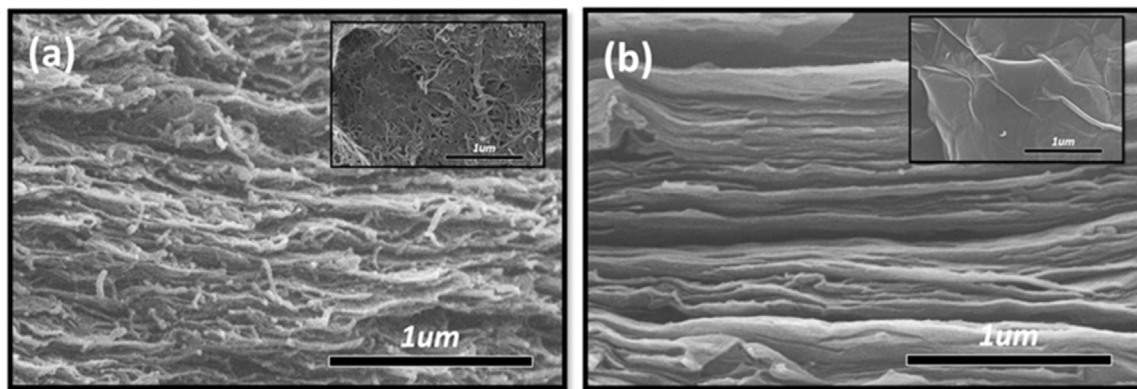


Fig. 25. SEM images of the rGO/CNT hybrid thin film; (a) cross-section view (Inset: basal plane view) and those of the rGO thin film electrode; (b) cross-section view (Inset: basal plane view). Reprinted with permission from Youn et al. (2014).

precipitated agglomerates forming its reduced form (rGO). The agglomeration usually decreases the active surface area and thus prevents the access of electrolyte ions into graphene sheets, deteriorating the final performance (Mao et al., 2012; Zhang et al., 2010). This problem might be circumvented by applying ESD. In the following part, carbon-based electrode materials, manganese oxide, ruthenium oxide, titanium-vanadium oxides, nickel oxide, and vanadium oxide composite electrodes made via ESD are summarised.

3.3.1. Carbon electrode materials for capacitors

Binder-free reduced graphene oxide (rGO)/carbon nanotube (CNT) hybrid thin film electrode were made using one-step ESD (Youn et al., 2014). Here the carbon nanotube was used as a nano-spacer to improve the electrochemical properties of the rGO/CNT hybrid thin film electrode, by sandwiching the CNT between the 2D rGO layers, so as to prevent restacking of the rGO sheets (Beidaghi & Wang, 2012). This was achieved by using a uniformly dispersed colloidal suspension of GO and CNTs in a mixture of water and ethanol by ultra-sonication. This dispersion then was used for the formation of the electrode by ESD with a suspension flow rate of 8–15 mL/h on a Pt-coated Si-wafers at 10–15 kV and 300 °C. Thus, sandwiching the CNT (Fig. 25) in the hybrid electrode increases the electrochemically effective surface area and also prevents agglomeration (restacking) of the rGO sheets. Cyclic voltammetry, galvanostatic charge/discharge test and electrochemical impedance spectroscopy, showed that the rGO/CNT hybrid electrode had better electrochemical performance than a plain rGO electrode in terms of specific capacitances and rate capabilities. The thin film electrode has a higher reversible specific capacitance of 187 F/g at 0.5 A/g and performed better having a rate capability and even showing 73% of the specific capacitance at 16 A/g (vs. 0.5 A/g) (see Fig. 26).

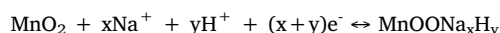
In another study, thin-film electrodes of graphene nano-platelets (GNPs) were fabricated with ESD. This combination of binder-free ESD using an open pore structure of graphene films results in an excellent power performance of the electrodes, as shown by cyclic voltammetry which showed almost rectangular curves even at a very high scan rate (Fig. 27). (Beidaghi, Wang, Gu, & Wang, 2012) A specific power and energy of about 75.46 kW/kg and 2.93 Wh/kg, respectively, at a 5 V/s scan rate was obtained for 1 μm thick electrodes, and about 53% of the initial specific capacitance of electrodes at low scan rates was retained at a scan rate of 20 V/s. The thickness of the thin-film electrodes had some influence on the rate capability, but even an electrode with a thickness of 6 μm retained about 30% if its initial capacitance at a very scan rate of 20 V/s. Hence, the GNP electrodes made with ESD proved to be promising as thin-films for energy storage.

3.3.2. Carbon nanotube (CNT) film electrodes

CNT film electrodes were fabricated by ESD from a CNT suspension, where acid treated CNTs were dispersed in an aqueous solvent through sonication. This suspension then was sprayed onto a metallic substrate (Kim, Nam, Ma, & Kim, 2006). The thin film electrodes showed well-entangled and interconnected porous structures which adhere well to the metallic substrate (Fig. 28). A specific capacitance of 108 F/g was obtained for the electrodes in 1 M H₂SO₄ at high rate capability (Fig. 28).

3.3.3. Mn_xO_y electrode materials

The focus here is on nanostructured manganese oxide layers without carbon additives deposited on stainless steel substrates. The electrochemistry of the layers is mainly affected by the MnO₂ morphology, resulting from the spraying conditions. The preferred stoichiometry of the manganese oxide is MnO₂, with a valence of 4+. A thermal treatment alone on the layers was not sufficient, but further oxidizing to MnO₂ by electrochemical means, revealed a significant improvement of the capacitance properties (Fig. 29a). This was explained by a change in morphology upon electrochemically annealing, leading to fine MnO₂ nanorods. The actual redox reactions are then:



The specific capacitance measured with cyclic voltammetry decreased of the non-electrochemically treated samples runs from 330

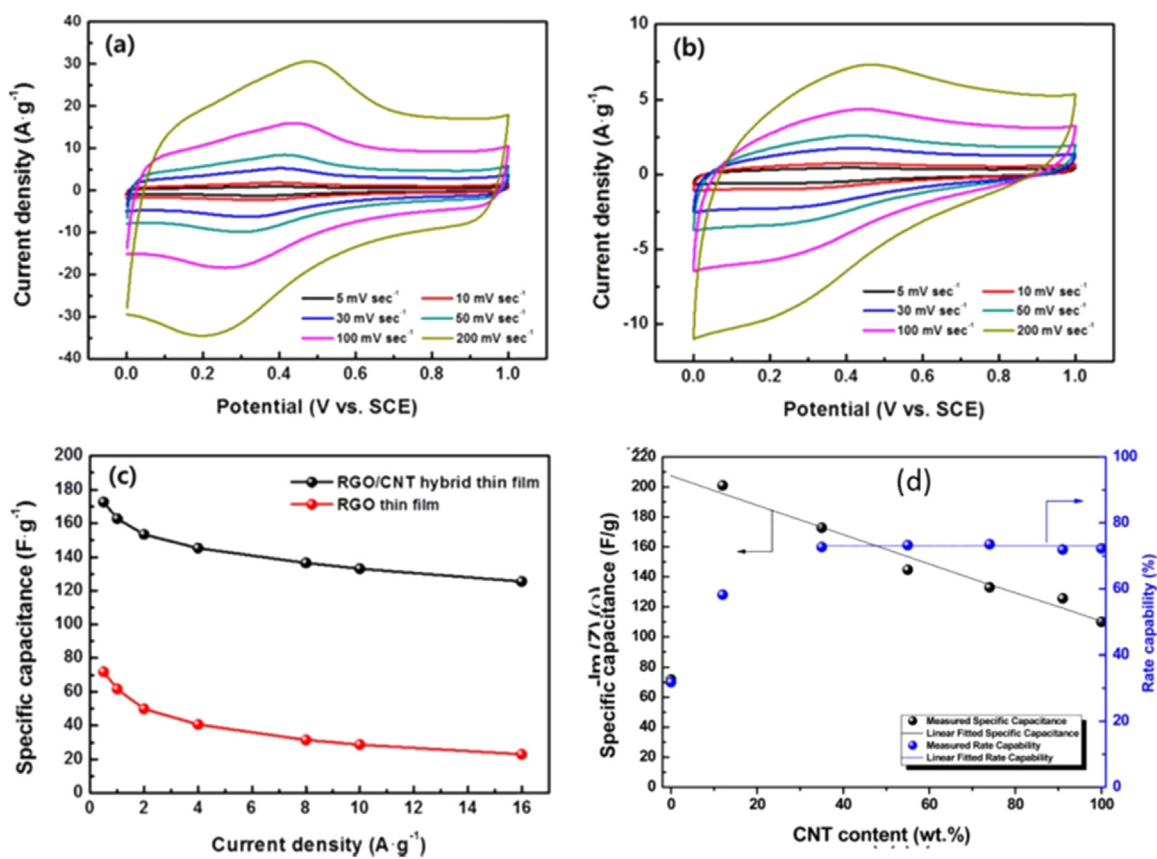


Fig. 26. Cyclic voltammograms of (a) the rGO thin film electrode and (b) the rGO/CNT hybrid electrode at various scan rates (5–200 mV/s). (c) The rate capabilities of the rGO thin film and rGO/CNT hybrid thin film electrode. (d) Specific capacitance and high rate capability of the rGO/CNT hybrid electrodes as a function of CNT content, pure rGO and pure CNT electrodes. Reprinted with permission from [Youn et al. \(2014\)](#).

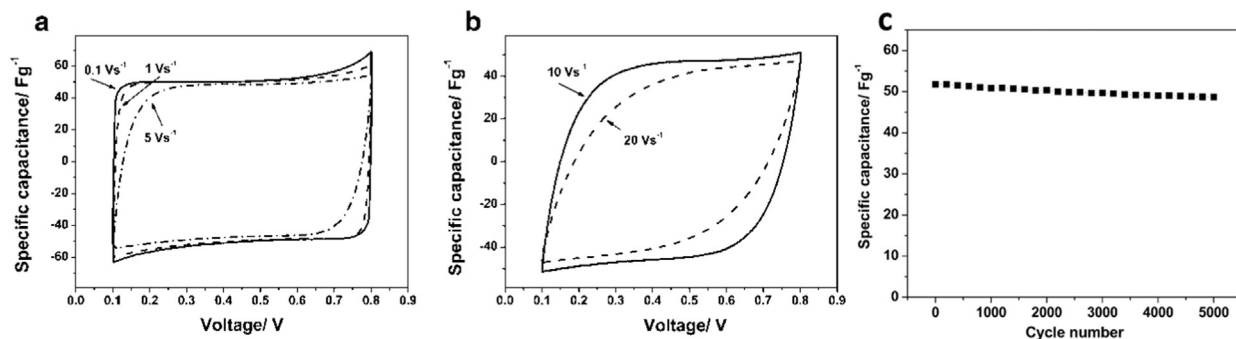


Fig. 27. Cyclic voltammograms recorded in 1 M Na_2SO_4 (vs. Ag/AgCl) of GNP electrodes at scan rates ranging from 0.1 to 20 V/s of a 1- μm -thick electrode (a, b). Cyclic stability tested at a 0.1-V/s CV scan rate (c). Reprinted with permission from [Beidaghi et al. \(2012\)](#).

down to 150 F/g with increasing loading of the active mass, i.e. 18–116 $\mu\text{g}/\text{cm}^2$, respectively ([Marsalek et al., 2015](#)). The electrochemically oxidized layers exhibited specific capacitances over 150 F/g ([Fig. 29](#)), which are comparable to the results published by other research groups, but here made with less expensive materials.

In another study forming MnO_2 via ESD ([Dai, Wan, Zhao, & Xie, 2006](#)), the hydrated MnO_2 film deposited at 230 °C from a KMnO_4 precursor solution is porous and cracked according to the SEM results. A specific capacitance of a thick deposited film was 149 F/g recorded at a scan rate of 500 mV/s and 200 F/g at a scan rate of 5 mV/s, showing good cyclic performance. The initial specific capacitance was 163 F/g and showed a 103% of the initial specific capacitance, which could be retained after 10,000 cycles at a scan rate of 50 mV/s. Here too, the specific capacitance decreased from 267 to 135 F/g by increasing the load of active mass from 0.06 to 0.2 mg/cm^2 .

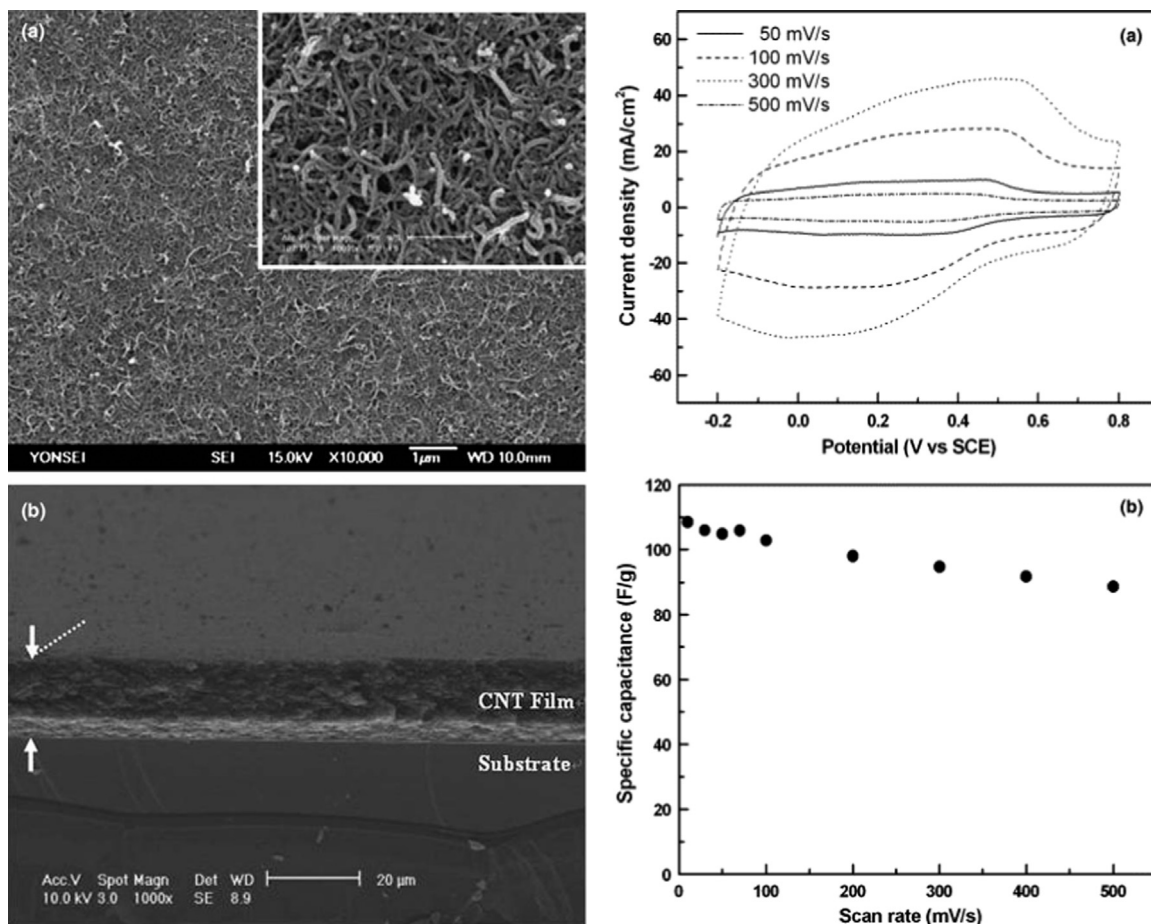


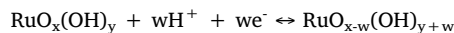
Fig. 28. Left panel: SEM images of (a) plane and (b) cross section views of CNT film electrode. Right panel: (a) Cyclic voltammograms and (b) specific capacitance of a CNT film electrode as a function of the potential scan rate. Reprinted with permission from Kim et al. (2006).

3.3.4. VO_2/TiO_2 electrode materials

Binder-free electrodes of VO_2/TiO_2 nano-sponges, having easily tailored nano-architectures and composition, were synthesized by ESD (Hu et al., 2015). To form the metal oxide nano-architectures as layers, an ethanol solution of NH_4VO_3 and oxalic acid was made at 70 °C, and another ethanol solution of titanium(IV)isopropoxide with acetic acid. Combinations of both solutions were prepared referred to as VT1 (Ti/V = 4), VT2 (Ti/V = 2), and VT3 (Ti/V = 1). To further dilute the solution, 40 mL 1, 2-propylene was added. Aluminium foils, nickel foams, and glass slides were used as substrates. ESD was done at a substrate temperature kept at 260 °C, with a distance between substrate and nozzle of 3 cm. Residual carbonaceous substances were oxidized by annealing at 350 °C in air for 15 min followed by an thermal treatment at 500 °C under 5% NH_3/Ar atmosphere for 90 min. The obtained VO_2/TiO_2 nano-sponges (Fig. 30) showed an interconnected pore network and thereby a synergistic effect of the high capacity of VO_2 and the stability of TiO_2 . The electrode exhibits a capacity of 86.2 mF/cm^2 (~548 F/g) and a cycleability with 84.3% retention after 1000 cycles (Fig. 30).

3.3.5. RuO_2 electrode materials

Ruthenium oxide thin films were fabricated by ESD with a precursor solution of $\text{RuCl}_3 \cdot x\text{H}_2\text{O}$ in a mixture of 80 vol% butyl carbitol and 20 vol% ethanol at a substrate temperature of 200 °C (Fig. 31) (Kim & Kim, 2004). The electrochemical protonation may be the most responsible process for the redox reaction of anhydrous ruthenium oxide thin film, according to:



The specific capacitance at a potential scan rate of 20 mV/s was 500 F/g and it decreased slightly with increasing potential scan rate up to 200 mV/s, also showing an excellent rate capability (Fig. 31).

Similar results were obtained by (Kim & Kim, 2001) using a one-step process ESD process to easily control the surface morphology. The as-prepared hydrated RuO_2 ($\text{RuO}_2 \cdot x\text{H}_2\text{O}$) thin films were amorphous, but become crystalline after annealing at temperatures > 200 °C. $\text{RuO}_2 \cdot x\text{H}_2\text{O}$ thin film electrode annealed at 200 °C showed a cyclic voltammogram indicative of a typical capacitive behaviour in 0.5 M H_2SO_4 electrolyte at a scan rate of 20 mV/s with an average specific capacitance of 650 F/g. The average specific capacitance was 640 F/g at 2 mV/s and 600 F/g at 50 mV/s, respectively, indicating that the average specific capacitance

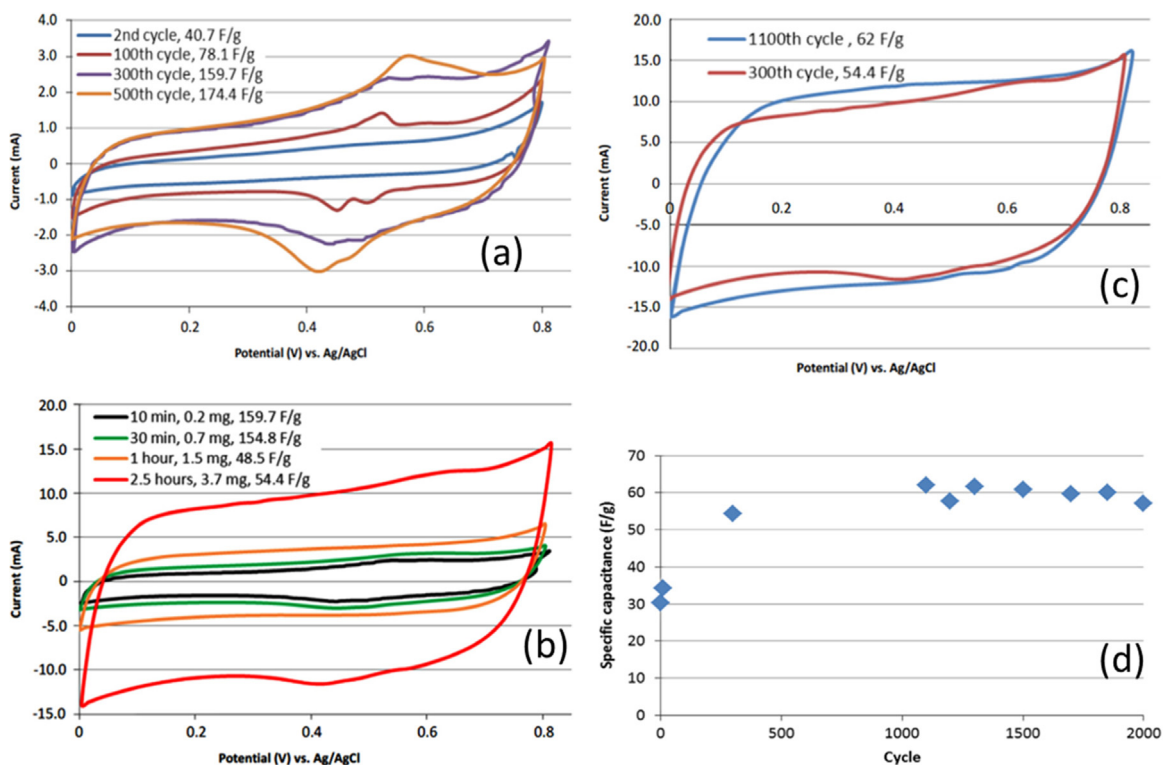


Fig. 29. (a) Voltammograms for a Mn_xO_y layer (0.2 mg/cm^2) deposited for 10 min (b) 300th cycle voltammograms for layers deposited for different periods. (c) 300th and 1100th cycle voltammogram for a layer deposited for 2.5 h. (d) Evolution of specific capacitance of the layer deposited for 2.5 h during cycling. Reprinted with permission from Marsalek, Chmelar, Pcedic, and Kosek (2015).

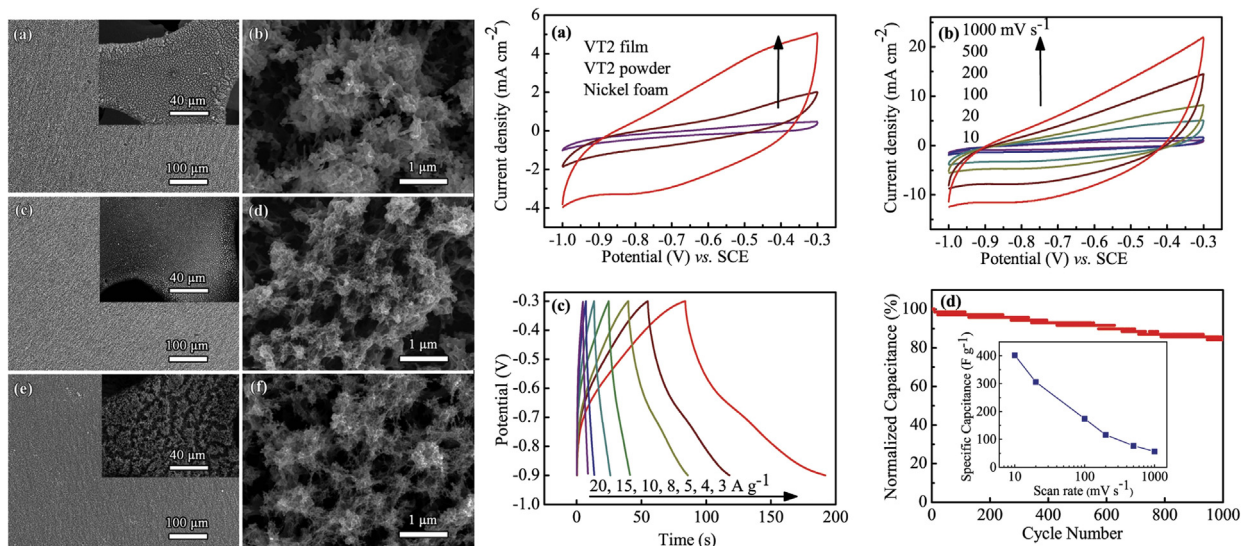


Fig. 30. Left panel: SEM images of VT films on Al-foil. (a, b) VT1, (c,d) VT2, and (e, f) VT3. The insets show films on Ni-foam. Right panel: Electrochemical performance of the VT2 film. CV curves for (a) the VT2 film, the VT2 powder and the Ni-foam (scan rate of 100 mV/s), and (b) the VT2 film at scan rates of 10, 20, 100, 200, 500, and 1000 mV/s . (c) Galvanostatic charge-discharge curves of the VT2 film at current densities of 3, 4, 5, 8, 10, 15, and 20 A/g . (d) Cycling performance at a current density of 10 A/g over 1000 cycles - the inset shows the specific capacitance as a function of the scan rate. Reprinted with permission from Hu et al. (2015).

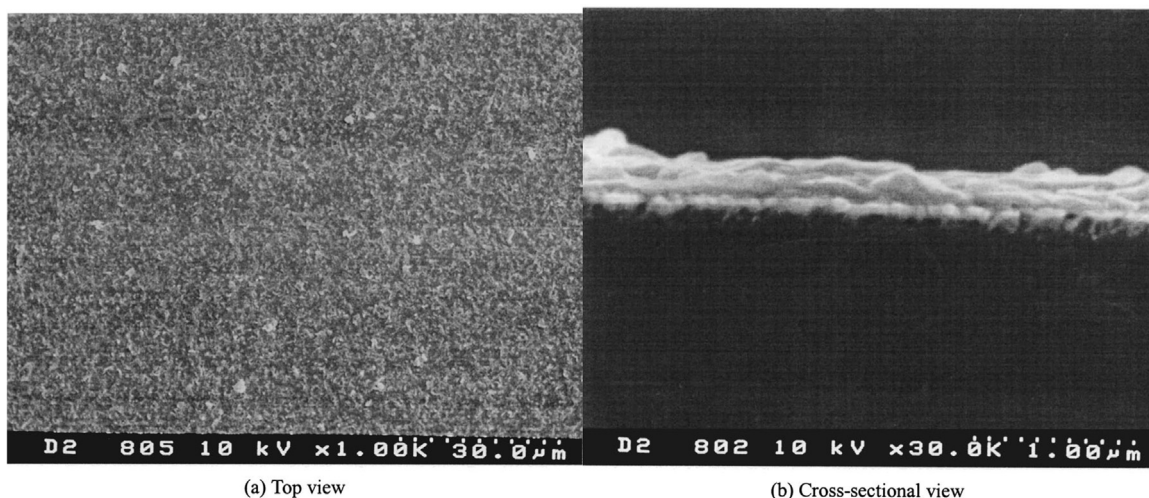


Fig. 31. SEM images of RuO₂ thin film prepared at 200 °C: (a) Top view, and (b) cross-section view. Reprinted with permission from Kim & Kim, (2004).

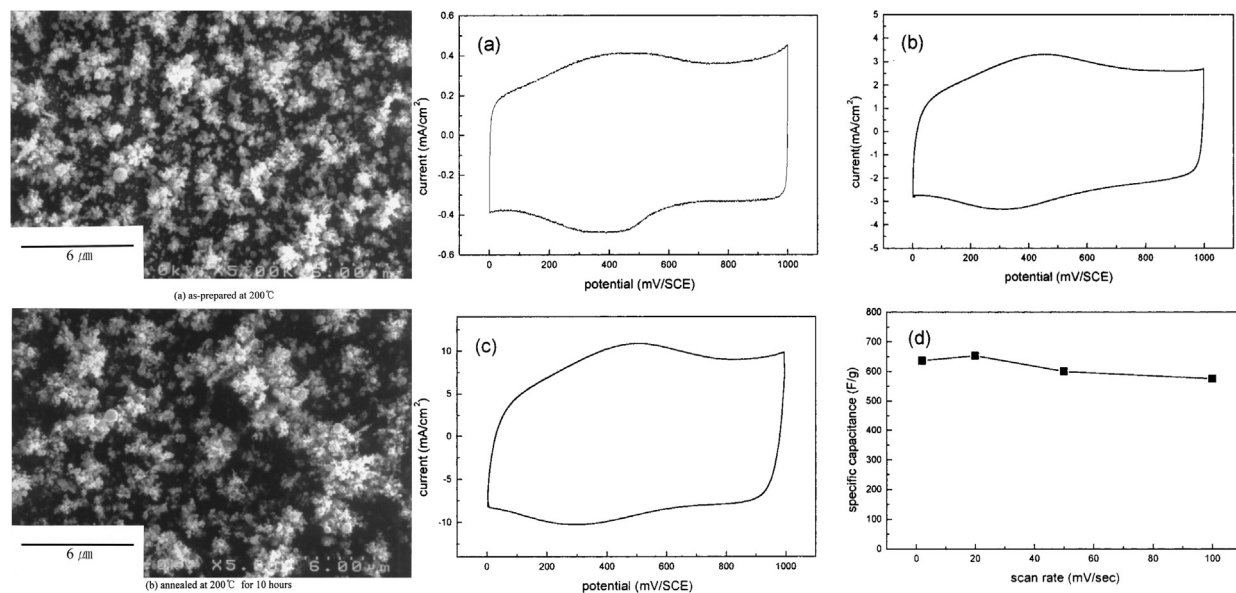


Fig. 32. Left panel: SEMs of ruthenium oxide thin film electrode for (a) as-prepared at 200 °C and (b) Right panel: CVs of ruthenium oxide thin film electrode annealed at 200 °C in 0.5 M H₂SO₄ at a scan rate of (a) 2 mV/s, (b) 20 mV/s, (c) 50 mV/s, (d) specific capacitance of ruthenium oxide thin film electrode at different scan rates. Reprinted with permission from Kim & Kim, (2001).

decreased only slightly with increasing scan rate (Fig. 32).

3.3.6. NiO@rGO electrode materials

A binder-free NiO@rGO composite supported on nickel foams was fabricated by ESD. A suspension of GO and nickel acetate was prepared in 1,2-propylene glycol (Zhang et al., 2015). A nickel foam substrate was heated to 250 °C, and the deposition was done with a flow rate of 3 mL/h at 20 kV. Then, the black nickel foam was rinsed several times and dried in air afterwards. The loading mass was about 0.8 mg/cm². The NiO nanoparticles were uniformly anchored onto the layered rGO sheets, thereby improving the electrolyte–electrode accessibility, allowing high electrochemical utilization of the NiO by maintaining open nano-channels of the composites (Fig. 33). This thus led to a high specific capacitance of 881 F/g at a current density of 0.5 A/g and about 75.7% of the capacitance was retained by increasing the current density to 50 A/g. Even after cycling for 3000 cycles at 20 A/g, 95% of the initial capacitance was delivered (Fig. 33).

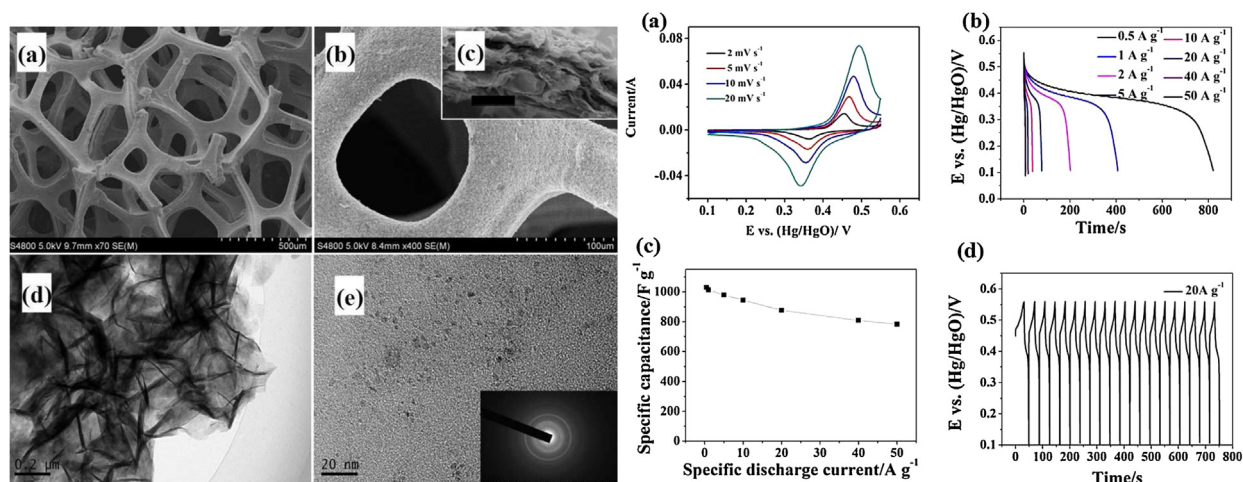


Fig. 33. Left panel: (a–b) SEM images, (c) cross-section SEM image, scale bar equals 600 nm, (d–e) TEM images and SAED pattern (inset) of the NiO@rGO composites. Right panel: (a) Cyclic voltammograms (b) Galvanostatic discharge curves of NiO@rGO composite films (c) Specific capacitances calculated from the discharge curves, (d) the galvanostatic charge-discharge curves at 20 A/g. Reprinted with permission from Zhang et al. (2015).

3.3.7. V_2O_5 electrode materials

In another study (Lee et al., 2017), polyacrylonitrile (PAN)/multi-walled carbon tube (MWNT) heteromat-mediated ultrahigh capacitance electrode sheets were used as an unusual electrode architecture. Here, vanadium pentoxide (V_2O_5) is applied as an electrode material to proof its feasibility. V_2O_5 electrode sheets are thus fabricated by a one-pot method via electrospinning (for V_2O_5 precursor/MWNT) and electrospinning (for PAN nanofiber) followed by calcination at 250 and 300 °C, so as to arrive at amorphous (V-250) or crystalline (V-300) V_2O_5 (Fig. 34). The heteromat V_2O_5 electrode sheets then offer 3D bicontinuous electron conduction pathways, facilitating the necessary redox reaction kinetics of V_2O_5 . The electrochemical reaction in V_2O_5 electrodes can be expressed as follows:



wherein x is the mole fraction of reacted K^+ ions.

Electrochemical data are collected in Fig. 35, where the caption explains the actual results. A substantially increase in the (electrode sheet-based) specific gravimetric electrode capacitances was obtained e.g. 134 F/g_{electrode} compared to 29 F/g_{electrode} for a reference V_2O_5 electrode, recorded at scan rate of 1 mV/s. Hence, the V_2O_5 electrode gave an significant increase of the specific energy/power densities as shown in the Ragone plot.

4. ESD for energy conversion devices ((O)LEDs and quantum dots)

The new generation of light sources light emitting diodes (LEDs) and organic light-emitting diodes (OLEDs), including polymer light-emitting diodes (PLEDs) attracted considerable attention as used in solid lighting devices. (O)LEDs are more efficient than most traditional light sources due to their long lifetime, high reliability, and high efficiency, making these interesting in many applications. Besides, they seem to be environmental friendly, due to use of less toxic materials. Recently, the research has focused on new methods of fabricating flexible, low-cost electronic components and devices, other than the (O)LEDs, e.g. flexible displays, organics photovoltaics (OPV), organic thin film transistors (OTFT), etc. Obviously, these products require mass and continuous production, such as the roll-to-roll (R2R) printing or coating. Among the employed techniques, non-contact coating methods, such as spray coating via, ESD and aerosol jet etc. are one of the most widely used. Only very recently, continuous and large area coating becomes available for future mass production (Kim et al., 2010a, 2010b). It remains however, important to realise that the surface roughness issue needs to be sougled out in order to arrive at a much more homogeneity in the layer thickness (Hwang, Bae, & Kim, 2014).

4.1. ESD for LEDs

Today's LEDs have efficiencies around 20% where the remaining energy is converted into heat at the junctions of the LED modules (Kuo, Auner, & Wu, 1994; Lee et al., 2005b; Shanmugan, Mutharasu, & Haslan, 2014). Unfortunately then, insufficient heat dissipation in LEDs, reduces the emission efficiency and also shortens a LED lifetime. Hence, thermal management is an important strategy to overcome these shortcomings. One of the solution is to form an isolation layer with very low thermal conductivity, which then gives a junction between the LED and metal Printed Circuit Board (PCB), providing a large thermal resistance, so the generated heat is rapidly transferred to a heat sink. Various ceramic interlayers showed improvements for the thermal conductivity of the base substrates and thus the performance of the device (Figuroa, Salas, & Oseguera, 2005; Yang et al., 2014; Yin, Tseng, & Zhao, 2013; Zheng, Ren, Li, & Wang, 2012). One of the solutions is an aluminium nitride (AlN) coating used for heat dissipation in the packaging

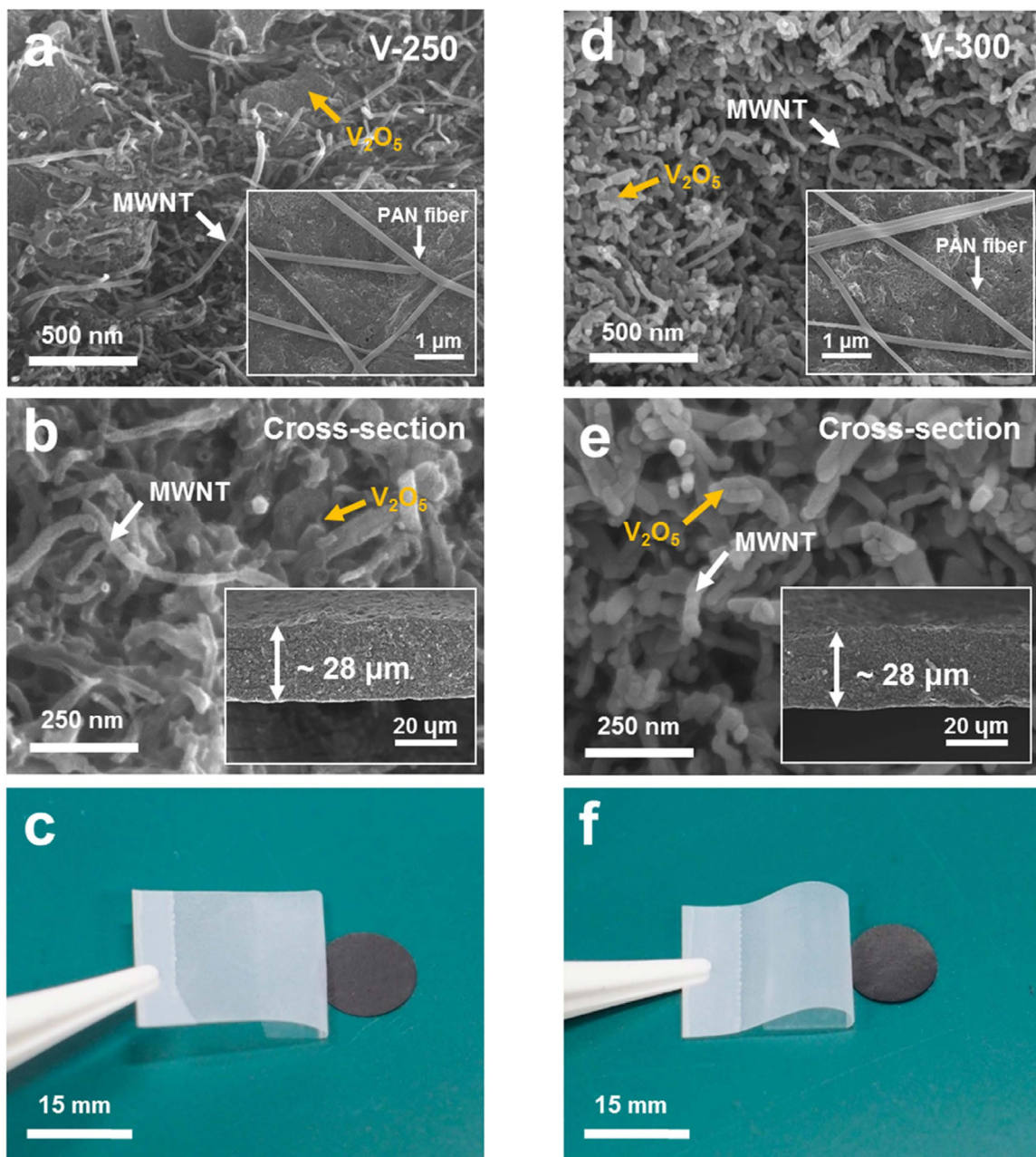


Fig. 34. Morphological characterization of V_2O_5 layers as defined in the text: (a-c) V-250 and (d-f) V-300 electrode sheets. (a,d) SEM surface images showing homogeneous dispersion of V_2O_5 , MWNTs and PAN nanofibers – the insets are low-magnification photos. (b,e) SEM cross-section images. (c,f) An adhesion test using commercial 3M scotch® tape. Reprinted with permission from Lee et al. (2017)

of LEDs, since this material has a high optical transparency and is chemically and thermally stable (Figuroa et al., 2005; Li, Ren, & Sun, 2007; Rada & Triplett, 2010; Rada, Triplett, Graham, & Kovaleski, 2008; Shen, Zhu, & Wang, 2015; Shinde & Goela, 2006; Zheng et al., 2012; Zuo, North, & Wert, 2001). However, as in many other new devices, cost reduction is an important requirement. Electrostatically sprayed AlN coatings, as a heat sink on Cu and Al substrates, provide the requirements for the electronics industry, as a highly conductive material with reasonable production costs (Jean, Jiang, Xu, & Chien, 2016). Applying these in a 1.2 W LED at 700 mA, the effect of the thermal resistance (R_{ja}) and the thermal performance such as cooling are shown in Fig. 36. The figure shows the temperature distribution during operation for 60 min and after switching off the current. It was further observed that R_{ja} for the Cu is greater than that for the Al substrate, i.e. $16.2^\circ\text{C}/\text{w}$ and $15.1^\circ\text{C}/\text{w}$, respectively. These results demonstrate that the temperature of the LED packages is significantly reduced if there is an AlN-coated Al substrate at a current of 700 mA, fabricated via ESD (Fig. 36).

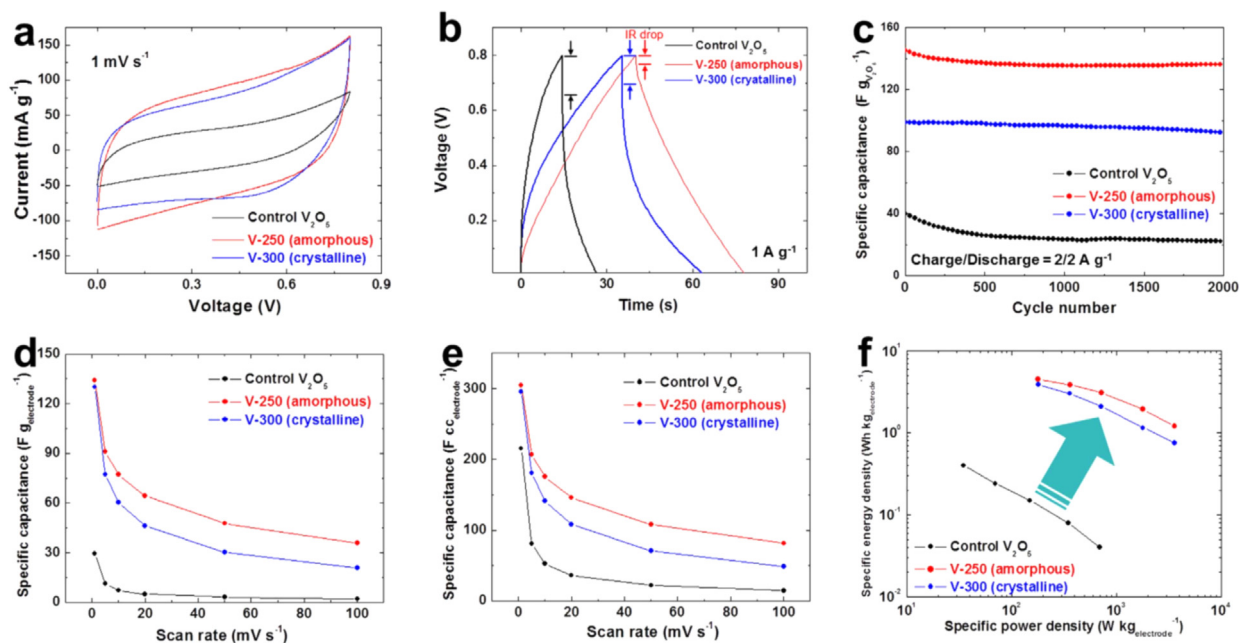


Fig. 35. Cyclic voltammety curves showing typical Faradaic pseudocapacitive behaviour, measured at a scan rate of 1 mV/s (a), galvanostatic charge/discharge profiles measured at 1.0 A/cm² (b), comparison in cycling performance between the different electrodes measured at 2.0 A/g (c), comparison in the (electrode sheet-based) specific gravimetric capacitance (F/g) between the different electrodes vs scan rate (d), comparison in the (electrode based) specific volumetric capacitance (F/cc) between the different electrodes vs scan rate (e), and a Ragone plot, with the cell weight taken as the electrode sheet weight only. Reprinted with permission from Lee et al. (2017).

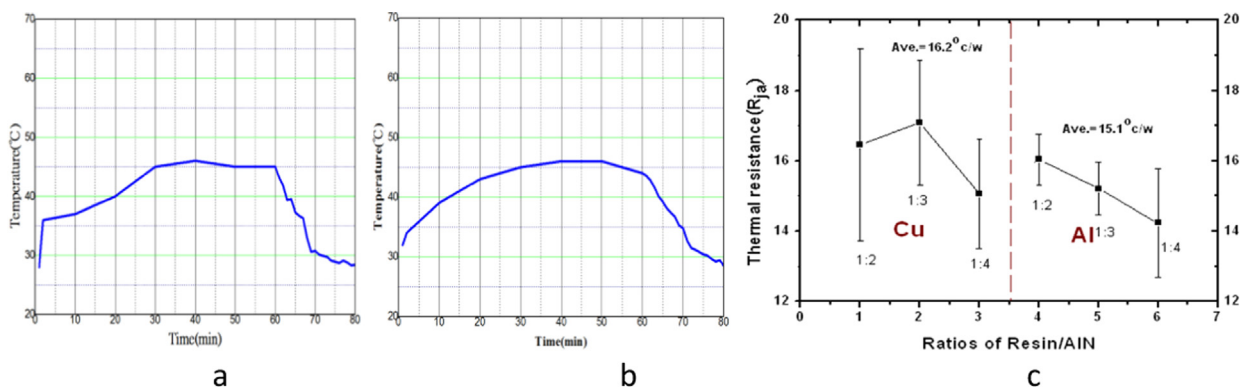


Fig. 36. Temperature profiles of an AlN coated Cu (a) and an Al (b) substrate, measured during applying a 700 mA current and after switching it off after 60 mins. A comparison of (R_{ja}) for a 1.2 W LED on AlN-coated Cu and Al substrates (c). Reprinted with permission from Jean et al., 2016.

4.2. ESD for OLEDs

(O)LEDs have attracted enormous interest, because they are light and flexible compared to more state-of-the-art inorganic electroluminescence (EL) materials used in the LEDs. Typically, there are two fabrication methods of thin-film OLEDs, e.g. vacuum deposition of low-molecular-weight organics, and casting polymer materials from solution, where the low-molecular-weight organic ELs are made via vacuum deposition, and the polymer-type OLEDs are then manufactured via casting. It however needs to mention that polymer materials are usually difficult to evaporate, making fabrication of a multi-layered structure complicated when using low-molecular-weight organics. Also, the solvents used for layer-to-layer deposition affects the interfaces by mutual dissolution. Therefore, ESD is an interesting alternative with great potential, where even patterning can be done. This patterning was carried out with a dichlorobenzene (DCB) solvent to form an Emissive layer (EML) on top of an ITO glass (Lee, Nguyen, Gim, & Ko, 2015). Here, the distance between the quartz nozzle with a 211 μm diameter and the substrate was 50–100 μm . The line patterning width was controlled by the distance between the nozzle and the substrate, under the cone-jet mode as shown in Fig. 37. Hence, the results proved that inkjet printing via ESD is a versatile method for optimal patterning to draw very narrow lines, with a jetting fluid diameter of only 15 μm , even after drying.

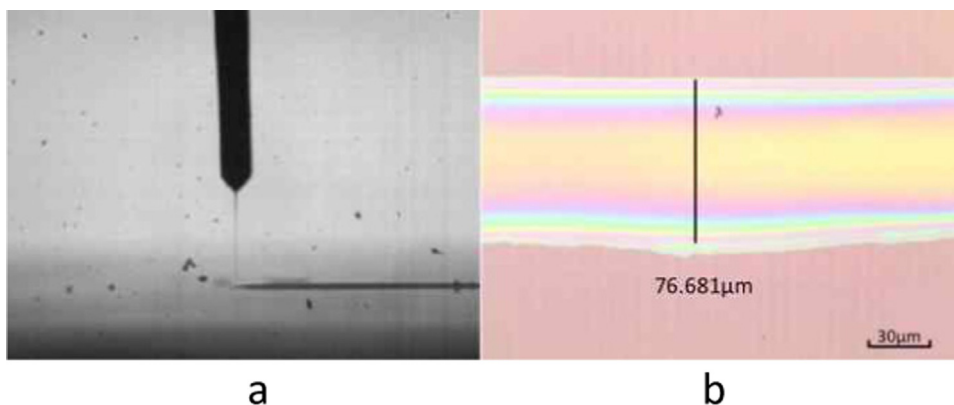


Fig. 37. Results of the patterning with dichlorobenzene solvent, an outside nozzle diameter of 211 μm , and a Jet thickness of 15 μm ; the ejection from the nozzle (a) and the patterned line (b). Reprinted with permission from Lee et al., 2015.

Table 2

Ratio of the PLED ink – data taken from Hwang et al. (2012).

	Ink 1 ^a	Ink 2 ^a
Poly(N-vinyl carbazole (PVK)	61	41.5
2-(4-biphenyl)-5-(4-tert-butylphenyl)-1,3,4-oxadiazole (PBD)	24	41.5
N,N'-diphenyl-N,N'-bis(3-methylphenyl)-[1,1'-biphenyl]-4,4'-diamine (TPD)	9	14.8
tris(2-(4-tolyl)phenylpyridine)iridium (Ir(mppy) ₃)	6	4.2

The difference between Ink1 and 2 is the ratio of hole and electron transport materials.

^a Each value refers to weight percentage of material in solution.

Table 3

Summary of device performances – data taken from Hwang et al. (2012).

Process	Ink	Solvent	EML (nm)	Cd/A (max)	Lm/W (max)
Spin coating	Ink1	CB	78	24	10.0
ESD	Ink1	CB/DCB (5:3)	100	15	6.0
ESD	Ink1	CB/DCB (5:3)	120	18	6.6
ESD	Ink2	CB/DCB (5:3)	70	18	7.5
ESD	Ink2	CB/DCB (5:3)	100	24	9.2
ESD	Ink2	CB/DCB (1:1)	103	23	8.6

EML: emissive layer; CB: chlorobenzene; DCB: dichlorobenzene.

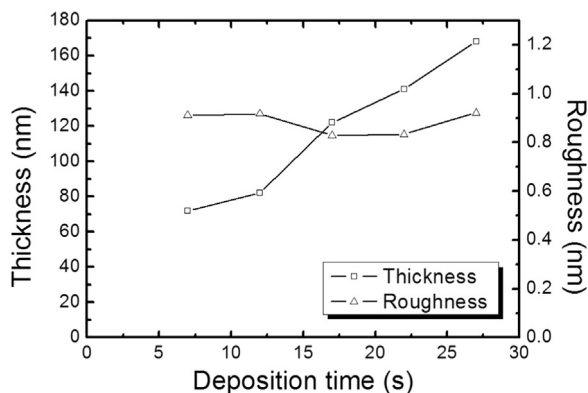


Fig. 38. PVK film thickness and roughness as a function of deposition time. Reprinted with permission from Ref. Hwang et al. (2012).

ESD was also used to deposit an organic layer for polymer organic light-emitting diode devices (Hwang, Xin, Cho, Cho, & Chae, 2012). The electro spray was used to produce nanometer-scale thin films via micro-sized droplets. PLED were thus made using a blended solution of either poly(N-vinyl carbazole) (PVK), 2-(4-biphenyl)-5-(4-tertbutylphenyl)-1,3,4-oxadiazole (PBD),

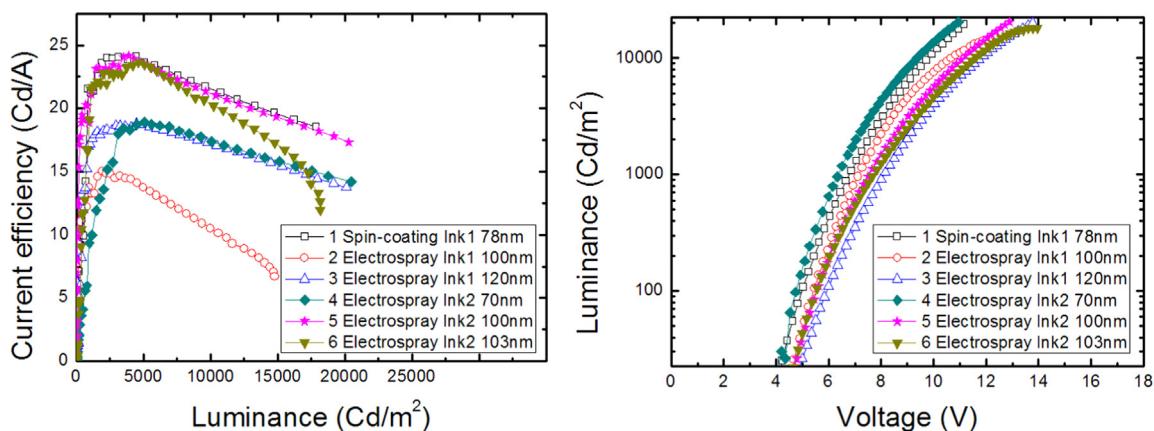


Fig. 39. Device performance made by spin-coating and ESD. The thicknesses of the EMLs are given in the insets. Reprinted with permission from Hwang et al. (2012).

N,N'-diphenyl-N,N'-Bis(3-methylphenyl)-[1,1'-biphenyl]-4,4'-diamine (TPD), and tris(2-(4-tolyl) phenylpyridine) iridium (Ir(mppy)₃) dissolved in chlorobenzene (CB), DCB, or a mixture of CB and 1,2-DCB. Two inks were applied as shown in Table 2 and Table 3.

Fig. 38 shows that a 70–150 nm thick light-emitting organic layers was formed with about 1 nm surface roughness. The photoluminescence (PL) at 407 nm was observed using electro sprayed poly(N-vinyl carbazole) films, whereas a peak at 410 nm was observed with the spin-coated ones. Similar difference in peak position was observed between aromatic and nonaromatic solvents in the spin-coating process.

PLED devices were manufactured with a ratio of PVK/PBD/TPD/Ir(mppy) = 61:24:9:6 (ink 1) for both the spin-coating and electro spray processes. With respect to the solvents, CB works best for the spin-coating process and DCB for the electro spray process. In Fig. 39, the current-voltage characteristics of the PVK film using different solvents and processing methods is shown. Samples with similar thickness, fabricated with aromatic solvents (mixtures of chlorobenzene, CB and dichlorobenzene, DCB) showed a higher

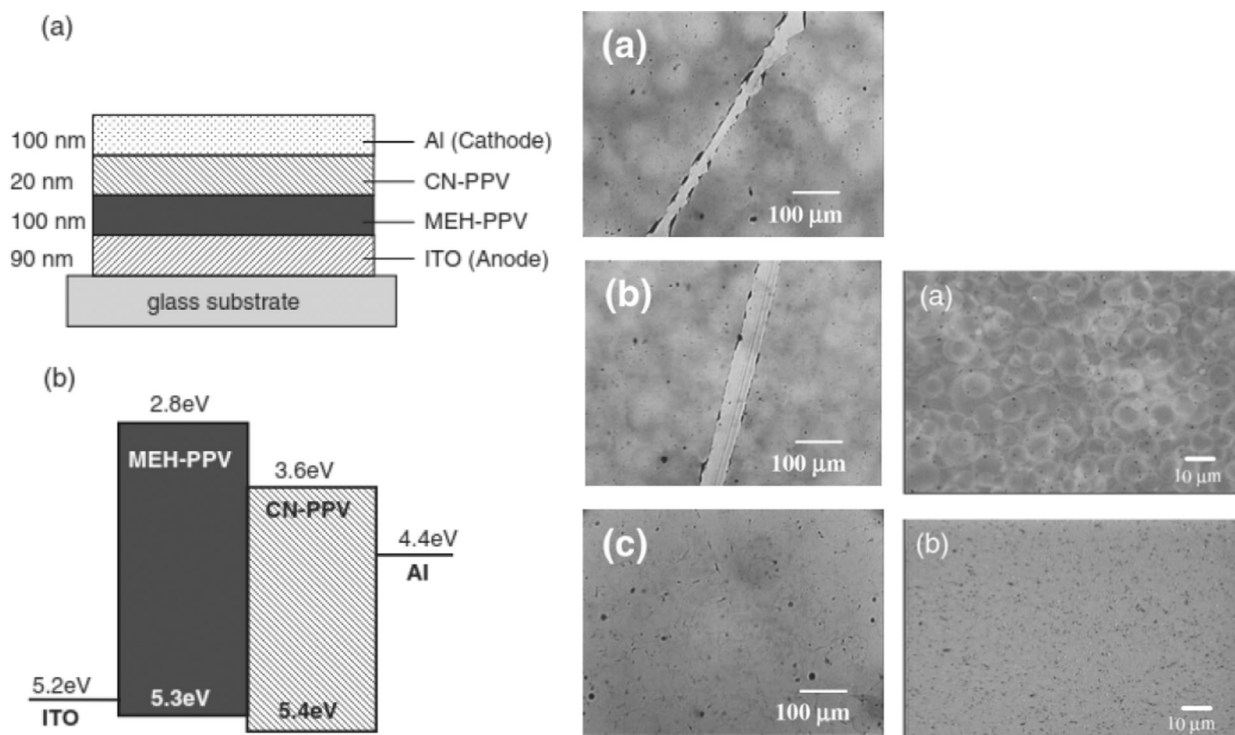


Fig. 40. Left panel: (a) Target multi-layered OLED structure and (b) energy diagram. Middle panel: Micrographs of MEH-PPV film surface formed by ESD. The ratios of MEH-PPV in o-DCB at 0.6 wt% to acetone were (a) 2:1, (b) 1:2, and (c) 1:5. The center line in (a) and (b) are scratches marked for thickness measurements. Right panel: Micrographs of MEH-PPV surfaces formed by ESD with nozzle inner diameters of 100 mm (a) and 30 mm (b). Reprinted with permission from Anzai et al., 2012.

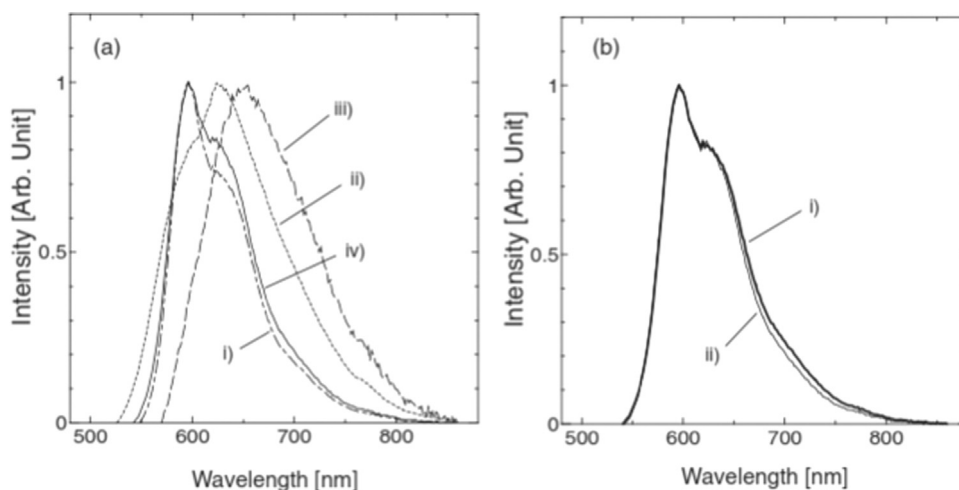


Fig. 41. (a) Fluorescence spectra of MEH-PPV (i), CN-PPV (ii), mixture of MEH-PPV and CN-PPV via spin-coating (iii), and CN-P Quantum DotsPV/MEH-PPV double layer formed by ESD (iv). (b) Spectra obtained from linear combination of CN-PPV and MEH-PPV (i) and spectra with a ratio of 1:4 and CN-PPV/MEH-PPV double layer (ii). Reprinted with permission from Anzai et al., 2012.

current density than those fabricated with a nonaromatic solvent (1, 2-dichloroethane, DCE). Also the PVK film made by electrospray showed a lower current density than that of spin-coated ones. Besides, these results proof that the PVK thin films were affected by the processing method and the molecular structure of the solvent as shown Fig. 39. Hence, it is possible to fabricate layers by electrospray with similar properties as with spin-coating by adjusting the solvent, i.e. they showed maximum current efficiency of 24 Cd/A, which is comparable with that of the spin-coating process.

In another study (Anzai, Watanabe, & Sakamoto, 2012), ESD was applied for manufacturing an overlayer on a thin film made via spin-coating so as to form a laminate structure. Unfortunately, the ESD process is not suitable for stacking various layers without any mixing effect (Fig. 40).

In this study, the emitted droplet size was minimized by the use of adding acetone to the solution. Two different polymer materials were used for the fabrication of the multi-layered structure. The first one was poly[2-methoxy-5-(2ethylhexyloxy)-1,4-phenylenevinylene] (MEH-PPV) and the second one was poly[2,5-di(hexyloxy)cyanoterephthalydene] (CN-PPV), but each of the materials was dissolved in an *o*-dichlorobenzene (*o*-DCB) solvent at a 0.6 and 0.4 wt%, respectively. PEDOT:PSS was then used to equalise and homogenise the indium tin oxide (ITO) glass substrate. The middle panel of Fig. 40 displays optical micrographs of the MEH-PPV film surface at various ratios of the original solution to acetone, showing the impact of the acetone. The nozzle to substrate distance was 8 cm, and the spray time was taken 1 h. The spectra in Fig. 41 were obtained from various mixed films of MEH-PPV and CN-PPV prepared by either successive spin coating or ESD. It turns out that for the ESD deposited films the mixed films of MEH-PPV and CN-PPV are clear linear combinations in contrast to the spin-coated samples. This obviously made clear that the double-layer structure is in place.

4.3. Quantum dots

Luminescent properties can also be achieved by introducing Quantum Dots (QDs) in chalcogenide glass films, where e.g. the QD-doped glass layer then serves as a compact, on-chip light source for planar photonic devices (Li et al., 2017). ESD in that respect is a

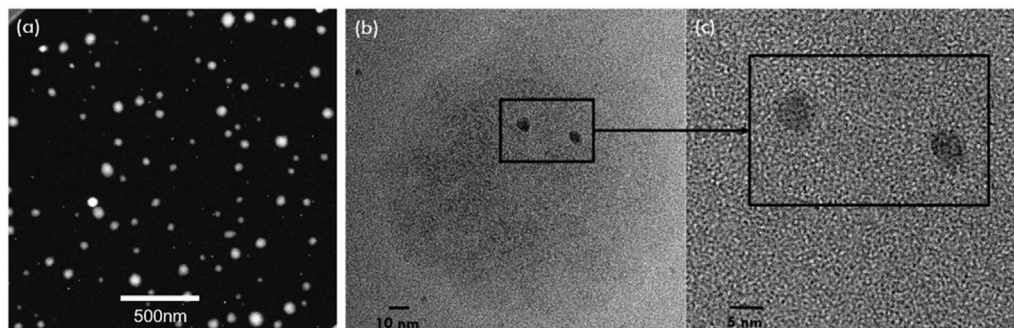


Fig. 42. TEM images of gold NPs doped $\text{Ge}_{23}\text{Sb}_7\text{S}_{70}$ made by ESD. (a) Dispersion of $\text{Ge}_{23}\text{Sb}_7\text{S}_{70}$ droplets; (b) evidence of a ~ 100 nm diameter droplet containing two gold NPs; (c) higher magnification showing NP size of nominally 5–10 nm. Reprinted with permission from Li et al., 2017.

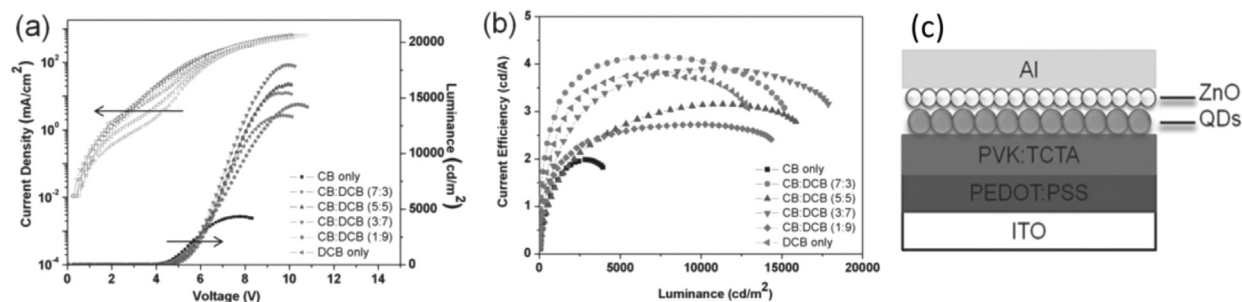


Fig. 43. ElectroLuminescence characteristics of QD-LEDs obtained with CB, DCB and the CB:DCB mixtures as solvents: a) I–V–L characteristics and b) current efficiency of the QD-LEDs fabricated by ESD, and (c) QD-LED device structure (ITO/PEDOT:PSS/(PVK:TCTA) (20 wt%)/QDs/ZnO/Al) Reprinted with permission from Ho et al. (2014).

versatile method from these layers as typically, well established methods as spin coating lead to excessive material waste, show little control on the pattern of the film and has difficulties in scaling-up. Here the concentration of the QDs in the ESD-solvent was chosen to ensure one or none QD is present per liquid droplet. The transmission electron microscopy images of the films proof QD dispersion with reduced 10 nm gold NPs and 5 nm QDs aggregations (Fig. 42). This dispersion is attributed to the isolation of an individual QD in one droplet and the way the solvent has been vaporised during the time of flight. Photoluminescence spectra of the films of chalcogenide glass doped with QDs reveals similar emission results as reported by the manufacturer.

Green-red (GR) and blue-red (BR) bilayer stacked quantum dots (QDs) were made via ESD, in a for large-scale, high throughput, uniform thin film fabrication system without using any annealing process (Yin et al., 2017). The morphology of the thin film is controlled by varying the flow rate, voltage (3.5–4.5 kV), distance between the substrate and electrode (~4 cm) and the deposition time (20 s). Here then, appropriate QDs were dispersed in solvents (hexane: octane = 4:1) and sprayed onto 1 cm² quartz collectors, so as to form a layer by layer stack. Nevertheless, for the mixed samples, equimolar B (or G) and R QDs were suspended in the solvents in advance., and those were sprayed for 40 s. The photo-behaviour of these QDs was analysed with several techniques and the observed results are then ascribed to the energy transfer between different visible QDs (heterotransfer), and were estimated as 0.57 ± 0.01 and 0.65 ± 0.02 ns for GR and BR systems, respectively, which agree well with theoretical calculations. It was further shown that with respect to their geometrical proximity, the mixed QD layers with GR and BR had qualitatively higher heterotransfer efficiencies of 64% and 81%, compared to stacked QD layers, with efficiencies of 23% and 64%, respectively.

In another study (Ho, Kim, Kim, Cho, & Chae, 2014) it was shown that QDs for LED fabrication using ESD leading to nanoscale thin QD-layers (25 nm) and smooth surfaces (roughness ~3.16 nm) has significant benefits including simple and flexible control, low cost, large-scale processability, and compatibility for multiple-layer-structure devices such as QD-LEDs. These layers were formed by a mixture of two aliphatic liquids as solvent (hexane: octane = 4:1). The ZnO nanoparticles were dispersed in ethanol (Fig. 43). The QD-LED demonstrated a maximum luminance of 23 000 cd/m² (see Fig. 43), a maximum current efficiency of ~6.0 cd/A, and a FWHM of about 35 nm. Hence, ESD proved to a promising process for the fabrication of multiple-layer-structured devices for a direct and nearly dry patterning for commercial production, as compared to the spin-coating process, where CB and DCB solvents cannot be used since they dissolve the underlying organic hole transport layers. Hence, it confirms the strength of ESD where these solvent can be easily employed, with minimal damage of the underlying organic layers.

5. Conclusions

In this review it was shown that electrohydrodynamic atomization (EHDA) or electrospraying stands out in thin film deposition (ESD) in different areas, such as solar cells, photoelectrochemical cells, rechargeable batteries, capacitors, and (O)LEDs as well as for the formation of layers for using quantum dots. Since charge transfer of either electrons or ions is an important issue for electrodes in those devices, the morphology of it, is of utmost importance, because it will reflect the exchange area for these charge carriers. Obviously, with ESD, several morphologies were achieved to suit the various requirements, so as to mention: flat, rough (porous), and reticular structures. Furthermore, the method of ESD is flexible as it allows non- or poor volatile precursors to use once dissolved in solution – provided the solvent is able to be atomised. This then opens up the possibility to form materials with complex compositions as is often seen in today's devices with improved performance.

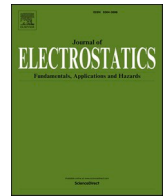
References

- Abbas, T. A., Slewa, L. H., Khizir, H. A., & Kakil, S. A. (2017). Synthesis of cobalt oxide (Co₃O₄) thin films by electrostatic spray pyrolysis technique (ESP). *The Journal of Materials Science: Materials in Electronics*, 28, 1951–1957.
- Abernathy, C., Bates, C., Jr., Anani, A., Haba, B., & Smestad, G. (1984). Production of single phase chalcopyrite CuInSe₂ by spray pyrolysis. *Applied Physics Lett*, 45, 890.
- Agostinho, L. L. F. (2013). *Electrohydrodynamic atomization in the simple-jet mode out-scaling and application (Ph.D. thesis)*. Delft, The Netherlands: Delft University of Technology (ISBN 978-90-6464-635-5).
- Ahn, S., Kim, C., Yun, J. H., Gwak, J., Jeong, S., Ryu, B.-H., & Yoon, K. (2010). CuInSe₂ (CIS) thin film solar cells by direct coating and selenization of solution precursors. *The Journal of Physical Chemistry C*, 114, 8108–8113.

- Ali, M., Abbas, M., Shah, S. K., Tuerhong, R., Generosi, A., Paci, B., ... Gunnella, R. (2012). Realization of solution processed multi-layer bulk heterojunction organic solar cells by electro-spray deposition. *Organic Electronics*, 13, 2130–2137.
- Altamura, G., Wang, M., & Choy, K.-L. (2015). Improving efficiency of electrostatic spray-assisted vapor deposited $\text{Cu}_2\text{ZnSn}(\text{S,Se})_4$ solar cells by modification of Mo/absorber interface. *Thin Solid Films*, 597, 19–24.
- Anzai, H., Watanabe, Y., & Sakamoto, T. (2012). *Japanese Journal of Applied Physics*, 51, 6S.
- Barrows, A. T., Pearson, A. J., Kwak, C. K., Dunbar, A. D. F., Buckley, A. R., & Lidzey, D. G. (2014). *Energy & Environmental Science*, 7, 2944–2950.
- Beidaghi, M., & Wang, C. (2012). Micro-supercapacitors based on interdigital electrodes of reduced graphene oxide and carbon nanotube composites with ultrahigh power handling performance. *Advanced Functional Material*, 22, 4501–4510.
- Beidaghi, M., Wang, Z. F., Gu, L., & Wang, C. L. (2012). Electrostatic spray deposition of graphene nanoplatelets for high-power thin-film supercapacitor electrodes. *The Journal of Solid State Electrochemistry*, 16, 3341.
- Bodnár, E., Grifoll, J., & Rosell-Llompert, J. (2018). Polymer solution electro-spraying: A tool for engineering particles and films with controlled morphology. *Journal of Aerosol Science* (present issue, pp to be filled).
- Bougnot, J., Duchemin, S., & Savelli, M. (1986). Chemical spray pyrolysis of CuInSe_2 thin films. *Solar Cells*, 16, 221.
- Burschka, J., Pellet, N., Moon, S. J., Humphry-Baker, R., Gao, P., Nazeeruddin, M. K., & Grätzel, M. (2013). *Nature*, 499, 316–319.
- Cao, F., & Prakash, J. (2002). A comparative electrochemical study of LiMn_2O_4 spinel thin-film and porous laminate. *Electrochimica Acta*, 47, 1607–1613.
- Castillo, J., Martin, S., Rodriguez-Perez, D., Higuera, F., & Garcia-Ybarra, P. (2018). Nanostructured porous coatings via electro-spray atomization and deposition of nanoparticle suspensions. *Journal of Aerosol Science* (present issue, pp to be filled).
- Chandrasekhar, P. S., Kumar, N., Swami, S. K., Dutta, V., & Komarala, V. K. (2016). Fabrication of perovskite films using an electrostatic assisted spray technique: The effect of the electric field on morphology, crystallinity and solar cell performance. *Nanoscale*, 8, 6792–6800.
- Chen, C. H., Buysman, A. A. J., Kelder, E. M., & Schoonman, J. (1995). Fabrication of LiCoO_2 thin film cathodes for rechargeable lithium battery by electrostatic spray pyrolysis. *Solid State Ionics*, 80, 1–4.
- Chen, C., Kelder, E. M., van der Put, P. J. J. M., & Schoonman, J. (1996a). Morphology control of thin LiCoO_2 . *Journal of Materials Chemistry*, 6(5), 765–771.
- Chen, C. H., Kelder, E. M., Jak, M. J. G., & Schoonman, J. (1996b). Electrostatic spray deposition of thin layers of cathode materials for lithium battery. *Solid State Ionics*, 86–88, 1301–1306.
- Cho, S. H., Hwang, S. W., Kim, B. H., Bae, K. Y., & Yoon, W. Y. (2016). Electrochemical properties of Li metal batteries with P (PEGMA)-coated lithium trivanadate cathode and Li power anode. *Journal of Nanoscience and Nanotechnology*, 16(10), 10607–10612.
- Chung, K. Y., Shu, D., & Kim, K. B. (2004). Determination of the potential range responsible for the replacement of surface film on LiMn_2O_4 . *Electrochimica Acta*, 49(6), 887–898.
- Chung, K. Y., Ryu, C.-W., & Kim, K.-B. (2005). Onset mechanism of Jahn-Teller distortion in 4 V LiMn_2O_4 and its suppression by $\text{LiM}_{0.05}\text{Mn}_{1.95}\text{O}_4$ (M = Co, Ni) coating. *Journal of the Electrochemical Society*, 152, A791.
- Dai, Y., Wan, K., Zhao, J., & Xie, J. (2006). Manganese oxide film electrodes prepared by electrostatic spray deposition for electrochemical capacitors from the KMnO_4 solution. *Journal of Power Sources*, 161(1), 737–742.
- Damien, D., Anjusree, G. S., Sreekumaran Nair, A., & Shaijumon, M. M. (2016). TiO_2 fibre/particle nanohybrids as efficient anodes for lithium-ion batteries. *RSC Advances*, 6(51), 45802–45808.
- Dhanabalan, A., Li, X., Agrawal, R., Chen, C., & Wang, C. (2013). Fabrication and characterization of SnO_2 /graphene composites as high capacity anodes for Li-ion batteries. *Nanomaterials*, 3(4), 606–614.
- Docampo, P., Hanusch, F., Stranks, S. D., Doblinger, M., Feckl, J. M., Ehrensperger, M., ... Bein, T. (2014). *Advanced Energy Materials*, 4, 140035.
- Dokko, K., Anzue, N., Mohamedi, M., Itoh, T., & Uchida, I. (2004). Raman spectro-electrochemistry of $\text{LiCo}_x\text{Mn}_{2-x}\text{O}_4$ thin film electrodes for 5 V lithium batteries. *Electrochemistry Communications*, 6(4), 384–388.
- Eberspacher, C., Fredric, C., Pauls, J., & Serra, K. (2001). Thin-film CIS alloy PV materials fabricated using non-vacuum, particles-based techniques. *Thin Solid Films*, 387, 18–22.
- Figueroa, U., Salas, O., & Oseguera, J. (2005). Deposition of AlN on Al substrates by reactive magnetron sputtering. *Surface Coating Technology*, 200, 1768–1776.
- Fujimoto, M., Kado, T., Takashima, W., Kaneto, K., & Hayase, S. (2006). Dye-sensitized solar cells fabricated by electro-spray coating using TiO_2 nanocrystal dispersion solution. *Journal of The Electrochemical Society*, 153(5), A826–A829.
- Fujimoto, K., Onoda, K., & Ito, S. (2007a). Exploration of layered-type pseudo four-component Li-Ni-Co-Ti oxides. *Applied Surface Science*, 254(3), 704–708.
- Fujimoto, K., Onoda, K., & Ito, S. (2007b). High-throughput preparation and characterization of powder and thin-film library for electrode materials. *Materials Science Forum*, 534–536, 469–472.
- Fujimoto, K., Ikezawa, K., & Ito, S. (2011). Charge–discharge properties of a layered-type $\text{Li}(\text{Ni},\text{Co},\text{Ti})\text{O}_2$ powder library. *Science and Technology of Advanced Materials*, 12(5), 54203.
- Fukuda, T., Takagi, K., Asano, T., Honda, Z., Kamata, N., Ueno, K., ... Tajima, Y. (2011). Bulk heterojunction organic photovoltaic cell fabricated by the electro-spray deposition method using mixed organic solvent. *Physica Status Solidi, RRL5*, 229–231.
- Fukuda, T., Takagi, K., Asano, T., Honda, Z., Kamata, N., Shirai, H., ... Tajima, I. Y. (2012). Improved power conversion efficiency of organic photovoltaic cell fabricated by electro-spray deposition method by mixing different solvents. *Japanese Journal of Applied Physics*, 51, 1–5.
- Fukuda, T., Toda, A., Takahira, K., Suzuki, K., Liao, Y., Hirahara, M., ... Osaka, I. (2016). Molecular ordering of spin-coated and electro-sprayed P3HT: PCBM thin films and their applications to photovoltaic cell. *Thin Solid Films*, 612, 373–380.
- Fukuda, T., Toda, A., Takahira, K., Kuzuhara, D., & Yoshimoto, N. (2017). Improved performance of organic photovoltaic cells with PTB7-Th: PC71 BM by optimized solvent evaporation time in electro-spray deposition. *Organic Electronics*, 48, 96–105.
- Ganan-Calvo, A., Lopez-Herrera, J., Herrada, M., Ramos, A., & Montanero, J. M. (2018). Review on the physics of electro-spray: From electrokinetics to the operating conditions of Taylor cone-jets, and beyond. *Journal of Aerosol Science* (present issue, pp to be filled).
- García-Tamayo, E., Valvo, M., Lafont, U., Locati, C., Munao, D., & Kelder, E. M. (2011). Nanostructured Fe_2O_3 and CuO composite electrodes for Li ion batteries synthesized and deposited in one step. *Journal of Power Sources*, 196(15), 6425–6432.
- Ho, M. D., Kim, N., Kim, D., Cho, S. M., & Chae, H. (2014). CdSe/ZnS quantum dot thin film formation by an electro-spray deposition process for light-emitting devices. *Small*, 10, 4142–4146.
- Hu, C. C., Xu, H., Liu, X., Zou, F., Qie, L., Huang, Y., & Hu, X. (2015). VO_2/TiO_2 nanosponges as binder-free electrodes for high performance supercapacitors. *Scientific Reports*, 5, 16012.
- Hu, G., Deng, X., Peng, Z., Du, K., Cao, Y., Liu, Z., & Xiao, Z. (2008). Co/Mn-coated LiNiO_2 cathode materials by solid-state reaction at room temperature. *Rare Metal Materials and Engineering*, 37(11), 1881–1886.
- Hu, H., Wang, D., Zhou, Y., Zhang, J., Lv, S., Pang, S., ... Cui, G. (2014). *RSC Advanced*, 4, 28964–28967.
- Hwang, J. K., Bae, S., & Kim, D. S. (2014). A development and evaluation of micro-gravure coater for printed electronics. *Japanese Journal of Applied Physics*, 53, 5S3.
- Hwang, W., Xin, G., Cho, M., Cho, S. M., & Chae, H. (2012). Electro-spray deposition of polymer thin films for organic light-emitting diodes. *Nanoscale Research Letters*, 7, 52.
- Jaworek, A., & Sobczyk, A. T. (2008). Electro-spraying route to nanotechnology: An overview. *Journal of Electrostatics*, 66, 197–219.
- Jaworek, A., Sobczyk, A. T., Krupa, A., Lackowski, M., & Czech, T. (2009). Electrostatic deposition of nanothin films on metal substrate. *Bulletin of the Polish Academy of Sciences Technical Sciences*, 57, 1.
- Jaworek, A., Sobczyk, A. T., & Krupa, A. (2018). Electro-spray application to powder production and surface coating. *Journal of Aerosol Science* (present issue, pp to be filled).
- Jean, M.-D., Jiang, J.-B., Xu, M.-S., & Chien, J.-Y. (2016). Using AlN-coated heat sink to improve the heat dissipation of LED packages. *MATEC Web of Conferences*, 71, 04005.
- Jeon, N. J., Lee, H. G., Kim, Y. C., Seo, J., Noh, J. H., Lee, J., & Seok, S. I. (2014a). *Journal of the American Chemical Society*, 136, 7837–7840.

- Jeon, N. J., Noh, J. H., Kim, Y. C., Yang, W. S., Ryu, S., & Seok, S. I. (2014b). *Natural Materials*, 13, 897–903.
- Jeon, N. J., Noh, J. H., Yang, W. S., Kim, Y. C., Ryu, S., Seo, J., & Seok, S. I. (2015). *Nature*, 517, 476–480.
- Kim, I.-H., & Kim, K.-B. (2001). Ruthenium oxide thin film electrodes for supercapacitors. *Solid State Letters*, 4(5), A62–A64.
- Kim, I.-H., & Kim, K.-B. (2004). Ruthenium oxide thin film electrodes prepared by electrostatic spray deposition and their charge storage mechanism. *Journal of The Electrochemical Society*, 151, E7–E13.
- Kim, J. H., Nam, K. W., Ma, S. B., & Kim, K. B. (2006). Fabrication and electrochemical properties of carbon nanotube film electrodes. *Carbon*, 44(10), 1963–1968.
- Kim, J.-S., Chung, W.-S., Kim, K., Kim, D. Y., Paeng, K. J., Jo, S. M., & Jang, S. Y. (2010). Performance optimization of polymer solar cells using electrostatically sprayed photoactive layers. *Advanced Functional Materials*, 20, 3538–3546.
- Kim, J. S., Choi, K. H., Kim, K. D., Kim, C. H., Bae, S. W., & Kim, D. S. (2010). An application of ESD technology for the R2R printing process. *Journal of Mechanical Science and Technology*, 24, 301.
- Kim, Y., Kim, G., Lee, J., & Lee, K. (2012). Morphology controlled bulk-heterojunction layers of fully electro-spray coated organic solar cells. *Solar Energy Materials & Solar Cells*, 105, 272–279.
- Kim, Y., Lee, L., Kang, H., Kim, G., Kim, N., & Lee, K. (2012). Controlled electro-spray deposition of highly conductive PEDOT: PSS films. *Solar Energy Materials & Solar Cells*, 9, 39–45.
- Koike, S., & Tatsumi, K. (2007). Preparation and performances of highly porous layered LiCoO_2 films for lithium batteries. *Journal of Power Sources*, 174(2), 976–980.
- Krishna, K. V., Dutta, V., & Paulson, P. D. (2003). Effect of electric field on spray deposited CdTe thin films. *Thin Solid Films*, 444, 17–22.
- Kuo, P. K. G., Auner, W., & Wu, Z. L. (1994). Microstructure and thermal conductivity of epitaxial AlN thin films. *Thin Solid Films*, 253, 223–227.
- Lafont, U., Anastasopol, A., Garcia-Tamayo, E., & Kelder, E. M. (2012). Electrostatic spray pyrolysis of $\text{LiNi}_{0.5}\text{Mn}_{1.5}\text{O}_4$ films for 3D Li-ion microbatteries. *Thin Solid Films*, 520(9), 3464–3471.
- Largeot, C., Portet, C., Chmiola, J., Taberna, P., Gogotsi, Y., & Simon, P. (2008). Relation between the ion size and pore size for an electric double-layer capacitor. *Journal of the American Chemical Society*, 30, 2730.
- Lee, J., Liang, K., An, K., & Lee, Y. (2005a). Nickel oxide/carbon nanotubes nanocomposite for electrochemical capacitance. *Synthesis Metals*, 150, 153.
- Lee, J. H., Kim, J. A., Kim, J.-M., Lee, S.-Y., Yeon, S.-H., & Lee, S.-Y. (2017). Beyond slurry-cast supercapacitor electrodes: PAN/MWNT heteroatom-mediated ultrahigh capacitance electrode sheets. *Scientific Reports*, 7, 41708.
- Lee, J. W., Cuomo, J. J., Cho, Y. S., & Keusseyan, R. L. (2005b). Aluminum nitride thin films on an LTCC substrate. *The Journal of the American Ceramic Society*, 88(7), 1977–1980.
- Lee, S. H., Nguyen, X. H., Gim, Y., & Ko, S. K. (2015). Study on electrohydrodynamic jetting performance of organic solvents. *Journal of Mechanical Science and Technology*, 29, 4767.
- Lee, T., Cho, K., Oh, J., & Shin, D. (2007). Fabrication of LiCoO_2 cathode powder for thin film battery by aerosol flame deposition. *Journal of Power Sources*, 174, 394–399.
- Lee, W., Seol, D. J., Cho, A. N., & Park, N. G. (2014). High-Efficiency Perovskite Solar Cells Based on the Black Polymorph of $\text{HC}(\text{NH}_2)_2\text{PbI}_3$. *Advanced Materials*, 26, 4991–4998.
- Li, C., Novak, S., Denisov, S. A., McClenaghan, N. D., Patel, N., Agarwal, A., ... Deng, W. W. (2017). Electrostatic spray deposition of quantum dot-doped $\text{Ge}_{23}\text{Sb}_7\text{S}_{70}$ chalcogenide glass films. *Thin Solid Films*, 626, 194–199.
- Li, F., Jiao, Y., Xie, S., & Li, J. (2015). Sponge-like porous TiO_2/ZnO nanodots for high efficiency dye-sensitized solar cells. *Journal of Power Sources*, 280, 373–378.
- Li, X., Ren, Z. A., & Sun, D. Q. (2007). An investigation of nitrated layer prepared by direct current nitrogen arc discharge. *Materials Science and Engineering A*, 443, 219–223.
- Li, X., & Wang, C. (2013). Engineering nanostructured anodes via electrostatic spray deposition for high performance lithium ion battery application. *Journal of Materials Chemistry A*, 1(2), 165–182.
- Liu, M. Z., Johnston, M. B., & Snaith, H. J. (2013). *Nature*, 501, 395–398.
- Mao, S., Wen, Z. H., Kim, H. J., Lu, G. H., Hurkey, P., & Chen, J. H. (2012). A general approach to one-pot fabrication of crumpled graphene-based nanohybrids for energy applications. *ACS Nano*, 6, 7505.
- Marsalek, J., Chmelar, J., Pecedic, J., & Kosek, J. (2015). Morphological and electrochemical study of Mn_xO_y nanoparticle layers prepared by electrostatic spray. *Chemistry and Engineering Science*, 123, 292–299.
- Milliron, D., Mitzi, D., Copel, M., & Murray, C. (2006). Solution-processed metal chalcogenide films for p-type transistors. *Chemistry Materials*, 18, 587–590.
- Mitzi, D., Kosbar, L., Murray, C., Copel, M., & Afzali, A. (2004). High-mobility ultrathin semiconducting films prepared by spin coating. *Nature*, 428, 299.
- Mitzi, D., Copel, M., & Murray, C. (2006). High-mobility p-type transistor based on a spin-coated metal telluride semiconductor. *Advanced Materials*, 18, 2448.
- Mitzi, D., Yuan, M., Liu, W., Kellock, A., Chey, S., Deline, V., & Schrott, A. (2008). A high-efficiency solution-deposited thin-film photovoltaic device. *Advanced Materials*, 20, 3657.
- Mitzi, D., Yuan, M., Liu, W., Kellock, A., Chey, S., Gignac, L., & Schrott, A. (2009). Hydrazine-based deposition route for device-quality CIGS films. *Thin Solid Films*, 517, 2158–2162.
- Mohamed, M., Makino, M., Dokko, K., Itoh, T., & Uchida, I. (2002a). Electrochemical investigation of $\text{LiNi}_{0.5}\text{Mn}_{1.5}\text{O}_4$ thin film intercalation electrodes. *Electrochimica Acta*, 48, 79–84.
- Mohamed, M., Takahashi, D., Itoh, T., & Uchida, I. (2002b). Electrochemical stability of thin film LiMn_2O_4 cathode in organic electrolyte solutions with different compositions at 55 °C. *Electrochimica Acta*, 47, 3483–3489.
- Mohamed, M., Takahashi, D., Itoh, T., Umeda, M., & Uchida, I. (2002c). ESD fabricated thin films of spinel LiMn_2O_4 for lithium microbatteries: I. Effects of thickness. *Journal of The Electrochemical Society*, 149(1), A19.
- Mooney, J., & Radding, S. (1982). Spray pyrolysis processing. *Annual Review of Materials Science*, 12, 81.
- Neagu, R., Djurado, E., Ortega, L., & Pagnier, T. (2006). ZrO_2 -based thin films synthesized by electrostatic spray deposition: Effect of post-deposition thermal treatments. *Solid State Ionics*, 177, 1443–1449.
- Nie, W., Tsai, H., Asadpour, R., Blancon, J. C., Neukirch, A. J., Gupta, G., ... Mohite, A. D. (2015). *Science*, 347, 6221–6224.
- Nishizawa, M., Uchiyama, T., Dokko, K., Yamada, K., Matsue, T., & Uchida, I. (1998). Electrochemical studies of spinel LiMn_2O_4 films prepared by electrostatic spray deposition. *Bulletin of the Chemical Society of Japan*, 71(8), 2011–2015.
- Niu, S., Lv, W., Zhou, G., Shi, H., Qin, X., Zheng, C., ... Yang, Q. H. (2016). Electrostatic-spraying an ultrathin, multifunctional and compact coating onto a cathode for a long-life and high-rate lithium-sulfur battery. *Nano Energy*, 30, 138–145.
- Panthani, M. G., Akhavan, V., Goodfellow, B., Schmidtke, J. P., Dunn, L., Dodabalapur, A., ... Korgel, B. A. (2008). Synthesis of CuInS_2 , CuInSe_2 , and $\text{Cu}(\text{In}_x\text{Ga}_{1-x})\text{Se}_2$ (CIGS) nanocrystal “Inks” for printable photovoltaics. *Journal of the American Chemical Society*, 130, 16770.
- Park, S. E., Hwang, J. Y., Kim, K., Jung, B., Kim, W., & Hwang, J. (2011). Spray deposition of electrohydrodynamically atomized polymer mixture for active layer fabrication in organic photovoltaics. *Solar Energy Materials & Solar Cells*, 95, 352–356.
- Pognon, G., Brousse, T., Demarconnay, L., & Belanger, D. (2011). Performance and stability of electrochemical capacitor based on anthraquinone modified activated carbon. *Journal of Power Sources*, 196, 4117.
- Qu, B. H., Chen, Y. J., Zhang, M., Hu, L. L., Lei, D. N., Lu, B. A., ... Wang, T. H. (2012). Cobalt sulfide nanoparticles decorated graphene composite electrodes for high capacity and power supercapacitors. *Nanoscale*, 4, 7810.
- Rada, N., Triplett, G., Graham, S., & Kovaleski, S. (2008). High-speed thermal analysis of high power diode arrays. *Solid State Electronics*, 52, 10.
- Rada, N. M., & Triplett, G. E. (2010). Thermal and spectral analysis of self-heating effects in high-power LEDs. *Solid State Electronics*, 54, 4.
- Raja Ram, P., Thangaraj, R., & Agnihotri, O. P. (1986). Thin film $\text{CdZnS}/\text{CuInSe}_2$ solar cells by spray pyrolysis. *Bulletin Materials Science*, 8, 279.
- Ramesh, M., Boopathi, K. M., Huang, T. Y., Huang, Y. C., Tsao, C. S., & Chu, C. W. (2015). *ACS Applied Materials Interfaces*, 7, 2359–2366.
- Roncallo, S., Painter, J. D., Cousins, M., Lane, D., & Rogers, K. (2008). A method to quantify the degree of uniformity of thickness of thin films. *Thin Solid Films*, 516, 8493–8497.

- Rosell-Llompert, J., Grifoll, J., & Loscertales, I. (2018). Electrospays in the cone-jet mode: From Taylor cone formation to spray development. *Journal of Aerosol Science* (present issue, pp to be filled).
- Scheideler, W. J., & Chen, C.-H. (2014). The minimum flow rate scaling of Taylor cone-jets issued from a nozzle. *Applied Physics Lett*, 104, 024103.
- Shanmugan, S., Mutharasu, D. A., & Haslan, H. (2014). A study on AlN thin film as thermal interface material for high power LED. *International Journal of Electronics and Computer Science Engineering*, 2(1), 296–300.
- Shay, J., Wagner, S., & Kasper, H. (1975). Efficient CuInSe₂/CdS solar cells. *Applied Physics Lett*, 27, 89.
- Shen, W. Q., Zhu, Y. W., & Wang, G. L. (2015). Luminescent properties of Sr₄Si₃O₈Cl₄:Eu²⁺, Bi³⁺ phosphors for near UV InGaN-based light-emitting-diodes. *Applied Science*, 5, 1494–1502.
- Shinde, S. L., & Goela, J. (Eds.). (2006). *High Thermal Conductivity Materials* New York: Springer.
- Shirakata, S., Murakami, T., Kariya, T., & Isomura, S. (1996). Preparation of CuInSe₂ thin films by chemical spray pyrolysis. *Japanese Journal of Applied Physics*, 35, 191.
- Shu, D., Yoon, K., Il, W., & Kim, K. (2003). Electrochemical investigations on electrostatic spray deposited LiMn₂O₄ films. *Journal of Power Sources*, 114, 0–10.
- Shui, J. L., Jiang, G. S., Xie, S., & Chen, C. H. (2004). Thin films of lithium manganese oxide spinel as cathode materials for secondary lithium batteries. *Electrochimica Acta*, 49, 2209–2213.
- Shui, J. L., Yu, Y., Yang, X. F., & Chen, C. H. (2006). LiCoPO₄-based ternary composite thin-film electrode for lithium secondary battery. *Electrochem Commission*, 8(7), 1087–1091.
- Sun, Y., Zhang, L., Wang, S., Lieberwirth, I., Yu, Y., & Chen, C. (2013). Walnut-like vanadium oxide film with high rate performance as a cathode material for rechargeable lithium batteries. *Journal of Power Sources*, 228, 7–13.
- Tomar, M., & Garcia, F. (1982). A ZnO/p-CuInSe₂ thin film solar cell prepared entirely by spray pyrolysis. *Thin Solid Films*, 90, 419–423.
- van Zomeren, A. A., Kelder, E. M., Marijnissen, J. C. M., & Schoonman, J. (1994). The production of thin films of LiMn₂O₄ by electrospaying. *Journal of Aerosol Science*, 25(6), 1229–1235.
- Wang, H., Casalongue, H. S., Liang, Y., & Dai, H. J. (2010). Ni(OH)₂ nanoplates grown on graphene as advanced electrochemical pseudocapacitor. *Journal of the American Chemical Society*, 132, 7472.
- Wang, M., Sun, Y., Chen, H., Zhang, Y., Wu, X., Huang, K., & Feng, S. (2017). Enhanced photoelectrochemical activity of nanostructured ZnFe₂O₄ thin films prepared by the electrospay technique. *CrystEngComm*, 19, 772–775.
- Wu, J., Chen, C., Hao, Y., & Wang, C. (2015a). Enhanced electrochemical performance of nanosheet ZnO/reduced graphene oxide composites as anode for lithium-ion batteries. *Colloids and Surfaces A: Physicochemical and Engineering Aspects*, 468, 17–21.
- Wu, J., Qin, X., Zhang, H., He, Y. B., Li, B., Ke, L., & Kang, F. (2015b). Multilayered silicon embedded porous carbon/graphene hybrid film as a high performance anode. *Carbon*, 84(1), 434–443.
- Wu, J. B., Li, Z. G., & Lin, Y. (2011). Porous NiO/Ag composite film for electrochemical capacitor application. *Electrochimica Acta*, 56, 2116.
- Xiao, Z., Bi, C., Shao, Y., Dong, Q., Wang, Q., Yuan, Y., ... Huang, J. (2014). *Energy Environment Science*, 7, 2619–2623.
- Yang, K. S., Chung, C. H., Tu, C. W., Wong, C. C., Yang, T. Y., & Lee, M. T. (2014). Thermal spreading resistance characteristics of a high power light emitting diode module. *Applied Thermal Engineering*, 70(1), 361–368.
- Yin, S., Tseng, K. J., & Zhao, J. (2013). Design of AlN-based micro-channel heat sink in direct bond copper for power electronics. *Applied Thermal Engineering*, 52(1), 120–129.
- Yin, W., Kim, N., Jeong, J., Kim, K. S., Chae, H., & Ahn, T. K. (2017). Efficient heterotransfer between visible quantum dots. *Journal of Physics and Chemistry C*, 121(9), 4799–4805.
- Yoon, H., Woo, J. H., Joshi, B., Ra, Y. M., Yoon, S. S., Kim, H. Y., ... James, S. C. (2012). CuInSe₂ (CIS) thin film solar cells by electrostatic spray deposition. *Journal of The Electrochemical Society*, 159(4), H444–H449.
- Yoon, H., Na, S. H., Choi, J. H., Kim, M. W., Kim, H., An, H. S., ... Yoon, S. S. (2014). Carbon- and oxygen-free Cu(InGa)(SSe)₂ solar cell with a 4.63% conversion efficiency by electrostatic spray deposition. *Applied Materials Interfaces*, 6, 8369–8377.
- Yoon, H., Kim, M. W., Kim, H., Al-Dey, S. S., James, S. C., Ahn, S., & Yoon, S. S. (2015). Three dimensional web-like fibrous CuInS₂ film. *Applied Surface Science*, 351, 588–593.
- Yoon, W., Ban, S., Lee, K., Kim, K., Kim, M. G., & Lee, J. M. (2001). Electrochemical characterization of layered LiCoO₂ films prepared by electrostatic spray deposition. *Journal of Power Sources*, 97–98, 282–286.
- Yoon, W. S., Chung, K. Y., Oh, K. H., & Kim, K. B. (2003). Changes in electronic structure of the electrochemically Li-ion deintercalated LiMn₂O₄ system investigated by soft X-ray absorption spectroscopy. *Journal of Power Sources*, 119–121, 706–709.
- Youn, H. C., Bak, S. M., Park, S. H., Yoon, S. B., Roh, K. C., & Kim, K. B. (2014). One-step preparation of reduced graphene oxide/carbon nanotube hybrid thin film by electrostatic spray deposition for supercapacitor applications. *Metals and Materials International*, 20, 975–981.
- Yu, T., Lin, B., Li, Q., Wang, X., Qu, W., Zhang, S., & Deng, C. (2016). First exploration of freestanding and flexible Na₂₊₂Fe_{2-x}(SO₄)@porous carbon nanofiber hybrid films with superior sodium intercalation for sodium ion batteries. *Physics Chemistry Chemistry Physics*, 18, 26933.
- Yu, Y., Shui, J. L., Jin, Y., & Chen, C. H. (2006). Electrochemical performance of nano-SiO₂ modified LiCoO₂ thin films fabricated by electrostatic spray deposition (ESD). *Electrochimica Acta*, 51(16), 3292–3296.
- Yurteri, C. U., Hartman, R. P. A., & Marijnissen, J. C. M. (2010). Producing pharmaceutical particles via electrospaying with an emphasis on nano and nano structured particles - a review. *KONA Powder and Particle Journal*, 28, 91–115.
- Zangmeister, C. D. (2010). Preparation and evaluation of graphite oxide reduced at 220 °C. *Chemistry Materials*, 22, 5625.
- Zhang, H., Gua, D., Zhu, J., Li, Q., Chen, L., & Wang, T. (2015). A layer-by-layer deposition strategy of fabricating NiO@ rGO composites for advanced electrochemical capacitors. *Electrochimica Acta*, 152, 378–382.
- Zhang, M., Lei, D. N., Yin, X. M., Chen, L. B., Li, Q. H., Wang, Y. G., & Wang, T. H. (2010). Fast synthesis of SnO₂/graphene composites by reducing graphene oxide with stannous ions. *J Materials Chemistry*, 20, 5538.
- Zhao, X. Y., Wang, X., Lim, S. W., Qi, D., Wang, R., Gao, Z. Q., ... Deng, W. W. (2014). Enhancement of the performance of organic solar cells by electrostatic spray deposition with optimal solvent system. *Solar Energy Materials & Solar Cells*, 121, 119–125.
- Zheng, X., Ren, Z., Li, X., & Wang, Y. (2012). Microstructural characterization and mechanical properties of nitrided layers on aluminum substrate prepared by nitrogen arc. *Applied Surface Science*, 259, 508–514.
- Zhou, H., Chen Qi, L. G., Luo, S., Song, T. B., Duan, H. S., Hong, Z., & Yang, Y. (2014). Interface engineering of highly efficient perovskite solar cells. *Science*, 345, 542–546.
- Zuo, Z. J., North, M. T., & Wert, K. L. (2001). High heat flux heat pipe mechanism for cooling of electronics. *IEEE Transactions on Components and Packaging Technologies*, 24(2), 220–225.
- Zhu, C., Kopold, P., van Aken, P. A., Maier, J., & Yu, Y. (2016). High power-high energy sodium battery based on threefold interpenetrating network. *Advanced Materials*, 28, 2409–2416.



On the minimum and maximum flowrate of electro spraying: A practical approach, based on fundamentals, for design purposes

J.C.M. Marijnissen^a, C.U. Yurteri^{b,*}, S.W. Karuga^c, R.P.A. Hartman^d

^a Institute of Nuclear Science and Technology, University of Nairobi, P. O. Box 30197-00100, Nairobi, Kenya

^b B.A.T. (Investments) Limited, Regents Park Road, Millbrook, Southampton SO15 8TL, UK

^c Department of Electrical and Information Engineering, University of Nairobi, P. O. Box 30197-00100, Nairobi, Kenya

^d Baker Hughes, Delftechpark 26, Delft, 2628 XH, the Netherlands

ARTICLE INFO

Keywords:

Electrospray
Minimum flow rate
Maximum flow rate
Cone-jet mode
Cone-jet window
Correlations

ABSTRACT

The minimum and maximum flow rates (Q_{\min} , Q_{\max}) limit the operational window of electro spraying (cone-jet mode). Literature does not give a general, experimentally proven, useable formula. We derived with fundamental physics and curve fitting a relation between Q_{\min} and Q_o ($= \frac{\epsilon_o \gamma}{\rho K}$), for Newtonian liquids with low/moderately high viscosities. The formula is corroborated by own experiments and data from literature. With the formula Q_{\min} can be obtained by only measuring some properties of the liquid to be sprayed. Q_{\max} is difficult to address. An empirical result and experimental data indicate a ratio of Q_{\max}/Q_{\min} between some tens and some hundreds.

1. Introduction

Nowadays Electrohydrodynamic Atomization (EHDA) or Electro spraying is a well established technique. Numerous papers on the subject have been published including review articles. In one of the review articles, written by Ref. [1]; a methodology to produce nano and micro particles with EHDA in the so called Cone-Jet mode, via scaling laws as developed by Refs. [2,3] is discussed. Appendix 1 gives a short summary. However, what is not treated in the article is the well-known fact that to work in the Cone-Jet mode the applied liquid flowrate (Q) has to be equal or above a certain minimum value, Q_{\min} . Besides a Q_{\min} there exists also a maximum flow rate, to stay in the Cone-Jet mode. In an applied voltage (for a specified electrode configuration) versus Q diagram an operational window for electro spraying in the Cone-Jet mode becomes visible (see e.g. Appendix 2). For real production, for design purpose, both Q_{\min} and Q_{\max} have to be known. In this article an estimation for Q_{\min} is derived and an indication how to find an approximate value for Q_{\max} is given.

2. An alternative approach to derive Q_{\min}

The minimum flowrate (Q_{\min}) for a certain liquid is the minimum flow rate at which it can be sprayed in the cone-jet mode. It is an interesting phenomenon, not only from a fundamental point of view but

also from a practical one, such as the smallest droplets, which can be produced for certain applications. Several authors reported on this phenomenon over a rather long period, such as [4] on the propagation speed of disturbances on the jet surface in relation to Q_{\min} , and proposed relationships for Q_{\min} by Rosell-Llompart and Fernández de la Mora in 1994 [5] and Gañán-Calvo in 1994 [6]. The experimental results of Chen and Pui (1997) [7] did not find a real fit with the proposed relations for Q_{\min} of the mentioned authors. In 2014 Scheideler and Chen [8] published a paper in where they adapt the Q_{\min} as proposed by Rosell-Llompart and Fernández de la Mora for low viscosity liquids, but another expression for high viscous liquids.

By studying the balance between the forces driving and opposing the liquid ejection in the cone-jet transition region [9], came up with two different Q_{\min} scaling laws. For the viscous limit, when $(\epsilon_r \delta_\mu)^{-1} \gg 1$, $Q_{\min} \sim Q_o \delta_\mu^{-1}$ and for the high-polarity limit, when $(\epsilon_r \delta_\mu)^{-1} \ll 1$, $Q_{\min} \sim Q_o \epsilon_r$, with an intermediate region with none of these valid. In here $\delta_\mu =$ electrohydrodynamic Reynolds number ($\delta_\mu = \left[\frac{\gamma^2 \rho \epsilon_o}{\mu^3 K} \right]^{1/3}$), where γ the surface tension, ρ is the density, K is electrical conductivity, μ is the viscosity, ϵ_o is vacuum permittivity, ϵ_r is relative dielectric constant, and $Q_o = \frac{\epsilon_o \gamma}{\rho K}$ as defined by Refs. [9–11].

In 2019 Gamero-Castaño and Magnani [12] gave an extensive overview of Q_{\min} in their article on the minimum flowrate of electro sprays in the cone-jet mode, in which they review the different articles

* Corresponding author.

E-mail address: caner_yurteri@bat.com (C.U. Yurteri).

including the latest ones. They conclude that the dimensionless minimum flow (Q_{\min}/Q_0) rate increases at decreasing Re for both liquids they studied, and increases with the dielectric constant at fixed Re. Their conclusion on ϵ_r is true for their limited data but cannot be generalized as we will see later. They hypothesize that perturbations to the flow upsetting the coupling between the variables involved in the energy transfer will grow once the transferred power exceeds a threshold, i.e. at sufficiently low flow rates.

As previously stated, [8] published an article on Q_{\min} for both low and high viscosities, and [13] published an article on electro spraying of highly viscous liquids. The results of these papers will be mentioned later. During the writing of this manuscript another paper came to our attention, and it is in reasonable agreement with our results, [14]. We would also like to refer to Ref. [15]; who wrote a very interesting qualitative analysis on Q_{\min} (of very polar liquids).

In this paper we derive, starting with fundamental physics, a very simple formula for Q_{\min} , which can be used as a good approximation for particle size design. We will compare the results of our formula with many data from literature, including the recent data from the paper by Ref. [11]. We also give an indication how to get an approximate value of Q_{\max} and give examples of Cone-Jet Mode operational windows.

In his PhD thesis Ref. [2] derived for the cone-jet mode models, which yield the shape of the liquid cone and jet, the electric fields in and outside the cone, and the surface charge density on the cone and jet surface. He also describes the process of the jet breaking up into droplets and derives scaling laws for the current through the liquid cone and for the produced droplet size. Although he did not go into details on Q_{\min} , he concludes in his theoretical derivation of the scaling of the current; “the presented theory yields that the minimum flowrate is most likely a result of the relative reduction in the velocity pressure (which is also called dynamic pressure) in the jet compared to the surface tension stress with decreasing liquid flow rate”.

By following this up and considering the liquid jet, we take as an initial assumption, to find a formula for Q_{\min} , that Q_{\min} is reached at equal values for the velocity pressure and the surface tension stress. So Q_{\min} is found when the velocity pressure times the jet cross sectional area (A) equals the surface tension times the perimeter of the jet, see Fig. 1. Where.

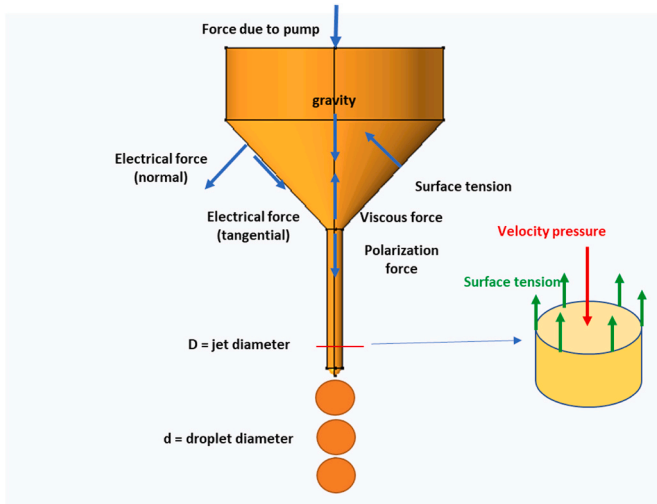


Fig. 1. Shows the cone jet region, including the transition. We used a downward spray configuration with a plate electrode for our studies, and as far as we know, the data provided was obtained in nozzle-plate configuration but not always with the nozzle oriented vertically.

$$\frac{1}{2} \rho v^2 A = \pi D \gamma \quad (1)$$

ρ = liquid density, v = liquid jet velocity, A = jet cross sectional area, D = jet diameter, d = droplet diameter, γ = liquid surface tension, with $v = \frac{Q}{A}$ and $A = \frac{\pi}{4} D^2$ equation (1) becomes

$$2\rho \frac{Q^2}{D^3} = \pi^2 \gamma \quad (2)$$

It has to be noted that Hartman in his dissertation did not consider real high viscosities. The highest ones are for ethylene glycol and sunflower oil, both with a viscosity of about 20 mPa s. [13] show that for highly viscous liquids (in the range of 560–1400 mPa s) the measured droplet diameters are about six times greater than those predicted by the Hartman droplet diameter scaling law (they mention in general that the measured droplet diameters are 2–6 times greater than those predicted by the scaling laws, they considered). The reason why the Hartman scaling laws are not valid for real high viscosities could be the fact that in the derivation of the scaling laws, viscosity effects have been neglected, which can (probably) not be done for real high viscosities [2]. Hartman only considers low viscous (non-viscous) liquids. So the initial formula, which will be derived here can only be used for liquids with low (e.g. 2-butanone with viscosity of 0.417 mPa s) and moderate viscosities (e.g. ethylene glycol with viscosity of about 20 mPa s). For liquids with higher viscosities is referred to the papers of [9,8]; and [13]. However, our final formula, for which fitting of data is employed, can approximately also be used for reasonably high viscosities as will be seen further in this paper.

Going back to equation (2), we have to find a relation between Q and D . First of all as an approximation for D , we use $d = 2D$. For the relation between Q and d we take the scaling laws as derived by Hartman. The Hartman scaling laws can be found in Appendix 1.

It seems to be realistic to assume varicose break up for Q_{\min} , because of the relatively low flow rate. However [11], mentioned whipping was observed in certain experiments on Q_{\min} . For our derivation of Q_{\min} , we will assume varicose break up. It is always possible to check if one really deals with varicose break up. A simple way to do this is explained in Appendix 1.

It has to be realized that by using these scaling laws some effects of liquid properties and nozzle configurations are neglected and approximations such as in the used constants, and by taking $d = 2D$, are introduced. The approximations will probably not have a big influence, but the liquid properties and the nozzle configuration could have. In Hartman’s dissertation he mentions that ion species have an influence on the current and this is also true for the nozzle diameter. He indicates that the scaling laws can be improved by taking these facts into consideration. He also mentions that the applied potential has an influence on the current through the liquid cone as also observed by others such as [16].

According to Ref. [2]; viscosity (if not very high as discussed earlier) has little influence on the current and the droplet size as long as the radial profile of the axial liquid velocity in the jet is almost flat, see appendix A1 and as reported before among others Gañán-Calvo and Montanero (2009) [17] and Gamero-Castaño and Magnani (2019) [12]. But with the extension of the current scaling law to non-flat profiles, viscosity is taken in to account. If in the droplet size scaling law, the measured current (so not the one from the current scaling law) is used then ion species, nozzle configuration and the applied potential difference might have little influence on the droplet size.

Taking all considerations into account, the derivation of Q_{\min} is as follows (for used formulas see Appendix 1):

$$d = c_d \left(\frac{\rho \epsilon_0 Q^4}{I^2} \right)^{1/6} = 2D \quad (\text{Formula A1.4}), \text{ we take } c_d = 2 \quad (3)$$

Giving,

$$D = \left(\frac{\rho \epsilon_0 Q^4}{I^2} \right)^{1/6} \quad (4)$$

Merging (4) and (2) yields,

$$\frac{2I\rho^{0.5}}{\varepsilon_o^{0.5}} = \pi^2\gamma \quad (5)$$

For a non flat profile $I = C_{VN}I^*$ (formulas of A1.1 and A1.3, see [Appendix 1](#) for C_{VN} explanation, there b equals 2.17, which we round here off to 2)

$$I = C_{VN}(2)(\gamma KQ)^{0.5} \quad (6)$$

Plugging (6) in (5) gives

$$Q_{min} = \frac{\pi^4}{2^4 C_{VN}^2} \frac{\varepsilon_o \gamma}{\rho K} = \frac{6.1}{C_{VN}^2} Q_o \quad (7)$$

Note that ε_r is not included in Q_{min} in equation (7).

It is interesting to see that [9] came up with an expression for Q_{min} for the viscous limit, $Q_{min} \sim Q_o \delta_\mu^{-1}$ (see introduction), which look like equation (7). In [figure A1.1 \(appendix 1\)](#) a log-log representation is certainly not a straight line. However if we consider separately low (say below 10) and high (say above 10) VNs, we can get 2 linear fits. The one for $VN > 10$ is $C_{VN} = 0.723 VN^{0.271}$.

The data in the graph above $VN = 10$ are much more scattered than data below 10. Also 10 is a rather arbitrary value. So it is possible to force the fitting to a power of 0.5 which gives $C_{VN} = 0.38VN^{0.5}$ (see [figure A1.1](#)).

This leads in equation (7) to $Q_{min} \sim Q_o/C_{VN}^2 \sim Q_o/VN$.

[10] use the dimensionless parameter $\delta_\mu \delta^{1/3} \sim \left[\frac{\gamma^2 \varepsilon_o^2}{\mu^2 K^2 Q} \right]^{1/3}$, where δ is the inverse of the dimensionless flow rate, i.e. $\delta = Q_o/Q$, and $\delta_\mu \delta^{1/3}$ is equal to our VN . So for $VN > 10$ is found $Q_{min} \sim Q_o/\delta_\mu \delta^{1/3}$

Which resembles $Q_{min} \sim Q_o \delta_\mu^{-1}$ (see earlier in this paper) but is not the same, since $\delta_\mu = \left[\frac{\rho \varepsilon_o \gamma^2}{K \mu^2} \right]^{1/3}$.

Coming back to our equation (7), for a flat profile $C_{VN} = 1$ so Q_{min} becomes,

$$Q_{min}(flat\ profile) = 6.1Q_o \quad (8)$$

So, to calculate Q_{min} using our formula, assume a flat profile and use equation (8) to calculate Q_{min} . Use this Q_{min} to calculate the VN number. If this VN number is low, say less than or equal to 1 then the Q_{min} is the right one. If the VN number is greater than 1 then the formula of Q_{min} for a non-flat profile has to be used, for this we use the C_{VN} as calculated with the Q_{min} for a flat profile. As a result, a new value for Q_{min} is found. This procedure or iteration is repeated until two subsequent iterations differ by less than 1%.

Let us consider first the results of some own experiments as described in [Appendix 2](#). In here the stability or operational window for the conjet (single jet), in the flowrate – applied electric potential plane, is given for some liquids. The details to find the Q_{min} , Q_{max} and the window are given in [Appendix 2](#). (See also [8,16,18] and [19]) It should be noted that for a given flowrate Q , the V range to be in the window is a function of the configuration of the spray set-up (as it concerns the electric field strength) and the surface tension of the liquid. The results for experiments done with 2-propanol with some nitrates dissolved in it, are shown in a stability window. The measured Q_{min} is about 5.56 nl/s. For the used configuration (nozzle to plate distance is 2 cm) the applied electric potential varies over the window from about 4 kV till about 6.5 kV (so 2–3.3 kV/cm). $Q_{min,est}$ (flat profile) equals to 4.97 nl/s. For this case the VN number is 0.51. So we assume a flat profile and $Q_{min,est}$ is 4.97 nl/s. [Appendix 2](#) also shows experimental results and operational windows for ethylene glycol and n-methyl-2-pyrrolidone (NMP). Note that 2-propanol and ethylene glycol have the same conductivity.

Although it is difficult to find reliable values for measured Q_{min} , we will now look at some examples from the literature. For example [8], state that the uncertainty in the Q_{min} measurements was typically within $\pm 30\%$, Chen and Pui (1997) mention “The minimum feed rate was limited by the liquid pump oscillation and the evaporation rate of test solutions”. They also state that “... , the determination of minimum

feed rates of solvents with high vapor pressure e.g., alcohol, 60% water +40% alcohol, and 85% water +15% alcohol, were difficult to define due to the high evaporation rate”. It seems prudent to assume that at least a part of the measured values for Q_{min} are only approximations indicating the order of magnitude.

Scheideler and Chen [8] present a large number of measured Q_{min} values for ethylene glycol, ethanol and some concentrations of glycerol-water mixtures. To create different conductivities, the liquids were doped with potassium chloride. As an example, we look at ethylene glycol with a conductivity (K) of $5.0E-4$ S/m. The outer diameter of the used nozzle is 150 μ m and the properties of ethylene glycol are provided in [Table 1](#). Equation (8) results in $Q_{min,est}(flat\ profile) = 4.7$ nl/s. For this $Q_{min,est}$ $VN = 0.093$, so we have a flat profile. The measured value as given by Scheideler and Chen is 6.9 nl/s. The same procedure has been followed for some other liquids and the results are found in [Table 1](#).

For ethanol in [Table 1](#) with $K = 5.0E-4$ S/m [8], give a measured value of $Q_{min} = 5.0$ nl/s. Our formula produces $Q_{min,est}(flat\ profile) = 3.01$ nl/s. For this $Q_{min,est}$, $VN = 0.863$. Although it is less than 1 and we consider it as a flat profile, we perform an iteration to see if the value changes.

To do this we use (7)

$$Q_{min,est}(nonflat\ profile) = \frac{6.1}{C_{VN}^2} \frac{\varepsilon_o \gamma}{\rho K}$$

From [Appendix 1](#):

$$\frac{1}{C_{VN}} = 1 - 0.1VN^{0.45} = 0.904,$$

$$C_{VN} = 1.107,$$

so

$$Q_{min,est}(nonflat\ profile) = \frac{6.1}{1.107^2} \frac{\varepsilon_o \gamma}{\rho K} = 2.46 \text{ nl} / \text{s}$$

So it decreased a bit (18%). As mentioned before we suggested to use VN less than or equal to 1 as a criterion for flatness. As seen for $VN = 0.863$, this is not completely justified. However, as an approach we assume it to be sufficient. The next liquid is heptane +0.3 wt %stadis, with a much lower conductivity ($K = 1.40E-6$ S/m) than the foregoing liquids, from a paper by Ref. [20]. The reported measured $Q_{min,meas}$ equals to about 158 nl/s. We calculate $Q_{min,est}(flat\ profile) = 1048.58$ nl/s and $VN = 14.87$, so certainly not a flat profile. $C_{VN} = 1.51$ and $Q_{min,est}(nonflat\ profile) = 461$ nl/s. In continuing the iteration step, we use the new Q_{min} to find $VN = 19.55$, and $1/C_{VN} = 0.619$, and $C_{VN} = 1.616$. So the new $Q_{min}(nonflat\ profile) = 402$ nl/s. After 2 more iteration steps, the criterion of a difference less than 1% between 2 follow-up iterations is satisfied, giving $Q_{min,est}(nonflat\ profile) = 389$ nl/s. Finally, we consider our own experiments as discussed in [Appendix 2](#), which utilized 2 propanol with dissolved nitrates.

As we can see from [Table 1](#), the values of $Q_{min,meas}$ and $Q_{min,est}$ for heptane are significantly different. This will be discussed later.

[Table 2](#) compares measured $Q_{min,meas}$ as found in literature, with a range of conductivities, viscosities and dielectric constants, with the $Q_{min,est}$ as calculated with our formula. Included are values for glycerol and glycerol water mixtures, but these liquids with high viscosities (order of 100, 1000 mPa s) will be considered in the next section. For [Table 2](#), iterations are done if needed.

[11,8] discuss with rational arguments that for high viscosity liquids (order of 100 mPa s or higher), the scaling for Q_{min} has a different form from the one for low and moderately low viscosities. It is prudent to consider these laws for high viscous liquids. Still we try our formula to explore how the results of our formula compare with theirs for higher viscosities, see [Table 2](#).

We first introduce the minimum flow rate scaling for high viscous liquids as used by Ref. [8].

Table 1

Comparison of Q_{min} in literature and $Q_{min,est}$ calculated by our formula (Where the author did not report the Q_{min} , we estimated it by digitizing the figure. Tang and Gomez Fig. 3 shows that Q_{min} is about 0.569 cc/h).

Liquid	[8] ethylene glycol + KCl	[8] ethanol + KCl	1st	[20] heptane + 0.3 wt% stadis	1st	2nd	3rd	iterations 4th	this study 2 propanol + nitrates
ρ (kg m ⁻³)	1110	790		684					785
μ (Pa s)	2.10E-02	1.20E-03		4.21E-04					2.38E-03
γ (N m ⁻¹)	4.80E-02	2.20E-02		1.86E-02					2.17E-02
K (S m ⁻¹)	5.00E-04	5.00E-04		1.40E-06					3.00E-04
ϵ/ϵ_0	41	25		1.93					19.26
ϵ_0 [C Ω^2 /(Nm Ω^2)]	8.85E-12	8.85E-12		8.85E-12					8.85E-12
$Q_0 = \epsilon_0 \gamma / \rho K$ [nl/s]	0.77	0.49		171.90					0.82
$Q_{min,meas}$ (nl/s)	6.9	5.0		158.06					5.56
$Q_{min,est(Flat)} = 6.1 * Q_0$ (nl/s)	4.67	3.01		1048.58					4.97
$Q_{min,est(non-flat)} = 6.1 * Q_0 / CVN\Omega^2$ (nl/s)			2.46		461	402	391	389	
VN	0.093	0.863	0.92	14.87	19.55	20.47	20.65	20.68	0.51
1/CVN			0.904		0.619	0.611	0.609	0.609	
CVN			1.107		1.616	1.637	1.641	1.642	
Profile	Flat	Flat		Non Flat					Flat

$$Q_{min} \sim \frac{\gamma D_n^2}{\mu} \tag{9a}$$

$$\text{or } Q_{min,meas} = C_{Dn} \frac{\gamma D_n^2}{\mu} \tag{9b}$$

In where D_n = Nozzle diameter [8] give outer nozzle diameter), with C_{Dn} a proportionality constant.

[8] measured Q_{min} for many cases of glycerol water mixtures and of glycerol, with 7 different outer nozzle diameters D_n (smallest 125 μ m, largest 840 μ m) and conductivities varying between 100 and 10,040 mS/m. For $Q_{min,est}$ with our formula, $Q_{min,meas}$ and their ratio, see Table 2. In this table also the values for Q_{min} as calculated with equation (9a) are given.

By comparing the $Q_{min,meas}$ and calculated with formula 9a, value for C_{Dn} can be calculated (Table 2). We consider only the data for glycerol, not for the glycerol-water mixtures, since Scheideler and Chen mention that Q_{min} of 90% glycerol was not completely independent of conductivity and eq. (9) may not be fully applicable at this viscosity. Although this is not mentioned for 96% glycerol, we do not include it. As can be seen there is a big spread in the C_{Dn} 's for glycerol, the largest being 5.53E-3 and the smallest 0.964E-3 with a tendency of getting smaller for larger D_n . So a ratio of 5.53/0.964 = 5.5. This ratio becomes much smaller when only one nozzle diameter is considered (e.g. 1.4 for D_n = 150 μ m from 5 measurements of different conductivities). Their measurements on glycerol make clear that C_{Dn} is a function of D_n .

2.1. Analysis of the results and discussion

At first sight the data in the previous section look rather scattered but let us analyze them in a sensible way. Since Scheideler and Chen provide us with many measurements on ethylene glycol for different conductivities and nozzle diameters, we start with ethylene glycol, sprayed with a nozzle of 150 μ m. We consider first one size diameter, because, as we have seen, the nozzle diameter can have an influence. Fig. 2a shows $Q_{min,meas}$ and $Q_{min,est}$ (with our formula) as a function of Q_0 , which is actually also a function of $1/K$. Fig. 2b gives the same data, but now expressed as the ratio of $Q_{min,est}$ over $Q_{min,meas}$. In both figures the $Q_{min,meas}$ data form a smooth line. As can be seen in Fig. 2b, for low values of Q_0 , the line becomes very steep. Fig. 2a and b indicate that for Q_0 close to 2 nl/s, our formula yields a comparable value to the measured ones.

Our $Q_{min,est}$ based on equation (7) is in Fig. 2a a straight line, as for all points we have to do with a flat profile. This is clearly different from the measured values.

In the derivation of equation (7) we used an equality of the forces by the velocity pressure and the surface tension, while it was stated “relative reduction in the velocity pressure to the surface tension stress”. This yielded the value of 6.1. A more realistic value of Q_{min} , and so indirectly about the ratio of the forces, can be obtained from the measured data.

To explain the shape of the curve is more complicated. Hartman mentions in his dissertation that in his model air friction is neglected and that when air friction is taken into account, it would result in a slightly thicker jet. Calculating the average jet velocity for the measured Q_{min} points for ethylene glycol in Fig. 2a, by using equation A1.5 (because of flat axial velocity profiles and varicose break up) and $D(\text{jet}) = 0.5 d$ (droplet), reveals that this velocity is about 16 m/s for $K = 100 \mu$ S/m and increases with K till about 74 m/s for $K = 9960 \mu$ S/m. So by going in Fig. 2a from right to left, the velocity increases and so does the stress due to air friction, resulting in an increased influence on the jet thickness D , see analysis provided in Appendix 3. An increase of D means an increase in Q_{min} (equation (2)). From the foregoing consideration it is evident that the prefactor in the formula for $Q_{min} \sim Q_0$ ($Q_{min} = \text{prefactor} \cdot Q_0$) should be found from experimental results and that it is a function of Q_0 .

For larger values of Q_0 , so for decreasing values of K , the curve of Fig. 2a flattens, so increasing the distance with the straight line of our formula for a flat profile. This is completely in line with our formula for a non-flat profile (equation (7)). For a decreasing K , and the rest of the liquid parameters constant, VN goes up and also does CVN , resulting in a decreasing $Q_{min,est}$. For ethylene glycol we do not have large values for Q_0 , so we look at the already mentioned example, Heptane +0.3 wt % Stadis (Tang and Gomes, 1996), with $Q_0 = 171.9$ nl/s. Realize that the liquid properties differ from the ones of ethylene glycol. As seen $Q_{min,meas} = 158.06$ nl/s and $Q_{min,est}$ with our formula with iterations is 389 nl/s. Without iterations, the difference with the straight line for $Q_{min,est(Flat profile)} = 1048.58$ nl/s becomes huge.

When we consider in Table 2 the data of Scheideler and Chen for ethylene glycol for values of the nozzle diameter different from 150 μ m, we see comparable values and tendencies for $Q_{min,meas}$ as a function of Q_0 (or K), as for $D_n = 150 \mu$ m, with the same behaviour for very high conductivities. To identify if for the considered data there is a dependency of $Q_{min,meas}$ on the nozzle diameter we can use the $Q_{min,meas}$ values, for one common value of K , i.e. $K = 500 \mu$ S/m. For $D_n = 150, 250, 330, 550,$ and 840μ m, the $Q_{min,meas}$ values are: 6.9, 9.7, 8.6, 8.9 and 8.9 nl/s respectively. This does not give an indication of a dependency. This is in contradiction with a result of [16]; who mention that for dioxane + formamide with $K = 0.32 \mu$ S/m $Q_{min,meas} = 0.05 \text{ mm}^3/\text{s}$ with OD of the capillary of 0.5 mm, and $Q_{min,meas} = 0.5 \text{ mm}^3/\text{s}$ for a capillary OD = 1 mm. We have to realize that conductivities of the two liquids are significantly different.

Table 2
Summary of $Q_{min,est}$, $Q_{min,meas}$ values for various liquids from literature.

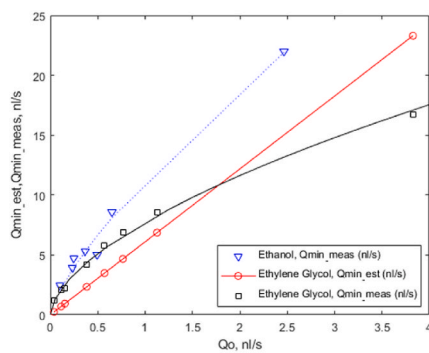
#	Ref.	Liquid	ρ (kg/m ³)	μ (Pa s)	γ (N/m)	K (S/m)	D_n (μ m)	Q_0 [nl/s]	$Q_{min,est}$ (nl/s)	$Q_{min,meas}$ (nl/s)	$Q_{min,est}/Q_{min,meas}$	Equation (9a) (nl/s)	C_{Dn}
1	x	EtOH	790	0.0012	0.022	0.0001	150	2.465	11.5	22.0	0.52		
2	x	EtOH	790	0.0012	0.022	0.0004	150	0.649	3.950	8.6	0.46		
3	x	EtOH	790	0.0012	0.022	0.0005	150	0.493	3.002	5.0	0.60		
4	x	EtOH	790	0.0012	0.022	0.0007	150	0.368	2.240	5.3	0.42		
5	x	EtOH	790	0.0012	0.022	0.0010	150	0.246	1.501	4.7	0.32		
6	x	EtOH	790	0.0012	0.022	0.0011	150	0.233	1.416	3.9	0.36		
7	x	EtOH	790	0.0012	0.022	0.0025	150	0.099	0.600	2.5	0.24		
8	x	EtOH	790	0.0012	0.022	0.0005	250	0.493	3.002	5.6	0.54		
9	x	EtOH	790	0.0012	0.022	0.0005	330	0.493	3.002	6.1	0.49		
10	x	EtOH	790	0.0012	0.022	0.0005	550	0.493	3.002	6.9	0.44		
11	x	EtOH	790	0.0012	0.022	0.0005	840	0.493	3.002	5.0	0.60		
12	x	EG	1110	0.021	0.048	0.0001	125	2.944	17.928	13.3	1.35		
13	x	EG	1110	0.021	0.048	0.0004	125	1.063	6.474	7.8	0.83		
14	x	EG	1110	0.021	0.048	0.0011	125	0.364	2.220	3.6	0.62		
15	x	EG	1110	0.021	0.048	0.0001	150	3.827	23.307	16.7	1.40		
16	x	EG	1110	0.021	0.048	0.0003	150	1.126	6.866	8.6	0.80		
17	x	EG	1110	0.021	0.048	0.0005	150	0.765	4.669	6.9	0.68		
18	x	EG	1110	0.021	0.048	0.0007	150	0.571	3.484	5.8	0.60		
19	x	EG	1110	0.021	0.048	0.0010	150	0.383	2.334	4.2	0.56		
20	x	EG	1110	0.021	0.048	0.0025	150	0.153	0.934	2.2	0.42		
21	x	EG	1110	0.021	0.048	0.0034	150	0.114	0.697	2.1	0.33		
22	x	EG	1110	0.021	0.048	0.0100	150	0.038	0.234	1.2	0.20		
23	x	EG	1110	0.021	0.048	0.0001	210	3.189	19.454	19.4	1.00		
24	x	EG	1110	0.021	0.048	0.0008	210	0.472	2.882	6.7	0.43		
25	x	EG	1110	0.021	0.048	0.0040	210	0.097	0.590	3.3	0.18		
26	x	EG	1110	0.021	0.048	0.0098	210	0.039	0.239	1.7	0.14		
27	x	EG	1110	0.021	0.048	0.0005	250	0.765	4.669	9.7	0.48		
28	x	EG	1110	0.021	0.048	0.0005	330	0.765	4.669	8.6	0.54		
29	x	EG	1110	0.021	0.048	0.0005	460	0.832	5.075	6.4	0.79		
30	x	EG	1110	0.021	0.048	0.0038	460	0.102	0.619	3.9	0.16		
31	x	EG	1110	0.021	0.048	5.00E-04	550	0.765	4.669	8.9	0.52		
32	x	EG	1110	0.021	0.048	3.70E-04	840	1.034	6.309	8.9	0.71		
33	x	EG	1110	0.021	0.048	5.00E-04	840	0.765	4.669	8.9	0.52		
34	x	EG	1110	0.021	0.048	9.10E-04	840	0.421	2.565	5.6	0.46		
35	x	EG	1110	0.021	0.048	3.45E-03	840	0.111	0.677	2.6	0.26		
36	x	EG	1110	0.021	0.048	1.05E-02	840	0.037	0.223	1.0	0.22		
37	xx	3 EG	1136	0.049	0.0454	5.04E-03	222–400 ⁱⁱ	0.070	0.428	3.7	0.12		
38	xxx	1 octanol	827	0.0072	0.0235	9.00E-07	210–220 ⁱⁱ	279.424	1704.484	138.9	12.27		
39	xxx	1 decanol	828	0.0118	0.028	3.00E-07	210–220 ⁱⁱ	997.585	4774	111.1	42.97		
40	x	90% G	1240	0.220	0.065	6.50E-04	150	0.714	4.354	8.9	0.49		
41	x	90% G	1240	0.220	0.065	1.00E-03	150	0.464	2.830	7.8	0.36		
42	x	90% G	1240	0.220	0.065	1.41E-03	150	0.329	2.007	7.5	0.27		
43	x	90% G	1240	0.220	0.065	3.90E-03	150	0.119	0.726	5.6	0.13		
44	x	96% G	1250	0.620	0.064	1.00E-03	150	0.453	2.764	5.6	0.49		
45	x	96% G	1250	0.620	0.064	1.10E-04	330	4.119	25.128	14.9	1.69		
46	x	96% G	1250	0.620	0.064	3.00E-04	330	1.510	9.213	15.3	0.60		
47	x	96% G	1250	0.620	0.064	7.24E-03	330	0.063	0.382	16.7	0.02		
48	x	G	1260	1.400	0.063	1.80E-04	125	2.458	14.996	3.8	3.95	703.1	5.40E-03
49	x	G	1260	1.400	0.063	9.10E-04	125	0.486	2.966	3.3	0.90	703.1	4.69E-03
50	x	G	1260	1.400	0.063	1.00E-04	150	4.425	26.993	5.1	5.29	1012.5	5.04E-03
51	x	G	1260	1.400	0.063	5.00E-04	150	0.885	5.399	5.3	1.02	1012.5	5.23E-03
52	x	G	1260	1.400	0.063	1.00E-03	150	0.443	2.699	4.3	0.63	1012.5	4.25E-03
53	x	G	1260	1.400	0.063	2.50E-03	150	0.177	1.080	5.6	0.19	1012.5	5.53E-03
54	x	G	1260	1.400	0.063	1.00E-02	150	0.044	0.269	3.9	0.07	1012.5	3.85E-03
55	x	G	1260	1.400	0.063	9.10E-04	210	0.486	2.966	8.4	0.35	1984.5	4.23E-03
56	x	G	1260	1.400	0.063	2.83E-03	210	0.156	0.954	8.3	0.11	1984.5	4.18E-03
57	x	G	1260	1.400	0.063	4.99E-03	210	0.089	0.541	8.5	0.06	1984.5	4.28E-03
58	x	G	1260	1.400	0.063	5.00E-04	250	0.885	5.399	12.5	0.43	2812.5	4.44E-03
59	x	G	1260	1.400	0.063	1.20E-04	330	3.688	22.494	11.9	1.89	4900.5	2.43E-03
60	x	G	1260	1.400	0.063	5.00E-04	330	0.885	5.399	18.1	0.30	4900.5	3.69E-03
61	x	G	1260	1.400	0.063	5.20E-04	330	0.851	5.191	13.1	0.40	4900.5	2.67E-03
62	x	G	1260	1.400	0.063	9.30E-04	330	0.476	2.902	13.3	0.22	4900.5	2.71E-03
63	x	G	1260	1.400	0.063	1.42E-03	330	0.312	1.901	12.8	0.15	4900.5	2.61E-03
64	x	G	1260	1.400	0.063	3.10E-03	330	0.143	0.871	13.9	0.06	4900.5	2.84E-03
65	x	G	1260	1.400	0.063	5.00E-04	550	0.885	5.399	37.5	0.14	13612.5	2.75E-03
66	x	G	1260	1.400	0.063	4.10E-04	840	1.079	6.584	51.4	0.13	31752.0	1.62E-03
67	x	G	1260	1.400	0.063	5.00E-04	840	0.885	5.399	47.2	0.11	31752.0	1.49E-03
68	x	G	1260	1.400	0.063	1.16E-03	840	0.381	2.327	36.1	0.06	31752.0	1.14E-03
69	x	G	1260	1.400	0.063	3.87E-03	840	0.114	0.697	30.6	0.02	31752.0	9.64E-04
70	x	G	1260	1.400	0.063	4.99E-03	840	0.089	0.541	30.6	0.02	31752.0	9.64E-04

x [8]; xx [5] from Tables 1 and 2, xxx [11]. EtOH = ethanol, EG = ethylene glycol, G = glycerol, TEG = Triethylene glycol, DEG = diethylene glycol. Nozzle diameter refers to outer diameter of nozzle except where indicated as ii, ii = inner – outer nozzle diameter. $Q_{min,est}$ values, iterations are done if needed (this is for 1 and 39). (N.B. for reader's information some of the data are rounded to fit the table, for exact values we refer to the original reference).

Now we examine in Table 2 the results for high viscous liquids. For 90% glycerol, with $\mu = 220$ mPa s, we see that for $D_n = 150$ μm , $Q_{\min, \text{meas}}$ decreases with increasing K and the ratio's of $Q_{\min, \text{est}}/Q_{\min, \text{meas}}$ are somewhat smaller than for ethylene glycol and that for the highest K , this ratio becomes small.

For 96% glycerol, with $\mu = 620$ mPa s, the similarity with ethylene glycol has gone. Here with increasing K (for $D_n = 330$ μm), $Q_{\min, \text{meas}}$ even slightly increases. It is remarkable that the values for the ratio's of $Q_{\min, \text{est}}$ over $Q_{\min, \text{meas}}$, are comparable with the ones for ethylene glycol, except for the high value of $K = 7240$ $\mu\text{S/m}$. For glycerol, with $\mu = 1400$ mPa s, for the different D_n 's, with increasing K , the $Q_{\min, \text{meas}}$ is almost constant. This is in agreement with equation (9). The exception is for $D_n = 840$ μm , where an increasing K goes with a decreasing $Q_{\min, \text{meas}}$. Again it is noticeable that with the exception of the two biggest nozzle diameters (550 and 840 μm) the ratios of $Q_{\min, \text{est}}/Q_{\min, \text{meas}}$ have the same tendency as the ratios for ethylene glycol, with the exception of the lowest K 's (100 and 180 $\mu\text{S/m}$). For high viscosities and lower conductivities, we don't have any data, so we're not going to speculate on it. The ratio for the highest K 's is the same as previously mentioned.

Finally, we look into a possible influence of the relative permittivity (ϵ_r). As seen ϵ_r does not appear in our formula, but [9] describe, as already mentioned, two scenarios, one with $Q_{\min} \propto Q_0 \cdot \epsilon_r$ and the other one with $Q_{\min} \propto Q_0/\delta_\mu$, with neither of the two valid for the intermediate region. To tackle this item we compiled in Table 3, the relevant information of a number of liquids, covering both the Q_0 and the $(\epsilon_r \cdot \delta_\mu)^{-1}$ domains. We will cover examples in the Q_0 domain from about 1 till a few hundred nl/s, for liquids where $(\epsilon_r \cdot \delta_\mu)^{-1} < 0.2$. For our formula we already discussed this region. As we see in Table 3, the factor $Q_{\min, \text{meas}}/Q_0 \cdot \epsilon_r$ varies rather widely (0.05 till 0.509), especially considering the indication in Fig. 2 of [9]; that the minimum value of $Q/Q_0 \cdot \epsilon_r$ is about 0.0125. If we look in Fig. 2a, the curve of $Q_{\min, \text{meas}}$ for ethanol as a function of Q_0 (see Table 2), lays well above the one for ethylene glycol. Since $\epsilon_r(\text{ethylene glycol}) = 41$ and $\epsilon_r(\text{ethanol}) = 25$, this is in contradiction with the scaling $Q_0 \cdot \epsilon_r$. It has to be noted that for the highest mentioned $\epsilon_r = 80$, $Q_{\min, \text{meas}}$ is 3.62 times larger than calculated with our formula ($Q_{\min, \text{estimated}}$ after iterations = 24.42 nl/s). For this case the factor $Q_{\min, \text{meas}}/Q_0 \cdot \epsilon_r$ is 0.17 and not really close to the indicated minimum. We conclude that these experimental values do not give a clear proof that Q_{\min} is proportional to ϵ_r . A short discussion on the intermediate and the $Q_{\min} \propto Q_0/\delta_\mu^{-1}$ regions sound to be warranted. In Table 3 there are three cases for ethylene glycol in the intermediate region. All three are far to the left in the Q_0 domain, because of their (rather) high K values. The other liquids in the intermediate region as given by Ref. [9] all have (rather) high K values (only no value given for sunflower oil). Also for the region in where $Q_{\min} \propto Q_0/\delta_\mu^{-1}$, the only (few) data given by Gañán-Calvo et al. are for (very) high K values, so (very) low Q_0 's. The only one for which we could find in the relevant literature a measured Q_{\min} value is for 3-ethylene glycol (d) [5], $Q_0 \cdot \delta_\mu^{-1} = 1.66$ nl/s



and $Q_{\min, \text{meas}} = 3.7$ nl/s. Our formula 8 (flat profile) yields 0.43 nl/s. Since we have only one value, we cannot further comment on this. As seen before Gamero-Castaño and Magnani (2019)Ref. [12] show that for the 2 liquids, they employed, the dimensionless minimum flow rate increases with ϵ_r at fixed Re . This is also true if their data are plotted as $Q_{\min} = f(Q_0)$ (then the PC curve ($\epsilon_r = 64.9$) lays above the TBP ($\epsilon_r = 8.91$)). In Fig. 2a we see that the curve for ethanol ($\epsilon_r = 25$) lays well above the one for ethylene glycol ($\epsilon_r = 41$). This is also true if the dimensionless Q_{\min} is plotted as function of Re (although there is no common Re). So their conclusion on ϵ_r (for their 2 liquids) can not be generalized.

2.2. Curve – fitting

In the foregoing we reasoned that the pre-factor in our formula $Q_{\min} \sim Q_0$ itself is a function of Q_0 . The modelling on which the derivation of our formula is based, is not detailed enough to provide us with that pre-factor. So we depend on reliable experimental data from literature and/or own measurements, and curve fitting. For the fitting we looked only for data, for which explicitly is mentioned that it considers minimum flowrates. We begin with liquids with lower viscosities. For this [8] provide us with an extensive data set for Ethylene glycol ($\mu = 21$ mPa s) and Ethanol ($\mu = 1.2$ mPa s), see Table 2. Q_0 values range from about 0.04 nl/s to about 4 nl/s.

Because of the very limited number of data, they have to be taken as one population from statistical point of view. Fig. 3 depicts the measured data-set and the fitted curve (based on log-log linear) is,

$$Q_{\min, \text{fit}} = 8.903 Q_0^{0.55} \text{ (nl/s)}. \quad (10)$$

For high values of Q_0 (so low values of K) there are only very few $Q_{\min, \text{meas}}$ data available [11]. present measurements of Q_{\min} for 1-octanol ($\mu = 7.2$ mPa s, $Q_0 = 279$ nl/s) $Q_{\min, \text{meas}} = 138.89$ nl/s and for 1-decanol ($\mu = 11.8$ mPa s, $Q_0 = 998$ nl/s) $Q_{\min, \text{meas}} = 111.1$ nl/s. For another low value of Q_0 we take 3-Ethylene glycol(d) from Rosell-Llompart and Fernández de la Mora (1994), ($\mu = 49$ mPa s from their Table 2), with $Q_0 = 0.0702$ nl/s and $Q_{\min, \text{meas}} = 3.7$ nl/s. In Fig. 4 these 3 values have been added to the ones in Fig. 3 and the curve fitting results in

$$Q_{\min, \text{fit}} = 8.175 Q_0^{0.474} \text{ (nl/s)}. \quad (11)$$

It is not overstated to say that the number of data points on which formula 11 is based is very small, especially for higher values of Q_0 . With more measured data the curve will become more reliable. Despite this shortcoming we will apply formula 11 to some Q_{\min} measurement data or to Q data, for which we expect to be close to Q_{\min} . In appendix 2 we find for 2-propanol ($\mu = 2.38$ mPa s, $Q_0 = 0.815$ nl/s) $Q_{\min, \text{meas}}$ is close to 5.56 nl/s and for Ethylene glycol ($\mu = 16.1$ mPa s, $Q_0 = 1.25$ nl/s) $Q_{\min, \text{meas}}$ is close to 5.56 nl/s. For 2-propanol formula 11 yields $Q_{\min, \text{fit}}$

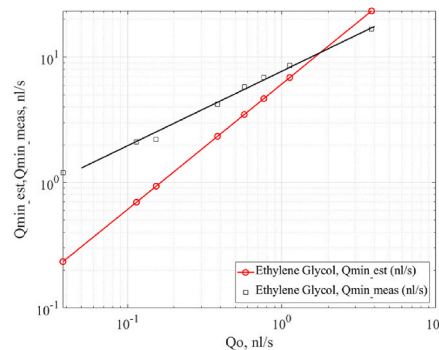


Fig. 2 a. $Q_{\min, \text{est}}$ and $Q_{\min, \text{meas}}$ as a function of Q_0 for 150 μm nozzle and test liquid ethylene glycol and, $Q_{\min, \text{meas}}$ as a function of Q_0 for 150 μm nozzle and test liquid ethanol, on a linear-linear plot (left side) and for ethylene glycol on a log-log plot (right side).

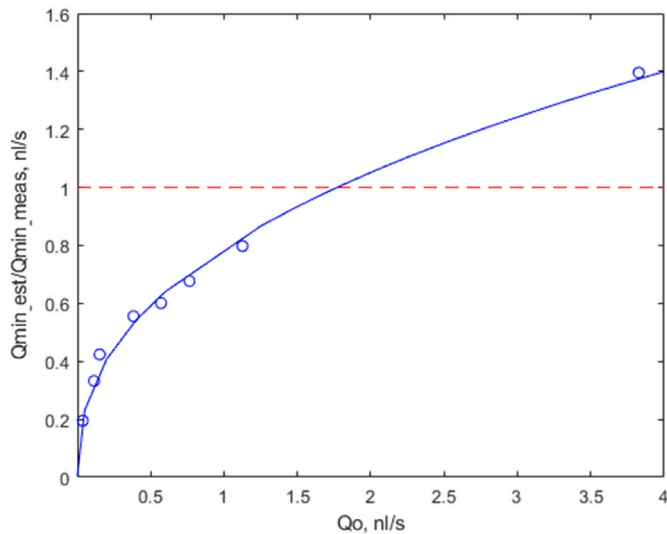


Fig. 2 b. Q_{min_est}/Q_{min_meas} as a function of Q_o for 150 μm nozzle and test liquid ethylene glycol.

= 7.42 nl/s and for ethylene glycol 9.09 nl/s [20]. show an extensive number of data of flow rates of Heptane + 0.3(wt)% stadis ($\mu = 0.421$ mPa s, $K = 1.4 \mu S/m$, $Q_o = 172$ nl/s), sprayed in the cone-jet mode. They do not explicitly mention Q_{min} for their lowest flow rate in e.g. their Fig. 2a, which is 0.25 cc/hr = 69 nl/s. Since the highest flow rate in that figure is 28 cc/hr = 7778 nl/s, so the ratio of the highest over the lowest is 113, we assume that 69 nl/s is not too far from Q_{min} , as follows from the next paragraph. For $Q_o = 172$ nl/s in formula 11, $Q_{min_fit} = 93.78$ nl/s [23]. give data for a very high $Q_o = 39,400$ nl/s, i.e. for Isopar +15% ButOH ($\mu = 1.73$ mPa s). They did experiments at six flow rates, of which the lowest is 3 ml/h = 833 nl/s. They also do not mention Q_{min} . It is unclear how close this value is to Q_{min} . The ratio between the highest mentioned flow rate (120 ml/h = 33,333 nl/s) and the lowest is 40. If we still use the Q_o in formula 11, we get 1232.40 nl/s [16]. give for dioxane + formamide ($\mu = 1.39$ mPa s, $K = 0.32 \mu S/m$, $Q_o = 940$ nl/s), $Q_{min} = 0.05$ mm³/s = 50 nl/s (Note: see former part on nozzle diameter) and formula 11 yields $Q_{min_fit} = 209.77$ nl/s. From Fig. 2 in Gañan-Calvo et al. (2013), we estimate for 1-octanol ($\mu = 8.1$ mPa s, $Q_o = 321$ nl/s), 1-decanol ($\mu = 11.79$ mPa s, $Q_o = 998$ nl/s) and 1-dodecanol ($\mu = 12.5$ mPa s, $Q_o = 2930$ nl/s), Q_{min_meas} respectively about 164 nl/s, 124 nl/s and 238 nl/s. Formula 11 gives for these cases respectively 126.06,

215.81 and 359.57 nl/s.

By applying formula 11 to the mentioned data we find for the ratio between Q_{min_meas} and Q_{min_fit} (formula (11)) values in increasing order 0.24, 0.57, 0.61, 0.66, 0.68, 0.74, 0.75, and 1.30.

Gamero-Castaño and Magnani (2019) [12] give the measured Q_{min} data (in their table they show the dimensionless Q_{min}) for 2 liquids (tributyl phosphate (TBP) and propylene carbonate (PC)), both for 7 different conductivities. Interestingly they did not use a syringe pump, which shows the induced flow rate, but an own constructed pump. We did not use their data for our curve fitting, but will discuss them here. For 2 data point Q_o proves to be between 8 and 9, for the rest Q_o is (much) lower. The $Q_{min_measured}/Q_{min_fit}$ values are with decreasing Q_o for PC 3.12, 1.79, 0.90, 0.86, 0.63, 0.32 and 0.23 and for TBP 0.35, 0.32, 0.27, 0.21, 0.17, 0.16, and 0.14. Despite some rather high and low ratios in the last series, regarding the mentioned uncertainties in the measured values and limited number of data, we consider formula 11 as at least not far off and for the purpose of design certainly sufficient. This is also true in relation to the result in a recent paper by Ref. [14]. They report for the minimum flowrate of diethylene glycol (DEG) with $\rho = 1118.0$ kg/m³, $\gamma = 0.0448$ N/m, $K = 2.4E-5$ S/m, $\epsilon_r = 6.66$ and $\mu = 0.0385$ Pa s, Q_{min} is about 14.75 nl/s. Our formula 11 yields 29.32 nl/s.

Fig. 5a depicts for high viscosity liquids, Q_{min_meas} as a function of Q_o for Glycerol ($\mu = 1400$ mPa s, see Table 2). Each nozzle diameter D_n has its own graph. For most nozzle diameters the measured Q_{min} data could be fitted by an almost horizontal line. This is in agreement with formula 9. The exception is for $D_n = 840 \mu m$, where the fitted line is absolutely not horizontal. Also for 96% glycerol ($\mu = 620$ mPa s) and $D_n = 330 \mu m$, the fit is an almost horizontal line, Fig. 5b. However for 90% glycerol ($\mu = 220$ mPa s), the pattern of Q_{min_meas} as function of Q_o follows that of liquids with a lower viscosity. The four values of Q_{min_meas} , with $D_n = 150 \mu m$, as given by Scheideler and Chen are: 8.9, 7.8, 7.5 and 5.6 nl/s, while formula 11 yields respectively: 6.97, 5.68, 4.83 and 2.98 nl/s, which gives a ratio of Q_{min_meas} over Q_{min_fit} of respectively 1.28, 1.37, 1.55 and 1.88. So we assume that for a liquid with $\mu = 220$ mPa s formula 11 is still applicable, although it has to be stated that we do not have any Q_{min_meas} values for higher Q_o values for this rather high viscosity. This remark is also true for real high viscosities.

2.3. Some thoughts on the maximum flow rate

Q_{min} has been discussed previously with the specific goal of making it easily useable for design purposes. For the same reason, it is of interest to have an indication on the maximum flow rate.

It is much more difficult to attribute a formula to Q_{max} than to Q_{min} ,

Table 3
Data compiled to investigate the influence of ϵ_r .

Liquid and Source	K [$\mu S/m$]	ϵ_r	Q_{min_meas} [nl/s]	Q_o [nl/s]	δ_μ	$(\epsilon_r \delta_\mu)^{-1}$	$Q_o \epsilon_r$ [nl/s]	$\frac{Q_{min_meas}}{Q_o \epsilon_r}$	$Q_o \delta_\mu^{-1}$ (nl/s)
1	340	41	8.6	1.13	0.19	0.13	46.3	0.186	-
1	100	41	16.7	3.83	0.29	0.08	157	0.106	-
2	100	25	22	2.46	2.70	0.015	61.5	0.358	-
3	102	80	~88.3	6.33	7.73	1.62E-3	506.4	0.17	-
4	1.4	1.93	~169	172	27.17	0.019	332	0.509	-
5	0.9	10	139	279	2.29	0.044	2790	0.050	-
1	2500	41	2.2	0.153	0.10	0.24	-	-	-
1	9960	41	1.2	0.0385	0.063	0.39	-	-	-
6	16,900	38.66	-	0.0228	-	~0.5	-	-	-
7	5040	23.7	3.7	0.0702	0.0422	~1	-	-	1.66

1. Ethylene glycol [8].
2. Ethanol, Scheideler and Chen (2014).
3. Deionized water [21].
4. Heptane +0.3(wt)% Stadis, Tang and Gomez (1996).
5. 1-octanol, Ponce Torres et al. (2018).
6. Ethylene glycol-3 [9,22].
7. 3-ethylene glycol, Rosell-Llompарт & Fernández de la Mora (1994) and Table 2 of this article.

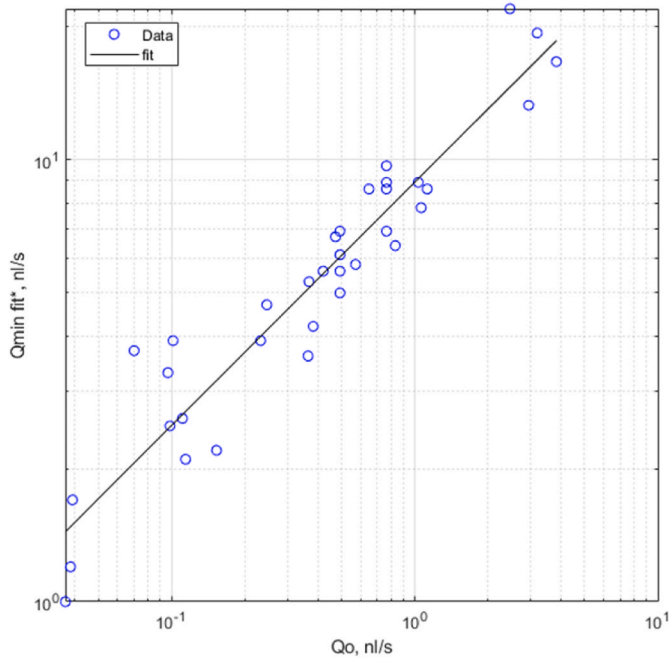


Fig. 3. This curve fit uses data from Ethylene Glycol and Ethanol (Scheideler and Chen), based on log-log fit. Correlation is $Q_{min_fit} = 8.903 Q_o^{0.55}$ (nl/s).

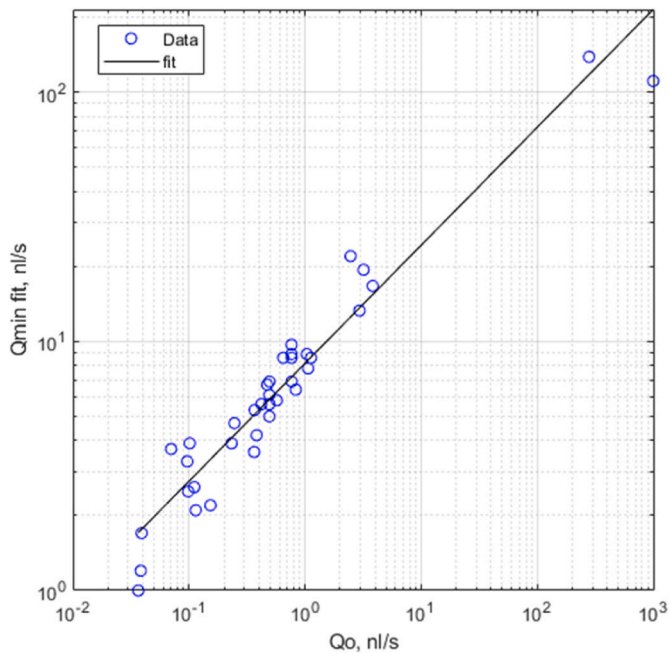


Fig. 4. Curve fitting is done using data of Ethylene Glycol, Ethanol (Scheideler and Chen), and Data from Rosell-Llompарт and Fernández de la Mora, and Ponce-Torres et al. (based on log-log fit). Correlation is $Q_{min_fit} = 8.175 Q_o^{0.474}$ (nl/s).

as explained for example by Ref. [19] and demonstrated by Ref. [18]. Q_{max} is dependent on a number of parameters [20]. report that the maximum liquid flow rate for the cone-jet decreases dramatically with increasing capillary diameter, so decreasing the Cone-jet operation window. Also [16] give as an example for dioxane + formamide, with $K = 36 \mu\text{S}/\text{m}$ ($Q_o = 8.35 \text{ nl/s}$) for a capillary of 0.5 mm a Q_{max} of about $0.3 \text{ mm}^3/\text{s}$, while for a finer capillary Q_{max} is at least four times higher. As seen already they also report a dependency of Q_{min} on the nozzle diameter. Chen and Pui (1997) state that there are many factors, which

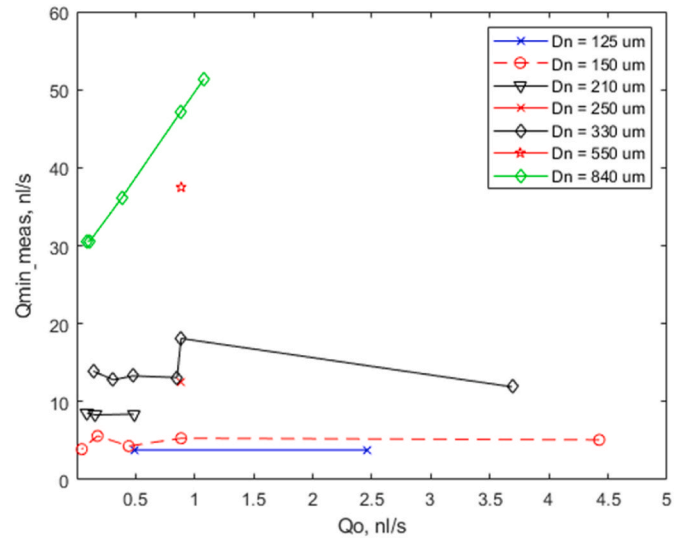


Fig. 5a. Q_{min_meas} as function of Q_o for glycerol ($\mu = 1.4 \text{ Pa s}$).

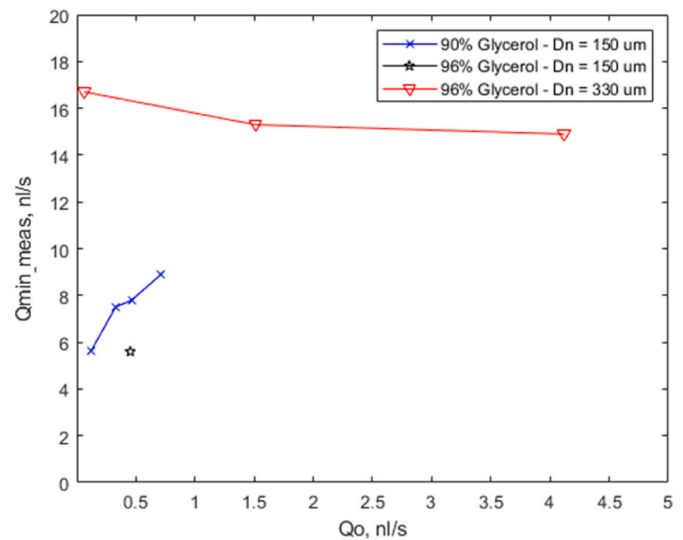


Fig. 5b. Q_{min_meas} as function of Q_o for 90% ($\mu = 0.22 \text{ Pa s}$) and 96% glycerol ($\mu = 0.62 \text{ Pa s}$).

could affect the operation envelop, including the set-up configuration, the physical properties of the liquid (also wettability of capillary) and the surrounding atmosphere. Also [5] state that Q_{max} is not as universal a quantity as Q_{min} .

To get an idea on Q_{max} we do not start with a fundamental discussion but with an empirical result as introduced by Chen and Pui (1997). Chen and Pui defined the maximum feed rate as the flow rate before the start of jet bifurcation. See also appendix 2.

Chen and Pui (1997) show for a number of liquids that for Q_{max} the ratio of d/R^* assumes the constant value of about 0.5. d is the produced droplet diameter and R^* is the inertial characteristic length $= (\rho Q^2 / \gamma)^{1/3}$, derived from the balance between the dynamic pressure and the capillary pressure. If we assume this to be true in general, then for Q_{max} ,

$$d = k(c) \left(\frac{\rho Q_{max}^2}{\gamma} \right)^{1/3} \text{ where } k(c) \text{ is } 0.5 \tag{12}$$

We use this with our scaling laws. For Q_{max} it is assumed that there is whipping of the jet. We consider the general case for I, i.e. a non-flat profile:

$$I = C_{VN} I^*, \quad I^* \text{ is taken as } 2(\gamma K Q)^{1/2} \text{ and } d = d_{whip} = \left[0.8 \frac{288 \epsilon_0 \gamma Q^2}{[C_{VN}^2 2(\gamma K Q)^{1/2}]^2} \right]^{1/3} \\ d = \frac{3.86 \epsilon_o^{1/3} Q^{1/3}}{C_{VN}^{2/3} K^{1/3}} \tag{13}$$

and equate this with equation (12)

$$d = 0.5 \left(\frac{\rho Q_{max}^2}{\gamma} \right)^{1/3} = \frac{3.86 \epsilon_o^{1/3} Q_{max}^{1/3}}{C_{VN}^{2/3} K^{1/3}}$$

So

$$Q_{max} = \frac{460.1 \epsilon_o \gamma}{C_{VN}^2 \rho K} = \frac{460.1}{C_{VN}^2} Q_o \tag{14}$$

For Q_{min} we found that the prefactor is a function of Q_o itself and our final formula is obtained by curve fitting. As we have hardly measured data for Q_{max} , we can not even dream of such a fit for Q_{max} , and also we have to keep in mind the remarks in the beginning of this paragraph. Fortunately we have some complete cone-jet windows in appendix 2, in where is described that for the considered liquids after increasing the flow rate beyond Q_{max} the cone jet shifted from the center to the side, i.e the jet deviated from the nozzle axis, so a global instability. For all three liquids the same small nozzle was used. For 2-propanol (+ some additives) with $Q_o = 0.815$ nl/s, $Q_{min,fit} = 7.42$ nl/s and $Q_{min,meas} = 5.56$ nl/s, so they are close to each other. Calculations show a flat profile and varicose break-up. Using equation (14), we get $Q_{max,est} = 374.9$ nl/s and $Q_{max,meas} = 416.7$ nl/s, which are rather close to each other as well (calculations show a flat profile and whipping break-up). The ratio of max to min is 75 for both estimations and measurements. Keeping the remarks made on Q_{max} in mind, we will consider some cases for which we have a measured value of Q_{max} , or a value for which we assume not to be too far off. Appendix 2 shows for ethylene glycol ($K = 300$ mS/m, $Q_o = 1.25$ nl/s), $Q_{min,meas}$ is about 5.56 nl/s and $Q_{max,meas} = 583.34$ nl/s, giving a ratio of max over min of 105. For heptane +0.3 (wt) % stadis ($K = 1.4$ μS/m, $Q_o = 172$ nl/s) [20], we presented already the ratio of the highest over the lowest flow rate as 113, noting that not explicitly is mentioned Q_{min} and Q_{max} . Also already mentioned are the minimum and maximum measured flowrates for isopar +15% ButOH ($Q_o = 39,400$ nl/s [23], with a ratio between max and min of 40. Again it is unclear how close these values are to Q_{min} and Q_{max} . For dioxane + formamide ($K = 0.32$ μS/m, $Q_o = 940$ nl/s), Cloupeau and Prunet-Foch give as $Q_{min,meas} = 50$ nl/s. In their Fig. 9, Q_{max} falls outside the diagram, but $Q_{max} > 10 \text{ mm}^3/\text{s} = 10,000$ nl/s, indicating a ratio $Q_{max}/Q_{min} > 200$. In the same figure a complete cone-jet window is given for dioxane + formamide with $K = 3$ μS/m ($Q_o = 100.2$ nl/s). From this figure Q_{max}/Q_{min} is estimated at about 60.

Lastly we look at data for n-butanol ($K = 15$ μS/m, $Q_o = 17.9$ nl/s) by Refs. [2,3,24]. From their Fig. 11 (2000), the highest measured flow rate is estimated at about 8300 nl/s and the lowest one at about 260 nl/s. Again, it is not mentioned that we have to do with Q_{max} and Q_{min} ,

Appendix 1. A brief, on the Viscosity Number and Scaling Laws

Several equations have been developed to estimate the size of the produced main droplet and the electric current flowing through a liquid sprayed in the cone-jet mode as a function of liquid properties and flow rate. See e.g. Refs. [1,2] and the references therein are referred to for a detailed, in-depth study.

although for the lowest flow rates in Figs. 14 and 15 of [24] for n-butanol, which are about the same as in Fig. 11 (2000) is mentioned: "... the measurements in this section were considerably closer to the minimum flow rate than in the previous section". So the ratio of the highest over the lowest measured flow rate is about 32. If we apply our formula 11 to n-butanol, $Q_{min,fit} 32.1$ nl/s nl/s, we find a much lower value than the lowest measured flow rate, which would mean a much wider operation window. It should be mentioned that the [2] experiments were performed with a cylindrically shaped nozzle, with a flat bottom with a diameter of 8 mm, having in the middle a hole of a few hundred micrometer. In contrast to the nozzle he used, for all discussed sprayed liquids until now, as far as we know, (rather) thin walled and/or sharp nozzles/capillaries have been used [23]. showed measured flow rates for isopar + n-butanol mixtures, using capillaries with OD of 1.4 and 1.6 mm, which seem a bit big, but much smaller than the one of [2].

3. Conclusions

Starting with [2] theoretical derivation of the scaling of the current for electro spraying in the cone-jet mode, and by using his scaling laws, it is found that Q_{min} is proportional to Q_o . The formula for Q_{min} , valid for Newtonian liquids with low till moderately high viscosities, is however only valid for a limited range in the Q_o domain. The model of Hartman is not detailed enough to derive quantitatively the formula for Q_{min} for smaller or bigger values of Q_o , than for the mentioned limited range in the Q_o domain. However, a qualitative explanation can be extracted from Hartman's work. We made it plausible that the pre-factor itself in $Q_{min} = \text{pre-factor} \cdot Q_o$ ($Q_{min} Q_o$) is a function of Q_o . Curve fitting on experimental data was used to find the pre-factor, which being a function of Q_o , combined with Q_o forms formula 11 in the text.

This formula can be used for liquids with viscosities up to a few hundred mPa s. It has to be noted that the curve fitting is based on a limited number of data, especially for the higher values of Q_o , so we expect that in the future, with more data, a refinement can be made. We also believe that for design purposes the formula is sufficiently close.

For design purposes it is also useful to have an indication of the maximum flow rate, Q_{max} . It proves that it is not possible to come up with a formula for Q_{max} . It is found though, by means of an empirical result and with very limited experimental data, that the ratio of Q_{max} over Q_{min} varies between some tens till a few hundreds. Own measurements for 2-propanol show a complete cone-jet mode operational window, with a value for the ration of Q_{max} over Q_{min} of 75.

We are confident that by only measuring the properties of the liquid to be sprayed, and by applying the results of this paper, a sound starting point is obtained for the design of particles and films, produced with electro spraying in the cone-jet mode.

Declaration of competing interest

The authors declare that they have no known competing financial interests or personal relationships that could have appeared to influence the work reported in this paper.

Data availability

data used in this research is tabulated and given as tables in the manuscript.

Hartman [2] derived theoretically the following electric current scaling law for liquids with a flat radial profile of the axial liquid velocity in the jet, $I^* = 2.17(\gamma K Q)$ (A1.1)

However, this equation was already reported by Ref. [25] with a bit different coefficient (see also Gañán-Calvo's scaling laws in Journal of Aerosol Science, 1999 [26]). In formula A1.1, I^* is the electric current for a jet with a flat velocity profile. The constant 2.17 is based on the experimental works of [10] and of [2]. For liquids where the radial velocity profile is not flat, but with the fluid velocity at the jet surface higher than in the jet center [2], derived an extension to the scaling law which relates I/I^* to the different parameters, for Newtonian liquids [1]. simplified this relation to equation A1.2, by curve fitting experimental data (figure A1.1) to

$$I/I^* = (1 - 0.1 * VN^{0.45})^{-1} \tag{A1.2}$$

Where I is the electric current for a jet with a non-flat axial fluid velocity profile [1], and VN (Viscosity Number) is the dimensionless number, $(\gamma^3 \epsilon_0^2 / \mu^3 K^2 Q)^{1/3}$, which was introduced by De la Mora and Loscertales (1994) as viscous parameter but this one includes ϵ_r . In 1997 Ganan-Calvo et al. introduced a dimensionless number in above form which is as also used by Ref. [2]; and which we called Viscosity Number. For low values of VN (practically $VN \leq 1$), corresponding to a high value for the combined values of K and μ , C_{VN} is about 1.

With $C_{VN} = I/I^*$ (A1.3)

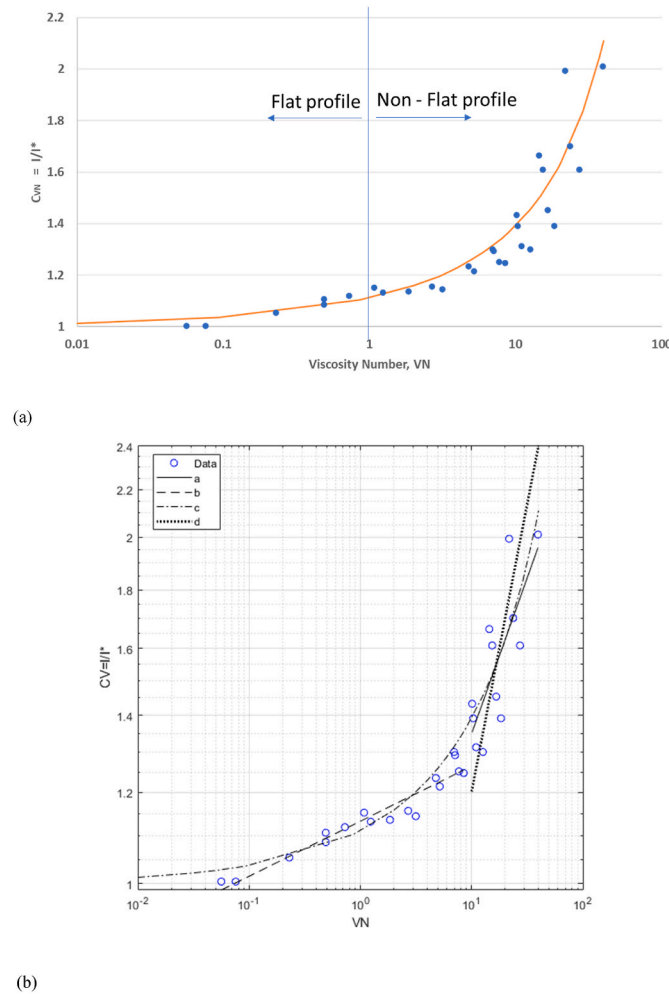


Fig. A1.1. (a) log-normal presentation of the data and best fit of I/I^* or C_{VN} vs Viscosity Number, VN , (b) log-log presentation of the data with curve fit 'c' and 2 separate log-log fits for $VN < 10$ 'b' and $VN > 10$ 'a' of I/I^* as well as $C_{VN} \sim VN^{0.5}$ 'd'.

The data presented in Ref. [1] ranges from 1 to 2 for C_{VN} . Despite the fact that data scattering is greater at high VN values than at low VN values, Equation A1.2 can be safely used up to VN values of about 10.

Hartman [2] also derived two scaling laws for the droplet size in the cone-jet mode. This is related to the jet break-up mechanism. The mechanism depends on the ratio of the normal electric stress over the surface tension stress in the jet. At a low value of this ratio, the jet breaks up due to varicose instabilities. At a higher value, which means for a certain liquid a higher flow rate, the jet starts to whip and the break up is influenced by both varicose and kink instabilities. For the varicose jet break-up regime [2] reports the following scaling law in the varicose jet break-up regime.

$$d_{d,varicose} = c_d \left(\frac{\rho \epsilon_0 Q^4}{I^2} \right)^{\frac{1}{6}} \tag{A1.4}$$

And, for a jet with a flat axial velocity profile, approximating 2.17 by 2 and taking c_d equals to 2, as reported by Ref. [1]; equation A1.4 becomes,

$$d_{d,varicose} = \left(\frac{16\rho\epsilon_0 Q^3}{\gamma K} \right)^{1/6} \tag{A1.5}$$

where $d_{d,varicose}$ denotes main droplet diameter, Q denotes flow rate, and K denotes liquid conductivity [3].

For the whipping jet break-up regime [2], developed the following droplet size scaling law:

$$d_{d,whipping} = \left(0.8 \frac{288\epsilon_0 \gamma Q^2}{I^2} \right)^{1/3} \tag{A1.6}$$

where $d_{d,whipping}$ is the droplet size predicted for a jet that breaks up in the whipping jet break-up regime. The constant 0.8 is based on, as Hartman mentions, highly scattered experimental data. Hartman reasons that more precise measurements could give a more accurate value for the constant 0.8, but 0.8 is certainly sufficient for our purpose.

Calculating both droplet sizes allows you to easily determine which of the two droplet size scaling laws, $d_{d,varicose}$ or $d_{d,whipping}$, should be used. The one which gives the smallest droplet size is the correct one. This indicates whether the jet is in the varicose or whipping regime.

For a spherical droplet, a simple derivation relates the diameter of the (final) solid particle (d_p) after drying to the droplet diameter [27] by Equation A1.7:

$$d_p = \sqrt[3]{f \frac{\rho_{droplet} d_{droplet}^3}{\rho_{particle}}} \tag{A1.7}$$

where f is the mass fraction of the material in the solution (-), $\rho_{droplet}$ is the density of the solution and $\rho_{particle}$ is the density of the final (product) particle (kg/m³). This is of course only true if the particle is not porous or not hollow.

Appendix 2. Cone-jet operational window

To experimentally determine the cone-jet operation window, three different liquids were used and their parameters are shown in Table A2.1. Among these parameters, relative permittivity, viscosity, surface tension and density were obtained from literature while conductivity was measured. The required conductivity was obtained by adding a few drops of a solution made from lithium nitrate, nickel nitrate and manganese nitrate in 2-propanol for experiment 1, n-methyl-2-pyrrolidone (NMP) for experiment 2 and ethylene glycol for experiment 3.

Table A2.1
Values of three different liquids parameters whose cone-jet operation window was experimentally determined

Physical parameters	Experiment 1	Experiment 2	Experiment 3
Solvent	2-propanol	n-methyl-2-pyrrolidone (NMP)	ethylene glycol
Conductivity (K) S m ⁻¹	0.0003	0.0011	0.0003
Density (ρ) kg m ⁻³	785	1027	1113
Surface tension (γ) N/m	0.0217	0.0418	0.0473
viscosity (μ) Pa s	0.00238	0.00165	0.0161
Relative permittivity	19.26	33	37

The experimental parameters for the electrospray process were.
 Nozzle type = Optimum® general purpose stainless steel dispense tips (Red).
 Nozzle inner diameter = 0.25 mm.
 Nozzle outer diameter = 0.52 mm.
 Nozzle to substrate distance = 2 cm.
 Operating temperature = room temperature (was not measured but expected to be around 25 °C).
 Orientation = downward spraying.

To get an idea of the starting flow rate for each liquid, Q_0 , $Q_{min,est}$ and $Q_{min,fit}$ values were calculated as shown in Table A2.2. The starting flow rate was critical in selecting a syringe with the correct diameter to cover the required flow rate range for each liquid.

Table A2.2
Calculated Q_0 and Q_{min} values for the three precursor liquids.

Parameter	2-propanol	NMP	ethylene glycol
$Q_0 = \frac{\epsilon_0 \gamma}{\rho K} \frac{nl}{s}$	0.815	0.3275	1.25
$Q_{min,est} = \frac{6.1}{C_{VN}^2} Q_0$	4.972	1.998	7.625
$Q_{min,est,flat} = 6.1 Q_0 \frac{nl}{s}$			
$Q_{min,fit} = 8.175 Q_0^{0.474} \frac{nl}{s}$	7.42	4.82	9.09

(note that 1E-12 m³/s = 1 nl/s).
 Using Q_{min} flat profile, the viscosity number (VN) is found to be less than one for all the three liquids leading to the selection of the equation for $Q_{min,est,flat}$.

To determine the cone-jet window for each precursor liquid, electrospray experiments were carried out spraying downwards in cone-jet mode using nozzle to plate setup, with nozzle on high voltage and plate grounded. After setting the pump at the selected starting flow rate, if possible close to the calculated Q_{min} , the applied voltage was then increased slowly starting from zero with an aim of attaining stable cone-jet mode. From the

experiments, it was observed that a steady cone could only be attained within a given range of the applied voltage. For instance, in experiment 1, a steady cone is attained at $Q = 55.56 \text{ nl/s}$ within a voltage range of 4.6–5.8 kV. Starting for these 3 liquids, with the lowest possible flow rate, as determined by the pump, the flow rate was then increased each time recording the voltage range within which a stable cone was observed, using the naked eye, and the values recorded as shown in Table A2.3. Before reaching V_1 , a pulsating cone was observed which turned into a stable cone for voltage values between V_1 and V_2 , then above V_2 the cone splits into multiple jets. For 2-propanol and ethylene glycol, the lowest flow rate values that could be measured are close to the minimum flow rates. However, for NMP no value for Q_{\min} or close to Q_{\min} could be measured with the available pump. For all the three liquids, the highest flow rate values measured are their maximum flow rates. When the flow rate is increased beyond the indicated Q_{\max} , the cone jet became unstable for all liquids, i.e. the cone jet shifted from the center to the side, i.e. the jet deviated from the nozzle axis. For each liquid, the experiments were performed in duplicate, and the average values later used to plot curves.

Table A2.3

Experimental flow rate and voltage values defining the cone-jet window for each precursor liquid used.

Precursor liquid	Flow rate (nl s^{-1})	Experiment 1		Experiment 2		Average	
		V_1 (kV)	V_2 (kV)	V_1 (kV)	V_2 (kV)	V_1 (kV)	V_2 (kV)
2-propanol	5.56	4.2	4.5	4.2	4.45	4.2	4.475
	13.89	4.25	4.8	4.25	4.75	4.25	4.775
	22.22	4.3	5.1	4.35	5.15	4.325	5.125
	27.78	4.35	5.15	4.4	5.3	4.375	5.225
	55.56	4.55	5.75	4.6	5.8	4.575	5.775
	138.89	5.2	6.1	5.1	6.2	5.15	6.15
	194.45	5.6	6.25	5.5	6.3	5.55	6.275
	277.78	6.1	6.45	6.0	6.45	6.05	6.45
	361.11	6.4	6.5	6.35	6.45	6.375	6.475
	416.67	6.4	6.4	6.35	6.35	6.375	6.375
NMP	27.78	8	8.9	8	8.8	8	8.85
	55.56	8.2	8.9	8.2	8.9	8.2	8.9
	83.33	8.4	8.95	8.4	8.95	8.4	8.95
	111.11	8.7	8.95	8.7	8.95	8.7	8.95
	138.89	9	9	9	9	9	9
	Ethylene glycol	5.56	6.5	6.7	6.9	7.1	6.7
8.33	6.5	6.8	6.9	7.4	6.7	7.1	
11.11	6.7	7	6.9	7.4	6.8	7.2	
13.89	6.8	7	6.9	7.4	6.9	7.2	
27.78	6.9	7.6	6.9	7.6	6.9	7.6	
55.56	6.8	7.7	6.8	7.7	6.8	7.7	
83.33	6.8	8.3	6.8	7.7	6.8	8	
111.11	6.8	8.3	6.8	7.7	6.8	8	
138.89	6.8	8.4	6.8	7.8	6.8	8.1	
277.78	7	8.4	7	7.8	7	8.1	
416.67	7.4	8.5	7.4	7.9	7.4	8.2	
555.56	8.4	8.5	8.4	8.5	8.4	8.5	
583.34	8.4	8.4	8.4	8.4	8.4	8.4	8.4

For each experiment, a curve of voltage versus flow rate was then plotted. The lowest measured flow rate values on the left side of the curve gave values close to the minimum flow rates for 2-propanol and ethylene glycol while the highest measured flow rate values on the right side of the curve gave values of the maximum flow rates for the three liquids.

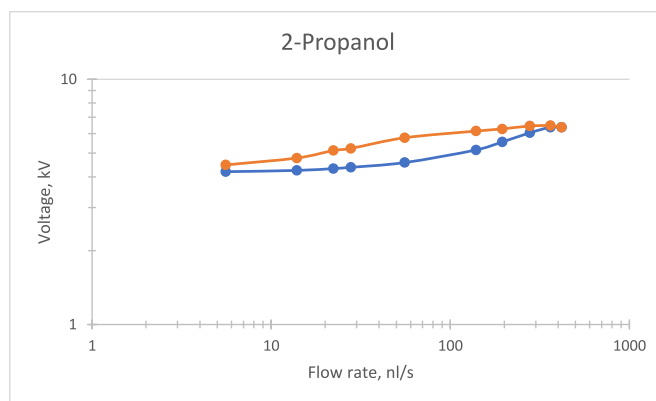


Fig. A2.1. Voltage-flow rate curve used for the determination of the minimum flow rate (Q_{\min}) and the cone jet window for 2-propanol.

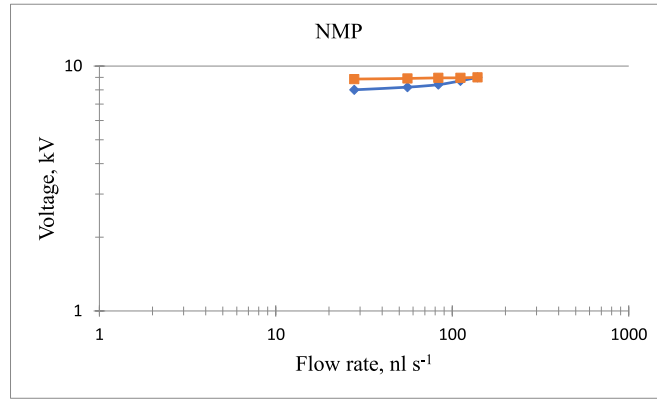


Fig. A2.2. Voltage-flow rate curve used for the determination of the cone-jet window for NMP.

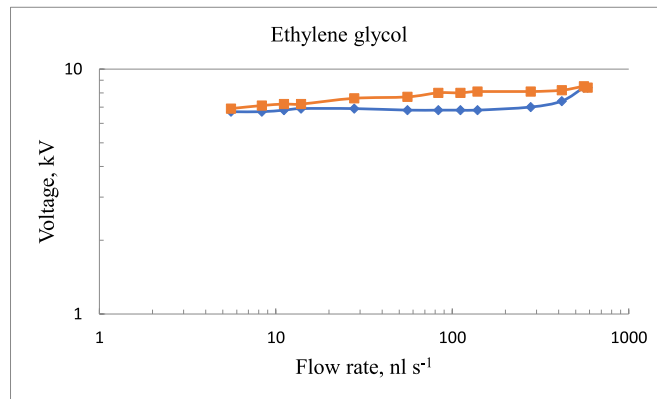


Fig. A2.3. Voltage-flow rate curve used for the determination of the minimum flow rate (Q_{min}) and the cone jet window for ethylene glycol

Appendix 3. Stress on the jet due to air friction

We consider the stress due to the air friction on the jet. Let us assume that it is

$$\sim \mu_g \frac{v}{D} \tag{A3.1}$$

Where μ_g is the gas (air) viscosity, D is the diameter of the jet, and v the velocity of the jet. So the air friction stress increases with increasing v and increases with decreasing D . We consider varicose break-up and a flat radial profile of the axial velocity in the jet.

For D we use equation (4):

$$D = \left(\frac{\rho \epsilon_o Q^4}{I^2} \right)^{\frac{1}{6}}$$

For I equation (6), with $C_{VN} = 1$

$$I = (2)(\gamma K Q)^{\frac{1}{2}}$$

So

$$D = \left(\frac{\rho \epsilon_o Q^3}{4\gamma K} \right)^{\frac{1}{6}} \text{ with } Q = Q_{min}$$

In general for a liquid with only changing K :

$$D \sim \frac{Q_{min}^{\frac{1}{2}}}{K^{\frac{1}{6}}}, Q_{min} \sim Q_o = \frac{\epsilon_o \gamma}{K \rho}$$

$$D \sim \left(\frac{\epsilon_o \gamma}{K \rho} \right)^{\frac{1}{2}} / K^{\frac{1}{6}} \sim \frac{1}{K^{\frac{1}{2}} K^{\frac{1}{6}}} = \frac{1}{K^{\frac{2}{3}}} \tag{A3.2}$$

$$v = \frac{Q_{min}}{A} \sim \frac{\epsilon_0 \gamma}{K \rho \left(\pi \frac{D^2}{4}\right)} \sim \frac{1}{KD^2} \quad \text{with (A3.2)} = \frac{1}{K \left(\frac{1}{K^{\frac{1}{3}}}\right)^2} = K^{\frac{1}{3}} \quad (\text{A3.3})$$

So for one liquid with only changing K: if K increases, D decreases and v increases, and the stress by the air friction increases.

Now we consider, as done in the text, ethylene glycol with i) K = 100 $\mu\text{S/m}$ and ii) K = 9960 $\mu\text{S/m}$ (in Table 2 this is rounded off till K = 0.0100 S/m). For both i) and ii) there is a flat velocity profile, and varicose break-up.

- i) For $K_i = 100 \mu\text{S/m}$, $v_i \sim 16 \text{ m/s}$ (see text). $D_i = \left(\frac{(1110)(8.85E-12)(16.7E-12)^3}{4(0.048)(0.0001)}\right)^{\frac{1}{6}} = 1.16E - 6\text{m}$.
- ii) For $K_{ii} = 9960 \mu\text{S/m}$, $v_{ii} \sim 74 \text{ m/s}$ (see text). $D_{ii} = \left(\frac{(1110)(8.85E-12)(1.2E-12)^3}{4(0.048)(9960E-6)}\right)^{\frac{1}{6}} = 1.44E - 7\text{m}$ so for case ii) equation (A3.1) $\sim (74/1.44E-7)$ and for i) $\sim (16/1.16E-6)$ and their ratio is about 37.

The difference will be less because of slip. For spherical aerosol particles the slip correction factor for $d = 1.16 \text{ mm}$ is $C_c \sim 1.13$ and for $d = 0.144 \text{ mm}$ is $C_c \sim 2.28$ (realize that C_c comes in the denominator of eq. A3.1). (Hinds 1998) [28]

N.B. if we compare these results with A3.2, we get

$$\frac{D_i}{D_{ii}} = \frac{\frac{1}{K_i^{\frac{1}{3}}}}{\frac{1}{K_{ii}^{\frac{1}{3}}}} = \frac{K_{ii}^{\frac{1}{3}}}{K_i^{\frac{1}{3}}}$$

so $D_i = \frac{K_{ii}^{\frac{1}{3}}}{K_i^{\frac{1}{3}}} D_{ii} = 3E - 6 \text{ m}$ (in reality $D_i = 1.16E-6 \text{ m}$, so slightly out but order of magnitude OK).

And with A3.3

$$\frac{v_i}{v_{ii}} = \frac{K_i^{\frac{1}{3}}}{K_{ii}^{\frac{1}{3}}} \text{ so } v_i = \frac{K_i^{\frac{1}{3}}}{K_{ii}^{\frac{1}{3}}} = 15.96 \text{ m/s}$$

References

- [1] C.U. Yurteri, R.P.A. Hartman, J.C.M. Marijnissen, Producing pharmaceutical particles via electrospraying with an emphasis on nano and nano structured particles - a review, *KONA Powder and Particle Journal* 28 (2010) 91–115, <https://doi.org/10.14356/kona.2010010>.
- [2] R.P.A. Hartman, Electrohydrodynamic Atomization in the Cone-Jet Mode. From Physical Modeling to Powder Production, Doctoral Thesis, TUDelft, 1998. <http://resolver.tudelft.nl/uuid:1e45ec16-5860-4977-8585-edaeeaa99f6b>.
- [3] R.P.A. Hartman, D.J. Brunner, D.M.A. DMA, J.C.M. Marijnissen, B. Scarlett, Jet break-up in electrohydrodynamic atomization in the cone-jet mode, *J. Aerosol Sci.* 31 (1) (2000) 65–95, [https://doi.org/10.1016/S0021-8502\(99\)00034-8](https://doi.org/10.1016/S0021-8502(99)00034-8).
- [4] A.M. Gañán Calvo, On the theory of electrohydrodynamically driven capillary jets, *J. Fluid Mech.* 335 (1997) 165–188, <https://doi.org/10.1017/S0022112096004466>.
- [5] J. Rosell Llompart, J. Fernández de la Mora, Generation of monodisperse droplets 0.3 to 4 μm in diameter from electrified cone-jets of highly conducting and viscous liquids, *J. Aerosol Sci.* 25 (6) (1994) 1093–1119, [https://doi.org/10.1016/0021-8502\(94\)90204-6](https://doi.org/10.1016/0021-8502(94)90204-6).
- [6] A.M. Gañán-Calvo, The size and charge of droplets in the electrospraying of polar liquids in cone-jet mode, and the minimum droplet size, *J. Aerosol Sci.* 25 (Supplement 1) (1994) 309–310, [https://doi.org/10.1016/0021-8502\(94\)90384-0](https://doi.org/10.1016/0021-8502(94)90384-0).
- [7] D.R. Chen, Y.H. David, D.Y.H. Pui, Experimental investigation of scaling laws for electrospraying: dielectric constant effect, *Aerosol Sci. Technol.* 27 (3) (1997) 367–380, <https://doi.org/10.1080/02786829708965479>.
- [8] W.J. Scheideleer, C.-H. Chen, The minimum flow rate scaling of Taylor cone-jets issued from a nozzle, *Appl. Phys. Lett.* 104 (2014), 024103, <https://doi.org/10.1063/1.4862263>.
- [9] A.M. Gañán-Calvo, N. Rebollo-Muñoz, J.M. Montanero, The minimum or natural rate of flow and droplet size ejected by Taylor cone-jets: physical symmetries and scaling laws, *New J. Phys.* 3 (15) (2013) 1367–2630, <https://doi.org/10.1088/1367-2630/15/3/033035>.
- [10] A.M. Gañán-Calvo, J. Dávila, A. Barrero, Current and droplet size in the electrospraying of liquids. Scaling laws, *J. Aerosol Sci.* 28 (2) (1997) 249–275, [https://doi.org/10.1016/S0021-8502\(96\)00433-8](https://doi.org/10.1016/S0021-8502(96)00433-8).
- [11] A. Ponce-Torres, N. Rebollo-Muñoz, M. Herrada, A. Gañán-Calvo, J. Montanero, The steady cone-jet mode of electrospraying close to the minimum volume stability limit, *J. Fluid Mech.* 857 (2018) 142–172, <https://doi.org/10.1017/jfm.2018.737>.
- [12] M. Gamero-Castaño, M. Magnani M, The minimum flow rate of electrosprays in the cone-jet mode, *J. Fluid Mech.* 876 (2019) 553–572, <https://doi.org/10.1017/jfm.2019.569>.
- [13] B.K. Ku, S.S. Kim, Electrospray characteristics of highly viscous liquids, *J. Aerosol Sci.* 33 (10) (2002) 1361–1378, [https://doi.org/10.1016/S0021-8502\(02\)00075-7](https://doi.org/10.1016/S0021-8502(02)00075-7).
- [14] Q. Wang, Z. Wang, S. Yang, B. Li, H. Xu, K. Yu, J. Wang, Experimental study on electrohydrodynamic atomization (EHDA) in stable cone-jet with middle viscous and low conductive liquid, *Exp. Therm. Fluid Sci.* 121 (2021), 110260, <https://doi.org/10.1016/j.expthermflusci.2020.110260>.
- [15] F.J. Higuera, Qualitative analysis of the minimum flow rate of a cone-jet of a very polar liquid, *J. Fluid Mech.* 816 (2017) pp428–441, <https://doi.org/10.1017/jfm.2017.111>.
- [16] M. Cloupeau, B. Prunet-Foch, Electrostatic spraying of liquids in cone-jet mode, *J. Electrostat.* 22 (2) (1989) 135–159, [https://doi.org/10.1016/0304-3886\(89\)90081-8](https://doi.org/10.1016/0304-3886(89)90081-8).
- [17] A.M. Gañán-Calvo, J.M. Montanero, Revision of capillary cone-jet physics: Electrospray and flow focusing, *Phys. Rev. E*, (2009), 79, {6}, 066305, doi = 10.1103/PhysRevE.79.066305.
- [18] J.L. Castillo, S. Martin, D. Rodriguez-Perez, F.J. Higuera, P.L. Garcia-Ybarra, Nanostructured porous coatings via electrospray atomization and deposition of nanoparticle suspensions, *J. Aerosol Sci.* 125 (2018) 148–163, <https://doi.org/10.1016/j.jaerosci.2018.03.004>.
- [19] A.M. Gañán-Calvo, J.M. López-Herrera, M.A. Herrada, A. Ramos, J.M. Montanero, Review on the physics of electrospray: from electrokinetics to the operating conditions of single and coaxial Taylor cone-jets, and AC electrospray, *J. Aerosol Sci.* 125 (2018) 32–56, <https://doi.org/10.1016/j.jaerosci.2018.05.002>.
- [20] K. Tang, A. Gomez, Monodisperse electrosprays of low electric conductivity liquids in the cone-jet mode, *J. Colloid Interface Sci.* 184 (2) (1996) 500–511, <https://doi.org/10.1006/jcis.1996.0645>.
- [21] K. Tang, A. Gomez, Generation by electrospray of monodisperse water droplets for targeted drug delivery by inhalation, *J. Aerosol Sci.* 25 (6) (1994) 1237–1249, [https://doi.org/10.1016/0021-8502\(94\)90212-7](https://doi.org/10.1016/0021-8502(94)90212-7).
- [22] J. Fernández de la Mora, I. Loscertales, The current emitted by highly conducting Taylor cones, *J. Fluid Mech.* 260 (1994) 155–184, <https://doi.org/10.1017/S0022112094003472>.
- [23] I. Hayati, A.I. Bailey, ThF. Tadros, Investigations into the mechanisms of electrohydrodynamic spraying of liquids I. Effect of electric field and the environment on pendant drops and factors affecting the formation of stable jets and atomization, *J. Colloid Interface Sci.* 117 (1) (1987) 205–221, [https://doi.org/10.1016/0021-9797\(87\)90185-8](https://doi.org/10.1016/0021-9797(87)90185-8).
- [24] R.P.A. Hartman, D.J. Brunner, D.M.A. Camelot, J.C.M. Marijnissen, B. Scarlett, Electrohydrodynamic atomization in the cone-jet mode physical modelling of the liquid cone and jet, *J. Aerosol Sci.* 30 (7) (1999) 823–849, [https://doi.org/10.1016/S0021-8502\(99\)00033-6](https://doi.org/10.1016/S0021-8502(99)00033-6).
- [25] A.M. Gañán-Calvo, A. Barrero, C. Pantano-Rubiño, The electrohydrodynamics of electrified conical menisci, *Journal of Aerosol Science* 24 (Suppl. 1) (1993) S19–S20, [https://doi.org/10.1016/0021-8502\(93\)90102-F](https://doi.org/10.1016/0021-8502(93)90102-F).

- [26] A.M. Gañán-Calvo, The surface charge in electrospraying: its nature and its universal scaling laws, *J. Aerosol Sci.* 30 (7) (1999) 863–872, [https://doi.org/10.1016/S0021-8502\(98\)00780-0](https://doi.org/10.1016/S0021-8502(98)00780-0).
- [27] J. van Erven, R. Moerman, C.M. Jan, C.M. Marijnissen Jan, Platinum nanoparticle production by EHDA, *Aerosol. Sci. Technol.* 39 (10) (2005) 929–934, <https://doi.org/10.1080/02786820500346587>.
- [28] W.C. Hinds, *Aerosol Technology: Properties, Behaviour, and Measurement of Airborne Particles*, second ed., Wiley, 1999.